DISSERTATION

Growth and structure of ultrathin silicates and germanates containing iron oxide

Im Fachbereich Physik der Freien Universität Berlin eingereichte
Dissertation zur Erlangung des Grades
Doktor der Naturwissenschaften (Dr. rer. nat.)
vorgelegt von

M.Sc. Gina Peschel

Berlin 2018

Die hier vorliegende Arbeit wurde am Fritz-Haber-Institut der Max-Planck Gesellschaft in der Abteilung Chemische Physik unter Anleitung von Prof. Dr. Hans-Joachim Freund, in der Spectro-Mikroskopie Arbeitsgruppe, Gruppenleiter Dr. Thomas Schmidt, angefertigt.

Erstgutachter: Prof. Dr. Hans-Joachim Freund
Zweitgutachter: Prof. Dr. Katharina Franke
Tag der Disputation: 20.09.2018

Abstract

This work presents a detailed study of ultrathin films of FeO, iron silicate, and iron germanate on Ru(0001). These two-dimensional structures are suitable model systems for catalytically active structures, such as zeolites, which are known for their good catalytic properties, for instance as molecular sieves or selective catalysts. This work applies the methods of LEEM, μLEED, μXPS and XPEEM for a detailed and comprehensive investigation of chemical and physical properties of these films. The temperature dependent film formation is studied in real-time and in situ.

Ultrathin FeO films were prepared by direct deposition of iron onto a Ru(0001) single crystal support at elevated temperatures. Dependent on the oxygen pressure monolayer-thick or bilayer-thick FeO films are found to grow in a Stranski-Krastanov growth, i.e. a complete wetting layer followed by three-dimensional islands, whereas the latter grow as Fe_3O_4 crystallites. Different metastable sub-phases are structurally and chemically characterized and their transformation into other more stable phases is addressed.

Ultrathin iron silicate films consist of a monolayer of silica on top of a monolayer of iron oxide. The work, presented in this thesis, brought new insights into the structure of these layers. In particular, the measurements suggest that the number of iron atoms per silica unit cell in the iron oxide layer is two and that an additional oxygen layer at the iron/ruthenium interface is present. The Fe-Fe distance is found to be adapted to the Si-O-Si distance in unstrained silicates, rather than being influenced by the ruthenium substrate. Four different preparation methods have been developed in order to study the film formation in dependence of temperature and oxygen pressure. The films were characterized with regard to their thermal stability and chemical and physical properties. Moreover, the iron silicate structure was varied and prepared with two layers of iron oxide or two layers of silica, respectively. Both additional layers are found to be stable if grown as complete layers, and adapted to the monolayer iron silicate film structure. The study of incomplete layers brought new insights into the dynamic processes and thermal stability. In particular, iron migration was found to start at iron silicate domains, when silicon was deposited on top of FeO islands. The migrating iron binds to silica in initially iron-free domains, where again iron silicate is formed. For monolayer-thick FeO films this takes in form of about 50 nm small isolated islands. In bilayer-thick FeO films a two-step process is found: First a rim is formed consisting of monolayer-thick iron silicate. In a second step small isolated islands are formed additionally.

Ultrathin iron germanate films are found to have almost the same structure as iron silicate films, i.e. a monolayer of germania is bound on top of a monolayer of iron oxide. However, the Fe-Fe distance is adapted to the length of Ge-O-Ge bonds in unstrained germanates. Different preparation methods show that these films are energetically stable in the investigated temperature (between 300 K and 840 K) and pressure (up to 10^{-6} mbar) range.

Zusammenfassung

Diese Arbeit präsentiert eine detaillierte Studie ultradünner Filme auf Ru(0001), wie FeO, Eisensilikat und Eisengermanat. Diese zweidimensionalen Strukturen sind geeignete Modellsysteme für katalytisch aktive Strukturen wie Zeolite, welche für ihre guten katalytischen Eigenschaften bekannt sind, z.B. als molekulares Sieb oder selektiver Katalysator. In dieser Arbeit werden die Methoden LEEM, μLEED, μXPS und XPEEM für eine detaillierte und umfassende Untersuchung der chemischen und physikalischen Eigenschaften dieser Filme verwendet. Ihre temperaturabhängige Filmentstehung wurde in Echtzeit und *in situ* untersucht.

Ultradünne FeO Filme wurden durch Aufdampfen von Eisen direkt auf eine Ru(0001) Einheitskristallunterlage bei hohen Temperaturen präpariert. Abhängig von dem Sauerstoffdruck wachsen monolagen- oder bilagendicke Filme im Stranski-Krastanov Wachstum, d.h. in Form einer Benetzungslage, gefolgt von dreidimensionalen Inseln. Letztere wachsen als Fe_3O_4 Kristallite. Verschiedene metastabile Unterphasen werden strukturell und chemisch charakterisiert und deren Umwandlung in andere, stabilere Unterphasen behandelt.

Ultradünne Eisensilikatfilme bestehen aus einer Monolage Silikat auf einer Monolage Eisenoxid. Die hier präsentierte Arbeit brachte neue Einblicke in die Struktur dieser Lagen. Insbesondere deuten die Messungen darauf hin, dass die Anzahl der Eisenatome pro Einheitszelle des Silikats in der Eisenoxidlage zwei ist und dass eine zusätzliche Sauerstofflage am Eisen/Ruthenium Übergang existiert. Zudem passt sich der Eisen-Eisen Abstand eher an den Si-O-Si Abstand in ungespannten Silikaten an, als dass es von dem Ruthenium Substrat beeinflusst wird. Vier verschiedene Präparationsmethoden wurden entwickelt, um die Filmausbildung in Abhängigkeit von der Temperatur und des Sauerstoffdrucks zu untersuchen. Die Filme wurden charakterisiert im Hinblick auf ihre thermische Stabilität, sowie ihren chemischen und physikalischen Eigenschaften. Desweiteren wurde die Eisensilikatstruktur variiiert und jeweils mit zwei Lagen Eisenoxid oder zwei Lagen Silikat präpariert. Beide zusätzlichen Lagen sind stabil bei geschlossenen Filmen und angepasst an die Struktur der Eisensilikatmonolage. Die Studie ungeschlossener Filme brachte neue Einblicke in die dynamischen Prozesse und thermische Stabilität dieser. Eisenmigration von Eisensilikatinseln wurde in Filmen gefunden, bei denen Silizium auf FeO aufgedampft wurde. Das migrierende Eisen bindet an Silikat in ursprünglich eisenfreien Domänen, wodurch erneut Eisensilikat geformt wird. Für monolagendicke FeO Filme geschieht dies in Form von 50 nm kleinen isolierten Inseln. In bilagendicken FeO Filmen gibt es einen zweistufigen Prozess: Erst bildet sich ein Rand aus monolagendickem Eisensilikat. In einem zweiten Schritt werden zusätzlich kleine isolierte Inseln geformt.

Ultradünne Eisengermanatfilme haben fast die gleiche Struktur wie Eisensilikatfilme, d.h. eine Monolage Germania ist auf einer Monolage Eisenoxid gebunden. Die Eisen-Eisen Abstände sind jedoch an die Ge-O-Ge Bindungslängen in stressfreien Germanaten angepasst. Verschiedene Präparationsmethoden zeigen, dass diese Filme energetisch stabil in dem untersuchten Temperatur- (300 K - 840 K) und Druckbereich ($\leq 10^{-6}$ mbar) sind.

Contents

Chapter 1

Introduction

1.1 Importance of silicates in industry and nature

Silica and silicates belong to the most abundant materials on earth. They are found as sand and rocks, and constitute a major part of the earth crust and mantle [36]. They can be easily purified, and large crystals with low impurities can be grown [18]. This accessibility makes them perfect candidates for functional materials.

In many of these appearances pure silica (silicon dioxide) is present in its diversity of crystal structures, while in others, compounds of silicon and silica with other materials are observed. Silicon can take over the cationic part (for instance in SiP_2O_7) or it can take over the anionic part as part of silicon dioxide (for instance Mg_2 $[SiO_4]$) [55]. The latter are termed silicates, and many include metal atoms. Since silica itself is inert, the addition of metal atoms makes it catalytically more active and the high diversity of silicate structures leads to industrial applications, adapted to the individual field of application.

Silica and silicates can be found in many geological forms and crystal structures, crystalline, polycrystalline and amorphous (vitreous) [40]. Moreover they have a large number of compelling characteristics like large thermal conductivity, excellent mechanical properties, moderate ionization energies, and high dielectric strength [18]. These characteristics make them suitable for a diversity of industrial applications. Besides the use as construction materials like glass, cement, clay and ceramics they are employed in microelectronics as material for semiconductor devices like transistors [18, 40, 108]. Moreover they are found in optical fibers and telescope glasses.

A special form of silicates is zeolites. Zeolites are known for their variable porous structure, which gives them a large catalytically active surface and a size selectivity for atoms and molecules. Thus they are used as molecular sieves. They consist of three-dimensional frameworks of interconnected tetrahedrons which typically contain silicon, aluminium, and oxygen atoms. In aluminosilicates it is common that 1/3 of the silicon Si^{4+} atoms are exchanged by Al^{3+} atoms, which results in a slightly higher electronegativity of the crystal. This electronegativity can be compensated by positive cations [38] like Na^+, Ca^{2+}, Mg^{2+} or Fe^{2+}, which are located in the voids between the tetrahedrons. These active cations can be substituted with other cations (ion exchangers). For instance sodium aluminosilicate (zeolite A) is used as water softener in detergents. In this case, calcium, responsible for limescale in the water, is bound to the zeolites and in return sodium is released to the water.

The incorporation of iron in zeolites enhances strongly the catalytic activity in many reactions such as the oxidation of benzene to phenol with nitrous oxide [32] or the reduction of nitrogen oxides [52,73] in catalysis. Iron zeolites have demonstrated the applicability as selective catalysts (in the form of Fe-ZSM-5) and as molecular sieves (Fe-MCM-41) [71]. In silicates iron is known to avoid tetrahedral sites of a silicate framework [71] and is often found in interstitial places like in fayalites Fe_2 SiO_4; or they form layers as in phyllosilicate nontronite with Fe:Si ratio of 1:2 [19].

1.2 Silicates as model systems

The structures and chemical reactions in industrial catalytic processes are complex in most cases. A way to understand the relevant catalytic processes is to prepare a simplified model system with reduced complexity on a 2D basis. With these models it is possible to learn more about the individual characteristics such as bonding strength, structural formation and structure-reactivity relations. Moreover due to the reduced dimensionality, properties can be explored that are due to the unique structure of 2D materials. Due to the thickness in the regime of single atomic layers, two-dimensional structures have an extraordinarily high surface to bulk ratio, or in the case of a monolayer, only surface properties. Key properties, such as electronic configuration or physical stability are strongly influenced by the surface. They can be selectively addressed and analyzed under UHV conditions. A comprehensive understanding of these properties allows a functionalization and a transfer to ambient conditions and utilization.

Metal substrates have proved to be a good basis for ultrathin two-dimensional silica layers. The first crystalline silica layer was prepared in 2000 on Mo(112) by Schroeder et al. [87]. Later, a preparation on Ru(0001) was successfully performed by Yang et al. in 2012 [107]. The structure of a silica monolayer consists of corner sharing tetrahedrons with oxygen atoms positioned in the corner of these tetrahedrons. Hereby, three oxygen atoms are in plane, building a top triangle of the tetrahedron, and the fourth oxygen atom binds perpendicular to the metal substrate [77,101]. Viewed from the top the silica layer is forming six-coordinated ring structures, giving rise to a (2x2) structure in LEED [87]. This silica monolayer is strongly bound to the substrate via the oxygen bridge [107].

While on Mo(112) only a silica monolayer is formed, on Pd(111) [97] and Pt(111) [109] only silica bilayer films can be prepared. In contrast to the monolayer the crystalline silica bilayer lacks the oxygen bridge between the silica layer and the substrate. In contrast, the oxygen binds within the two silica layers and thus, saturates itself. This results in an only van-der-Waals bound double layer [107]. It is furthermore possible to transfer the silica bilayer from the as-prepared metal atom to a different substrate [9,11], making it applicable for industrial applications. The silica bilayer can be crystalline, zig-zag structured or vitreous [49] yielding the according diffraction patterns in the form of a (2x2) structure, a star, or an isotropic ring shape. In the vitreous form, the coordination number varies between 4 up to 9-fold rings. On Pd(111) [97] only the crystalline and on Pt(111) [109] only the vitreous bilayer was found. Whether a film can be crystalline, vitreous or both is defined by the lattice mismatch between the substrate and the unperturbed bond distance in the silica bilayer [97]. The monolayer only forms a crystalline structure due to the strong bonding to the substrate.

The strength of the metal-oxygen bond was found to be decisive for the presence of a

monolayer, bilayer or both [89]. Compared to the strong Mo-O bond , the Pt-O bond is very weak. Ruthenium has an intermediate Ru-O bond strength. In fact, on Ru(0001) the complete variety of phases can be found: crystalline monolayer films, as well as crystalline, zig-zag and vitreous bilayer silica films [49]. In case of the silica bilayer, the zig-zag bilayer can be transformed into the crystalline bilayer by oxidation. Subsequently, the vitreous phases can be produced through phase transitions from the crystalline bilayer. Important for the individual arrangement of the two-dimensional silica films is the oxygen layer between the Ru(0001) substrate and the silica layer. For instance a depletion of the oxygen layer in silica monolayer films changes the arrangement of the layer regarding the Ru(0001) substrate from a (2x2) orientation to a (2x2)R30° orientation [44].

The silica mono- and bilayers are inert. In analogy to three-dimensional silicates, the addition of metal atoms can enhance catalytic activity of the films and approach the industrially used systems. The first addition to the silica system was aluminum in 2012 [13] in order to prepare aluminosilicate bilayer films. Depending on the Al:Si ratio, domains are found that either contain aluminum or are aluminum free. The aluminum atoms substitute silicon atoms in the upper and in the lower level of such a bilayer. However, Loewenstein's rule permits Al-O-Al bonds [56], so that aluminum atoms are never found next to each other within one layer. In aluminum-containing domains aluminum is homogeneously distributed [13].

In 2013 the addition of iron to silica films was studied by Włodarczyk et al. [103]. Unlike aluminum, iron does not simply substitute silicon atoms. In the DFT calculations by Włodarczyk et al., a silica bilayer is used as a basis and one iron atom per unit cell per time is added to the matrix. The calculations indicated that iron substitutes silicon atoms only in the lower level of a silica bilayer. Every additional iron atom favors a position close to already existing iron atoms. The close-packed situation indicates that the lower level of such a silica bilayer is completely filled with iron. As a result the iron layer shifts relative to the silica layer on top. In contrast, actual measurements showed no (2x2) structure as suggested by simulations, but rather a 30° rotated structure, as well as Moiré spots. Moreover IRAS and XPS results indicate a two-layered film with silica on top of an iron oxide layer. The same kind of layer structure was found for Ti-atoms [25]. Moreover pure silica domains were found to be more likely in crystalline form, when in contact to iron silicate [53]. A combination of iron and aluminum showed the separation of pure iron silicate and aluminosilicate domains. Only for high Fe/(Si+Al) molar ratios iron silicate forms aluminium clusters on top [96].

Up to now only the final structure of these ultrathin iron silicate films has been reported. The formation process, energetic dependencies and the real structure remain unknown. The main part of this thesis concentrates on these open questions using the methods LEEM, μLEED, μXPS and XPEEM. They are addressed in chapter 4.

1.3 Germanates

Germanium is part of the group IV materials and one period higher than silicon. Group IV materials in general are interesting for many applications, for instance in optoelectronics [79] and electronic memory [16]. Germania, as well as silica, can be found in quartz- and vitreous forms [69] and turn out to have similar bonding lengths. Moreover the ionization potentials and electronegativities are similar [29]. Thus, germania can be seen as an excellent chemical and structural analogue to silica [98]. Germanates at ambient conditions can even be used as model structures for high pressure silicates [29]. As a difference the refraction index of germania and its electron mobility are larger than those of silica. Germanium can be integrated into a silica matrix, either by doping or by the preparation of mixed glasses. Examples for doping are optical fibers, in which the silica core is doped by germanium in order to increase the refractive index, while the cladding material is pure silica [76]. Already in the 1950s mixed GeO_2-SiO_2 glasses have been investigated. It was found that individual tetrahedra of GeO_4 and SiO_4 build a corner-linked network, with Ge-O-Ge, Ge-O-Si and Si-O-Si bonds. In average the Ge-O-Ge and Ge-O-Si bonds have mean angles similar to that in pure GeO_2 glasses [57], which shows how nicely germania integrates into silica glasses. Moreover, silica glasses containing germanium have a lower amount of small size rings, i.e. fewer defect lines. The mixing of germanium and silicon can be performed in different material types, like the olivine type [78], willemite type [37] and zeolite type [5, 6]. Apart from intermixed silicon-germanium systems, silicon can also be completely exchanged by germanium. For instance, the usage of germanium in MOSFETS could lead to a performance increase, due to the higher electron and hole mobility of germanium in contrast to silicon [64, 111].

While these mixed glasses often are three-dimensional networks, the investigation of ultrathin two-dimensional films opens the possibility to study model systems. As discussed in the previous section ultrathin layers of silica have been investigated extensively [10, 15, 39, 45, 90]. Lately, ultrathin monolayer films of germania have been produced on Ru(0001) [51]. The germania monolayer consists of corner-sharing GeO_4 tetrahedra. Similar to the silica monolayer the germania monolayer consists of six-fold coordinated ring systems in plane which are linked via oxygen atoms to the Ru(0001). The monolayer is strongly bound to the Ru(0001) substrate. In contrast to ultrathin silica monolayer the germania monolayer has more variations in the angular arrangement of the tetrahedral building units and a more graded interaction of the films system with Ru(0001) [51].

Using the knowledge of ultrathin germania layers on Ru(0001), the next step is to substitute silicon in iron silicate films by germanium. Due to the similar properties and bond lengths this is expected to be possible. Chapter 5 in this work investigates ultrathin layers of iron germanate on a Ru(0001) substrate.

1.4 Structure of this thesis

This work is divided into three main parts.

Chapter 3 investigates ultrathin FeO layer on Ru(0001). As it turns out a high variety of FeO phases can be formed due to small variations in the pressure regime. It is known that a monolayer and bilayer of FeO can grown by direct iron deposition dependent on the oxygen pressure [68]. This work investigates the individual phases within a monolayer or a bilayer of FeO, as well as their chemical structure. Section 3.1 investigates the different phases of monolayer FeO layers, section 3.2 bilayer phases and section 3.3 investigates a pressure regime where both phases grow simultaneously.

Chapter 4 is the main chapter of this work and investigates ultrathin layer of iron silicate on Ru(0001). The specific formation process of iron silicate is followed in situ and is analyzed in real time. In chapters 4.1-4.2 four different preparation methods are investigated giving rise to detailed information about film formation and their dependencies. The preparation methods are devided into two sections: In chapter 4.1 combined preparation methods are used, i.e. iron and silicon are deposited in the same condition. In section 4.2 stepwise preparation methods are shown, whereby either FeO or SiO_2 are pre-prepared before silicon or iron is deposited, respectively. In chapter 4.3 multiple layers of either FeO or SiO_2 are investigated, with only one layer of silicon or iron, respectively (section4.3.1: ML SiO_2/BL FeO/Ru(0001) and section 4.3.2: BL SiO_2/ML FeO/Ru(0001)). In both cases a stepwise preparation method is used. Apart from the possibility of multilayer films and their properties, these investigations give insight in the bonding strength of the Fe-O-Si bond. In chapter 4.4 incomplete layers are shown using different preparation methods. In section 4.4.1 the combined preparation method is used, making free arrangement of iron and silicon possible. In section 4.4.2 and 4.4.3 the stepwise preparation method is used, i.e. utilizing islands of monolayer (section 4.4.2) and bilayer FeO islands (section 4.4.3) as a basis for silicon deposition and thus, iron silicate formation. Here, the energetic stability and the border conditions can be investigated.

Finally, Chapter 5 investigates ultrathin iron germanate films on Ru(0001) for the first time. It will be shown that these films exist. The films will be characterized in correlation to their differences and similarities to iron silicate films.

Chapter 2

Methods and theory

2.1 Setup: SMART instrument

The experiments presented in this thesis have been carried out with the so-called SMART instrument (Spectro-Microscope with Aberration correction for Many Relevant Techniques). The instrument is located at the synchrotron BESSY II (Helmholtz Center Berlin) and is attached to the high flux-density undulator beamline UE49-PGM. Complementary to the soft x-rays from the synchrotron light source the sample can be illuminated by electrons using an electron gun. As a result, the instrument combines microscopic, diffraction and spectroscopic information of reflected and photoemitted electrons at the identical sample position. These different approaches were combined to employ the following experimental methods in this thesis:

Electron gun: LEEM (Low Energy Electron Microscopy), DF-LEEM (Dark-Field LEEM), LEEM-IV (intensity vs. voltage LEEM),μLEED (Micro spot Low Energy Electron Diffraction), LEED-IV (intensity vs. voltage LEED).

Synchrotron light: XPEEM (X-ray Photoemission Electron Microscopy), μXPS (Micro spot X-ray Photoelectron Spectroscopy.

The methods used in this thesis will be explained in this chapter in more detail.

To achieve the world records for lateral resolution (2.6 nm in LEEM [86]), aberration correction and energy filtering was employed in the imaging column of the instrument. The energy resolution is 180 meV [24]. The range of magnification is 500 – 100000, i.e. a field of view of 80 μm up to 0.4 μm.

The experiments are performed in situ and can be observed in real-time quasi in video rate. Using the electron gun a maximum pressure of up to $1.0 \cdot 10^{-4}$ mbar can be applied in the vicinity of the sample. For the use of synchrotron light, the pressure must be lower than $1.0 \cdot 10^{-7}$ mbar in order to open the valve to the beamline. The base pressure of the instruments main chamber is $2.0 \cdot 10^{-10}$ mbar. The sample is mounted on a transferable commercial elmitec sample holder. The sample temperature can be increased up to more than 1600 K, whereby the temperature is measured either by a spot-welded thermocouple on the sample holder or by an external infrared pyrometer. Typically the temperature is determined by the combination of both methods, where the TC is employed at temperatures below 520 K and the pyrometer above.

The scheme of the SMART-instrument is depicted in Fig. 2.1. A general overview of the

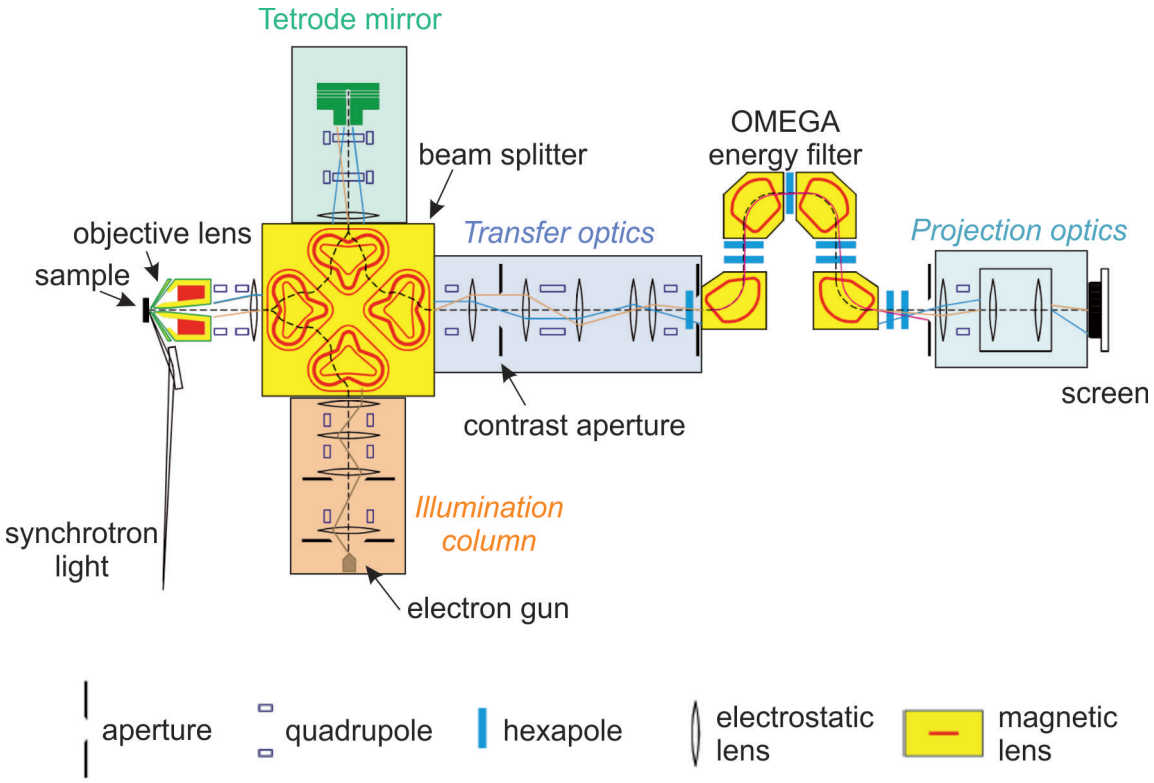

Figure 2.1 Schematic visualization of the SMART instrument.

individual parts of this instrument can be found in [8, 102].

In this instrument either electrons or synchrotron light can be used for the measurements. Both situations will be explained in more detail in the following sections.

For LEEM, DF-LEEM, LEEM-IV, μ-LEED and LEED-IV an electron beam is directed onto the sample. This electron beam is produced by a field emitter electron gun, making use of the Schottky effect. Electrons are produced by thermionic emission from a tungsten field emitter tip, which is zirconium oxide coated. The emitter potential is -15 kV. The tip points through a hole in Wehnelt cylinder focusing the electron beam. In 0.7 mm in front of the tip the extractor electrode is located with a potential of about +6 kV regarding the tip. The strong field together with the small tip radius enables the field effect, which bends the vacuum level down, thus reducing the work function. This enables a high electron emission already at 1800 K, the used temperature for the emitter. The advantage of the Schottky field effect emitter are (i) small energy broadening between 0.3 and 0.5 eV (compared to 0.7 – 1 eV at a LaB6 cathode) and (ii) high brilliance (intensity per emission area and per emission angle). Finally the beam is accelerated to the anode, an aperture at ground potential about 2 mm in front of the extractor, where the electrons reach the maximum kinetic energy of 15 keV.

Electrons leaving this electron emitter pass the illumination column in which the beam diameter is set by lenses and focused as a parallel electron beam into the magnetic beam splitter. The beam splitter consists of four sectors, in each magnetic fields are produce by three coils with specific shape, which enables a 90° deflection of the electrons without dispersion. The special focusing of the beam splitter transfers the image at the entrance

one to one to the exit plane, whereas the divergence of the beam in not changed. The double symmetry of the system leads to a vanishing of second-order aberrations [62, 102]. Direction and strength of the deflection is defined by the Lorentz force $F_L = q(\vec{v} \times \vec{B})$. Here, q is the charge of the electrons, $\vec{v}$ the corresponding velocity and $\vec{B}$ the magnetic field, produced by the coils. In the following, the electrons are introduced to the so-called cathode lens [33]. The cathode lens is composed by the objective lens, which is directly located at the beam splitter, and the sample, which acts as a lens as well. The sample voltage is -15 kV superimposed by small variation, which can be varied between -4 and +1000 V. This variation is called start voltage (StV) and creates a difference between the emitter voltage of the electron gun and the sample voltage (including work function difference), but also a potential difference between sample and energy analyzer, which will be discussed later. Thus, the electrons are exposed to an effective potential which influences how the electrons approach the sample. The electron beam homogenously illuminates an area of approximately 5 μm on the sample. As a result all information is taken only from this particular area. If the applied StV is not high enough to overcome the workfunction barrier of the sample, the electrons are back reflected, without interaction inside of the sample. This mode is called "mirror electron microscopy" (MEM). For higher values of StV the electrons can overcome this barrier and interact with the sample and are (elastically and inelastically) back-scattered and diffracted. Due to the low energies the mean free path of the electrons is in the order of 0.5-5 nm and provides a reduced interaction of the electron in one volume element with the neighboring volume element. The emitted electrons can be used for imaging in the mode of "low energy electron microscopy" (LEEM). The energetic border between these modes is addressed to as MEM-LEEM border. From this the workfunction can be determined. The utilized substrate in this thesis is Ru(0001). The workfunction of a Ru(0001) substrate known in literature [12] is 5.44 eV. The measured MEM-LEEM border in our instrument is 2.58 eV. Thus, our measured MEM-LEEM border has to be corrected by an offset of +2.86 eV in order to get the real workfunction. This offset is the same for all measurements and therefore allows the determination of absolute work function values for other surfaces.

The synchrotron light illuminates the sample at grazing incidence under an angle of 20°, increasing the illuminated area, and reducing the penetration depth of the x-rays. Due to the interaction of the X-rays with the illuminated matter, electrons are emitted due to the photoelectric effect. Depending on the incident photon energy hν and the binding energy E_B of the electrons, the emitted electrons have a certain kinetic energy which is determined by $E_{kin} = h\nu - E_B - \phi$ with the binding energy E_B and ϕ the work function. By tuning the photon energy such that the resulting kinetic energy is in the range of 50 to 100 eV, the mean free path of the emitted electrons in the material is minimal according to the universal curve [88]. This results in making this experimental method not only chemically selective, but also very surface sensitive.

The electrodes of the objective lens are at ground potential. Thus, the electrons leaving the sample are accelerated in the direction of the objective lens, reaching a kinetic energy of 15 kV. Afterwards the electrons pass the beam splitter again and are transferred to a tetrode mirror [72, 80]. The objective lens causes aberrations, which leads to a decreased lateral resolution. In the tetrode mirror spherical and chromatic aberrations are corrected. It consists of several equipotential surfaces in a curved form. Electrons with different kinetic energies are back reflected on different equipotential surfaces. Moreover due to their curved shape the beam is focused, similar to a parabolic mirror for light rays. Here, the

tetrode mirror also introduces spherical and chromatic aberrations, but with opposite sign. By choosing the proper potentials in the mirror, theses aberrations can compensate the aberrations of the objective lens. Therefore, the overall aberrations can be canceled out up to the third order for spherical and first order for chromatic aberrations.

Due to the intersection of incoming and outgoing electron beams, the electron per volume concentration is the highest in this area of the instrument. The same charge of the electrons leads to a repulsion of nearby electrons, preventing an arbitrary high concentration of electrons per volume. This effect is called space charge effect and leads to a decreased lateral resolution.

Since the synchrotron light produces much more electrons than the incoming electrons in LEEM mode (with much lower energy), the XPEEM image has a worse resolution limit (18 nm) than the LEEM image (2.6 nm). One possibility to overcome this drawback is the introduction of an additional aperture in the beam splitter to filter out the high amount of secondary electrons, and let only the core electrons pass. This approach is followed by our group within the development of the SMART II instrument.

The aberration corrected electrons pass the beam splitter for a third time and enter the transfer optics. With the transfer optics the operation modes (microscopy, diffraction, spectroscopy) and the individual magnification can be defined. Additionally a contrast aperture is attached, which is in the image of the back focal plane for LEEM. By changing the optical setting, the intermediate image can be placed into the same aperture, this time acting as a selective area aperture for μLEED. In the following, the electrons pass a special imaging energy analyzer, the omega filter [81]. It consists of four magnetic sector fields, each deflecting the electrons by about 90°. With this geometry all second rank aberrations are canceled out by symmetry and a 1:1 image at the entrance and the exit of the energy filter are achieved. Additional hexapoles in the energy filter increase the energy resolution. Only electrons with a specific energy can be chosen to pass the energy filter. Electrons with a different energy vary in their trajectory through the filter and thus cannot pass. The energy selection is done by an exit slit, which in turn defines the energy resolution and is usually in the regime of 500 meV energy bandwidth. Afterwards the electrons are guided through projection units onto a channel plate, which amplifies the amount of electrons. Behind that a phosphorous screen converts the electrons to photons, which are then detected by a CCD camera.

2.2 Structure and diffraction

Diffraction theory

LEEM and LEED both make use of low energy electrons interacting with the sample surface. In the following the theoretical background of LEED method is discussed. A more detailed description can be found in [4, 43, 66].

First, an ideal three dimensional lattice should be considered. Every atom in this lattice can be addressed by using the translational vector $\vec{T}$

$$\vec{T} = n_1\vec{a_1} + n_2\vec{a_2} + n_3\vec{a_3} \tag{E 1}$$

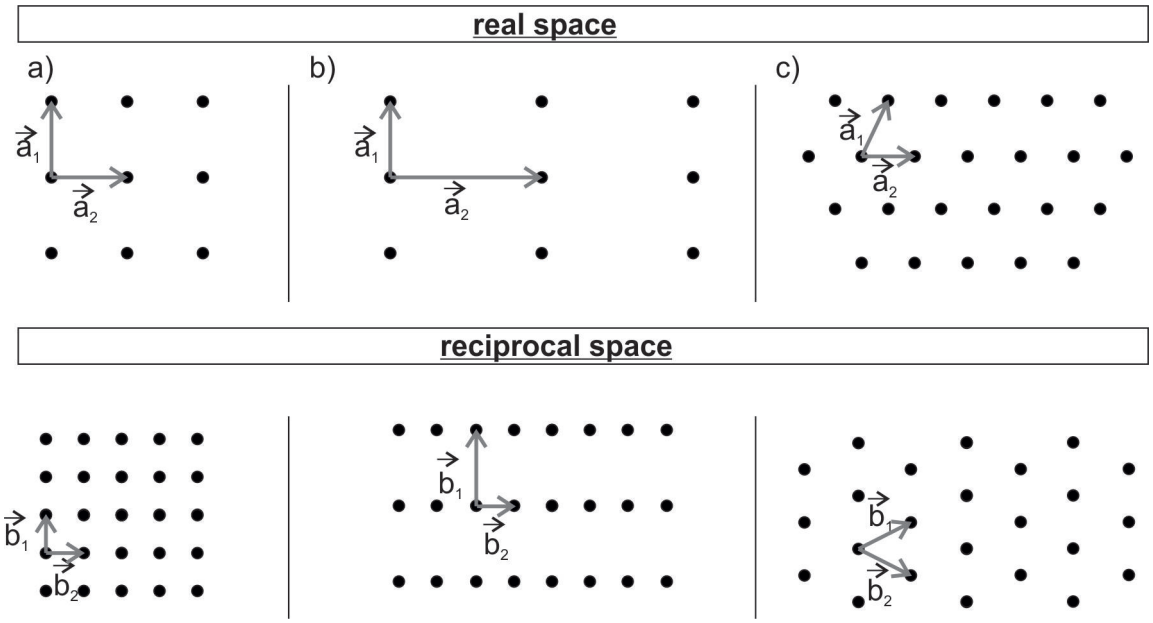

Figure 2.2 Real space vs. reciprocal space of a (100) lattice (a-b) and a (111) lattice (c-d) for two dimensions.

Here, $\vec{a_1}$,$\vec{a_1}$ and $\vec{a_1}$ are the basis vectors and n_1, n_2 and n_3 any integer. Every point in the periodic lattice has the electron density $\rho(\vec{r}) = \rho(\vec{r} + \vec{T})$, whereby $\vec{r}$ can be any point in the lattice. Using a Fourier series the electron density at the point $\vec{r}$ is found to be

$$\rho(\vec{r}) = \sum_{\vec{G}} n_G e^{i\vec{G}\vec{r}} \tag{E 2}$$

While $\vec{r}$ defines a point in real space, $\vec{G}$ addresses the reciprocal space. The reciprocal lattice vector is defined as

$$\vec{G} = h\vec{b_1} + k\vec{b_2} + l\vec{b_3} \tag{E 3}$$

Hereby, $\vec{b_1}$, $\vec{b_1}$ and $\vec{b_1}$ are the reciprocal basis vectors and h,k and l any integer. These lattice vectors are referred to as Miller indices. The real and reciprocal basis vectors are connected as follows

$$\vec{b_1} = 2\pi\frac{\vec{a_2} \times \vec{a_3}}{\vec{a_1} \cdot \vec{a_2} \times \vec{a_3}}; \vec{b_2} = 2\pi\frac{\vec{a_3} \times \vec{a_1}}{\vec{a_1} \cdot \vec{a_3} \times \vec{a_3}}; \vec{b_3} = 2\pi\frac{\vec{a_1} \times \vec{a_2}}{\vec{a_1} \cdot \vec{a_3} \times \vec{a_3}}; \tag{E 4}$$

In particular the following rule is applied: $\vec{a_i} \cdot \vec{b_j} = 2\pi\delta_{ij}$ for $i \neq j$ and $\delta_{ij} = 1$ for $i = j$. Examples for the lattice vectors in real space and their corresponding reciprocal space are given in Fig. 2.2. The lattice vector $\vec{a_i}$ is perpendicular on the reciprocal lattice vector $\vec{b_j}$.

In LEED a surface is illuminated with an electron beam. As a result (elastic and inelastic) scattering and diffraction takes place. First electron diffraction (or elastic scattering) in real space is discussed. For the following description it is useful to describe the beam of electrons by their wave character after De Broglie with a wavelength λ

$$\lambda = h/p \tag{E 5}$$

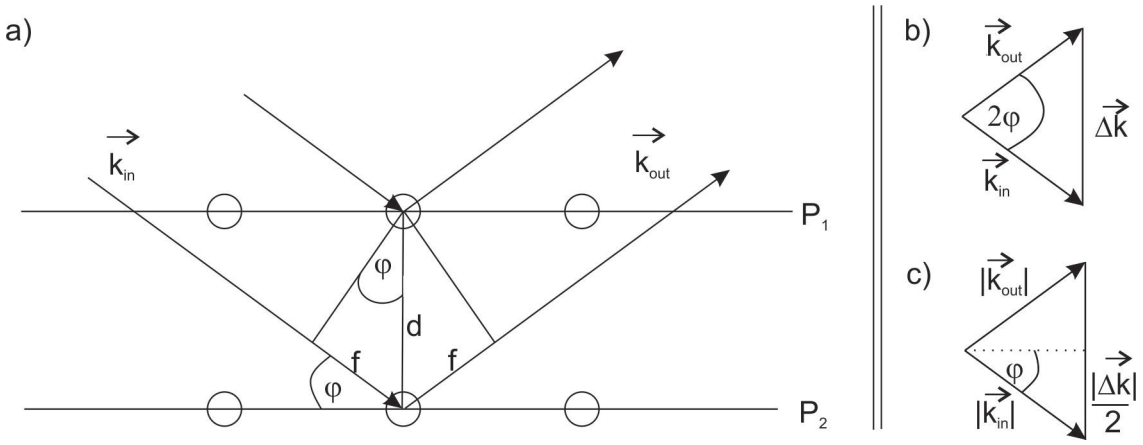

Figure 2.3 a) Two rays of one wave front being reflected by an angle φ on two atoms. The path difference between these two rays is $2f$. Depiction of the incoming and outgoing wave vectors b) and their absolute values c) and introduction wave vector K.

Hereby, h is the Plancks constant and p the momentum of an electron. Moreover, the absolute value of the wave vector $\vec{k}$ of these electrons can be described as

$$\left|\vec{k}\right| = \frac{2\pi}{\lambda} \tag{E 6}$$

In the following an elastic scattering event is discussed. The situation is depicted in Fig. 2.3. A wave front with wave vector $\vec{k_{in}}$ is reflected on two atoms in two different lattice planes P_1 and P_2 of a crystal, respectively. The distance between these lattice planes is d. The back reflected wave has the wave vector $\vec{k_{out}}$. Comparing the rays meeting lattice plane P_1 and lattice plane P_2, a path difference of $2f$ is found (see Fig. 2.3. For constructive interference this path difference $2f$ has to be a multiple n of the wavelength λ.

$$2f = 2d \cdot \sin\varphi = n\lambda \tag{E 7}$$

Only in case of constructive interference a diffraction spot is present. This equation is called Bragg-condition. A Bragg-reflex can only be present for wavelengths $\lambda \leq 2d$. The vector subtraction of the incoming and outgoing wave vector leads to a new wave vector $\left|\Delta\vec{k}\right| = \vec{k_{in}} - \vec{k_{out}}$ (see Fig. 2.3b). For an elastic scattering process $\left|\vec{k_{in}}\right|$ and $\left|\vec{k_{out}}\right|$ must be identical. Thus, the absolute value $\left|\Delta\vec{k}\right|$ can be determined by Fig. 2.3c) as:

$$\left|\Delta\vec{k}\right| = 2\sin\varphi\left|\vec{k_i}\right| = 2\sin\varphi\frac{2\pi}{\lambda} \tag{E 8}$$

In fact, if the Bragg condition is valid and constructive interference is present it follows

$$\left|\Delta\vec{k}\right| = n\frac{2\pi}{d} = \left|\vec{G}\right| \tag{E 9}$$

Here $\vec{G}$ is the already introduced reciprocal lattice vector. This equation is called Laue condition.

The Bragg equation is a simplified model to describe diffraction. For precise description a scattering model should be applied (see also [43]). Nevertheless the outcome is the same,

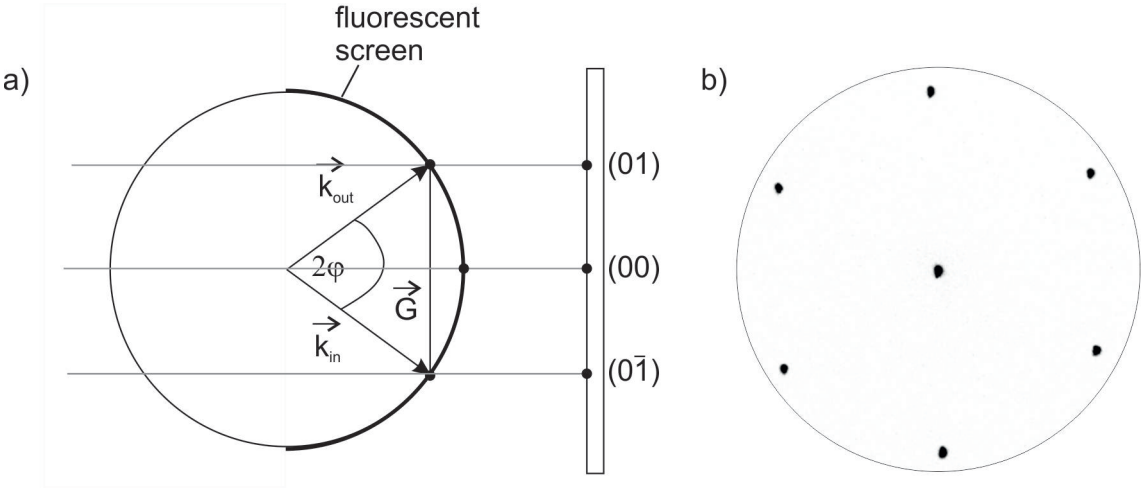

Figure 2.4 a) Construction of the Ewald sphere for incoming and outgoing wave vectors following the Laue condition in reciprocal space. The rods depict the atomic planes in z-direction. The individual rods are numbered by their hk value (hk) and thus indentify the individual atomic order. The right hemisphere equals the commercial fluorescent LEED screen. b) LEED image of a Ru(0001) crystal as measured in the SMART system. StV = 42 eV.

i.e. the Laue condition.

A possibility to construct the Laue condition is to draw the so-called Ewald sphere, as depicted in Fig. 2.4a. In this case surface instead of bulk structures are investigates. Therefore the points in the reciprocal space become rods, perpendicular to the surface. The intercepts of the Ewald sphere with theses rods illustrate the points of constructive interference in reciprocal space. The right hemisphere illustrates a typical fluorescent LEED screen, as it is used in a commercial LEED apparatus. A typical LEED image as measured with the SMART instrument is shown in Fig. 2.4b. With increasing kinetic energy the diameter of the Ewald sphere is enlarged. Thus, higher order spots become visible. In a commercial LEED system, the angle of the diffracted electrons are displayed, thus the LEED spots move towards the center of the screen when the energy is increased. In a cathode lens system with a quasi-homogeneous electric acceleration field in front of the surface, the momentum of the electrons is imaged onto the detector. Therefore the positions of the surface LEED spots do not change if the electron energy is changed.

LEEM, DF-LEEM and μLEED realization in the apparatus

In a commercial LEED system an electron gun is attached directly in front of the sample Surrounding the gun a fluorescent screen is used in order to detect the back diffracted electrons. The (00) spot is covered by the electron gun (so-called back view system).

In 1962 Ernst Bauer invented a combined LEEM-LEED system. LEEM is hereby the imaging counterpart of LEED. Similar to the commercial LEED apparatus, the sample is illuminated by an electron gun. However, different to the commercial LEED system, incoming and outgoing electron beams are separated by using a magnetic beam splitter. With this, all electrons coming from the sample are used for detection, including the elastically backscattered electrons, which give rise to the (00) spot.

The electrons are guided through a lens system, whereby the first lens is the so-called objective lens (see section 2.1). The electron beam is focused in the back focal plane of the objective lens, i.e., here the LEED image is produced (reciprocal space). Behind this point the electron beam widen again, giving rise to the LEEM image (real space). Depending on the setting of transfer lenses the position of the back focal plane can be varied, and with this it can be defined, whether the LEED pattern or LEEM image is displayed at the detector.

In the SMART system a contrast aperture is implemented. In the LEEM mode the back focal plane set to the position of this aperture, so that a selection of a specific LEED spot is possible. For the so-called Bright-field LEEM only the (00) spot passes the aperture. Other k-contributions are blocked. By choosing only the elastically scattered electron (condensed in the (00) spot), the lateral resolution can be enhanced. In the following chapters this mode is addressed to as LEEM mode. By changing a deflector in front of the sample a diffraction spot with a different k-vector can be chosen to pass the contrast aperture. This mode is called Dark-field LEEM (DF-LEEM). In the following chapters this mode is addressed to as dark-field analysis. When using this mode only the areas giving rise to this specific diffraction spot is bright. In the LEED mode of the SMART instrument, the intermediate image plane is transferred into the plane of the contrast aperture, and a small surface area is selected. With the magnification of M=20 for this intermediate image plane, and the aperture size of typically 30 μm, the size of the selected area $d_{AoI} = 30\,\mu\text{m}/\text{M} = 1.5\,\mu\text{m}$. Now, with this set-up, all LEED spots can pass this aperture and the complete LEED pattern can be detected. The positions of the LEED spots remain constant, even if the Ewald sphere increases at higher energy. Due to these settings the modes can be easily switched between the method of LEEM and LEED during the measurement without mechanical change of apertures.

The contrast in a LEEM image results from either the phase contrast or the amplitude contrast. Electrons coming from different terraces have a phase contrast. In case this phase difference is λ, the difference between the terraces is invisible, however, a path difference of $\lambda/2$ is visible. For instance, step bunches are found as black lines in the image, due to destructive interference. In the amplitude contrast differences in diffraction conditions lead to a contrast between different materials or facets in a material. In the dark-field LEEM only areas corresponding to a specific LEED spot are bright. Therefore the individual LEED pattern of a specific domain visible in LEEM can be deduced. Moreover symmetries for LEED pattern of a specific superstructure can be found, by using neighboring LEED spots of a specific pattern, for instance a (2x2) pattern. One example is the structure of a 2O-Ru(0001) vs. the 3O-Ru(0001) coverage. While both LEED pattern show a (2x2) structure, they differ in their symmetry of the spot intensity. The 2O-Ru(0001) structure has a 2-fold symmetry, while the 3O-Ru(0001) structure has a 3-fold symmetry and can thus be distinguished from each other. The spot position in LEED images gives information about the atomic structure, the size and shape of the unit cell or simply the presence of a superstructure. Moreover it can be used to judge the sample quality. In order to determine the atomic arrangement within the unit cell, one has to perform LEED-IV measurements and analysis.

The variation of the start voltage (StV) of the electrons gives rise to a characteristic intensity curve. Hereby both, individual LEED spots, as well as defined areas in the LEEM image can be used. The corresponding curves are called LEED-IV and LEEM-IV, respectively. LEEM-IV has the advantage to select specific areas in the field of view and thus

get information of a specified regions, which might be either to choose (defect-free) terraces or also to address different domains. Typically energies lower than 50 eV are used for LEEM-IV analysis, since the intensity drops strongly and with this the signal-to-noise ratio increases.

In LEED-IV the characteristic curves for individual LEED spots can be measured. The main information is found in the (00) spots, however also the superstructure curves have a characteristic structure. In LEED-IV typically energies up to several hundred eV can be choosen. The LEEM-IV and LEED-IV curve intensity evolution of the individual diffractions spots can be described as

$$I(\vec{k_{in}}, \vec{k_{out}}) = F(\vec{k_{in}}, \vec{k_{out}}) \cdot G(\vec{k_{in}}, \vec{k_{out}}) \quad \text{(E 10)}$$

Hereby, $F(\vec{k_{in}}, \vec{k_{out}})$ is the intensity structure factor and $G(\vec{k_{in}}, \vec{k_{out}})$ the intensity form factor. The intensity form factor gives information about the lateral periodicity of the surface and the surface defect structure smaller than the resolution limit of LEEM. It mainly requires the kinetic theory of diffraction. Here, mainly the diffraction spot position and the shape of the spots is included. In the intensity structure factor the atomic structure of a surface is probed, thus the atomic positions within the lateral periodicity units can be extracted. Here, the relative intensities of the diffraction spots are probed.

A simulation of LEEM-IV or LEED-IV curve requires several effects to be considered. While a theory based on elastic scattering gives good results for energies larger than 200 eV [95], for lower energies the curves cannot be reproduced. For energies lower than 100 eV, which is typically used for LEEM-IV no agreement is achieved. To achieve good results in this energy regime multiple scattering, inelastic scattering and in particular losses through inelastic scattering have to be taken into account [8, 26]. Especially for energies lower than 100 eV a very detailed angular distribution of the scattering by the individual atoms need to be fully considered. Good results are achieved by using material-specific dielectric functions. Nevertheless, the energy range below 10 eV shows large derivations. Additionally surface effects, like the shape of the boundary between vacuum and the condensed matter cause deviations. In the simplest model a sharp planar interface is present, which is polarizable and has the dielectric constant ϵ. Here incident electrons can produce an image charge in the medium [8, 50, 93] and thus a image potential $(z) = (\epsilon - 1)/(\epsilon + 1) \cdot 1/4z$. For ideal metals with $\epsilon = -\infty$ follows $(z) = -1/4z$. Hereby z is the distance in z-direction. Such an image charge also has an influence on the position of the MEM-LEEM border. For instance a material with high electronegativity in the top most layer increases the MEM-LEEM border to higher energies. In this work a Ru(0001) substrate is used. The MEM-LEEM border is found to be at 2.58 eV (work function: 5.44 eV [12]). If the surface is 3O-oxygen terminated the border is strongly increased up to 3.5 eV. Another effect that is found to be reproduced in a LEEM-IV or LEED-IV spectrum is the quantum size effect for thin films with parallel boundary conditions. Analogue to the Fabry-Perot etalon for optical light, individual intensity oscillations in the LEEM-IV spectra correspond to the interference at the individual interfaces of each layer [7]. The number of these intensity oscillations in the LEEM-IV or LEED-IV spectra corresponds to the number of atomic layers. Multiple orders of this effect can be present, also in the low energy region $\leq$10 eV.

As described, the large number of influences on the LEEM-IV and LEED-IV structure makes a simulation of these curves rather difficult. However, since all these effect create a very element and arrangement specific curve, it can be used as a fingerprint in order to check the similarity of the prepared films.

2.3 Spectroscopy

In the last chapter the methods using the electron gun were described. In this chapter the synchrotron light is used. In the following the methods of XPEEM and μ-spot XPS will be discussed.

Both methods are based on the photoelectric effect. The energy of an incident photon hν is absorbed by an atom and excites an electron. If the photon energy is greater than the binding energy E_B and the workfunction ϕ_{Sample} the electron can leave the sample.

If only the sample is taken into account, then the following energy conservation is true:

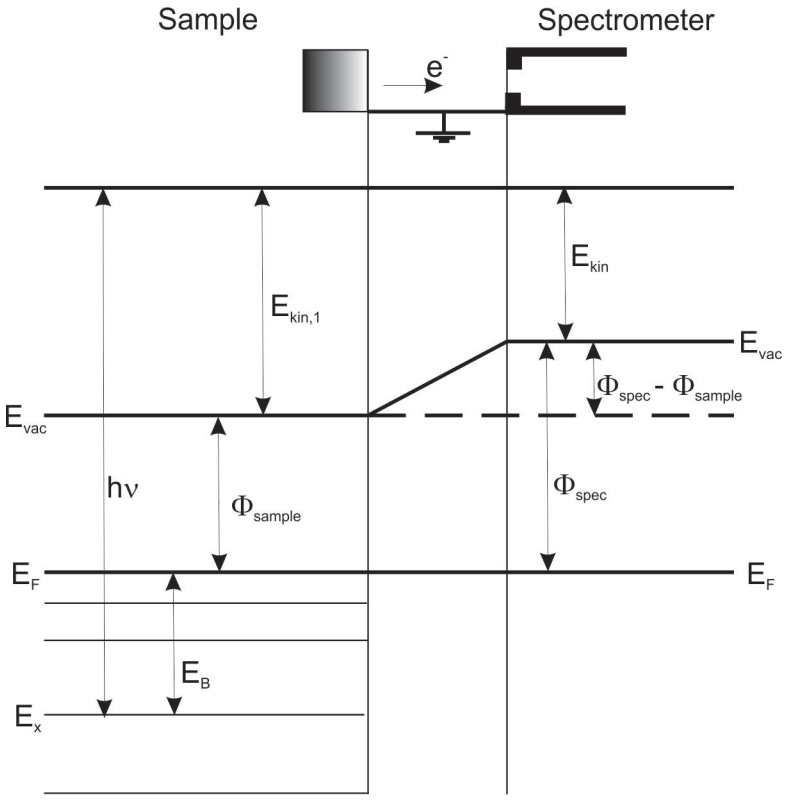

Figure 2.5 Schematic representation of the energy levels in sample and spectrometer (adapted from [3]). Hereby E_F is the Fermi level of the sample, E_{vac} the vacuum level and ϕ_{Sample} and ϕ_{Spec} the workfunction of the sample and spectrometer, respectively. E_B indicates the binding energy corresponding to a specific energy level E_x.

$$h\nu = E_{kin,1} + E_B + \phi_{Sample} \tag{E 11}$$

For the respective energy level see Fig. 2.5. However, the energies of the sample are measured using a spectrometer. Due to different vacuum levels of the sample and the spectrometer E_{vac} the kinetic energy measured in the spectrometer corresponds to the vacuum level of the spectrometer, not the sample. Thus, what is measured is

$$h\nu = E_{kin} + E_B + \phi_{Spec} \tag{E 12}$$

or

$$E_B = h\nu - E_{kin} - \phi_{Spec} \tag{E 13}$$

A scheme of a typical XPS spectra is shown in Fig. 2.6. Hereby the intensity is plotted in dependence on the (measured) kinetic energy E_{kin} or binding energy (BE) which can be calculated using equation E 13. The signal intensity correlates with the number of emitters.

The dominant intensity in XPS spectra results of electrons losing their energy while leaving

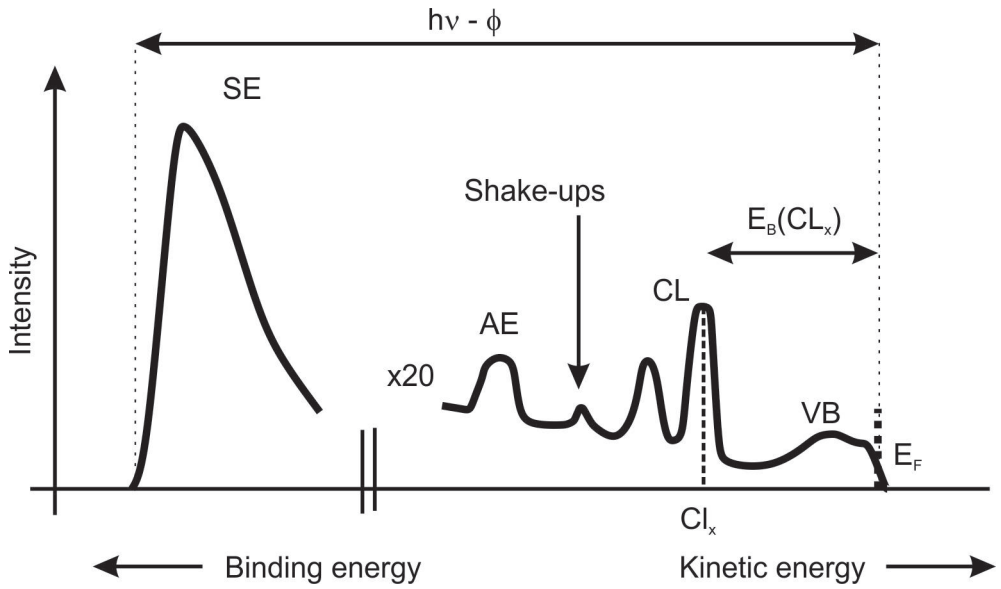

Figure 2.6 Schematic XPS spectrum including the Secondary electron edge SE, the core level CL, the Auger electrons AE, the valence band VB, the Fermi edge E_F and shake-ups (adapted from [30]).

the sample due to inelastic scattering processes. Most electrons have just slightly enough kinetic energy to overcome the work function of a sample. They sum up to a very strong intensity at low kinetic energies, the so-called secondary electron edge SE. By fitting the SE edge on the lower kinetic energy site the relative workfunction of the sample can be determined. Ineleastically scattered electrons with higher kinetic energy contribute to a secondary electron tail, which decreases with increasing kinetic energy. Additional intensity in discrete lines can be found in core electron levels CL, Auger transitions AE and shake ups. The core levels give rise to element specific information. Energetic shifts of these lines give information about the chemical surrounding. Auger electrons are found for states corresponding to Auger transitions. The Auger-effect can be described in three steps: (i) an electron A is excited by either electrons or photons from the energy level E_1 into an unoccupied state, leaving behind a vacancy in level E_1. (ii) A second electron B in a higher energy level E_2 falls down into the level E_1, releasing the energy E_2-E_1. (iii) A third electron C in level E_3 may take this energy and is emitted. The electron C is the Auger electron. It has an element typical kinetic energy, and this energy does not depend on the energy of the primary excitation, as long as the energy was sufficient high enough to create the vacancy in E_1. The Auger transition are commonly named by the involed core levels E_1, E_2, E_3, e.g. KLL.

While core electrons correspond to the individual binding energy of a specific energy level, the Auger electrons have the kinetic energy fitting to a specific energetic difference between two specific energy levels E_2-E_1-E_B. Thus, core level can be distinguished from Auger level

by variation of the photon energy. While the kinetic energy of the core electrons shift with the photon energy (see equation E 13), the kinetic energy of the Auger electrons remains constant. The part of the diagram with highest kinetic energy is the valence band. For metals the valence band edge is the Fermi energy E_F and follows the Fermi-Dirac distribution.

XPEEM and μXPS realization with the SMART instrument

The method of XPS is very surface sensitive, due to the utilized (low) kinetic energy. The electron inelastic mean free path depends on the kinetic energy and is typically estimated by the so-called "universal curve" [88]. In the kinetic energy range between 50 eV and 120 eV the technique is surface sensitive to the topmost layer only (around 6 Å). A great advantage of the synchrotron light is the possibility to vary the photon energy and therefore to tune the kinetic energy of the photo-emitted electrons. At the UE49-PGM beamline of BESSY II the energy can be varied between 90 eV up to 1200 eV. This provides the possibility for depth profile analysis, i.e. to measure the same element line with a surface sensitive energy (e.g. 70 eV) and a higher kinetic energy (e.g. 250 eV). Since in this work a layered material is investigated the individual influence of the first and second layer can be distinguished in that way. The measured kinetic energies can be transformed into the binding energy by using equation E 13. In our instrument the work function of the detector is not known, however the valence band edge can be measured. The valence band is typically not in the kinetic energy range for surface sensitive probing. In this work ultrathin films on a Ru(0001) crystal are investigated. Thus, the main influence on the measured valence band edge is coming from the Ru(0001) crystal. Since ruthenium is a metal, it has no present band gap between the occupied and the unoccupied bands. As a result, the valence band edge of the occupied states can be assumed to be at the same position as the Fermi edge. This can be used to calibrate the binding energy out of the measured kinetic energy (see Fig. 2.6. This has been done for every measured XPS spectra in this work.

In the SMART instrument μXPS is measured in the so-called dispersive plane mode. For this mode a field aperture is set in front of the energy filter. The exit slit present for the fine selection of the energy is taken out of the system. As a result the electron beam can be dispersed with a detectable energy range of 17 eV in the energy filter. This energy-dispersed beam profile can then be mapped on the screen and gives the intensity as a function of the electrons kinetic energy. The StV (start voltage) set defines the energy in the center of this image, i.e. StV $\pm$ 8.5 eV. Hereby, the horizontal axis shows the energy dispersion, while the vertical axis shows the lateral distribution of the specific sample surface. While a sample surface of 50 μm^2 is illuminated by the synchrotron light, a special aperture can be set to select only information of a circular area of 5 μm^2 or even smaller, depending on apperture size and image magnification.

Furthermore, the core electrons can be used in the imaging mode, i.e. XPEEM mode. Hereby, a specific energy can be selected with the exit slit set behind the energy filter. With varying the StV at the sample, it is possible to scan the kinetic energy of the emitted photoelectrons and a complete XPS core level spectra with lateral resolution is obtained. Hereby, detailed information about the element concentration in neighboring domains can be analyzed. Therefore, not only an element-specific mapping is possible, but also the in-

dividual core level shape can be measured directly and thus, allows the distinction between different species of the same element (e.g. the elucidation of different oxidation states).

Chapter 3

Ultrathin layers of FeO on Ru(0001)

The main topic of this work is iron silicate. It can be described as a FeO-like layer on Ru(0001) with a silica monolayer on top. These two layers are bond through oxygen (Fe-O-Si bond). Apart from preparing iron silicate by sequential deposition of both, Si and Fe (in chapter 4.1), it can also be prepared by the deposition of silicon on a pre-prepared FeO monolayer (see chapter 4.2.1). Moreover, in section 4.3.1, it will be shown that also a FeO bilayer can be used as start. In the mentioned chapters complete layers of $FeSiO_x$ are used on the basis of complete layers of FeO. This is a useful approach in order to gain general information about the chemical and structural properties of iron silicate films. In contrast, in sections 4.4.2 and 4.4.3 incomplete FeO layers are utilized. With this dynamic processes and stabilities can be investigated. In order to understand the nature of the FeO-like (complete and incomplete) layer as part of iron silicate, the individual properties of FeO are of interest. They will be discussed in this chapter.

In general different iron oxide phases exist, highly dependent on the preparation conditions such as oxidation gas pressure, temperature and iron concentration. Here, the oxidation kinetics during epitaxial growth is of high interest. At RT four thermodynamically stable iron oxide phases are known: FeO_{1+x} (wüstite), Fe_3O_4 (magnetite), α-Fe_2O_3 (haematite) and γ- Fe_2O_3 (maghemite). Structural models for first three phases are given in Fig. 3.1.

α-Fe_2O_3 is the thermodynamically most stable form at RT for all oxygen pressures. It consists of a closed-packed hexagonal structure with lattice constants $a = 5.034\,\text{Å}$ and $c = 13.752\,\text{Å}$. The iron atoms are in the Fe^{3+} state. Fe_3O_4 has an inverse spinel structure, which comprises iron atoms tetrahedrically coordinated in Fe^{2+} state and also octahedrically coordinated in Fe^{3+} state. As a result an alternative expression is $FeO{\cdot}Fe_2O_3$ with an atomic ratio of Fe^{2+}: $Fe^{3+}$of 1:2 [105]. On Ru(0001) they are known to grow in triangular shaped islands as a third layer of FeO [83].

Of main interest for the later iron silicate films are the properties and growth conditions of ultrathin layers of FeO_{1+x}. FeO_{1+x}consists of a stack of alternating layers of Fe^{2+} cations and O^{2-} anions. Both are arranged in a hexagonal lattice form. With increasing iron content the lattice constant increases from 4.28 Å to 4.32 Å [100] in high oxygen pressures. On a Ru(0001) support up to four atomic layers are stable [41] in contrast to Pt(111) with only two stable atomic layers [100]. At higher iron amount Fe_3O_4 occurs. The reason is the higher affinity of Ru to iron and oxygen as compared to platinum, as well as a higher surface free energy of Ru and a gain of Madelung energy [41]. On Ru(0001) the interlayer distance shrinks with increasing layer number from 1.25 Å (bulk) to 0.6 Å (three and four

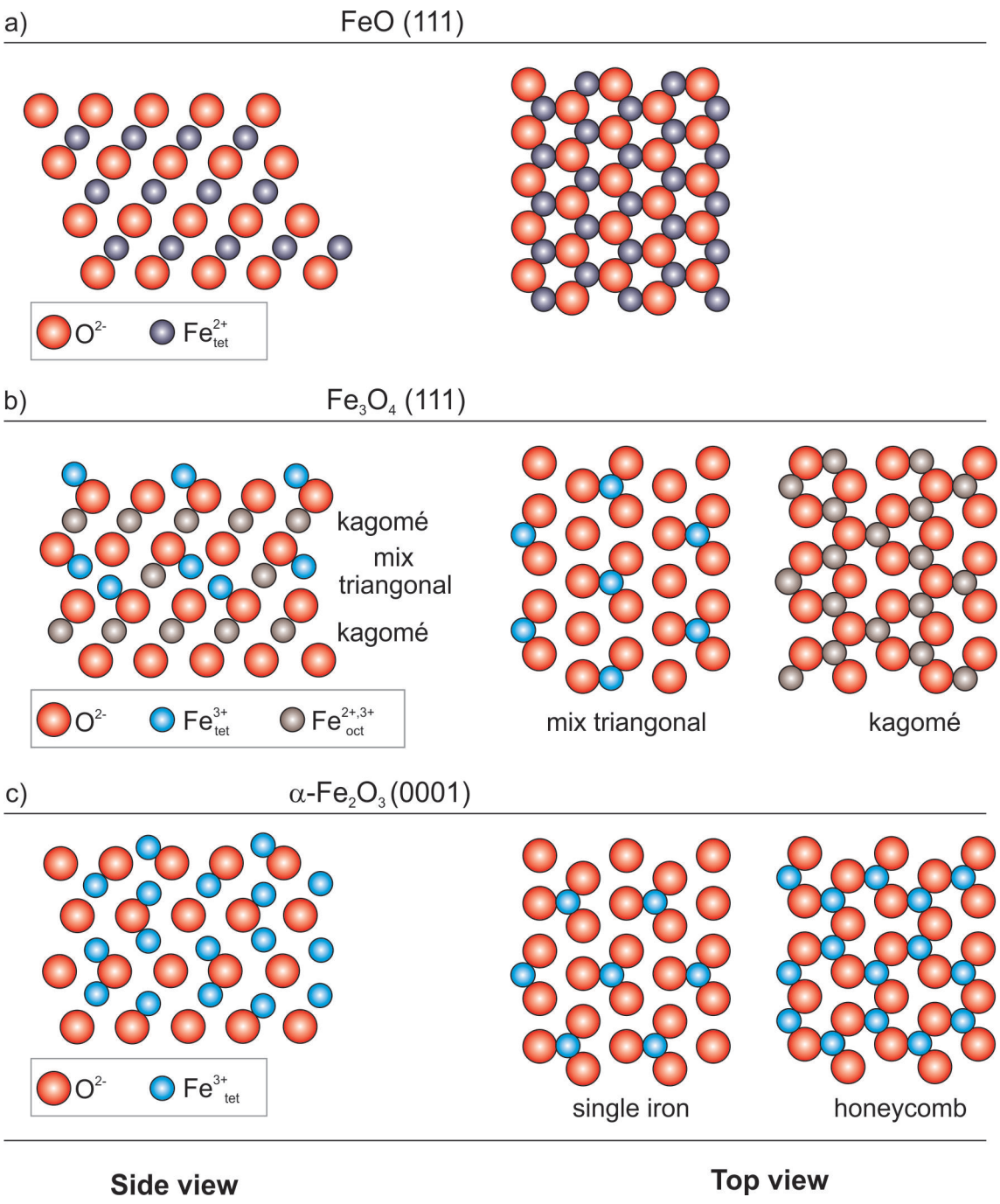

Figure 3.1 Atomic arrangement of the following iron oxide phases: a) FeO, b) Fe_3O_4 and c) α-Fe_2O_3. Image based on [42].

monolayer) in order to minimize the dipole moment and thus, stabilize the film [41].

The standard method to prepare FeO_{1+x} on Ru(0001) is the deposition of iron at RT in UHV, followed by an oxidation in $1.0 \cdot 10^{-6}$ mbar to 900-1000 K. Ketteler et al. have shown that FeO_{1+x} may be produced by one-turn deposition, i.e. the deposition of the complete iron amount at once or by cumulative iron deposition. While in one-turn deposition layers of a maximum of four monolayer height can be grown, in the cumulative method FeO_{1+x}

grows only monolayer thick (when in the first step less than a monolayer of FeO is deposited). Continued cumulative growth is leading to the formation of Fe_3O_4. With both methods monolayer thick FeO_{1+x} islands can be formed. The structure of FeO_{1+x} on the Ru(0001) or the Pt(111) support is a Moiré pattern. When prepared with the as described method a Moiré reconstruction of "7 on 8" atoms is found for the first two layer, meaning that 7 iron atoms fit commensurably on 8 Ru(0001) atoms [41]. For three or four monolayers a structure of "6 on 8" is produced, due to a relaxation within one layer to 3.58 Å, which enables the shortened interlayer distance and thus, the minimized dipole moment.

De la Figuera et al. [68] have shown that FeO_{1+x} can also be prepared by deposition at elevated temperature in oxygen atmosphere. Here, the Ru(0001) substrate is covered with oxygen even before iron is landing on the surface. The first FeO_{1+x} layer grows in the form of islands that continue to grow until the first layer is closed. The precise oxygen background pressure proved to be very critical for the film growth. In an oxygen background pressure of 10^{-8} mbar a monolayer FeO_{1+x} film grows, while in 10^{-7} mbar directly a bilayer FeO_{1+x} film grows. The authors have judged the layer thickness by deposition time and STM measurements. The Moiré structure exhibits a "6 on 7" reconstruction. De la Figuera et al. performed a LEEM, LEED and STM study. However, spectroscopic results are missing.

In the present work, monolayer (section 3.1) and bilayer FeO_{1+x} films (section 3.2) have been prepared using the second method, namely the deposition of iron at elevated temperature in oxygen atmosphere.

3.1 Monolayer growth

This chapter discusses the monolayer films of FeO_{1+x}. For this, iron is deposited at 800 K in an oxygen pressure of low 10^{-8} mbar. At these conditions iron oxide starts to grow at step edges and impurities, first growing on individual terraces before growing over step edges. The monolayer of FeO_{1+x} is defined with the closure of these films. A typical growth is shown in Fig. 3.2. For a detailed analysis such as XPS, LEEM-IV etc. the films were cooled down rapidly without applying additional oxygen. The growth mode for a pressure of $1.0 \cdot 10^{-8}$ mbar and $2.0 \cdot 10^{-8}$ mbar seems to be very similar, when observed in LEEM. Also the necessary time to form a closed layer matches. However, their structure differs strongly, as could be seen in their diffraction patterns Fig. 3.3a and b.

At a pressure of $1.0 \cdot 10^{-8}$ mbar rotational domains are growing simultaneously. The LEED image is shown in Fig. 3.3a. The individual structures superimposed in LEED are separated in Fig. 3.4. Two rotated structures with Moiré spots are present, together with a (very blurry) (2x2) structure. The rotated structures have a 1.15 times larger unit cell than Ru(0001) and are rotated by an angle of +/- 17°, respectively (Wood notation: (1.15x1.15)R17° and (1.15x1.15)R163°, respectively). For future reference this phase (defined as the sum of all growing structures) is called ML1. The structural models of the two rotated domains are shown in Fig. 3.5a and b.

A slightly higher pressure of $2.0 \cdot 10^{-8}$ mbar leads to a Moiré pattern, surrounding the (0,0) spot and the substrate spots (Fig. 3.3b). This LEED pattern is well known for FeO_{1+x} films on Ru(0001) showing the "6 on 7" reconstruction. The structural model is given in Fig. 3.5c. For further reference this phase will be called ML2.

A chemical comparison between phase ML1 and ML2 is shown in Fig. 3.7. The XPS data is taken from closed films of the individual phase. As it turns out, their chemical composition is the same for both phases. The Fe 3p shows an Fe^{2+} configuration (53.6 eV). This correlates nicely with the LEED pattern that suggested the presence of FeO_{1+x}. The O 1s lines have a maximum at 528.9 eV. Since their chemical composition is the same, the only difference between ML1 and ML2 must be their structure.

The LEEM-IV curve of both phases is shown in Fig. 3.6. Phase ML1 and ML2 share nearly the same MEM-LEEM-border at 2.56 eV(ML1) vs. 2.54 eV (ML2), indicating the same dipole moment or arrangement of oxygen in the top most layer. This value matches the value of a clean Ru(0001) substrate [44]. In LEEM-IV up to 13.7 eV the characteristics are similar: Both have a very broad peak at 4.4 eV (ML1) and 4.7 eV (ML2) and a very distinct peak at 12.6 eV, which is characteristic for a monolayer. Only for higher energies the curves differ. ML1 shows a broad peak around 15.8 eV and a maximum at 19.2 eV. ML2 shows a small peak at 14 eV a dip at 15.6 eV and finally a peak at 20.1 eV.

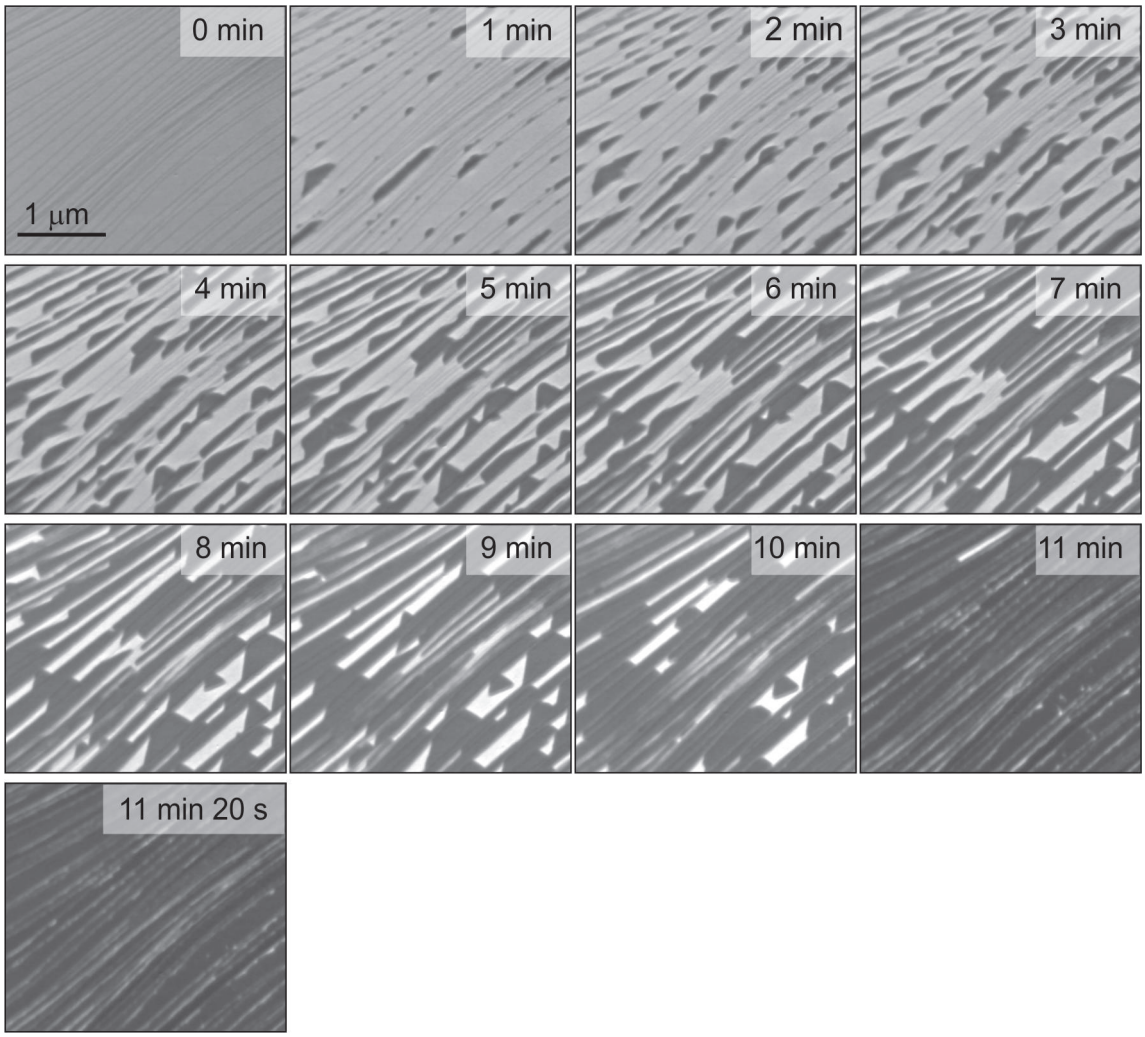

Figure 3.2 LEEM images during Fe deposition at 800 K in $1.0 \cdot 10^{-8}$ mbar (phase ML1). The images are taken at 20 eV. The intensity scaling is kept constant.

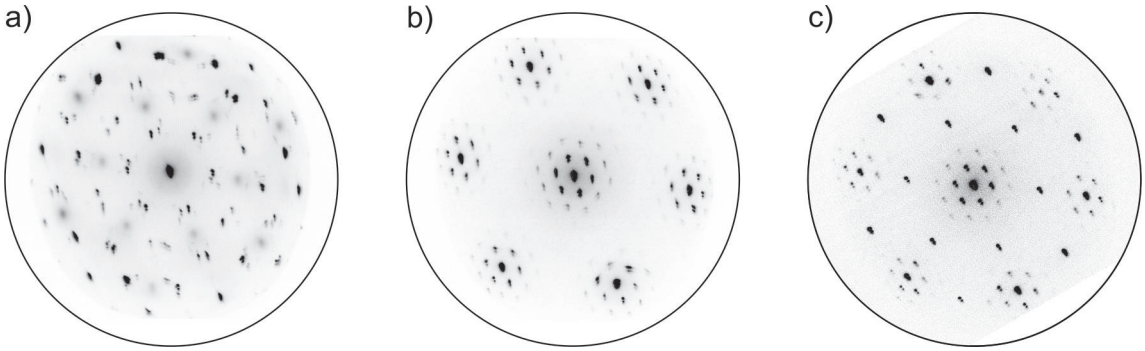

Figure 3.3 LEED images of the individual monolayer FeO phases. a) ML1, b) ML2 and c) ML3. All images are taken at 42 eV.

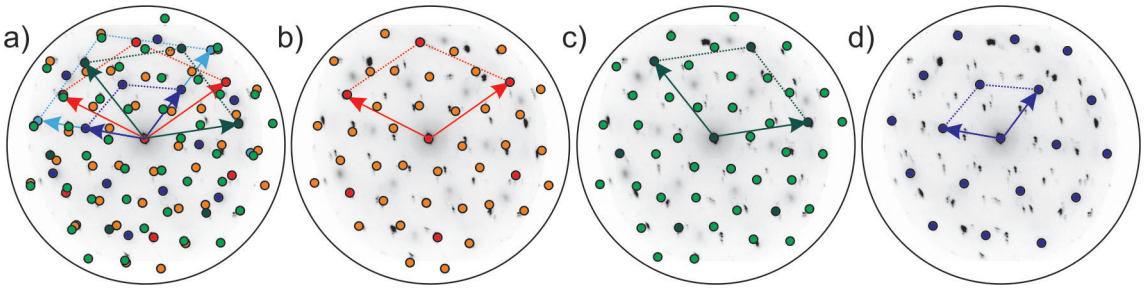

Figure 3.4 Rotated domains marked in the LEED image of ML1 (see 3.3a) at 42 eV. a) Superposition of all identified domains. The individual domains are given in b)-d). b) and c) rotated phases. d) (2x2) phase.

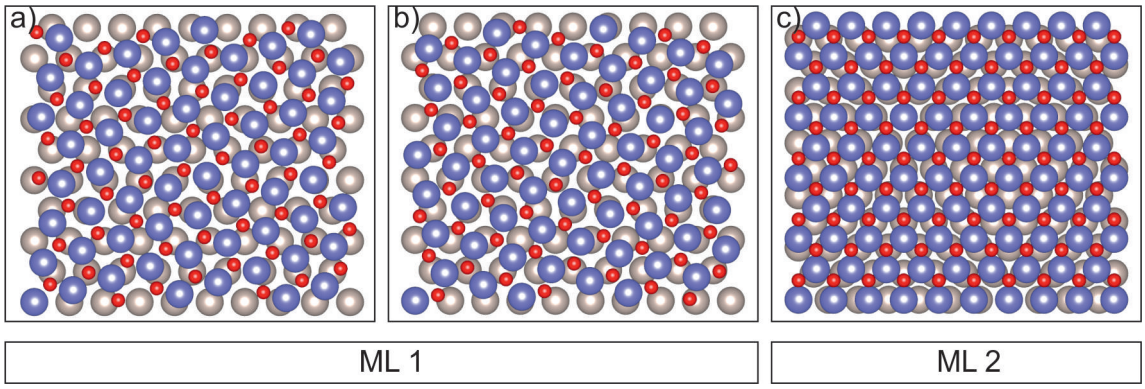

Figure 3.5 Top view on monolayer iron oxide films grown at 800 K in a)-b) $1.0 \cdot 10^{-8}$ mbar (monolayer phase ML1) and c) $2.0 \cdot 10^{-8}$ mbar (monolayer phase ML2). The structures are based on the measured LEED images in Fig. 3.3a for the monolayer phase ML1 and 3.3b for monolayer phase ML2. The LEED image of the monolayer phase ML1 shows the superposition of several domains as shown in Fig. 3.4. In Wood notation: a) (1.15x1.15)R17°, b) (1.15x1.15)R163°, c) (1.17x1.17) and Moiré structure. Red: Oxygen. Violet: Iron. Gray: Ruthenium.

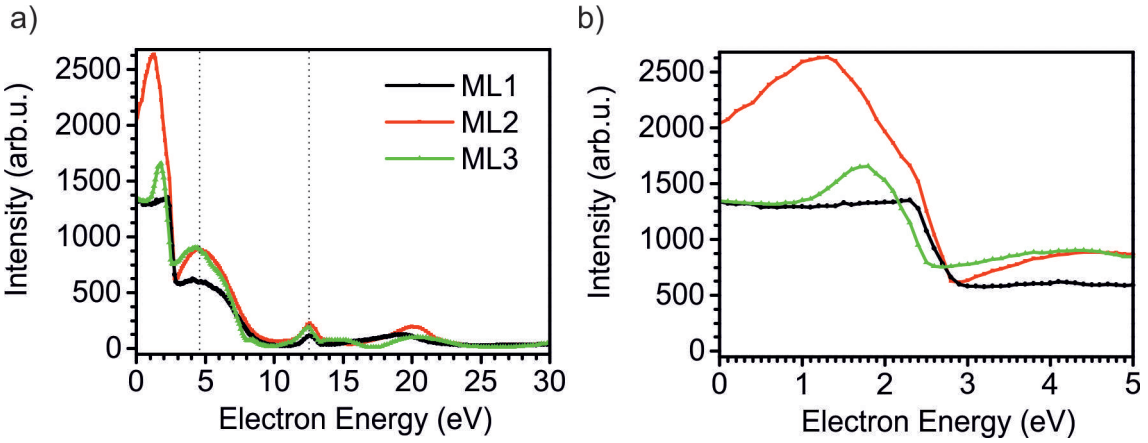

Figure 3.6 Characteristics for the individual monolayer phases. a) LEEM-IV curve and b) MEM-LEEM border. The lines in a) indicate the characteristic peaks present for all monolayer FeO phases.

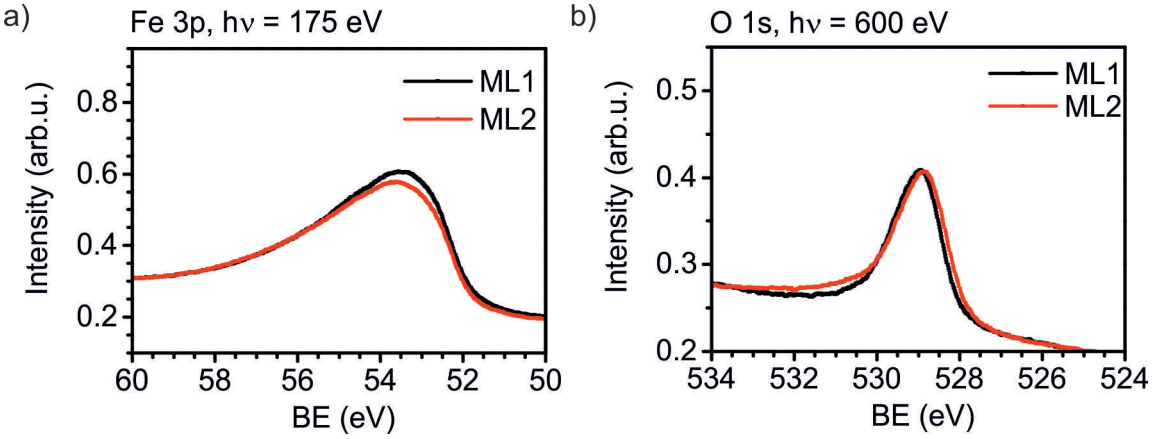

Figure 3.7 XPS curves of phases ML1 and ML2. a) Fe 3p line. b) O 1s line.

Before the layer of ML2 closes in some cases iron oxide transforms into a third phase. In Fig. 3.8 such a transformation is shown. The gray phase corresponds to ML2 and the dark gray phase to ML3. The transformation can be very fast, as images show at 6 min 52 s and 6 min 54 s. Between these two seconds a complete terrace of several micrometer in size transforms. Due to these fast changes it can be assumed that the amount of material remains constant. However slight structural changes or changes in the oxygen termination are likely. Indeed, the LEED pattern shows additional (2x2) spots. The LEED pattern was taken in an area containing both, the ML2 and ML3 phases. In order to prove that the (2x2) spots correspond strictly to ML3 a dark field analysis was performed as shown in Fig. 3.9. The MEM-LEEM border of ML3 is at 2.28 eV, i.e. nealy 0.3 eV smaller than ML1, ML2, and the bare Ru(0001) substrate (2.58 eV [44]). This indicates that more oxygen atoms are underneath the iron layer than on top. The LEEM-IV curve (Fig. 3.6) shows similar to ML1 and ML2 a main peak at 4.4 eV and a sharp peak at 12.5 eV. For higher energies it is strongly different, showing a peak at 14 eV and 15 eV, as well as a broad peak at 20.4 eV. In Fig. 3.10 a model for the ML3 phase in comparison to the ML2 phase is proposed. Here, the (2x2) spots can be realized by a switching of the oxygen atoms underneath the film, so that the remaining oxygen atoms on top of the film are ordered

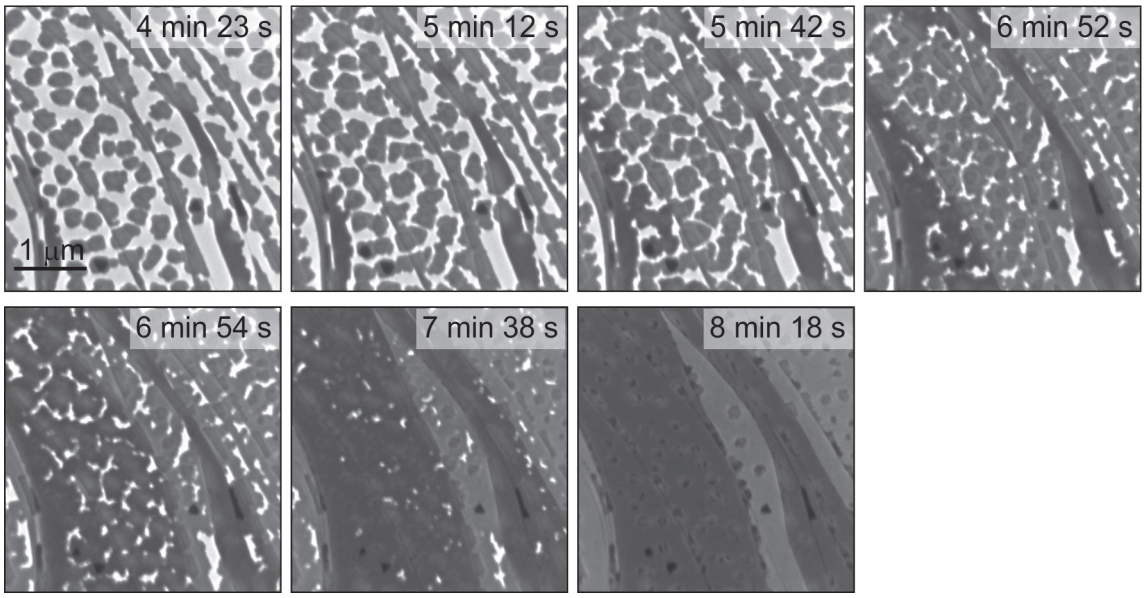

Figure 3.8 Transformation of ML2 (gray) into ML3 (dark gray) during iron deposition in $2.0 \cdot 10^{-8}$ mbar at 800 K. LEEM images taken at 20 eV.

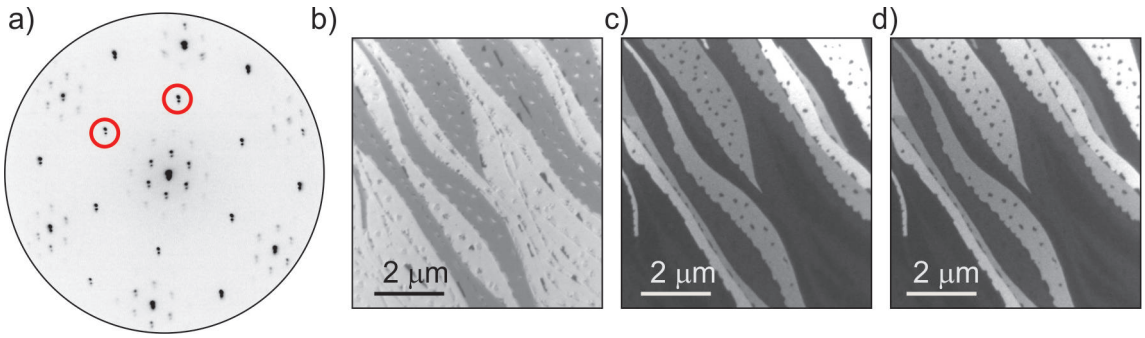

Figure 3.9 Film containing phase ML2 and ML3. a) LEED image at 42 eV of an area containing both phases. b) Bright field LEEM at 20 eV. The bright and dark grey phase corresponds to ML2 and ML3, respectively. c)-d) Dark field images at 42 eV using the (2x2) spots indicated in a). The individual images correspond to the lower left (c) and upper right (d) spots marked by red circles.

in a (2x2) reconstruction. In fact, the switching of oxygen atoms from on top of the iron layer to underneath the iron layer would lower the dipole moment on the surface and thus, explains the drastic decrease of the MEM-LEEM border.

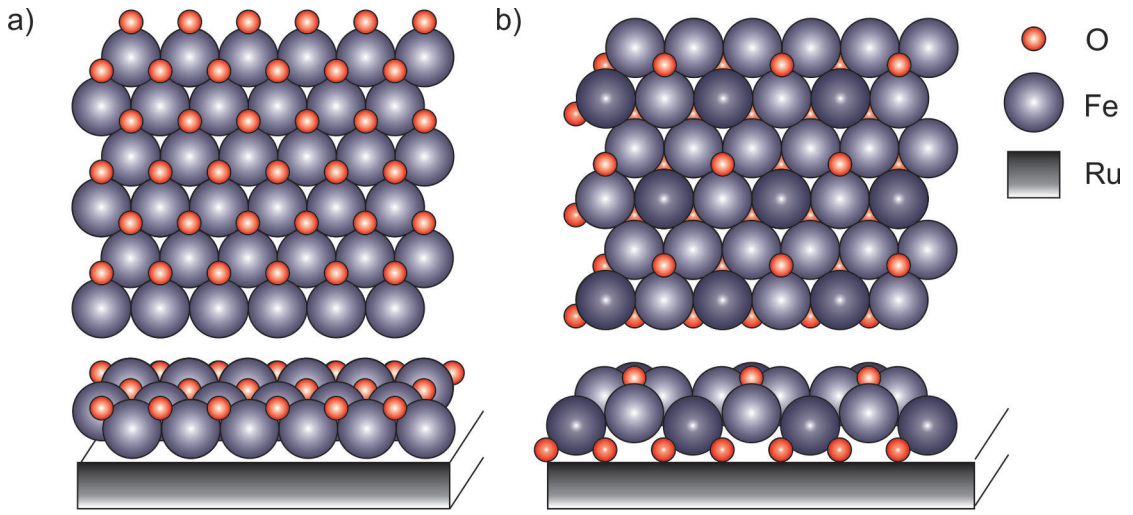

Figure 3.10 Proposed model for the monolayer FeO phases ML2 (a) and ML3 (b) in top and side view.

Oxidation of the FeO monolayer

In the following, the influence of oxygen pressure and temperature on the as-prepared monolayer of FeO_{1+x} is discussed. In chapter 4 iron silicate is investigated. Different preparation methods are shown, however they all combine an oxidation step in $1.0 \cdot 10^{-6}$ mbar at elevated temperatures. Therefore the question is important, how stable the FeO_{1+x} monolayer is upon oxidation. As a result it is possible to find conditions for a stable FeO_{1+x} film and thus, the influence of silicon in the later experiments. The two monolayer phases ML1 and ML2 are chemically identical, as shown in Fig. 3.7. From this point of view both phases could be used for the oxidation experiment. However, the structures of ML1 (rotational domains) and ML2 (Moiré structure) are very different. Since the Moiré structure is the typical (optimal) FeO structure it is interesting to clarify, whether ML1 can be transformed into ML2 through oxidation. Therefore the following oxidation experiment was performed with ML1.

In the following data of the oxidized closed monolayer phase ML1 are shown. Hereby the as-deposited film is oxidized at RT, at 660 K and finally at 800 K in an oxygen pressure of $1.0 \cdot 10^{-6}$ mbar. The evolution of the film due to oxidation is shown in LEED and LEEM in Fig. 3.11. As will be shown different domains appear. Their individual LEEM-IV curves are given in Fig. 3.12. In Fig. 3.14 the XPS results, taken from the sum of all domains at one surface are given.

The as-prepared monolayer phase ML1 consists of two rotational domains having a 1.5 times larger unit cell than Ru(0001). The layer chosen for this experiment is closed and is homogeneous in LEEM. The LEEM-IV curve (Fig. 3.12) shows a maximum at 4.4 eV and the typical distinct peak at 12.6 eV. The curve continues with at relatively broad peak at 15.8 eV with maximum at 19.2 eV. The MEM-LEEM border is found at 2.56 eV. Iron is in the Fe^{2+} state with its maximum at 53.6 eV (see Fig. 3.14a). In Fig. 3.14b the O 1s line is shown. The maximum is found at 529.9 eV.

First, the film is oxidized at RT in $1.0 \cdot 10^{-6}$ mbar for 15 min. The LEED pattern remains unchanged (Fig. 3.11b). However, in LEEM two different domains are visible that can be

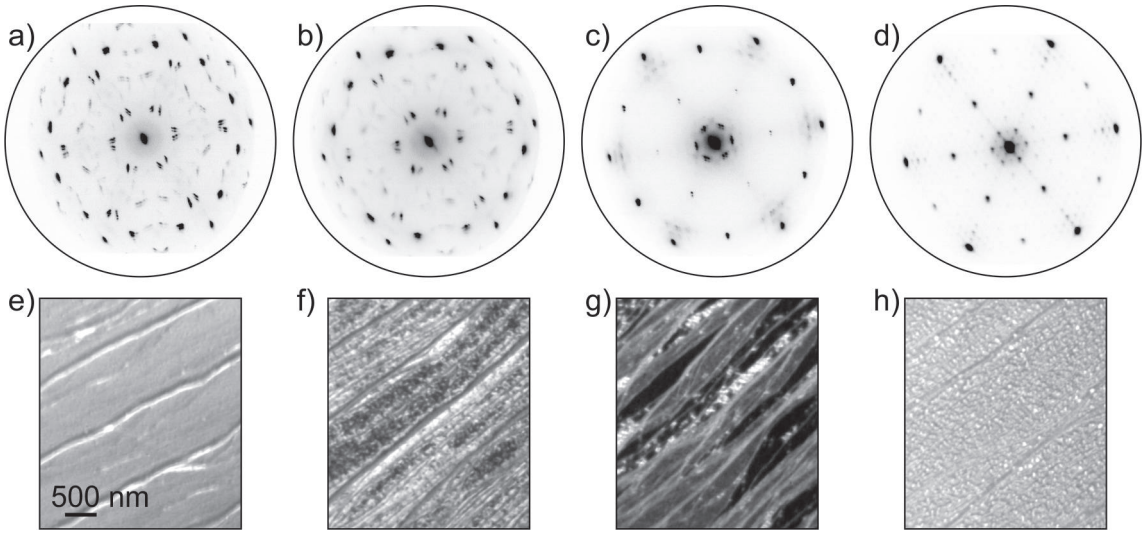

Figure 3.11 Oxidation states of ML1. a, e) after deposition. b, f) oxidation at RT. c, g) Oxidation at 660 K. d, h) Oxidation at 800 K. The LEED images are taken at 42 eV. The LEEM images e-g) are taken at 17 eV and image h) at 20 eV.

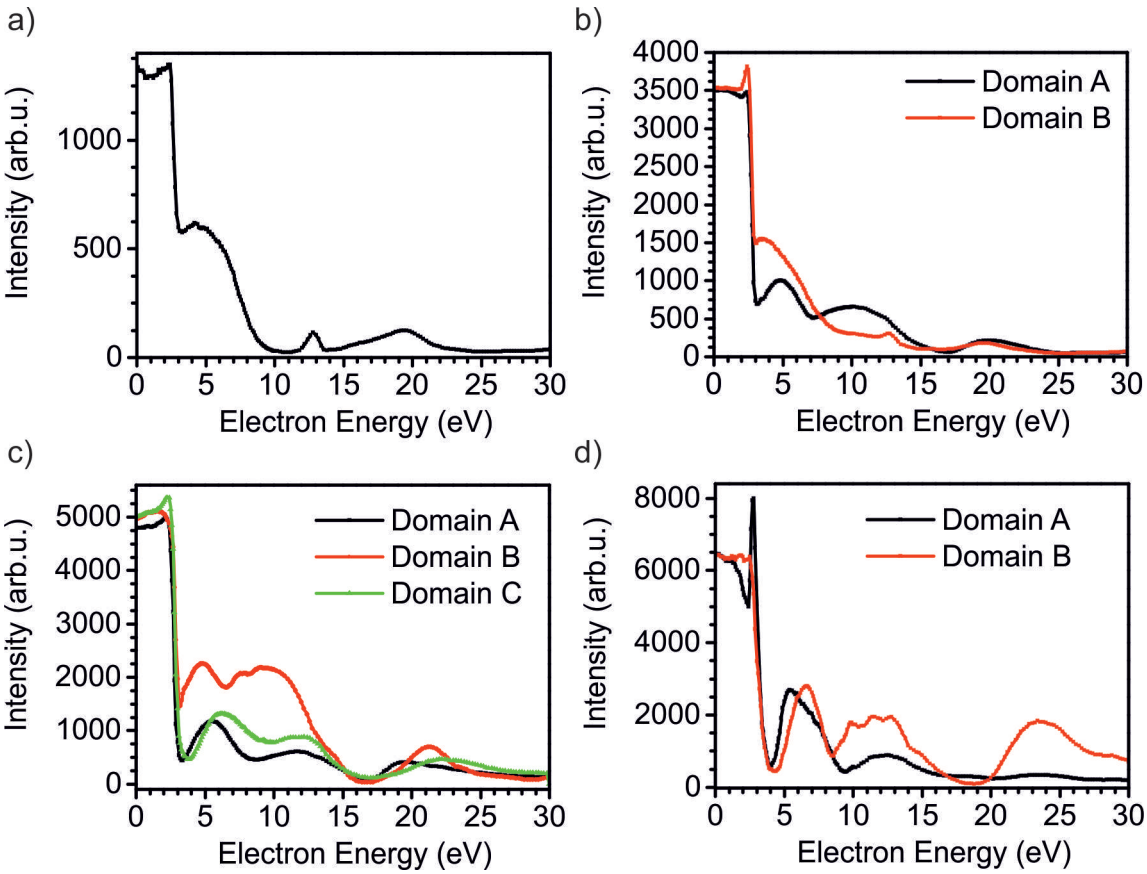

Figure 3.12 LEEM-IV curves of a) homogeneous layer of monolayer phase ML1. b-d) Individual domains developing after oxidation in $1.0 \cdot 10^{-6}$ mbar at b) RT, c) 660 K and d) 800 K.

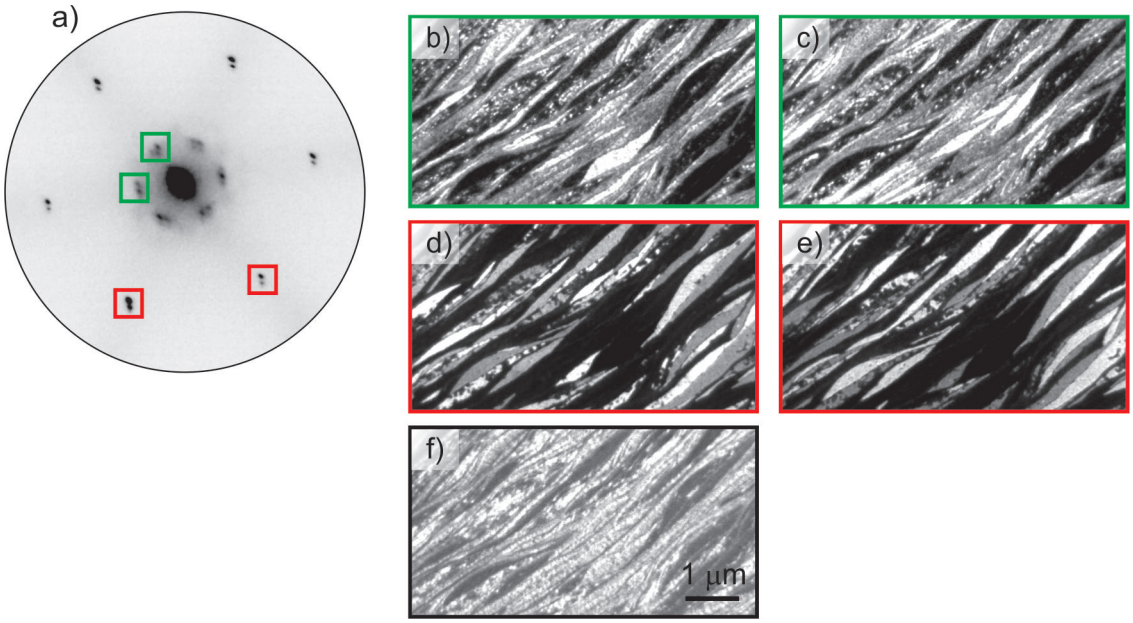

Figure 3.13 Darkfield analysis after oxidation in $1.0 \cdot 10^{-6}$ mbar at 660 K. a) LEED at 20 eV. Darkfield images of the in a) indicated spots (clock-wise) at 20 eV of b-c) Moiré spots and d-e) (2x2) spots. f) LEEM at 17 eV.

found on different terraces. The LEEM image at 17 eV is given in Fig. 3.11f). At this energy one phase is dark (addressed to as domain A), while the other is gray (domain B). The LEEM-IV curve of domain A indicates that this phase has changed upon oxidation. The energy for the MEM-LEEM transition is slightly increased to 2.69 eV, corresponding to a work function change of 0.13 eV, which indicates a higher number of oxygen atoms on top of iron. The most prominent change is the missing of the prior sharp peak at 12.6 eV, which is replaced by a broad peak with maximum at 10 eV. Thus, the characteristics typical for all monolayer phases are missing. Apart from that the peaks at 5 eV and 19 eV remain with slightly different shape. Contrary to domain A, domain B still shows the same characteristics as the as-prepared film. As a result structural changes can be excluded. The oxidation of the film is visible in the emergence of iron atoms in the Fe^{3+} state (Fe 3p line given in Fig. 3.14a). The number of iron atoms in the Fe^{2+} state strongly decreases. Thus, the higher availability of oxygen influences the iron atoms to bind additionally to another oxygen atom per iron atom. The O 1s line has increased in intensity, the peak position is nearly unchanged (see Fig. 3.14b).

The oxidation at RT has already shown that some areas (domain A) change upon oxidation. However, other remains unchanged. Now, the influence of temperature is evaluated. For this the film is oxidized at 660 K in $1.0 \cdot 10^{-6}$ mbar. During this step the LEED image changes drastically (see Fig. 3.11c). The rotational structure disappeared and a non-rotated Moiré structure has formed surrounding the (0,0) spot. Close to the substrate spots three rotational domains are visible. The angle between these domains is 6°, respectively. Additionally a relatively weak (2x2) structure is present. Also in LEEM three different domains are visible. The LEEM image at 17 eV is given in Fig. 3.11g). At this energy domain A is gray, domain B is dark and domain C is bright. Domain C is only visible at the border of domain A. The transition energy from MEM to LEEM for domain A, domain B and domain C are 2.73 eV, 2.86 eV and 2.83 eV, respectively, corresponding to

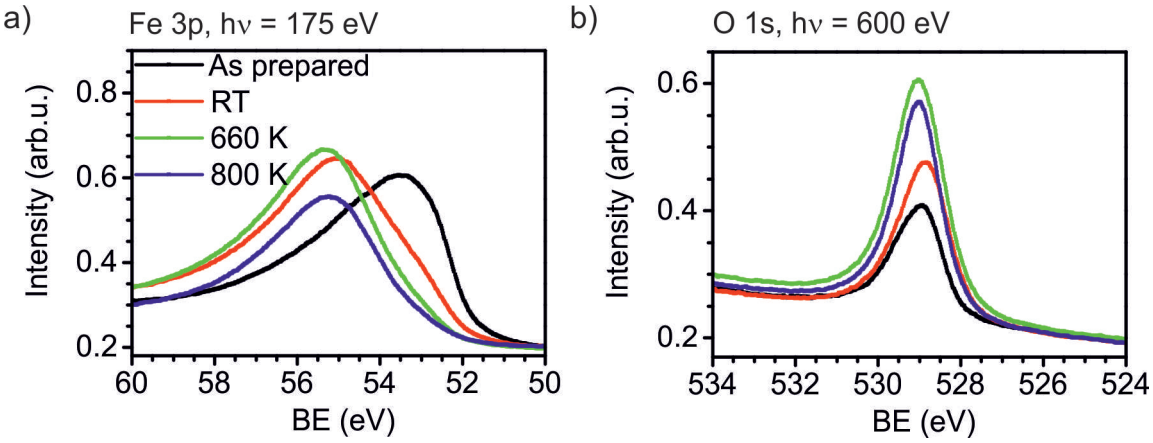

Figure 3.14 XPS analysis of monolayer FeO phase ML1 oxidized in $1.0 \cdot 10^{-6}$ mbar at the indicated temperatures. a) Fe 3p, hν = 175 eV. b) O 1s, hν = 600 eV.

work function differences of 0.15 eV, 0.28 eV and 0.25 eV referred to Ru(0001), respectively. Thus, this oxidation step has increased the MEM-LEEM border for all domains in comparison to the oxidation step at RT. LEEM-IV curves of domain A and domain C are very similar, showing only minor shifts. In fact, the number and position of their peaks resemble strongly domain A at RT. The LEEM-IV curve of domain B has stronger pronounced peaks. Many characteristics are similar, like the peak at 5 eV and the dip at 16.6 eV. The main differences are very intense, broad peaks in the energy range between 6.5 and 10.5 eV. The surface is mostly covered with domain A. In fact, the size of the domains resembles strongly domain A after oxidation at RT. In the LEED pattern, both a Moiré structure (with three domains rotated by 6°) and a (2x2) structure are visible. By dark field measurements the individual LEED spots can be assigned to individual domains visible in LEEM. Unfortunately the (10) spots of the substrate are not accessible at the low energy used. Nevertheless, domains giving rise to the (2x2) structure can be differentiated from domains with a Moiré structure. Dark field measurements are shown in Fig. 3.13. As it turns out the (2x2) structure and the Moiré structure correspond to different domains. Domain A gives rise to a Moiré structure, while domain B gives rise to the (2x2) structure. Oxygen covered Ru(0001) gives rise to a (2x2) structure, thus the (2x2) structure present here can be already a sign for that. The LEEM-IV structure of domain B might be in turn interpreted as an overlap of a 3O-covered Ru(0001) structure with the presence of iron oxide. Domain C is located at the border of domain A and contains both structures. It can be interpreted as an intermediate structure. Both, dark field images using the (2x2) spots and Moiré spots show a contrast change, when switching between neighboring LEED spots. This is an influence of the individual terrace, being either the A or the B type terrace of the ABAB stacking structure of the Ru support. With the help of the dark field analysis domain A can be assigned to the Moiré structure, while domain B gives rise to a (2x2) structure. The Fe 3p line (see Fig. 3.14a) shows that iron is only present in the Fe^{3+} state. This seems to be the energetically most stable state. The O 1s line in Fig. 3.14b is minimally shifted to higher binding energy and much more intense than the previous measurement after oxidation at RT.

For the final oxidation, the temperature was increased to 800 K, staying at $1.0 \cdot 10^{-6}$ mbar oxygen pressure. As a consequence the intensity of the (2x2) spots strongly increased and three different domains in the Moiré pattern at 660 K emerged to only one phase (see

Fig. 3.11d and h). Additionally higher order spots are present, indicating a good long range order. In LEEM one very large domain (domain A) and a very small domain (domain B) are visible. The corresponding LEEM-IV curve identifies domain B clearly as 3O-covered Ru(0001), i.e. as holes in the film. They are mainly present at step edges. The desorption of iron is also visible in the decrease in the Fe 3p line and O 1s line.

In summary, a monolayer of FeO is not stable upon oxidation at elevated temperatures. The process during oxidation is shown as model in Fig. 3.15. While originally the FeO monolayer (phase ML1) is closed (Fig. 3.15a), after the oxidation at RT two different areas are found (Fig. 3.15b): Domain A and domain B. Domain A transforms through oxidation already at RT. During this process in LEEM-IV the peak at 12.6 eV, characteristic for the monolayer FeO films, disappears. At the same time the oxidation state of iron increases from Fe^{2+} to Fe^{3+}. With elevated temperatures (see Fig. 3.15c) for the oxidation at 660 K) this domain grows and changes its structure (as visible in LEED). The multiple rotated domains of ML1 originally having an angle of +/- 17° corresponding to Ru(0001) rotate. As a result rotational domains with an angle of -6°, 0, +6°) regarding Ru(0001) are found at 660 K. Domain B is unchanged at RT (still showing the original fingerprint), but at 660 K iron is reduced in this domain. As an result, in domain B small iron-rich (FeO) and iron-free (holes down to the 3O-covered Ru(0001) substrate) are found. The holes give rise to a (2x2) structure. The border region between domain A and B is an intermediate region (domain C), where characteristics of domain A and B are found. At 800 K (Fig. 3.15d) domain A is the largest domain and has the typical LEED pattern for FeO on Ru(0001).

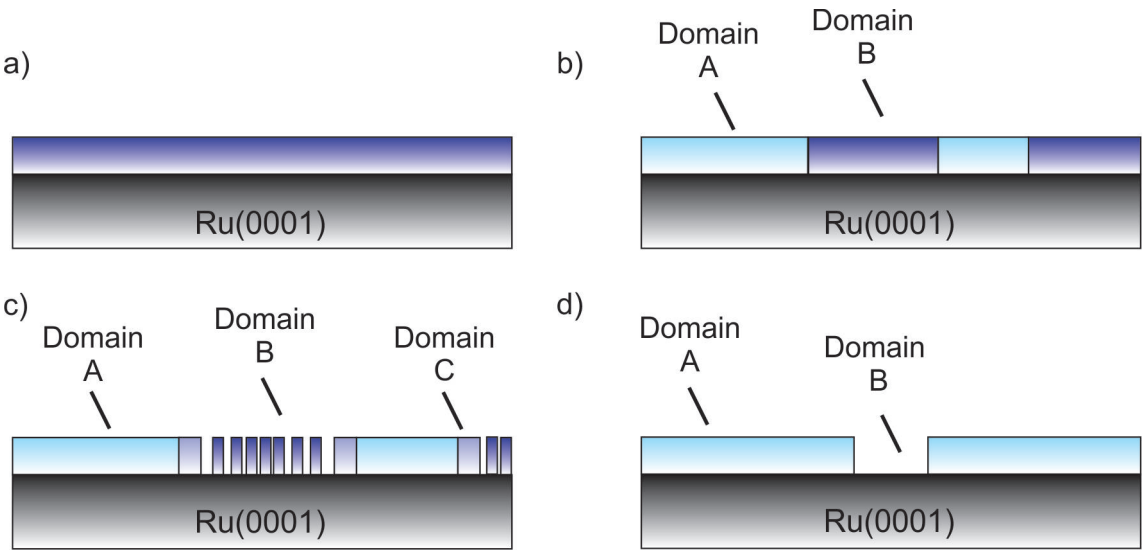

Figure 3.15 Model for the oxidized FeO monolayer (oxygen pressure $1.0 \cdot 10^{-6}$ mbar). a) Closed layer of FeO (phase ML1). b) Oxidation at RT. Domain A transforms structurally (LEEM-IV fingerprint changes) and partially chemically from the Fe^{2+} into Fe^{3+} oxidation state. Domain B remains unchanged. c) Oxidation at 660 K. Domain A similar to b). In domain B the iron amount is reduced and small holes down to the Ru(0001) substrate appear. At the border between domain A and domain B exists an intermediate region assigned as domain C. d) Oxidation at 800 K. Domain A is dominantly found. In domain B iron is vanished, i.e. domain B are holes in the film down to the 3O-covered Ru(0001) substrate.

In contrast, domain B is iron free, i.e. a hole down to the 3O-covered Ru(0001) substrate. Since domain A enlarged, while domain B loses its iron amount, it can be assumed that iron migrates from domain B into domain A.

3.2 Bilayer growth

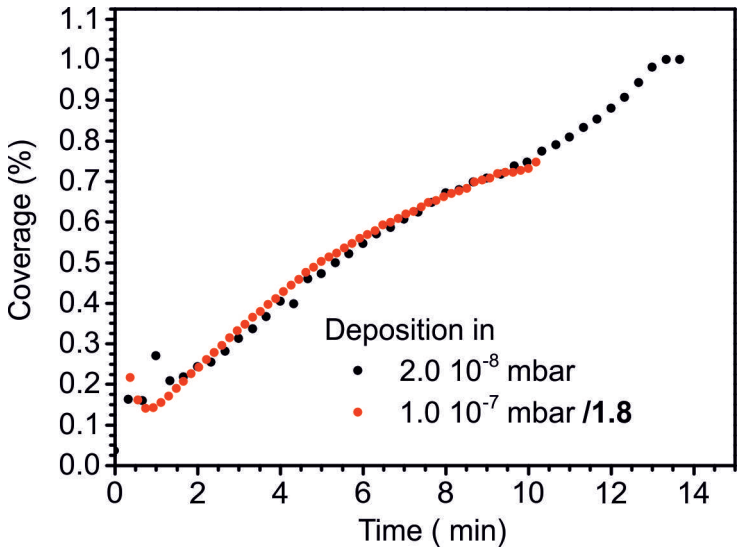

Figure 3.16 FeO coverage during iron deposition in an oxygen pressure of $2.0 \cdot 10^{-8}$ mbar and $1.0 \cdot 10^{-7}$ mbar. The individual time for the deposition in $1.0 \cdot 10^{-7}$ mbar is divided by a factor of 1.8.

The growth mode of iron oxide at elevated temperatures (i.e. 800 K) depends strongly on the oxygen pressure. Oxygen pressures of $1.0-2.0 \cdot 10^{-8}$ mbar lead to a monolayer growth of FeO_{1+x}, as was shown in section 3.1. In a pressure of $1.0 \cdot 10^{-7}$ mbar FeO_{1+x} grows directly as a bilayer. Indeed the iron deposition time in $1.0 \cdot 10^{-7}$ mbar is twice that in $1.0 - 2.0 \cdot 10^{-8}$ mbar. Furthermore, STM images published by the group of de la Figuera et al. [68] show that islands prepared in this way have twice the apparent height as those expected for a monolayer of FeO. In this chapter the growth mode and the characteristics of these bilayer FeO_{1+x} film are investigated.

The growth of iron oxide at 800 K in $1.0 \cdot 10^{-7}$ mbar is shown in Fig. 3.17. Step edges and impurities are nucleation centers for the adsorbed iron atoms. Two different phases are growing as seen by LEEM (at 20 eV): a gray phase and a dark phase. For future reference they will be addressed as BL1 and BL2, respectively. BL1 is found in a much higher amount than BL2, so it can be considered as the main phase. Both phases continue to grow until the layer is closed. Compared to the deposition in $1.0 - 2.0 \cdot 10^{-8}$ mbar the deposition rate in $1.0 \cdot 10^{-7}$ mbar is 1.8 times longer (see Fig. 3.16). In Fig. 3.18a the superimposed LEED pattern (including both phases, BL1 and BL2) is given. A Moiré pattern with a "6 on 7" reconstruction is formed. The distances of the LEED spots fit nicely to those of the monolayer phase ML2 (see Fig. 3.3b). However, the bilayer phases show more spots of higher order.

In Fig. 3.18b the LEEM-IV curve is shown. For both phases BL1 and BL2 the MEM-

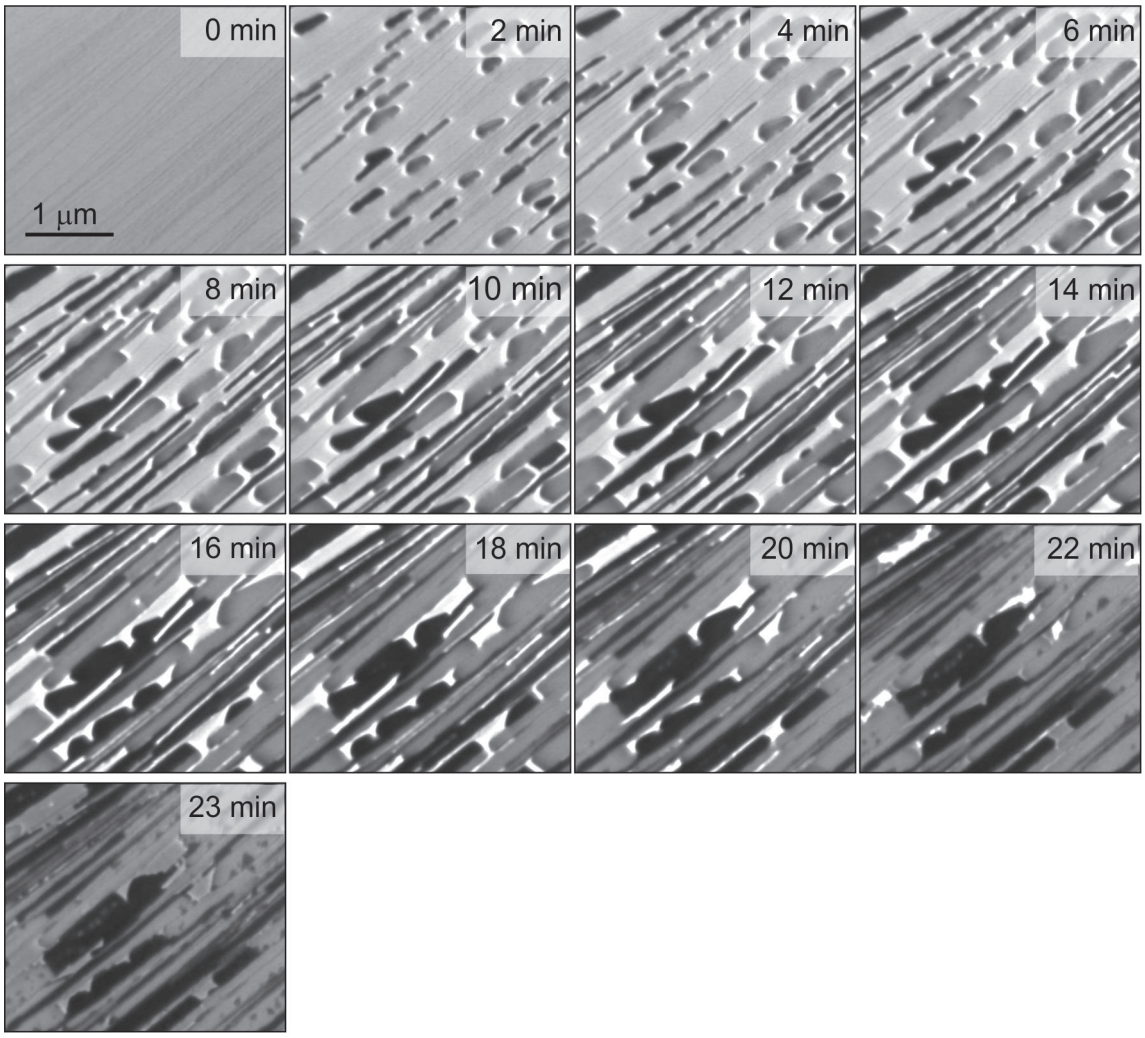

Figure 3.17 Iron deposition in an oxygen pressure of $1.0 \cdot 10^{-7}$ mbar at 800 K. After 2 min two different phases are growing. The gray one is addressed as BL1, the dark one as BL2. The intensity scaling is kept constant for all images.

LEEM transition is identical at 2.4 eV. For comparison, the MEM-LEEM transition for clean Ru(0001) is at 2.58 eV. Thus, the oxygen concentration on top is smaller than the iron concentration. Up to 12 eV the LEEM-IV curves of BL1 and BL2 match. Characteristic for BL1 is a broad band with two peaks at 17.3 eV and 19.6 eV. BL2 on the other hand has one peak at 19 eV and a relatively broad peak at 25 eV. The shared peak at 12 eV is typical for the bilayer phase. In contrast, all monolayer phases share a distinct peak at 12.6 eV.

XPS results are shown in Fig. 3.19 taken in a region, which contained both phases, BL1 and BL2. The peak positions for BL1 and BL2 match. Individual differences will be addressed later in this chapter. The Fe 3p shows a broad peak with overlapped Fe^{3+} and Fe^{2+} states at 55.6 eV and 53.6 eV, respectively. This is a clear difference to the monolayer preparation, where only a Fe^{2+} state is found. Moreover, the typical FeO_{1+x} layer does only contain a Fe^{2+} state. As a result, the iron oxide layer prepared in this way does have the same structure as a typical FeO bilayer (as could be seen in LEED), however the concentration of oxygen is higher. This indicates an additional oxygen layer. The O 1s line shows one

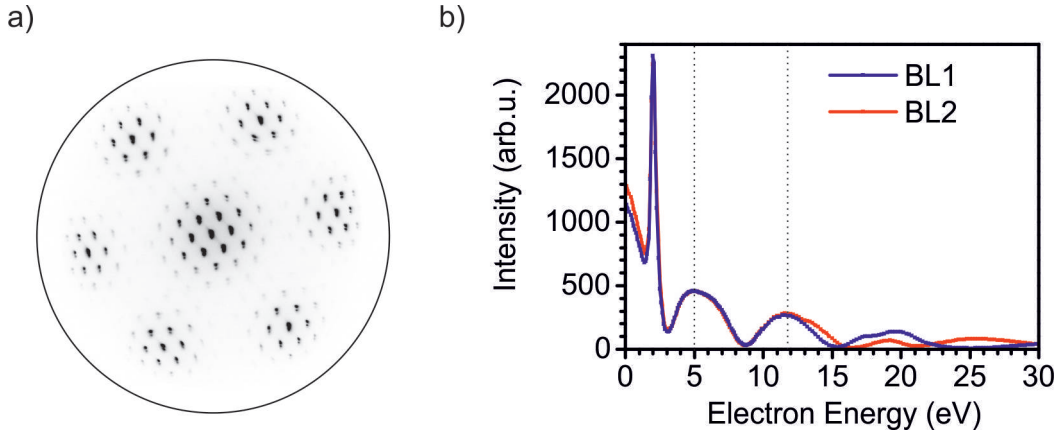

Figure 3.18 Structural characterization of the FeO bilayer deposited at $1.0 \cdot 10^{-7}$ mbar. a) Overall LEED image at 42 eV. b) LEEM-IV curves of phase BL1 and BL2. The lines indicate the characteristic peaks present in all bilayer FeO layers.

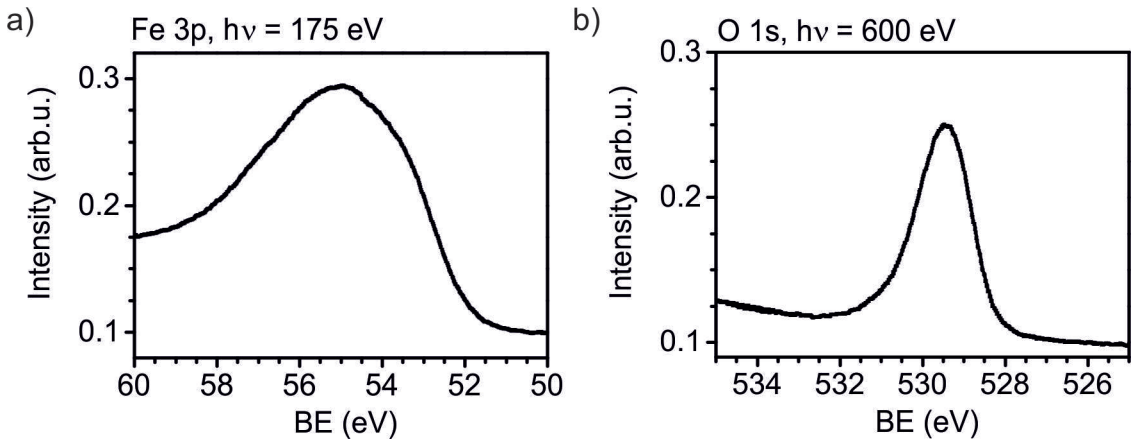

Figure 3.19 XPS characterization of the FeO bilayer. a) Fe 3p line, hν= 175 eV. b) O 1s line, hν = 600 eV.

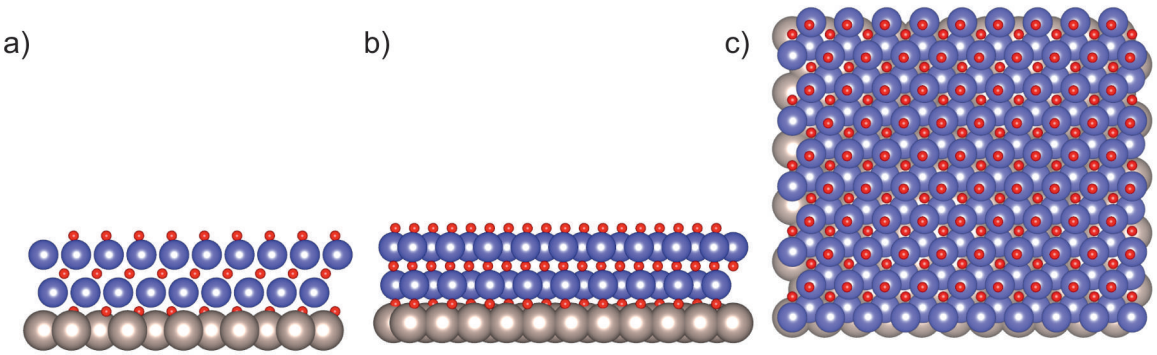

Figure 3.20 Structural model of a bilayer of FeO, as grown at 800 K in $1.0 \cdot 10^{-7}$ mbar. In this structure the measured LEED image (Fig. 3.18a), the deposition rate (Fig. 3.16) and the XPS results (Fig. 3.19) are included. a) x-direction, b) y-direction and c) z-direction. Gray: Ru. Red: O. Violet: Fe.

peak at 529.4 eV. This is slightly shifted to the monolayer preparation.

Phase BL2 can be transformed into BL1. Typically the complete island is transformed at once. A transformation of BL2 to BL1 happens very often already during the iron deposition as is shown in Fig. 3.21. Here, the transforming islands are marked with red, green and violet circles. In all three marked islands the switching is visible from one image to the next (delay time 2 s per image). However, it still remains a mystery why some islands switch, while others remain. The retransformation from BL1 into BL2 was not observed, which indicates that BL1 is energetically favorable in these conditions.

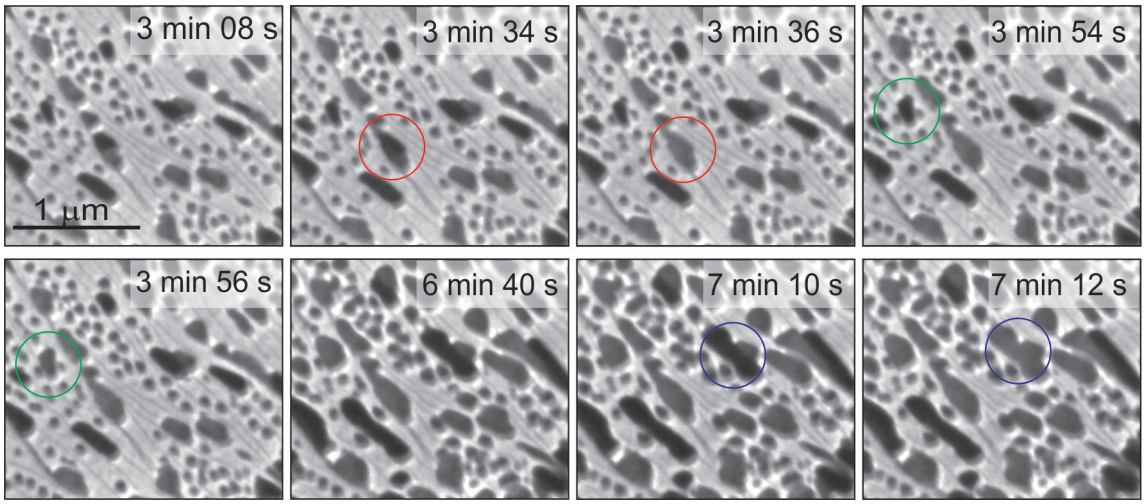

Figure 3.21 Transformation of BL2 (black phase) to BL1 (dark gray phase). The series of LEEM images were taken at 20 eV during iron deposition at 800 K in $1.0 \cdot 10^{-7}$ mbar.

Oxidation of the FeO bilayer

The influence of oxygen can be measured by raising the oxygen pressure up to $1.0 \cdot 10^{-6}$ mbar. A sequence during this process at 800 K is shown in Fig. 3.22. As a basis a bilayer is grown at 800 eV in $1.0 \cdot 10^{-7}$ mbar. The bilayer contains both BL1 (gray) and BL2 (dark) domains (see Fig. 3.22). Subsequently, the pressure is increased up to $1.0 \cdot 10^{-6}$ mbar, while the temperature was kept constant. During this pressure increasesome of the BL2 domains switch to BL1, however, most of the BL2 domains remain stable at first. When staying at this pressure some areas of BL1 become slightly darker (Fig. 3.22b) and act as origin for the presence of a white domain, which can be identified as holes in the film down to the Ru support (white areas in Fig. 3.22c). With continued oxidation at $1.0 \cdot 10^{-6}$ mbar these holes increase and at the same time domains of BL2 transform to BL1 (Fig. 3.22d). As a result the increase of the holes correlates directly with the transformation of BL2 to BL1. One reason might be that the intercalation of oxygen enables the transformation of BL2 to BL1 either through a shift in stacking or via enhancing the oxygen amount in the BL2 phase. A further explanation might be a difference in the iron amount between BL1 and BL2. Thus the iron atoms missing in the holes might increase the iron amount in phase BL2, which in turn transforms the BL2 to BL1. In Fig. 3.22e the transformation of all domains from BL2 to BL1 is complete. The size of the holes is unchanged. After some more minutes of oxidation a new kind of domains appears, having a triangular shape, which are growing in

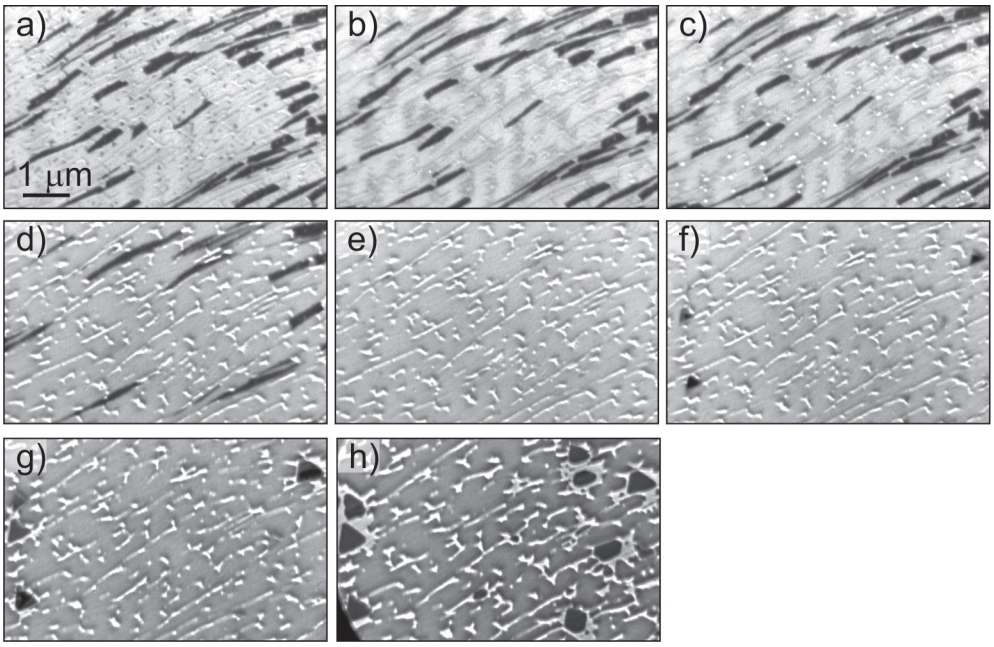

Figure 3.22 Oxidation of a closed bilayer of FeO_{1+x} in $1.0 \cdot 10^{-6}$ mbar. a) After deposition of iron in $1.0 \cdot 10^{-7}$ mbar at 800 K. b-f) Oxidation in $1.0 \cdot 10^{-6}$ mbar at 800 K. b) 3 min and 30 s, c) 4 min, d) 5 min 22 s, e) 6 min and f) 10 min. g-h) Increase in temperature in $1.0 \cdot 10^{-6}$ mbar to g) 860 K and h) 900 K. LEEM images taken at 20 eV.

size. The positions of the triangles cannot be associated with the earlier positions of BL2. With prolonged oxidation the triangles are growing and at the same time the surrounding iron is consumed, as can be seen in the increase of holes in the film. In the Fig. 3.22g and h the temperature is increased to 860 K and 900 K, respectively. The triangles grow faster at higher temperature. A triangular shape is typical for Fe_3O_4 formation [83]. As already discussed, Fe_3O_4 consists of three layers. Here, the formation of BL1 into Fe_3O_4 with consumption of surrounding iron atoms shows that BL1 is indeed a bilayer and differs from the monolayer phase in section 3.1. For the monolayer a transformation to Fe_3O_4 or the presence of triangles of this kind was not observed, even if the film was oxidized at 800 K in $1.0 \cdot 10^{-6}$ mbar.

In fact the appearance of triangles grown on top of a closed layer of the bilayer FeO_{1+x} phase was also observed for continued deposition of iron after the completion of the first layer (see Fig. 3.17 at 28 min of iron deposition). This again indicates the nature of the film, directly grown as a bilayer.

3.3 Intermediate pressure regime

The monolayer and bilayer phases can be separated by using either a pressure $1.0 - 2.0 \cdot 10^{-8}$ mbar or $1.0 \cdot 10^{-7}$ mbar. However in an intermediate pressure of $5.0 \cdot 10^{-8}$ mbar both, the monolayer phase ML1 and the bilayer phases BL1 and BL2 are growing. Such a growth is shown in Fig. 3.23. First, the bilayer phases BL1 and BL2 grow, starting at step edges. The concentrations of BL1 and BL2 do not differ in comparison to the deposition in an

oxygen pressure of $1.0 \cdot 10^{-7}$ mbar. After 4 min a new phase appears, growing at step edges and mostly on the upper or lower terrace next to a bilayer phase island. This can be either a BL1 or a BL2 phase, however in most cases it grows in contact to BL1. The monolayer phase grows much faster than the bilayer phase, which is understandable by the different number of FeO_{1+x} layers. Thus, the closed film (containing monolayer and bilayer phases) contains mostly the monolayer phase. The time span before monolayer phase starts to grow can be varied by increasing/decreasing the oxygen pressure. The reason whether a monolayer, a bilayer or both grows might be the oxygen amount present on the surface before iron lands on the surface [63, 68].

In Fig. 3.24a a LEEM image at 14 eV of such a nearly closed layer is shown. In contrast to the LEEM-image at 20 eV (as used in Fig. 3.23) the individual phases have a more pronounced contrast. As will be justified below, the darkest phase consists of holes down to the

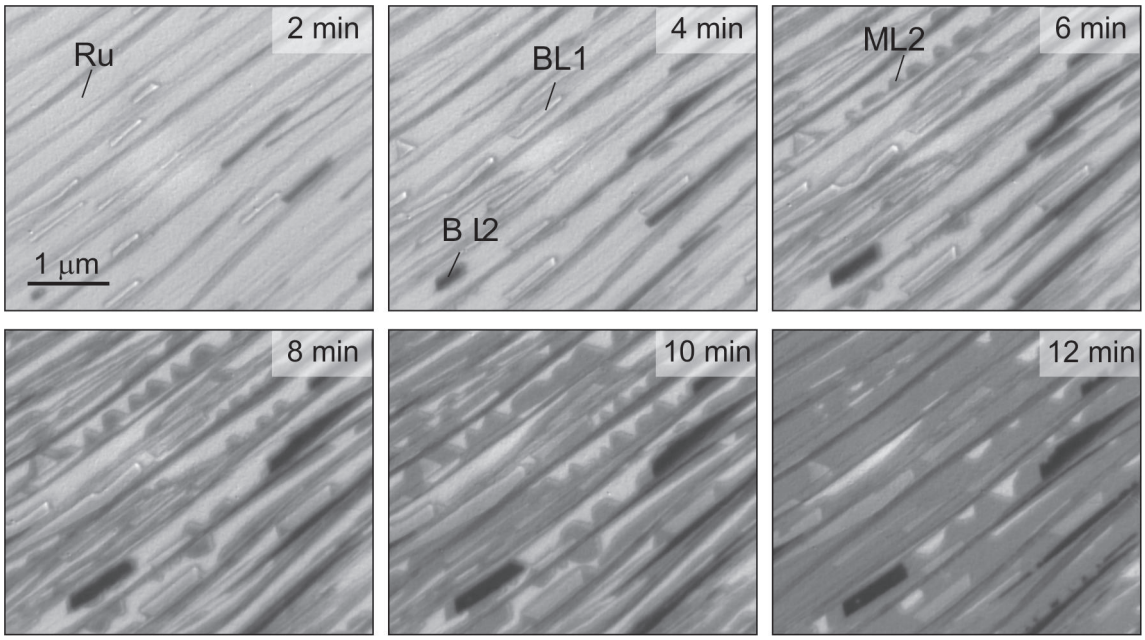

Figure 3.23 FeO_{1+x} growth at a pressure of $5.0 \cdot 10^{-8}$ mbar. The LEEM images were taken at 20 eV at the indicated times during iron deposition at 800 K.

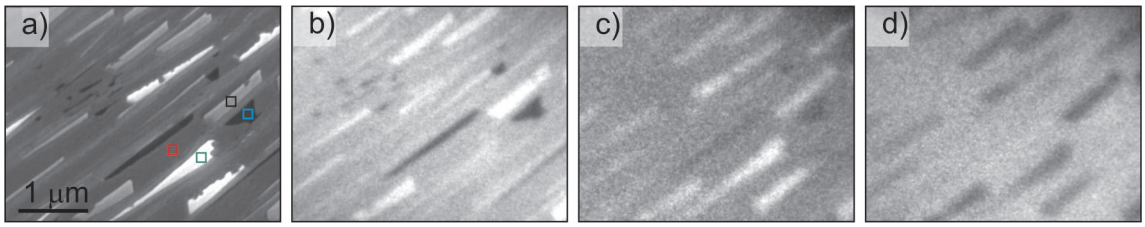

Figure 3.24 a) LEEM and b-d) XPEEM images of a preparation with bilayer and monolayer FeO_{1+x} phases. a) LEEM image at 14 eV. The individual phases are marked with black (BL1), red (ML2), green (BL2) and blue (Ru-substrate). XPEEM images of the b) Fe 3p line (E_{kin} = 117.7 eV, hν = 175 eV), c) O 1s line (E_{kin} = 117.5 eV, hν = 650 eV) and d) Ru $3d_{5/2}$ line (E_{kin} = 117.5 eV, hν= 400 eV).

Ru-substrate (indicated with a blue square). The dominating dark gray domains consist of the monolayer ML2 domain (red square). The bright gray domains (black square) and bright domains (green square) are the bilayer FeO_{1+x} domains BL1 and BL2, respectively. This is shown by the XPEEM images of the same spot in Fig. 3.24b-d. XPEEM is a useful tool not only to measure the XPS characteristics of a specific domain, but also to compare directly the individual amounts of the elements in different domains. XPEEM scans taken at domains marked in Fig. 3.24 are shown in Fig. 3.25. In Fig. 3.25a the Fe 3p line is given. The violet curve of the Ru-substrate does not show any iron, which confirms the absence of an iron oxide layer between the grown domains. As shown for the XPS Fe 3p lines of the individual phase, shifts between the bilayer phases BL1 and BL2 and the monolayer phase ML2 are obvious. In the monolayer phase ML2 iron atoms are in the Fe^{2+} state, while the bilayer phases have additional iron atoms in Fe^{3+} state. The difference in the iron amount in the individual phase is especially interesting. First of all, the peak intensity of the ML2 phase is approximately half peak that of the BL1 phase. This fits nicely to the allocation of monolayer vs. bilayer phase FeO_{1+x} phase. However, the difference between the BL1 and BL2 phase is more interesting. The intensity of the Fe 3p line of

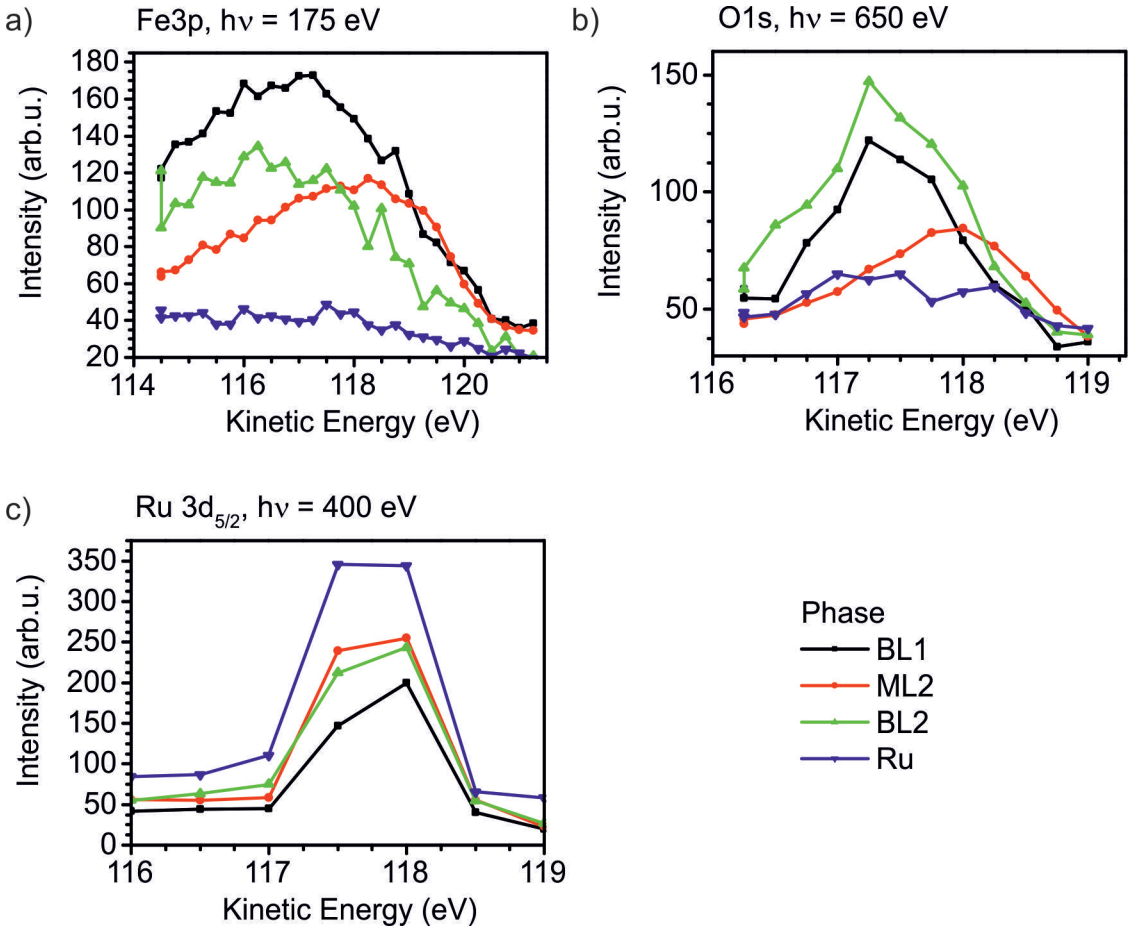

Figure 3.25 XPEEM scan of the a) Fe 3p line ($h\nu$ = 175 eV), b) O 1s line (hν= 650 eV) and c) Ru $3d_{5/2}$ line (hν = 400 eV). In Fig. 3.24 selected XPEEM images are shown. The corresponding energy is indicated as a dotted line. In Fig. 3.24a the individual monolayer and bilayer phases are indicated in LEEM and XPEEM by color.

the BL2 phase is much lower than the one of the BL1 phase. In fact, the intensity of the BL2 phase is very similar to the monolayer phase ML2. In Fig. 3.25b the O 1s lines for the individual phases are given. Similar to the individual XPS measurements of the pure bilayer and monolayer phases the shift between the monolayer ML2 and bilayer phases are reproduced. Also the oxygen amount, given by the peak intensity, of the bilayer phase BL1 is considerably higher than the peak intensity of the monolayer phase ML1, as would be expected for one oxygen layer in the monolayer vs. two oxygen layer in the bilayer. The line corresponding to the Ru-substrate shows different peak positions at 117.25 eV and 118.25 eV. The slightly decreased intensity at 117.25 eV might correspond to intensity variations in form of background noise. The difference between BL1 and BL2 is evident. While the peak position of the O 1s line is the same, the oxygen amount of BL2 is much higher than the oxygen amount in BL1. This would indicate, that the iron reduction in BL2 might correspond to damping. However, the energy for the MEM-LEEM transition and therefore the work function is the same for BL1 and BL2 as was shown in Fig. 3.18b. Thus, the top most layer has an identical dipole moment. It should also be mentioned that BL2 contains much more oxygen atoms than the monolayer phase. This indicates that there must be an additional (oxygen) layer. In Fig. 3.25 the Ru $3d_{5/2}$ is shown, which should give insight into the overall damping. The free Ru substrate has the highest line intensity, since the signal is undamped. Bilayer phase BL2 and ML1 damp the Ru signal nearly equally strong. The BL1 is damping the Ru signal most strongly.

The XPEEM results of the bilayer phases BL1 and BL2 differ strongly. On one hand, the Ru 3d line indicates a stronger damping of the BL1 phase compared to the BL2 phase. Moreover, the Fe 3p line is larger for BL1 than for BL2. Both lines indicate a higher iron amount in BL1 than BL2. One the other hand, BL2 shows a much more pronounced O 1s line than BL1. This indicates a higher oxygen content in BL2.

There might be three possible explanations at this point: A) The BL2 phase is in fact a higher oxidized monolayer phase. B) The BL2 phase is a bilayer phase, but contains a different unit cell than the BL1 phase. C) The oxygen atoms are differently positioned in the BL1 and BL2 phases and thus lead to different damping.

The oxygen amount is higher and thus, the damping of the second iron layer is higher. Explanation A suggest that BL2 has the same amount of iron as a monolayer phase, but an additional oxygen layer, i.e. the iron layer is enclosed by two oxygen layer. While the XPEEM data fit very well to this explanation (similar intensity in the Fe 3p and Ru 3d line), the very fast transformation from BL2 to BL1 cannot be explained. Moreover, the characteristic LEEM-IV peak at 12.6 eV for monolayer phases (compare Fig. 3.6a) is not present in the LEEM-IV curve of BL2 (see Fig. 3.18b). This indicates that BL2 is indeed a bilayer FeO phase.

Explanation B suggests that the lateral iron concentration in BL1 and BL2 is different. However, a different structure is expected to lead to a different LEED pattern. Since in BL1 and BL2 the same LEED pattern is found, this explanation seems to be unlikely.

Explanation C suggests that differently oriented oxygen lead to different damping of the iron and oxygen signal. For instance a different damping would be expected for oxygen positioned in top or hcp adsorption sides. This explanation requires only small differences between the BL1 and BL2 phase, which fits to the very fast transformation from BL2 to BL1.Thus, this explanation seems be this explanation the most promising one.

In summary, a mixture of FeO monolayer and bilayer phases grow if the pressure is set

between $2.0 \cdot 10^{-8}$ mbar and $1.0 \cdot 10^{-7}$ mbar. The higher the pressure the higher the amount of bilayer compounds. In this intermediate range grows first bilayer phases BL1 and BL2. After a pressure dependent time (the higher the pressure, the longer the time) domains with monolayer phase ML1 grow next to the bilayer phases. As was already observed in chapters 3.1 and 3.2 domains with monolayer phase ML1 grow nearly twice as fast as domains with bilayer phases. XPEEM results enable direct comparison of oxygen and iron contents of the individual phases. As expected, contains ML1 less iron and less oxygen as the bilayer phases (in particular BL1). Moreover the ML1 phase does contain only Fe^{2+} states, while the bilayer phases contain Fe^{2+} and Fe^{3+} states. The O 1s line does not only show that the ML1 phase contains less oxygen, but also a significant shift is found between the O 1s line in ML1 and BL1. This fits to the asumption that the bilayer is enclosed by oxygen layer on top and underneath iron (O/Fe/O/Fe/O/Ru(0001)), while the monolayer in contains only one oxygen layer on top (O/Fe/Ru) (see chapters 3.1 and 3.2 for further information. The two bilayer phases BL1 and BL2 differ strongly in their elemental intensities in XPEEM, but not positions. Different explanations for the different XPEEM results are discussed. Since BL2 is fastly tranformed into BL1, the differences between these two phases must be small. Thus, most reasonable explanation is a difference in the position of oxygen, which leads to different damping of either oxygen or iron.

3.4 Summary of mono- and bilayer FeO Films

In this chapter monolayer and bilayer FeO films on Ru(0001) are investigated. The films are prepared by direct deposition at 800 K. As it turns out, the necessary oxygen amount is very critical for the grown phases. An overview of the individual phases is given in tabular 3.1.

The monolayer FeO_{1+x} film (section 3.1) exhibits three different phases. A deposition in $1.0 \cdot 10^{-8}$ mbar leads to rotated hexagonal domains (phase ML1). A deposition at slightly higher pressures of $2.0 \cdot 10^{-8}$ mbar leads to a Moiré structure (phase ML2) with a "6 on 7"

	Monolayer phases			Bilayer phases	
	ML1	ML2	ML3	BL1	BL2
Pressure in mbar	$1.0 \cdot 10^{-8}$	$2.0 \cdot 10^{-8}$	$2.0 \cdot 10^{-8}$	$1.0 \cdot 10^{-7}$	$1.0 \cdot 10^{-7}$
Structure	Rotational domains	Moiré	Moiré+ (2x2)	Moiré	Moiré
Transformation	-	into ML3	-	-	into BL1
Fe oxidation state	Fe^{2+}			Fe^{2+} and Fe^{3+}	
MEM-LEEM	2.56 eV	2.54 eV	2.28 eV	2.4 eV	2.4 eV
Workfunction	5.42 eV	5.40 eV	5.14 eV	5.26 eV	5.26 eV

Table 3.1 Overview of the individual monolayer and bilayer phases of FeO, prepared by direct iron deposition at 800 K in oxygen background (pressure as indicated).

reconstruction. Both structures are identical in their chemical state, showing the Fe^{2+} state typical for FeO. The reason for the formation of phase ML1 or ML2 is most likely the oxygen amount present on the surface before iron is landing; or alternatively the precise available oxygen amount in the surrounding. Phase ML2 can switch to another phase (ML3). The transformation is very fast and possible for domains of several micrometers. The LEED pattern of ML3 shows additionally to the Moiré structure (2x2) spots. Most likely a change in the oxygen termination produces a buckling of the film and thus, the (2x2) structure. A transformation of ML1 into ML2 was not observed, even if the amount of available oxygen is increased. The oxidation of the monolayer phase ML1 is leading to an iron oxidation state of Fe^{3+} accompanied by holes in the film.

In a pressure of $1.0 \cdot 10^{-7}$ mbar during iron deposition a bilayer-thick film grows. In section 3.2 its characteristics are described in detail. Different from the monolayer growth not one homogeneous phase, but two phases grow simultaneously (phases BL1 and BL2). Both phases give rise to Moiré structures. However, in contrast to a typical FeO_{1+x} layer a Fe^{3+} state is detected. Thus, we propose an additional layer of oxygen positioned between the last iron layer and the Ru(0001) substrate. BL2 can transform to BL1 either self-contained during iron-deposition or mediated through increased oxygen pressure. Here also complete domains switch within two seconds. The reason might be the difference in oxygen termination between Phase BL2 and BL1. An oxidation in an oxygen pressure of $1.0 \cdot 10^{-6}$ mbar transforms first BL2 into BL1, before the formation of triangles becomes evident. In the surrounding of the triangles holes are formed, indicating the consumption of iron in order to increase the size of the triangles. The growth of Fe_3O_4 as triangles on top of a bilayer of FeO is known [83] and most likely the case also for the present observation.

At intermediate pressure of $5.0 \cdot 10^{-8}$ mbar both, monolayer and bilayer domains are formed (section 3.3). When the iron deposition starts bilayer domains are growing. After some time additionally monolayer domains form. The time at which the monolayer domains start to grow is varied with a change in the pressure. A pressure of $6.0 \cdot 10^{-8}$ mbar prolongs the necessary time. Both domains continue to grow until the layer is closed.

Chapter 4

Ultrathin layers of $FeSiO_x$ on Ru(0001)

Iron oxides and silicates are one of the most abundant materials on earth. Iron silicates are found in the earth crust and mantle as fayalites Fe_2SiO_4 or under even higher pressures as perovskite structures $(Fe_x\ Mg_{1-x})SiO_3$ [58]. In industries iron silicates are found in cement and as a by-products in construction materials, i.e in Chalkopyrit ($CuFeS_2$) together with Sand SiO_2 and recycling material. There it can be crystalline or amorphous and be used as fill material in construction works.

Iron in silicates can take over various tasks. In aluminosilicate zeolites iron atoms can serve as cations. In aluminosilicate the Si^{4+} is replaced by Al^{3+}. The cationic iron can then compensate the electronegativity introduced by the Al. In natural zeolites however, iron is rather a contamination than effectively taking over the cationic part. In artificial zeolites on the other side iron can be included purposeful to act as the desired charge compensator. Two examples are Fe-ZSM-5 and Fe-MCM-41 [71].

Different to aluminium, iron mostly avoids being part of the tetrahedral framework built by silica. Either it is acts as counterions, for instance in the pores of zeolites, or it can even form a layer, if the iron ratio is large enough as in phyllosilicate nontronite [71]. Only in rare cases they are found in tetrahedral sites like in ferriannite [71]. The reason for this different behaviour of aluminium and iron is believed to be their different ionic radii differs in the tetrahedral environment (Al^{3+}: 0.39 Å, Fe^{3+}: 0.49 Å [91]).

The results found for three-dimensional zeolites, proved to be also true in the two-dimensional case. Aluminium substitutes silicon atoms in the upper and lower level of a silica bilayer. Theoretical models suggest, that iron is only found in the lower level of the silica bilayer. Experimentally it turns out, that iron is not simply substituting silicon atoms, but a two-layered system is formed [103]. In contact to the Ru(0001) substrate a layer of iron oxide forms (having Fe-O-Fe bonds in XPS). On top of this iron oxide layer a monolayer of silica exists (Si-O-Si bonds), which give rise to a by 30° rotated structure. The silicon atoms are bound through oxygen to the iron atoms underneath (Si-O-Fe bonds) [96].

As Włodarczyk et al. [103] have shown, iron silicate can be grown by subsequent deposition of Si and Fe on a 3O-(2x2)-Ru(0001) substrate, followed by an oxidation step. In the following this preparation method will be called "combined preparation" method, due to the subsequential deposition of silicon and iron in the same conditions. Since the final iron silicate films of R. Włodarczyk et al. were analysed with XPS and STM, there were no

information presented about the growth and formation process of these iron silicate films. Furthermore, information about the film homogeneity on micrometer scale is not easily accessible with STM technique. In the approach in this work iron silicate will be prepared using the techniques of LEEM, μLEED, XPEEM and μXPS. The SMART instrument enables to prepare the film not only in situ, but also to observe the individual film formation in real time.

In section 4.1.1 a similar approach as in Włodarczyk et al. [103] is chosen in order to check comparability of the results given with STM data. In section 4.1.2 the recipe is adapted by the deposition of iron and silicon (in this order) in UHV conditions and without 3O treatment. As a consequence only a small amount of oxygen (mostly residual in surrounding UHV conditions) is available upon iron and silicon deposition. The influence of oxygen during the first contact of iron, silicon and the Ru substrate should be evaluated. This preparation method will be called "combined UHV preparation".

Iron silicate is described as a silica monolayer on top of an iron oxide layer. In order to prove this assumption in chapter 4.2.1 iron silicate is prepared by the deposition of silicon on top of a pre-prepared FeO monolayer. Since in this preparation two separate steps are performed (first FeO production, second iron silicate formation) this method will be called "stepwise preparation" method in the following. In section 4.2.2 this preparation is reversed by the pre-preparation of a monolayer of silica, before in a second step iron is deposited. This preparation method will be addressed as "stepwise reversed preparation" method.

In chapter 4.3 the "stepwise preparation" method is used to prepare iron silicate with multiple layer of either FeO (section 4.3.1) or silica (section 4.3.2). This offers the possibility to investigate the strength of the Fe-O-Si bond and the influence on the additional layer.

In chapters 4.1, 4.2 and 4.3 complete layers of iron silicate are produced. This offers the possibility to check the homogeneity of the film. XPS and LEED are typically taken out of an area of four micrometer size. As a result the measured data is only taken in areas of homogeneous iron silicate. However incomplete films offer the possibility to investigate the kinetic and structure of the film and elucidates the energetically favoured arrangement of the iron silicate films. The possibility for iron and silicon to arrange freely is given using the "combined preparation" method (section 4.4.1). Domain formation of iron silicate is found, whereby the domain size and form is defined by energetic minimization of the film. In section 4.4.2 the "stepwise preparation" method is used. Here, the domain size is defined by the production of FeO monolayer islands, before silicon is deposited. Hereby it is possible to compare iron silicate islands with the FeO islands pre-prepared. As these FeO islands are well known (see section 3.1) in their number of iron atoms per unit cell, a variation of size might directly give a hint on the composition and number of iron atoms per unit cell of the iron oxide layer in iron silicate. Finally in section 4.4.3 bilayer-thick FeO islands are prepared before silicon is deposited. Similar to section 4.4.2 the bilayer-thick FeO islands are well known (compare section 3.2) and thus, a variation gives direct insight into the present iron silicate structure.

4.1 "Combined" approach

This chapter concentrates on the so called "combined" approach, meaning that iron and silicon are deposited subsequential in the same conditions. In section 4.1.1 silicon and iron are deposited on a 3O-covered Ru(0001) substrate in oxygen gas pressure. As a result during the deposition process both silicon and iron become oxidized. Since this preparation method equals the one used in literature [103], the result can be nicely compared with LEED, STM and IRAS measurements. In this work the fingerprint in LEEM-IV, LEED-IV and XPS are determined.

Up to now only information about the final iron silicate film are known. The measurements in this work concentrate on the preparation process. In fact the individual temperatures for oxidation and structural arrangement are determined. This enables to achieve more information about the bonding mechanism and structure of ultrathin iron silicate layer. Furthermore, the preparation details give information about the structure of the film. Up to now the structure of the iron oxide layer in iron silicate is not well known. In particular the number of iron atoms per unit cell is of interest. Additional DFT simulations in order to fit the iron silicate structure better are given in collaborations with R. Włodarczyk and J. Sauer.

In section 4.1.2 the preparation is varied in order to evaluate the influence of oxygen on the film formation. Therefore, iron and silicon are deposited in UHV conditions on a freshly cleaned Ru(0001) substrate. This preparation method will be addressed to as "combined UHV preparation" method.

4.1.1 Combined preparation method (Si+Fe/3O-Ru(0001))

This section focuses on the "combined preparation" method, meaning silicon and iron are deposited at the same preparation step. As a very first step, the Ru(0001) crystal is prepared to produce a 3O-(2x2) oxygen termination. For this the Ru(0001) crystal is oxidized at 1170 K for 10 min in $1.0 \cdot 10^{-6}$ mbar oxygen pressure. Afterwards the sample is cooled down in oxygen to RT (room temperature). The result is a closed-packed oxygen coverage on top of Ru, giving rise to a (2x2) structure. In dark-field experiments a three-fold symmetry is found, when choosing neighbouring (2x2) spots (see Fig. 4.1a. Since a SiO_2 layer on Ru(0001) is also giving rise to a (2x2) structure, it is important to distinguish between this and (2x2) structure caused by 3O. The corresponding fingerprint (LEEM-IV curve) is given in Fig. 4.1b. Characteristic for a 3O-(2x2) structure is its disappearance at temperature exceeding 620 K. The reason is its large mobility at this temperature. Apart from the 3O structure on a Ru(0001) crystal 1O, 2O and 4O structures are possible. Their formation is highly dependent on temperature and oxygen dose [35,44,70,74]. The 1O and 3O structures give both rise to a p(2x2) structure, the 2O structure to a (2x1) structure and the 4O to a (1x1) structure [44]. Apart from changes in the LEEM-IV signature the p(2x2) and p(2x1) can be distinguished by dark field analysis, since the (2x2) structure is three-fold and the (2x1) structure is two-fold.

At RT Si is deposited on the 3O-(2x2)-Ru(0001) substrate in $2.0 \cdot 10^{-7}$ mbar. The Si amount equals the amount necessary to form a ML of SiO_2. As a result the (2x2) structure of the oxygen coverage becomes blurry and very weak (Fig. 4.2a). The reason is that Si

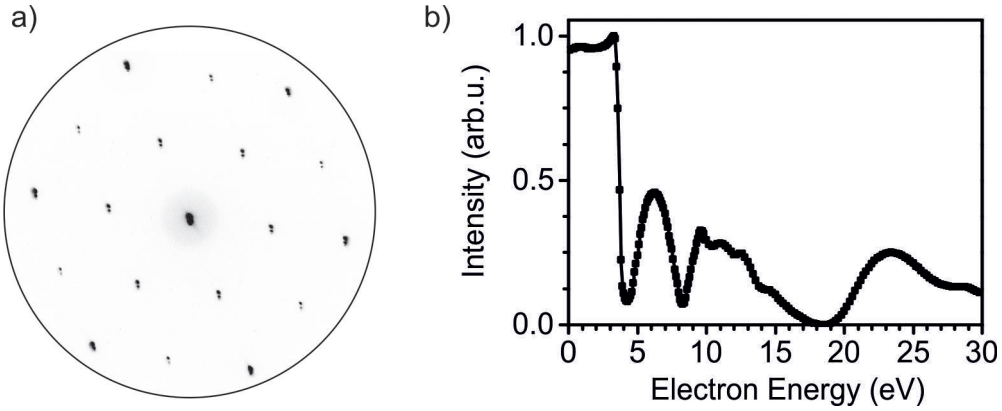

Figure 4.1 Ru-(2x2)-3O characteristics. a) LEED at 42 eV and b) LEEM-IV curve.

is very disordered after deposition at RT. This can also be seen in the LEEM-IV curve (Fig. 4.4a). Apart from one main peak at 6.5 eV the spectrum is rather unobtrusive. The MEM-LEEM border is present at 3.05 eV (Fig. 4.4b). The XPS spectra of the O 1s, Fe 3p and Si 2p line are given in Fig. 4.6a-b, c-d and e-f, respectively. The Si 2p line indicates that Si is completely oxidized in the Si^{4+} state. The FWHM is rather broad (1.9 eV), i.e. different Si bonds are present. This might be Si bound to Ru through oxygen (Si-O-Ru) or Si bound to other Si atoms (Si-O-Si). In fact the O 1s XPS spectrum shows the presence of 2 peaks at 529.3 eV and 531 eV. It is known that Si-O-Si is found at 531 eV, while 529.3 eV corresponds to oxygen bound to Ru (O-Ru) [44]. Depth profile shows that the ratio of the intensities I(529.3 eV) : I(531.0 eV) is increased when using a photon energy of 780 eV,

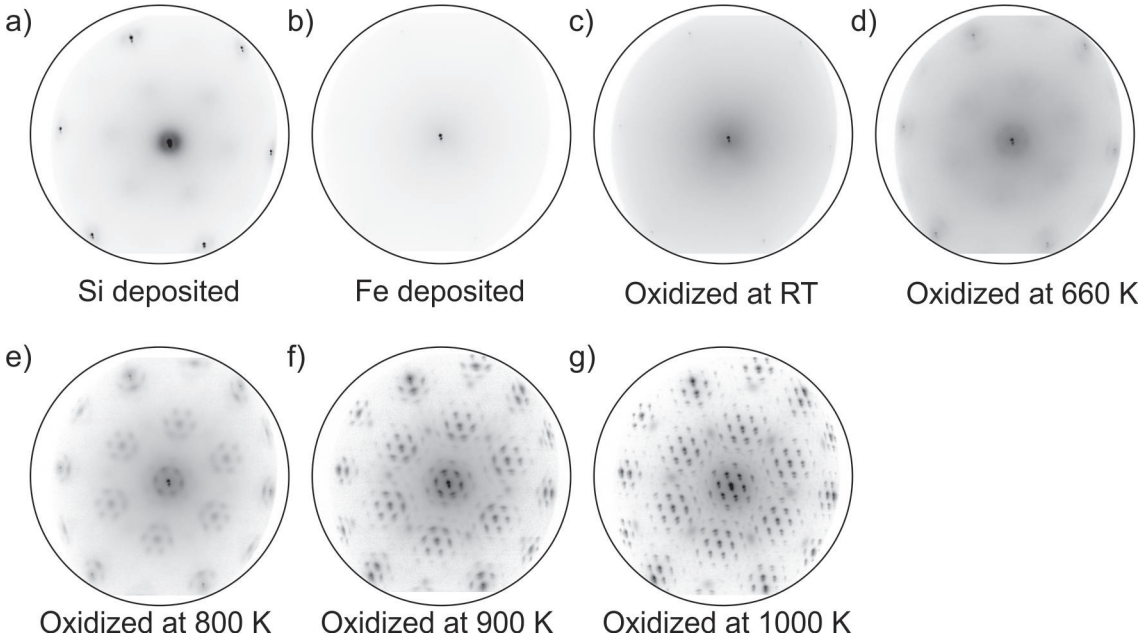

Figure 4.2 LEED study of iron silicate for the "combined preparation" method (Si+Fe/ 3O-Ru(0001)). The images are taken at RT. The (2x2) spots for 900 and 1000 K are only present for temperature lower than 620 K. As a conclusion, it must be oxygen-related. All images are taken at 42 eV.

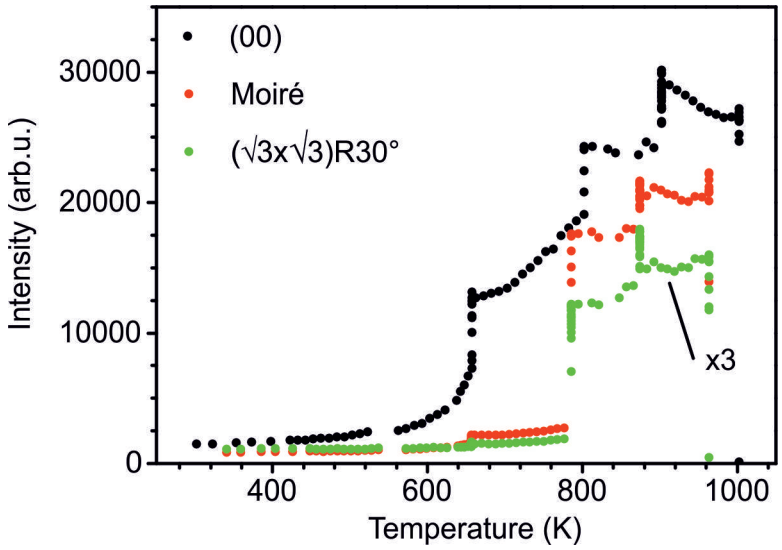

Figure 4.3 Spot intensity of the (00), Moiré and $(\sqrt{3}\times\sqrt{3})R30°$ spot during annealing of iron silicate using the "combined preparation" method (Si+Fe/3O-Ru(0001)). The $(\sqrt{3}\times\sqrt{3})R30°$ structure refers to a silica structure that is rotated by 30° regarding a complete iron oxide layer. The oxygen pressure during temperature increase is $1.0 \cdot 10^{-6}$ mbar.

instead of 600 eV. Thus, the component 529.3 eV is closer to the Ru(0001) substrate than the one at 531 eV. This confirms the earlier assignment. Silicon binds already at RT to the available oxygen. As shown recently [44] the 3O-coverage on the Ru(0001) surface is not sufficient to completely oxidize a the silicon amount necessary to form a monolayer silicon. However, the surrounding oxygen is necessary for complete oxidation. For a higher silicon amount the additional silicon atoms are reduced, as visible in the Si 2p line.

Subsequently to silicon deposition iron is deposited in $2.0 \cdot 10^{-7}$ mbar of oxygen. The residual (2x2) spots disappear, only the (00) spot remains (Fig. 4.2b). The MEM-LEEM border is strongly lowered to 2.71 eV (Fig. 4.4b). This indicates a lower dipole on the surface. However, the LEEM-IV curve (4.4a is rather unchanged. Altogether iron is disordered, similar to silicon. In XPS the O 1s component at 529.3 eV, which corresponds to iron oxide, is strongly increased. This positions fits also to pure FeO on Ru(0001). At 780 eV photon energy the ratio of I(529.3 eV): I(531.0 eV) is even stronger. The Si 2p line shows that silicon remains completely oxidized in the Si^{4+} state even after iron deposition. The reason is the higher dissociation energy of the Si-O bond (798 kJ/mol), compared to the Fe-O bond (409 kJ/mol) [2,17]. The Fe 3p line shows that iron is in the Fe^{2+} and Fe^{0} state. As already discussed, iron can only bind to oxygen available in the surrounding, since Si-O bonds are not broken. As a result it is only partially oxidized.

The films is oxidized in $1.0 \cdot 10^{-6}$ mbar at RT for 30 min. The structure does not change during this step, as is visible by the unchanged LEEM-IV curve and MEM-LEEM border (Fig. 4.4). LEED shows a blurry halo surrounding the (00) spot (Fig. 4.2c). The main impact of this oxidation step is visible in the iron layer. Iron binds to the available oxygen, which reduces strongly the number of metallic iron. Most of the iron atoms are in the Fe^{2+} state, but also a clear amount of iron atoms are in the Fe^{3+} state. This effect is also visible in a further increased ratio of I(529.3 eV): I(531.0 eV). Hereby, only the component at 529.3 eV is rising, while the other is unchanged. These results fit to the unchanged Si 2p

line.

As follows, the film is annealed in $1.0 \cdot 10^{-6}$ mbar. The film was annealed stepwise up to 660 K, 800 K, 900 K and 1000 K in LEED conditions. The individual LEED images are shown in Fig. 4.2d-g. The evolution of the intensity of the (00) spot, one Moiré spot and a the by 30° rotated spots are given in Fig. 4.3. In case the iron oxide layer equals in its number of iron atoms a FeO layer, these spots may be identified a $(\sqrt{3} \times \sqrt{3})R30°$ structure resulting from silica on top of an iron oxide layer. For each step the films is held at the specific temperature for 30 min before cooling the sample fast. Measurements, such as XPS, LEEM-IV and LEEM were performed at RT. The temperature is slowly increased with approximately 2 K per second.

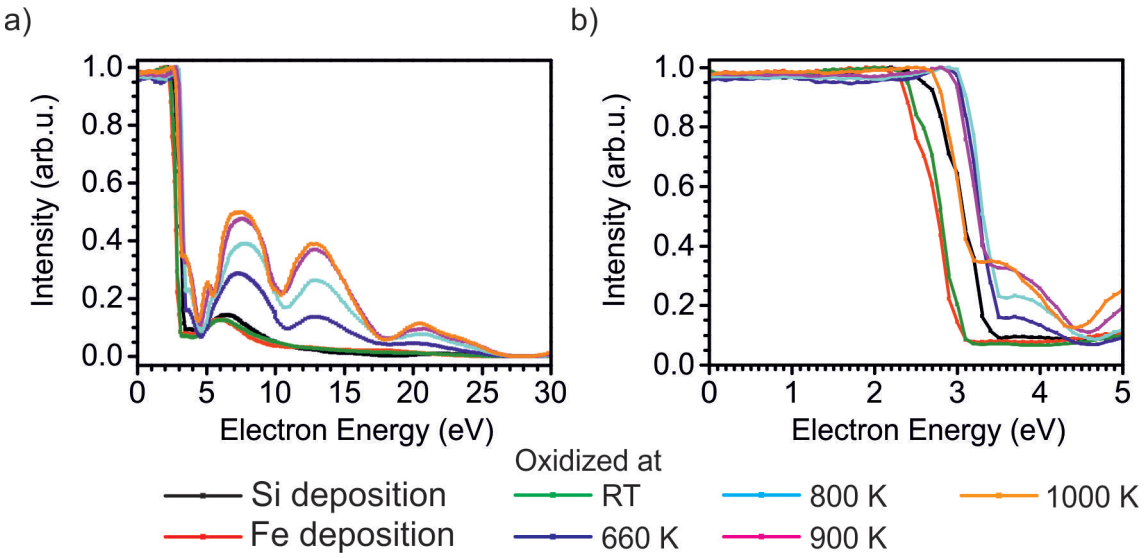

Figure 4.4 LEEM-IV curve for the individual preparation steps of iron silicate using the "combined preparation" method (Si+Fe/3O-Ru(0001)). Silicon and iron are deposited in $2.0 \cdot 10^{-7}$ mbar. The oxidation was done in a pressure of $1.0 \cdot 10^{-6}$ mbar.

Preparation step	Energetic position of the MEM-LEEM border (eV)	Workfunction (eV) (referenced to clean Ru(0001) with 5.44 eV [12])
3O-(2x2)-Ru(0001)	3.5	6.36
Si deposition	3.05	5.91
Fe deposition	2.71	5.57
Oxidation at RT	2.78	5.64
Oxidation at 660 K	3.24	6.10
Oxidation at 800 K	3.27	6.13
Oxidation at 900 K	3.17	6.03
Oxidation at 1000 K	2.97	5.83

Table 4.1 Overview on the MEM-LEEM border evolution for the individual preparation steps of the "combined preparation" method (Si+Fe/3O-Ru(0001)).The MEM-LEEM values are measured with an accuracy of ± 0.02 eV.

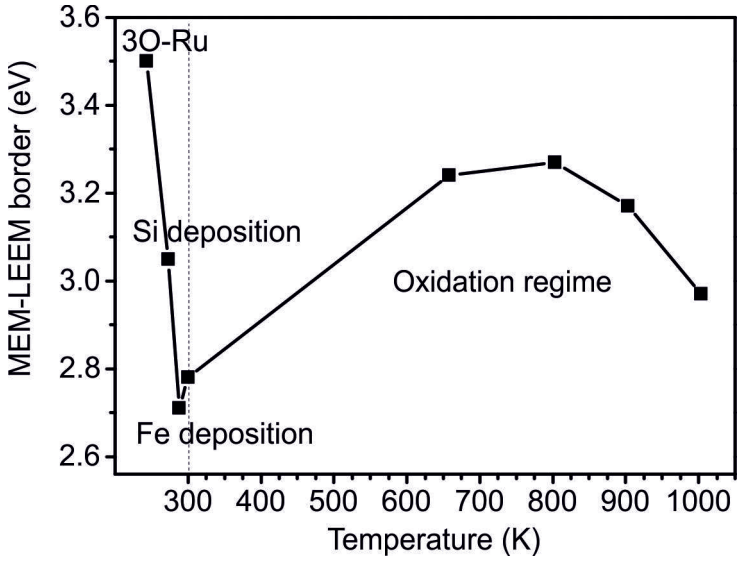

Figure 4.5 MEM-LEEM border evolution for the individual preparation steps of iron silicate using the "combined preparation" method (Si+Fe/3O-Ru(0001)). Silicon and iron are deposited in $2.0 \cdot 10^{-7}$ mbar. The oxidation was done in a pressure of $1.0 \cdot 10^{-6}$ mbar.

First the sample is annealed up to 660 K. At this temperature the film starts to arrange, as the formation of a superstructure indicates. At 660 K intensity in the distance of (2x2) spots starts to agglomerate in a circular form. With increasing time blurry spots are formed, which are rotated by 30° regarding the Ru(0001) substrate. At the same time surrounding the (00) spot the halo increases in intensity and starts to form a Moiré pattern. After 30 min the spots still did not develop completely, but are still blurry. Thus, the formation process is still not finished. The LEEM-IV curve shows the formation progress. It is strongly altered. The LEEM-IV curve shows a strong dip at 4.6 eV. The former peak at 6.5 eV is shifted to 7.5 eV being broader and developed. Furthermore a strong peak with nearly half the intensity as the one at 7.5 eV is present at 13 eV. The MEM-LEEM border is strongly increased from 2.71 eV (oxidation at RT) up to 3.24 eV and thus, even higher than the one after silicon deposition (3.05 eV), but not as high as for a 3O-coverage. This indicates an increased surface dipole. The O 1s line undergoes a strong increase. Now, a third component at 530 eV is present, additional to the one at 531.0 eV (Si-O-Si bond) and 529.3 eV (Fe-O-Ru, Fe-O-Fe, Ru-O). Since this peak is positioned energetically intermediate to the Si-O-Si and Fe-O-Fe bond. IRAS measurements in Włodarczyk et al. [103] indicate the presence of a Fe-O-Si bond, additional to the Si-O-Si and Fe-O-Fe bond. Thus, this intermediate XPS peak corresponds most likely to the Fe-O-Si line [103] and will be addressed in such way from now on. The intensity of the Si-O-Si line is strongly increased. This might indicates, that especially the Si atoms start to arrange, optimizing their bonding. The Si 2p line is shifted to lower binding energy and is still in the Si^{4+} configuration. The shift correlates with the workfunction increase. The Fe 3p line shows a lower peak intensity compared to the oxidation at RT. The Fe^{3+} component is now the strongest component, the number of Fe^{2+} decreased strongly.

The next temperature step is 800 K. During annealing the spots become more sharp and intense. Surrounding the (00) spots and close to the substrate spots a Moiré pattern develops. Additionally (2x2) spots rotated by 30° are present, again surrounded by Moiré

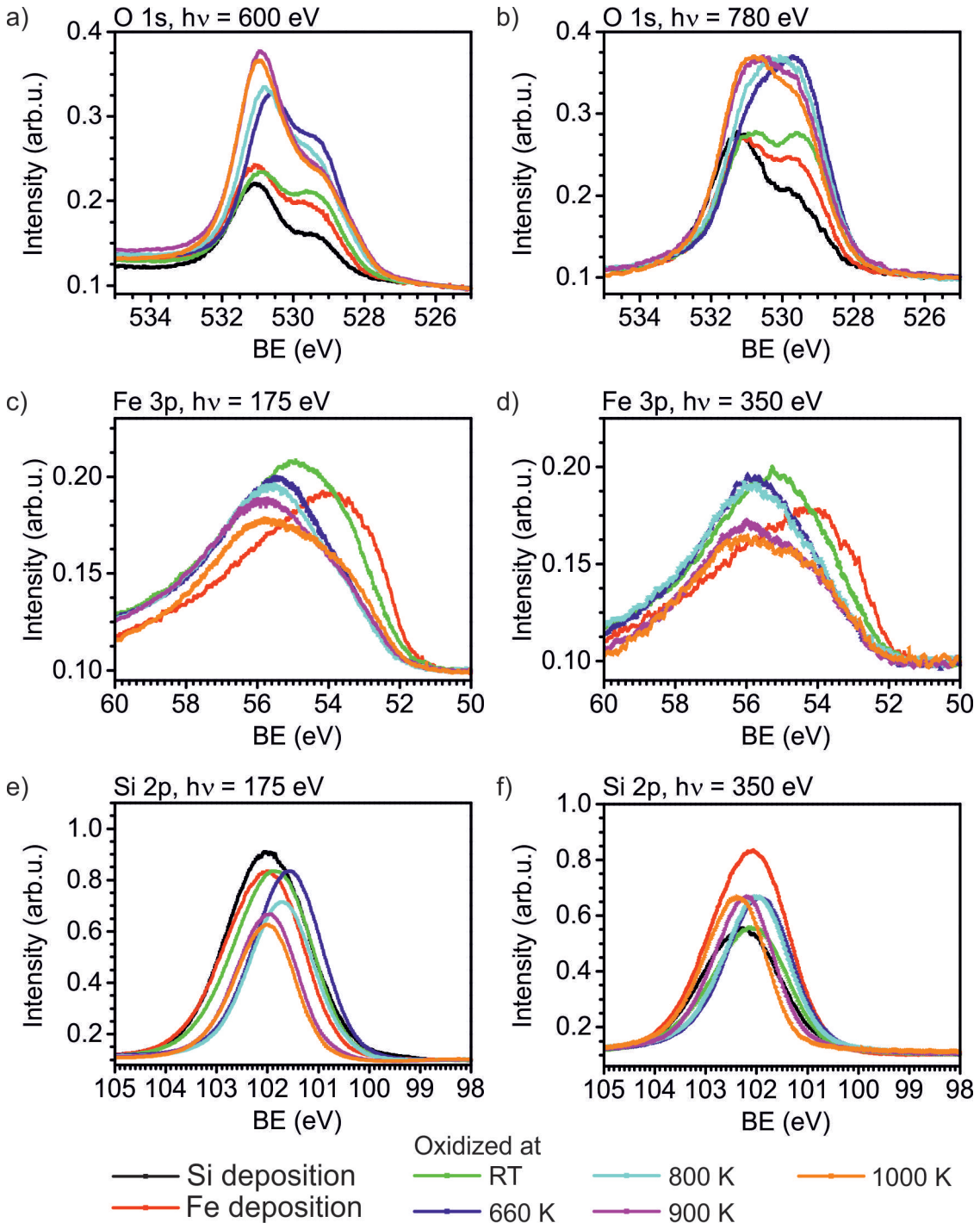

Figure 4.6 Temperature dependent XPS analysis of iron silicate using the "combined preparation" method (Si+Fe/3O-Ru(0001)). O 1s line for a photon energy of a) 600 eV and b) 780 eV. Fe 3p line for a photon energy of c) 175 eV and d) 350 eV. Si 2p line for a photon energy of e) 175 eV and f) 350 eV. The measurements are taken at RT.

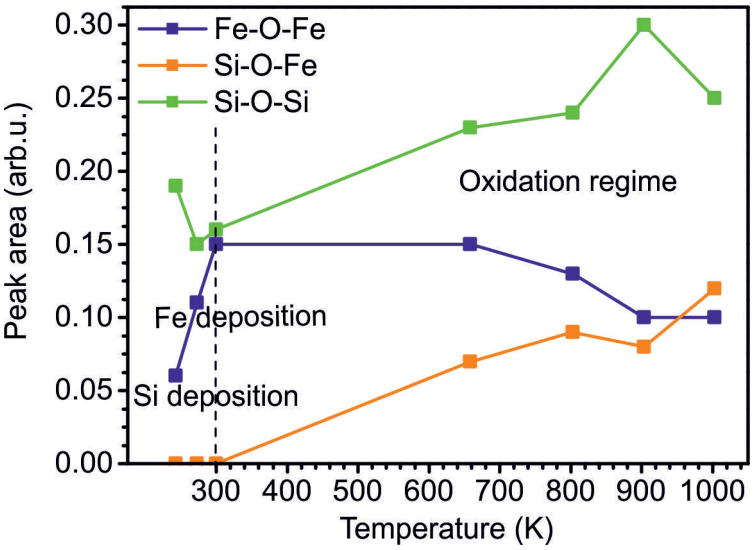

Figure 4.7 Evolution of the Fe-O-Fe, Fe-O-Si and Si-O-Si components of the O 1s line at 600 eV (Fig. 4.6a) of an iron silicate film using the "combined preparation" method (Si+Fe/3O-Ru(0001)).

spots. The intensity of the 30° rotated (2x2) spots and Moiré pattern is equally strong. The improved arrangement is visible in the LEED curve and by the increase of the specific peaks in the LEEM-IV curve. The features at 7.5 eV and 13.0 eV increase and a third peak evolves at 20.5 eV. In the range close to the MEM-LEEM border, the main dip at 4.5 eV is rather unchanged, but a shoulder develops at 5.5 eV. In XPS, the O 1s line shows a decrease in the Fe-O-Fe component and a slight increase of the Si-O-Si component. The Fe-O-Si component is slightly increased. Varying the photon energy to 780 eV, it turns out that the Si-O-Si line and the Fe-O-Fe line are equally strong. In comparison to 660 K at the photon energy of 780 eV mainly the Si-O-Si line is increased. The Fe 3p line is unchanged. The unchanged Fe 3p line shows that the overall iron content remains constant. As a result the decrease in the Fe-O-Fe line is not due to loss of iron by evaporation but rather due to iron rearrangement. For instance a damping might be an explanation. One possible explanation is the migration of iron underneath silicon.

As follows the temperature is increased up to 900 K. First, the (2x2) spots rotated by 30° become more intense, then the surrounding Moiré spots increase their intensity. As a remark, the (2x2) spots, visible in Fig. 4.2f, are due to oxygen on the surface and thus, do not exist at 900 K. This indicates the presence of holes in the film, as also seen in LEEM. In LEEM-IV the peaks already present at 800 eV become more pronounced. Apart from that the shoulder at 5.5 eV, present already at 800 eV develops into a dip. The MEM-LEEM border decreases to 3.17 eV (-0.1 eV). The O 1s line shows that the Fe-O-Fe component is further decreased, while the Si-O-Si is increased. This is accompanied with a decrease of the Fe^{2+} component in the Fe 3p line as well. The Fe^{3+} component remains constant. The decrease of the Fe-O-Fe component and the Fe^{2+} component of the Fe 3p line are also present at photon energies with a higher free mean path (i.e. a photon energy of 780 eV for O 1s and 350 eV for Fe 3p). Apart from rearrangement of iron and silicon, like iron migrating closer to the substrate and thus, being damped by silicon on top, a loss of iron should be considered, since the temperature exceeds the one of stable iron oxide (without silicon).

For 1000 K LEED the spot width becomes smaller, the Moiré spots and (2x2) spots rotated by 30° are equally intense. Higher order spots are appearing, indicating a good long-range order. The MEM-LEEM border is further decreased to 2.97 eV. Apart from that the LEEM-IV curve is unchanged. The same is true for the XPS O 1s line. Only the Fe-O-Fe line is slightly increased, when using higher photon energy of 780 eV. The Fe^{2+} component in the Fe 3p line decreases further, while the Fe^{3+} component rises.

Summary of the formation process for the "combined preparation" method

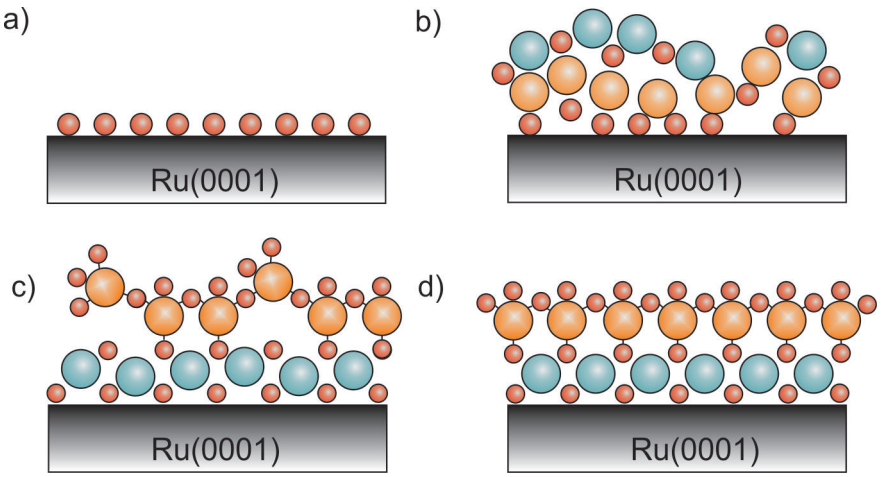

Figure 4.8 Iron silicate formation process using the "combined preparation" method (Si+Fe/3O-Ru(0001)). a) 3O-covered Ru(0001) substrate. b) Silicon and subsequential iron deposition at RT. Silicon is in the Si^{4+} state (completely oxidized), iron only partially oxidized.The film is disordered. c) Oxidation at 660 K. Iron migrates underneath the silicon layer. The iron silicate arrangement begins to form. d) Oxidation at 1000 K. Final film. Red: Oxygen. Violet: Iron. Yellow: Silicon.

In summary a monolayer of iron silicate was prepared by using the so-called "combined preparation" method. The temperature dependent film formation is depicted in Fig. 4.8). First, the Ru(0001) substrate is oxidized at 900 K in $1.0 \cdot 10^{-6}$ mbar. As a result a 3O-(2x2) oxygen layer forms on the Ru(0001) substrate (Fig. 4.8a). At RT a monolayer of silicon is deposited in $2.0 \cdot 10^{-7}$ mbar. Due to the oxygen layer on the substrate and the surrounding oxygen in the chamber silicon becomes completely oxidized in the Si^{4+} state. Subsequential a monolayer of iron is deposited in the same oxygen pressure (Fig. 4.8b). Iron is only partially oxidized with Fe^0 and Fe^{2+} components, while silicon remains completely oxidized. The resulting film is disordered. Finally the film is oxidized in $1.0 \cdot 10^{-6}$ mbar. Already at 660 K the latter iron silicate fingerprint, as well as the corresponding LEED pattern starts to develop: a Moiré pattern, together with (2x2) spots rotated by 30° (Fig. 4.8c). Both the Moiré structure as well as the rotated (2x2) spots is appearing at the same time. In the O 1s line three different components are visible: Si-O-Si, Si-O-Fe and Fe-O-Fe/ Fe-O-Ru. At higher temperatures than 660 K only the crystallinity is improves, which can be seen by the decreased spot size of the LEED structure with increasing intensity, as well as the increase in the LEEM-IV peaks regarding the MEM intensity. With increasing crystallinity

(improved LEED structure) the Fe-O-Fe/Fe-O-Ru component decreases. This can be explained by migration of iron atoms underneath silicon, and thus increased damping of the iron atoms by the silicon layer on top. This indicates the separation of an iron oxide and a silica layer, as proposed in Włodarczyk et al. [103]. This effect is strongest between 660 K and 800 K. At 1000 K the final iron silicate layer is found (Fig. 4.8d).

4.1.2 Combined UHV preparation method (Fe+Si(UHV)/Ru(0001))

Iron silicate is formed as oxygen bonds between Fe-O-Fe, Si-O-Si and Fe-O-Si. Thus, individual oxygen bonds and their formation are crucial for film formation. The "combined preparation" method in section 4.1.1 offers a many surrounding oxygen even before silicon or iron are deposited. On the one hand the Ru(0001) surface was already covered by a closed-packed oxygen 3O-(2x2) layer and on the other hand silicon and iron are deposited in an oxygen surrounding of $2.0 \cdot 10^{-7}$ mbar. As it turned out, directly after its deposition silicon is completely oxidized. Thus, in the moment iron was deposited onto the surface the silicon bonds are already present. Due to its higher bonding strength, only some iron atoms are partly oxidized. Most likely this is due to the surrounding oxygen. In this chapter neither iron, nor silicon are oxygen saturation when they get in contact. In the "combined UHV method" first iron and subsequently silicon are deposited at RT on a freshly cleaned Ru(0001) substrate. No 3O-coverage has been prepared. However, residual oxygen is present on the surface and in the surrounding (background pressure $7.0 \cdot 10^{-9}$ mbar). A shallow (2x2) structure is visible after cleaning the surface.

The LEED after iron deposition shows a six-fold star pattern, rotated by 30° with respect to the substrate spots (Fig. 4.2a. This pattern is only present in case of very low amount of oxygen . Here, it should be prevented for silicon to be oxidized before iron is deposited. Thus, iron is deposited first in UHV conditions. Directly afterwards, silicon is deposited. As a result the LEED pattern converts into a shallow (2x2) structure (Fig. 4.2b). This indicates, that either silicon is already slightly ordered or alternatively oxygen. Since iron as well as silicon is deposited without adding an oxygen background most likely oxygen is not the reason. In the O 1s line (Fig. 4.13 a) two peaks are present at 529.8 eV and 530.8 eV. From their position they correspond to Si-O-Si and Si-O-Fe bonds, respectively. Fe-O-Fe or Fe-O-Ru bonds are not detected. The intensity of the O 1s line is rather low. This is in agreement with the XPS results of silicon (Si 2p line Fig. 4.13c) and iron (Fe 3p line Fig. 4.13b). Iron atoms are found in the metallic and Fe^{2+} state. Silicon atoms are mainly found in the Si^{2+} state. Thus one silicon atom is bound to two oxygen atoms in average. Apart from that some silicon atoms are also less oxidized. As visible in depth profile (i.e. using a photon energy of 350 eV instead of 175 eV), the species that are only in the Si^{1+} or even metallic state are mainly present in contact to iron, rather than on top of the film. The large oxygen affinity of silicon is mirrored in these results. Moreover the residual oxygen on the Ru(0001) sample proves to be rather low. Thus the main influence seems to have the residual oxygen in the chamber that enables silicon to partially oxidize during its deposition. The MEM-LEEM border is at 2.3 eV (see Fig. 4.11b), i.e. the value is lower as for a 1O-covered Ru(0001) surface [44].

The film is oxidized in $1.0 \cdot 10^{-6}$ mbar for 30 min, without further oxidation. The former (2x2) spots become blurry with oxidation time (Fig. 4.9c). As a result, the (2x2) spots

Preparation step	Energetic position of the MEM-LEEM border (eV)	Workfunction (eV) (referenced to clean Ru(0001) with 5.44 eV [12])
Fe + Si deposition	2.30	5.16
Oxidation at RT	2.32	5.18
Oxidation at 650 K	2.89	5.75
Oxidation at 900 K	2.97	5.83

Table 4.2 Overview on the MEM-LEEM border evolution for the individual preparation steps of the "combined UHV preparation" method (Fe+Si (UHV)/Ru(0001)). The MEM-LEEM values are measured with an accuracy of ± 0.02 eV.

must result from Fe-Si bonds, which are broken as soon as more oxygen is available. During this step oxygen is able to intercalate through silicon. This results in a O 1s component at 529.0 eV that can be either Fe-O-Fe or Fe-O-Ru or O-Ru bonds. The Fe 3p line confirms that iron is oxidized. The main component is Fe^{2+}, while the Fe^0 component is minimized. Even Fe^{3+} components are present, which might either imply an additional oxygen bond of iron to either Ru or Si. Similar to iron, silicon is strongly oxidized. The Si 2p line shows both Si^{4+} and Si^{2+} components. This means some silicon atoms are still relatively free, i.e. not bond in a matrix of silica and thus, are in the Si^{2+} state, while the main part of silicon atoms are already bond to 4 other oxygen atoms in structural compound. The O 1s line shows a strong rise of the Si-O-Si line that is in great alignment to the findings in the Si 2p line (twice the intensity as before). Moreover the Si-O-Fe line has also improved (by

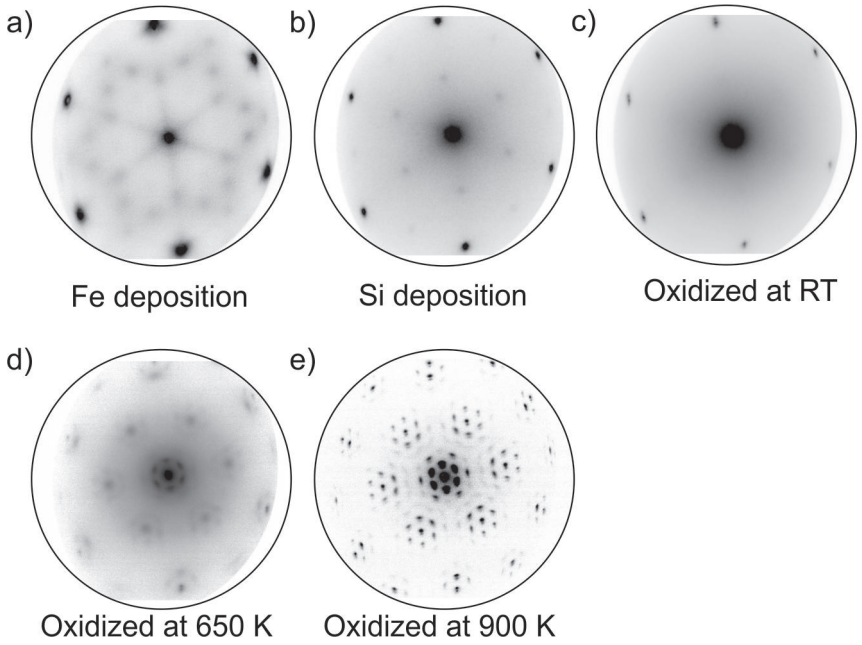

Figure 4.9 LEED pattern of the individual preparation steps iron silicate using the "combined UHV preparation" method (Fe+Si(UHV)/Ru(0001)). Iron and silicon are deposited in UHV conditions. The oxidation is done in $1.0 \cdot 10^{-6}$ mbar. All LEED images are taken at 42 eV and RT.

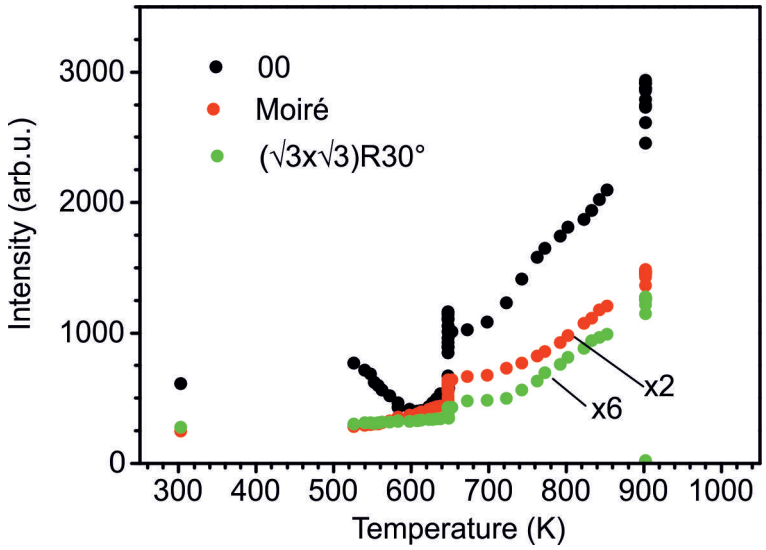

Figure 4.10 Spot intensities of the (00), Moiré and $(\sqrt{3}\times\sqrt{3})R30°$ spots during the oxidation in $1.0 \cdot 10^{-6}$ mbar of an iron silicate layer using the "combined UHV preparation" method (Fe+Si(UHV)/Ru(0001)). The $(\sqrt{3} \times \sqrt{3})R30°$ structure refers to a silica structure that is rotated by 30° regarding a complete iron oxide layer. Iron and silicon are deposited subsequent in UHV conditions.

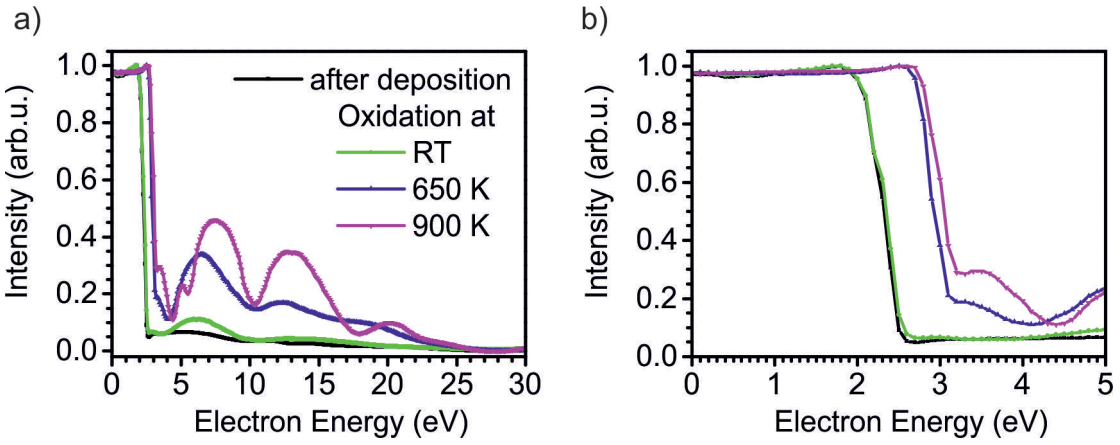

Figure 4.11 LEEM-IV characteristics for iron silicate using the "combined UHV preparation" method (Fe+Si(UHV)/Ru(0001)). Iron and silicon are deposited in UHV conditions and subsequently oxidized in $1.0 \cdot 10^{-6}$ mbar. LEEM-IV curves measured at RT.

a factor of three). This already indicates that the Fe^{3+} component corresponds at least partially to Si-O-Fe bonds. Even though the film is strongly oxidized, the MEM-LEEM border is unchanged at 2.3 eV. The reason might be that the temperature is not sufficient for silicon and iron to rearrange.

The temperature is increased in $1.0 \cdot 10^{-6}$ mbar. The oxidation was followed in LEED. The intensity behavior of the individual spots is given in Fig. 4.10. At 570 K iron begins to order forming a Moiré pattern surrounding the (00) spots. Shortly after Moiré spots appear nearby substrate spots. This is nearly 100 K below the temperature, where the Moiré spots appear for the "combined preparation" method. This might correspond to fact, that iron must not diffuse to get in contact to Ru(0001). At 650 K by 30° rotated (2x2) spots,

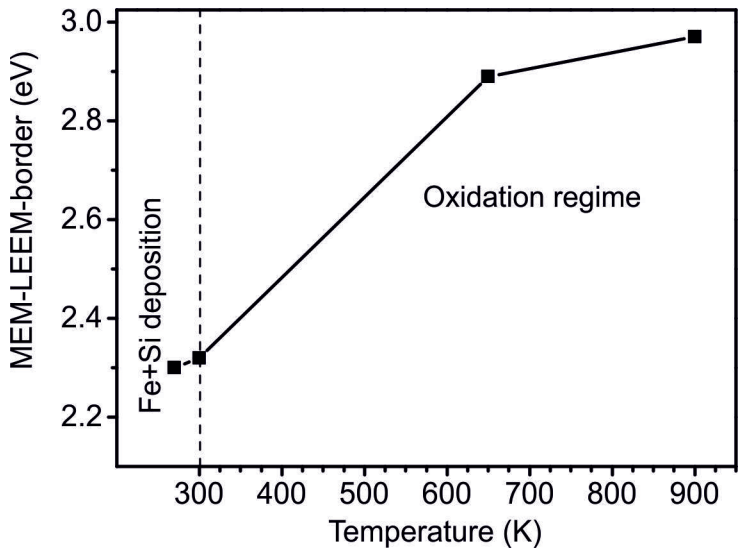

Figure 4.12 MEM-LEEM border for the individual preparation steps of iron silicate using the "combined UHV preparation" method (Fe+Si(UHV)/Ru(0001)). Iron and silicon are deposited at RT in UHV conditions. The oxygen pressure during oxidation is $1.0 \cdot 10^{-6}$ mbar. The MEM-LEEM values are determined by a fit of the MEM-LEEM border presented in Fig. 4.11b. The error of this fit is 0.02 eV.

together with their surrounding Moiré spots start to develop. After 10 min at 650 K the Moiré pattern as well as the by 30° rotated (2x2) spots are nicely visible (Fig. 4.9d). The rotated (2x2) spots are even more pronounced as the surrounding Moiré pattern. They indicate the arrangement of the SiO_2 layer. The intensity and sharpness of the LEED spots are better than for the "combined preparation" step at similar temperatures. One reason might be the opposite deposition order of Si and Fe. However, the main reason is likely to be the strong Si-O-Si bonds that are present before iron is deposited in the "combined preparation" method. As a consequence they have to be broken before they can rearrange and bind to iron atoms. Thus, a higher temperature (i.e. thermal activation) is needed. The MEM-LEEM border is strongly shifted to 2.89 eV. The LEEM-IV curve has developed several characteristic peaks at 6.5 eV, 12.5 eV and 18 eV. Moreover the characteristic dip at 4 eV is present. All of these peaks are shifted by 0.5 eV regarding the final iron silicate characteristic. Moreover the tail for energies above 18.0 eV is different to the final structure, as well as the LEEM-IV characteristic for the "combined preparation" method at a similar temperature. Apart from the structure the O 1s line indicates a increase in all three components. The Si-O-Si component has doubled its intensity and the Si 2p line shows that now all Si atoms are completely oxidized in the Si^{4+} state. This corresponds to the arrangement of silicon atoms. The Fe 3p line indicates that both the Fe^{2+} as well as the Fe^{3+} component is increased. Also the Si-O-Fe bond of the O 1s line barely changed. This indicates that all available bonds between silicon and iron are already saturated at RT.

In the final oxidation step up to 900 K all spots increase their intensity and sharpness. The corresponding LEED image is shown in Fig. 4.9e. Thus the structure improves its homogeneity. The MEM-LEEM border is further increased up to 2.97 eV (Fig. 4.11b). The LEEM-IV curve matches perfectly the one for the "combined preparation" method. The Si-O-Si and the Fe-O-Fe line is further increased. However, the Fe-O-Si remains unchanged. Again this indicates that the possible Fe-O-Si links are already saturated at RT. The Fe^{3+}

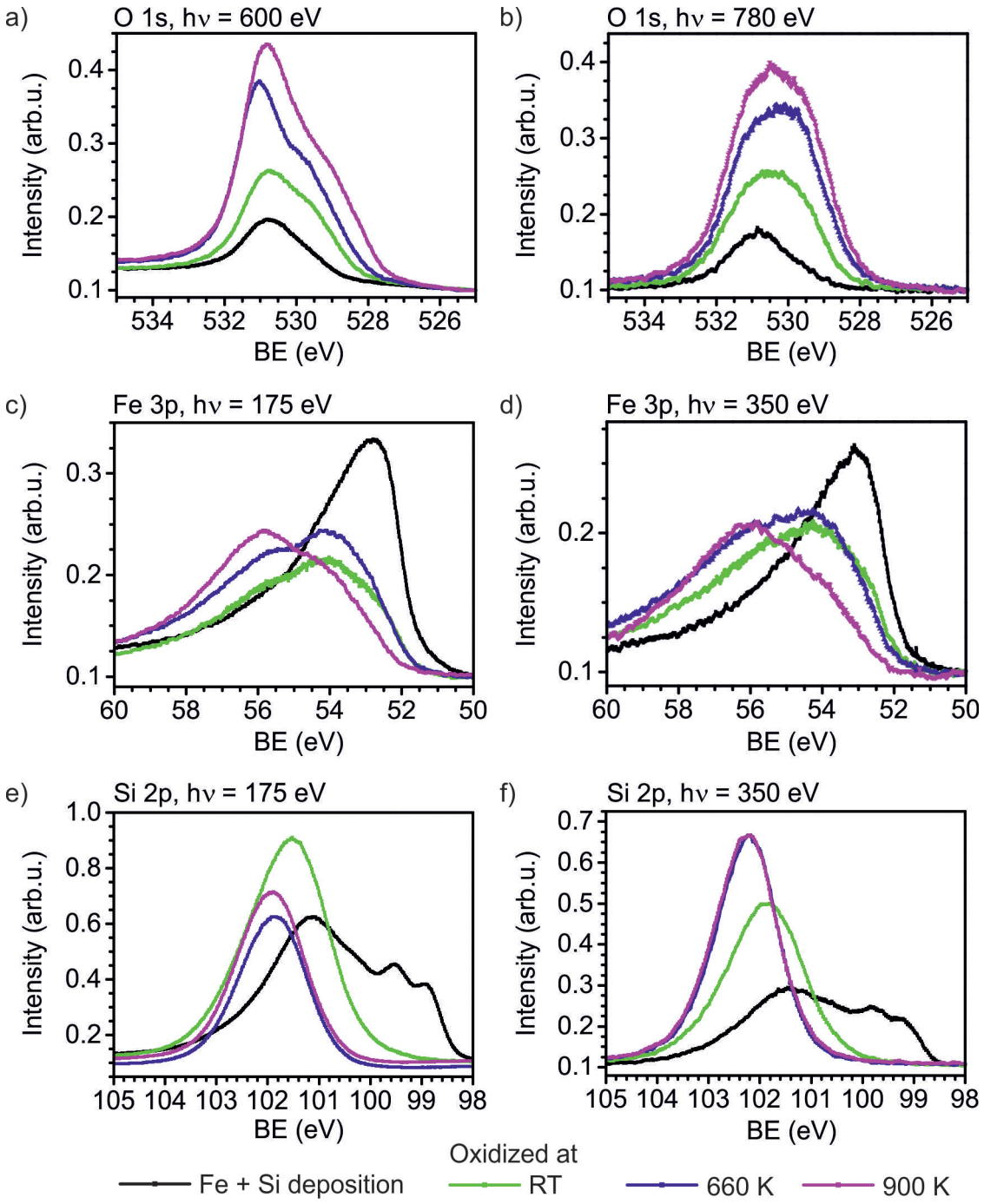

Figure 4.13 XPS analysis of iron silicate using the "combined UHV preparation" method (Fe+Si(UHV)/Ru(0001)). O 1s line for a photon energy of a) 600 eV and b) 780 eV. Fe 3p line for a photon energy of c) 175 eV and d) 350 eV. Si 2p line for a photon energy of e) 175 eV and f) 350 eV. The measurements are taken at RT.

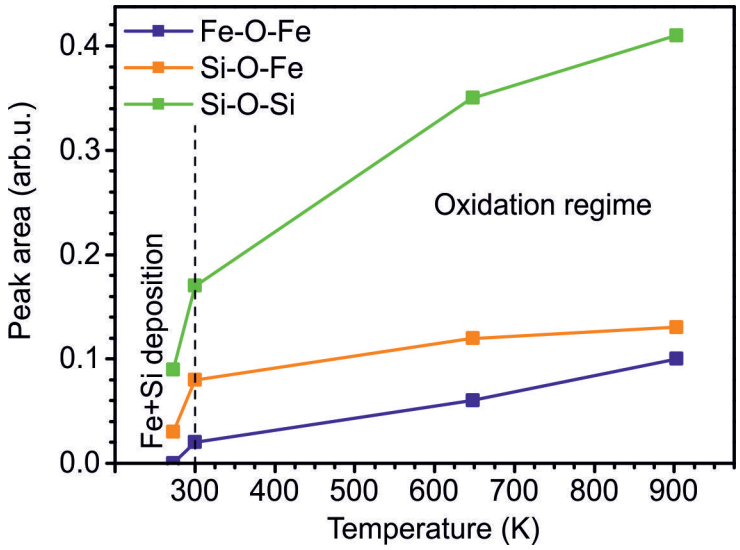

Figure 4.14 Evolution of the Fe-O-Fe, Fe-O-Si and Si-O-Si components of the O 1s line at 600 eV (Fig. 4.13a) of an iron silicate film using the "combined UHV preparation" method (Fe+Si(UHV)/Ru(0001)).

component increased in its intensity, while the Fe^{2+} line decreases. The higher oxidation number corresponds to the increase in Fe-O-Fe and Fe-O-Ru line. Since the Fe-O-Si line is unchanged the rise in the oxidation number corresponds most likely to Fe-O-Ru bonds.

Summary of the formation process for the "combined UHV preparation" method

The formation process of iron silicate using the "combined UHV preparation" method is depicted in Fig. 4.15. Iron and silicon are deposited at RT in UHV conditions (Fig. 4.15a). Due to the residual oxygen atoms in the chamber some iron and silicon atoms are oxidized. However, all oxygen bonds are either Si-O-Si or Si-O-Fe bonds. No Fe-O-Fe/Fe-O-Ru bonds are detected. The layer is disordered. At RT the layer is oxidized in $1.0 \cdot 10^{-6}$ mbar. Oxygen can intercalate to the iron layer and Fe-O-Fe/Fe-O-Ru bonds are formed. Also silicon becomes better oxidized, so that only Si^{4+} and Si^{2+} bonds are present. Afterwards the film is further oxidized in elevated temperatures in $1.0 \cdot 10^{-6}$ mbar. Already at 570 K the iron oxide layer orders in form of a Moiré structure with "8 on 9" reconstruction (Fig. 4.15c). Silicon is still disordered. At 650 K the silica layer orders and the rotated (2x2) structure is visible (Fig. 4.15d). With increasing temperature the crystallinity of the layer improves. At 900 K the same iron silicate signature as for the "combined preparation" method (section 4.1.1) is found (Fig. 4.15e).

The final iron silicate structure prepared with the "combined UHV preparation" method fits nicely to the one achieved with the "combined preparation" method. In Fig. 4.16 the LEEM-IV and in Fig. 4.17 the LEED-IV fingerprints are compared for the individual preparation method. The LEEM-IV curves for both preparations match each other nearly perfectly for the final structure. However, for the "combined preparation" method the film needs to be annealed to 1000 K to fit the MEM-LEEM border and with this to the exact positions of the peaks and dips in the spectra for the "combined UHV preparation" at 900 K. The LEED-IV curves show for both preparation methods the same dips and peaks.

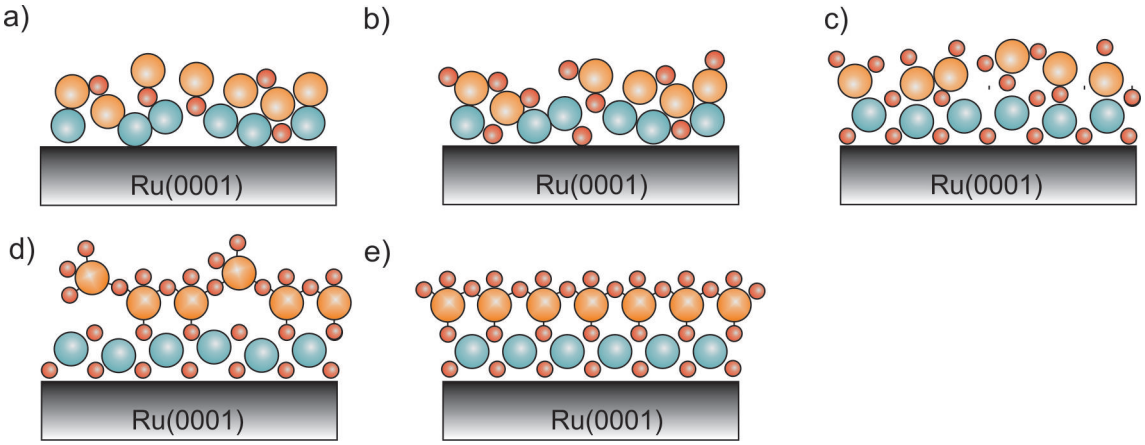

Figure 4.15 Iron silicate formation process using the "combined UHV preparation" method (Fe+Si/Ru(0001)). a) Iron and silicon deposition at RT in UHV conditions. The layer is disordered. The residual oxygen in the surrounding oxidizes silicon partially, so that only silicon related oxygen bonds are detected (Si-O-Si and Si-O-Fe bonds, no Fe-O-Fe/Fe-O-Ru bonds). b-e) film formation during oxidation in $1.0 \cdot 10^{-6}$ mbar. b) Oxidation at RT. Iron and silicon become better oxidized. Now also Fe-O-Fe/Fe-O-Ru bonds form. c) Oxidiation at 570 K. Iron arranges in a Moiré pattern. The silicon layer is still disordered. d) Oxidation at 650 K. Silicon arranges in a rotated (2x2) structure. Complete oxidation of silicon (Si^{4+}) and iron (Fe^{2+} and Fe^{3+}). e) Oxidation at 900 K. Final iron silicate film. Red: Oxygen. Violet: Iron. Yellow: Silicon.

The individual peak intensities, however, vary for the "combined preparation" method between 900 K and 1000 K. Similar to the LEEM-IV curves, the LEED-IV curve for the "combined UHV preparation" at 900 K fit better to the LEED-IV curve of the "combined preparation" method at 1000 K than for 900 K. Thus, the "combined preparation" method needs 100 K higher annealing temperatures compared to the preparation in UHV. Most likely this results out of a strong Si-O-Si bond that forms in the "combined preparation" method already at RT and needs to broken in order to form Si-O-Fe bonds. Thus, higher activation temperatures are needed.

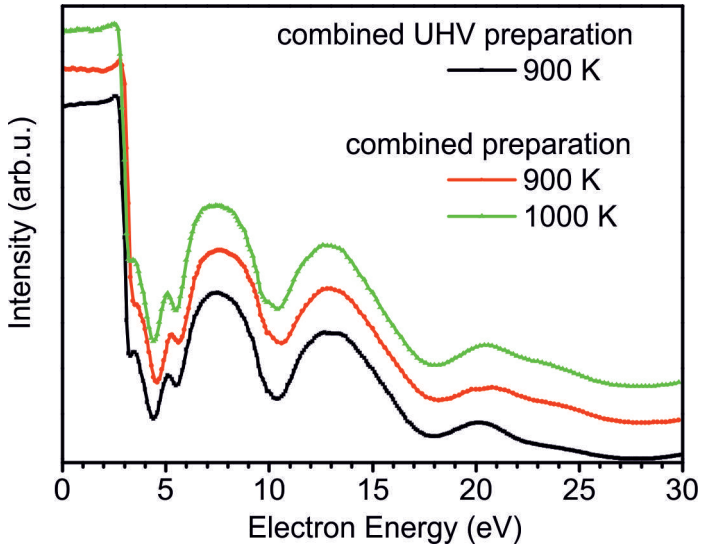

Figure 4.16 LEEM-IV characteristics comparing iron silicate layer prepared with the "combined preparation" method (Si+Fe/3O-Ru(0001)) and the "combined UHV preparation" method (Fe+Si(UHV)/Ru(0001)).

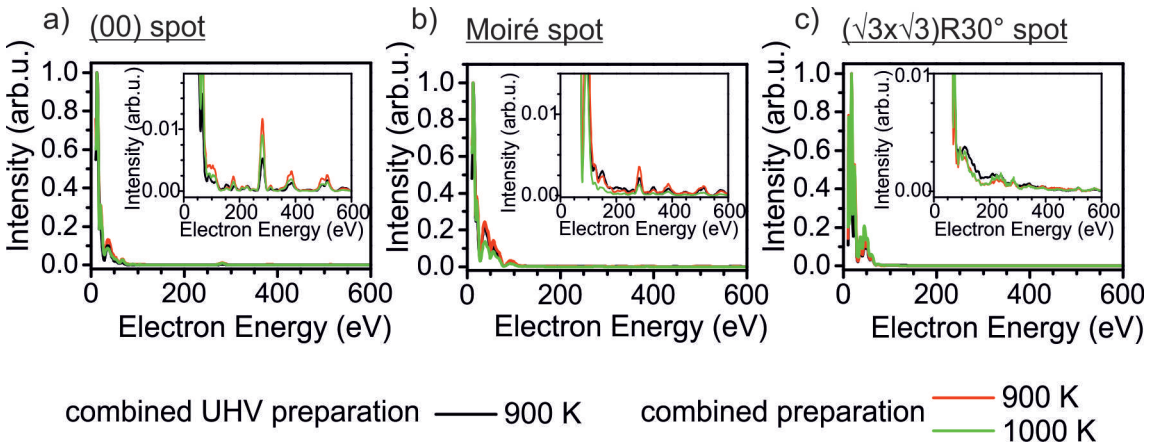

Figure 4.17 LEED-IV curves comparing the fingerprints of iron silicate prepared with the "combined preparation" method (Si+Fe/3O-Ru(0001)) and the "combined UHV preparation" method (Fe+Si(UHV)/Ru(0001)). The chosen LEED spots are a) the (00) spot, b) a Moiré spot and c) a $(\sqrt{3} \times \sqrt{3})R30°$ spot regarding a complete iron oxide layer. The oxidation temperature for both preparation methods is 900 K.

4.1.3 Summary and conclusion of the "combined" approach

The "combined UHV preparation" method (section 4.1.2) leads to the same iron silicate film, as can be seen by the LEEM-IV and LEED-IV fingerprints. The characteristic fingerprints in LEEM-IV and LEED-IV are given in fig. 4.18 and 4.19. The iron silicate layer will be referred in the following as $FeSiO_x$.

While the final film structure is similar for both preparation methods, the necessary tem-

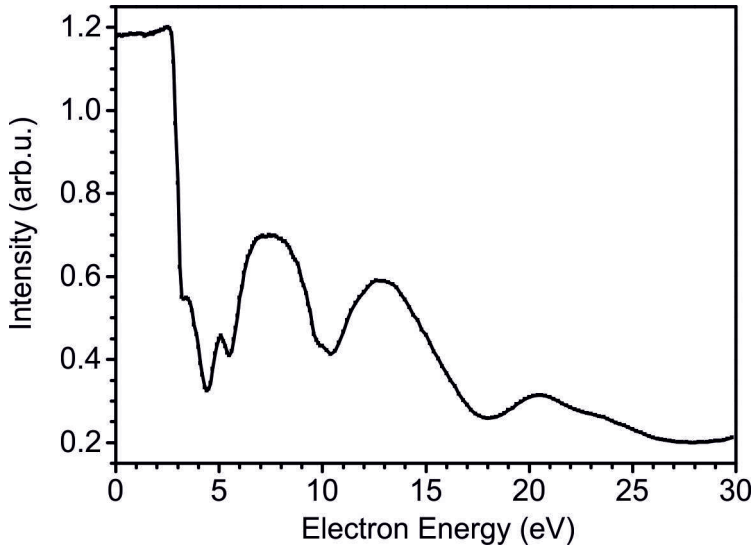

Figure 4.18 LEEM-IV fingerprint of iron silicate on Ru(0001). The data shown here is for 1000 K for the "combined preparation" method (Si+Fe/3O-Ru(0001)).

perature differs by 100 K. Exactly the same film structure is found at 1000 K and 900 K for the "combined preparation" vs. "combined UHV preparation" method, respectively, judging by the LEEM-IV and LEED-IV fingerprint. In both preparation methods first, the iron oxide layer forms, before the silica layer arranges, as can be seen by the subsequent appearance of the Moiré spots and silica superstructure spots. In the "combined UHV preparation" method iron arranges already at 570 K. The silicon atoms arrange at 650 K. In the "combined preparation" method both iron and silicon start to arrange at 660 K. Since Si-O-Si and Si-O-Ru bonds need to be broken, before iron can intercalate to the silicon/ruthenium interface in order to form iron oxide, a higher temperature is needed. The individual temperature dependencies are shown in table 4.3.

The "combined preparation" method uses the same preparation principle as described in [103]. As a result the iron silicate film in this chapter can be directly compared with the STM, XPS and IRAS results given in this paper. The LEED pattern shows the superposition of a Moiré pattern and (2x2) spots rotated by 30°. Pure FeO monolayer films (see section 3.1) share the existence of a Moiré pattern with the iron silicate films. In contrast, the (2x2) pattern rotated by 30° only appears if silicon is present. This indicates that iron silicate can indeed be described by a silica monolayer on top of a FeO-like iron oxide layer, where the silica layer is rotated by 30° regarding the iron oxide layer. However the dimensions of the iron oxide layer differ from a pure FeO layer.

A Moiré pattern is the result of two lattices that are similar and interfere with each other. The distances of the Moiré spots in iron silicate give rise to a "8 on 9" structure, meaning

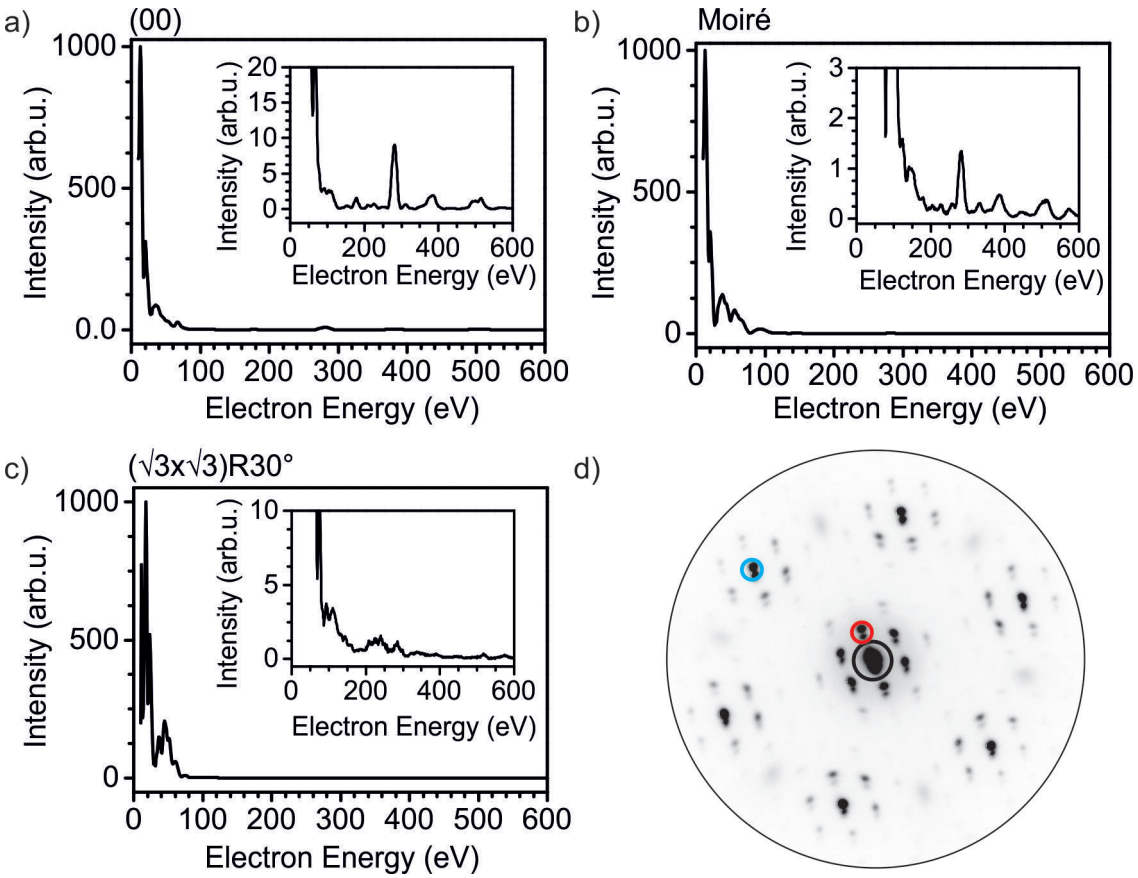

Figure 4.19 LEED-IV fingerprint of iron silicate. The data shown here is corresponds to the 1000 K for the "combined preparation" method (Si+Fe/3O-Ru(0001)) after oxidation at 1000 K. a) (00) spot, marked black in d). b) Moiré spot, marked red in d). c) $(\sqrt{3}\times\sqrt{3})R30°$ regarding a complete iron oxide layer, marked blue in d). d) LEED image at 20 eV.

that 8 atoms of the superlattice fit commensurable on 9 atoms of the sublattice. In analogy to FeO on Ru(0001) this means, 8 Fe atoms fit commensurable on 9 Ru atoms. The Ru-Ru distance for a Ru(0001) substrate is 2.706 Å. As a result the Fe-Fe distance in the iron oxide layer in iron silicate can be calculated as 3.044 Å. The pure FeO monolayer is found to have a "6 on 7" reconstruction (see section 3.1), and thus a Fe-Fe distance of 3.157 Å. This shows that the FeO-like layer of iron silicate is strongly compressed in comparison to silicon free FeO films on Ru(0001). The compression of the FeO-like layer indicates that the silicon layer does not simply grow on top of a FeO layer that was built independently from silicon. This suggests that silicon has a great influence on the formation process (Fe-Fe distance) of the FeO-like layer and that the Si-O-Fe bond is stronger than expected.

R. Włodarczyk et al. [103] simulated the implementation of iron atoms into a SiO_2 bilayer. The simulations are based on a pristine SiO_2 bilayer unit cell and added one iron atom per unit cell per time. In these calculations it turned out, that iron tends to substitute silicon atoms only in the lower level of the silica bilayer. Taking this into account it is likely that iron is migrating underneath silicon, when the temperature is sufficient for optimal mobility of the iron atoms.

In contrast to the calculations performed in [103] iron does not simply substitute silicon

	Combined	**Combined UHV**
preparation	Si, Fe subsequently at RT on 3O-Ru in $2.0 \cdot 10^{-7}$ mbar	Si, Fe subsequently at RT in UHV
	Si+Fe/3O-Ru(0001)	Fe+Si(UHV)/Ru(0001)
Necessary T	1000 K	900 K
Appearance of Moiré spots	660 K	570 K
Appearance of $(\sqrt{3} \times \sqrt{3})R30°$ spots	660 K	650 K
Strongest intensity rise of Moiré spots	800 K	660 K
Strongest intensity rise of $(\sqrt{3} \times \sqrt{3})R30°$ spots	800 K	660 K

Table 4.3 Temperature dependencies of preparation methods using the "combined" approach.The $(\sqrt{3}\times\sqrt{3})R30°$ structure refers to a silica structure that is rotated by 30° regarding a complete iron oxide layer.

and remains in the matrix of a silica bilayer. If this would be the case, both, an unrotated (2x2) structure and no Moiré pattern would be expected. The existence of a Moiré pattern indicates that the iron oxide layer is on top of the Ru(0001) substrate. As a consequence silica must be on top of the iron oxide layer. Moreover, XPS measurements of the O 1s lines indicate individual components for the Si-O-Si and Fe-O-Fe or Fe-O-Ru line. Additional a Si-O-Fe bond is found, which connects the iron oxide and silica layer. Taking a closer look on the (2x2) spots rotated by 30°, they can also be interpreted as silica monolayer oriented commensurable in form of a $(\sqrt{3} \times \sqrt{3})R30°$ regarding a complete iron oxide layer underneath (see Fig. 4.23). This fits also the IRAS measurements shown in [103]. The authors state that iron silicate shows only one line at $1005\,\mathrm{cm}^{-1}$, which increases with rising Fe:Si ratio, while the lines typical for silica ($1300\,\mathrm{cm}^{-1}$ and $674\,\mathrm{cm}^{-1}$) decrease without shift. This is a sign for a two-component film and fit to the findings in this work.

The lattice constant of a free-standing silica bilayer is computed to be 5.24 [27] - 5.32 Å [89]. The lattice constant of a silica monolayer and bilayer should be identical. A silica layer on Ru(0001) (without iron) gives rise to a (2x2) structure. As a result, a silica layer on Ru(0001) has a unit cell with a size of 5.41 Å (=$2 \cdot 2.706$ Å). Following the LEED pattern of iron silicate, silica orders in a $(\sqrt{3} \times \sqrt{3})R30°$ reconstruction regarding a complete iron oxide layer underneath (see Fig. 4.20a for silica unit cell). The iron atoms itself have a "8 on 9" reconstruction on Ru(0001), i.e. an Fe-Fe distance of 3.044 Å. From this the size of the silica unit cell can be calculated to be 5.48 Å. Therefore the SiO_2 layer in iron silicate is slightly more stretched as the SiO_2 layer on pure Ru(0001) compared to the computed free-standing bilayer. In Fig. 4.20b the geometry of an unstrained Si-O-Si bond is shown from evaluation of existing structures. The value of 3.06 Å for the Si-O-Si distance is found by evaluation of 141 nearest-neighbor Si$\cdots$Si distances in silicates and silica [67], judging

by the highest occurrence. In more recent DFT calculations of the free-standing silica bilayer, a similar value of 3.07 Å is computed [59].

The intermediate angle for these unstrained Si-O-Si bonds is found to be 144° [67]. The reason for this wide angle is assumed to be the combination of Si···Si repulsion and overlap of the Si 3d and O 2p orbitals [55]. In principle the Si-O-Si angle can be between 120° and 180° and the Si-O distance between 1.57 Å and 1.72 Å [55]. However energy is required to expand or compress the Si-O bond. In case of 144° and a Si···Si-distance of 3.06 Å, the Si-O distance can be calculated to 1.61 Å (see Fig. 4.20b). These values can be seen as an optimal Si-O-Si arrangement in real conditions. In fact, the value of an unstrained Si···Si distance of 3.06 Å fits nicely to the Fe-Fe distance, suggested by our measurements, of 3.044 Å ("8 on 9" reconstruction). This shows that the iron atoms arrange accordingly to an optimal Si-O-Si distance (compression of 0.5% only regarding the unstrained Si-O-Si distance).

The XPS measurements of the O 1s line (see Fig. 4.6a and Fig. 4.7) indicate the existence of a Fe-O-Si bond. The electronegativity (χ_M), of the individual metal atom M has a large influence on the position of the electron density maxima in a Si-O-M bond [55] and thus changes the ionicity of a Si-O bond. The electronegativity of iron in $Fe_2[Si_2O_6]$ is determined as $\chi_{Fe} = 1.64$ [84]. In this system also a Si-$O_{(A)}$-Si-$O_{(B)}$-M bond is found, which makes the system comparable to the iron silicate film in this work (here, Si-$O_{(A)}$-Si is found in plane of the silica layer, while the Si-$O_{(B)}$-Fe bond is perpendicular). However, while the order of magnitude is assumed to be similar, the precise value will be different. The electronegativity of six-coordinated silicon, which is the case for $Fe_2[Si_2O_6]$, is $\chi_{Si} = 1.74$ [55]. For four-coordinated silicon, the electronegativity is slightly higher with 1.81 [29]. Since the electronegativity of iron is lower than the one of silicon, iron transfers more electrons to the intermediate oxygen atom in the Fe-O-Si bond than silicon. Therefore the electron density maximum is shifted between the silicon atom and oxygen atom $O_{(B)}$ towards the Si atom. Nevertheless, the electronegativities of silicon and iron are not very different, therefore this shift is not very large.

What remains an open question is the exact packing situation of the FeO-like layer. The calculated model in [103] started with the silica bilayer. Since in this model iron atoms

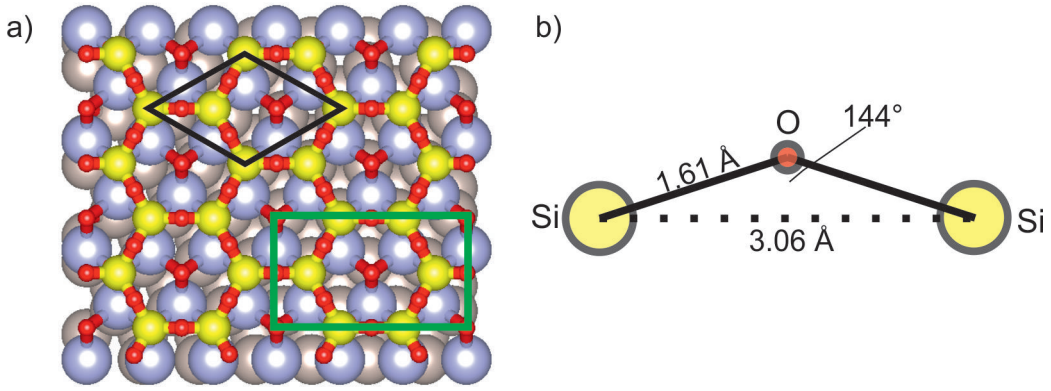

Figure 4.20 Geometry of the a) in black unit cell of the silica layer in the proposed iron silicate structure with complete iron oxide layer (three iron atoms per silica unit cell). Green: unit cell used in the calculation by R. Włodarczyk. b) Si-O-Si distances (adapted from [67]) for an unstrained Si-O-Si group. Red: Oxygen. Violet: Iron. Yellow: Silicon. Gray: Ruthenium.

only substitute silicon in the lower level of the silica bilayer the highest amount are two iron atoms per silica unit cell. A FeO layer on the other side contains three iron atoms per silica unit cell. In collaboration with R. Włodarczyk DFT calculations have been performed using the Vienna Ab initio Simulation Package (VASP) [47, 48], varying the iron content underneath. As output calculated IRAS results are given, which in turn, can be compared with the measured IRAS results in [103].

The actual unit cell of iron silicate includes an iron oxide layer with "8 on 9" reconstruction on Ru(0001) and a monolayer of silica on top, which is rotated by 30°. However, this unit cell is very large and would thus need a high wall clock time for the calculations. In order to reduce this time, the unit cell has been minimized assuming the silica monolayer is unrotated regarding the iron oxide layer. Two different cases have been chosen for two vs. three iron atoms per silica unit cell: Case I and case II. In case I the iron silicate adlayer is unrotated regarding the Ru(0001) substrate, while in case II the adlayer is rotated by 30° regarding the Ru(0001) layer. Case I and case II are calculated for two and three iron atoms per silica unit cell. These cases are assigned as follows: I2, I3 and II2 and II3. The letter assigns the assumed orientation of the adlayer, while the number addresses the number of iron atoms per unit cell (two or three). Models for the individual calculations

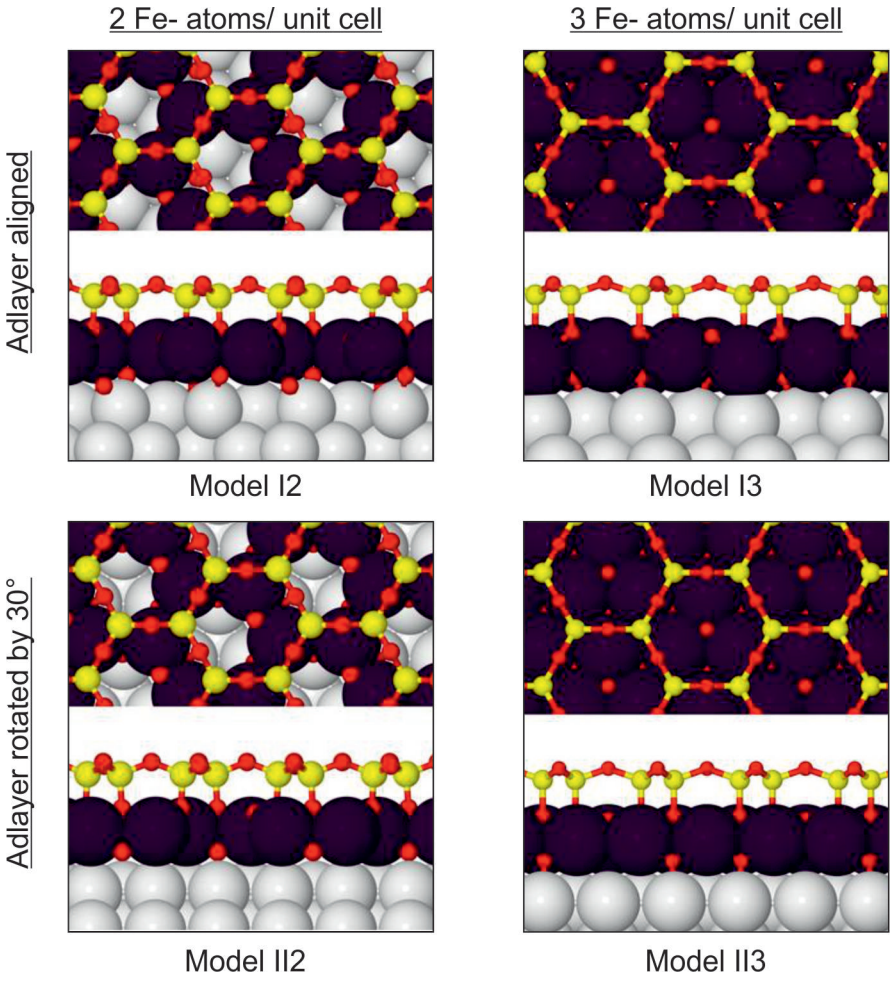

Figure 4.21 Top and side views of the individual calculated models by R. Włodarczyk and J. Sauer. Red: Oxygen. Violet: Iron. Yellow: Silicon.

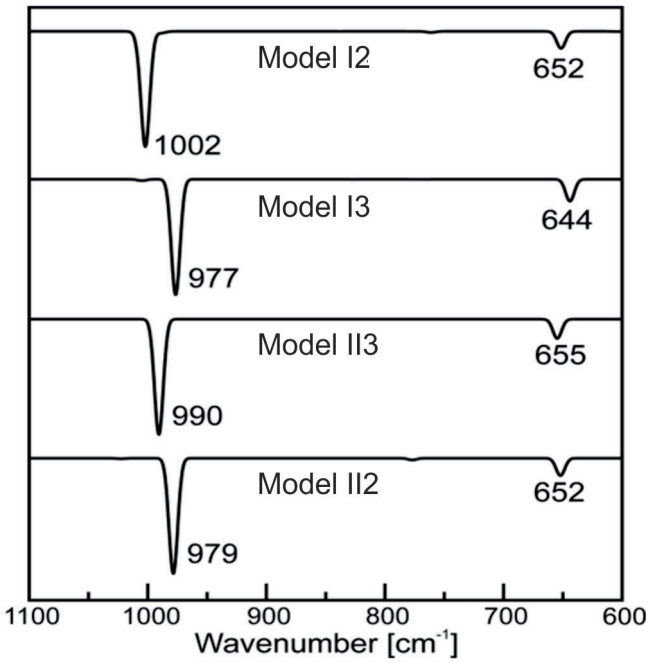

Figure 4.22 Calculated IRAS spectra fitting to the indicated models by R. Włodarczyk and J. Sauer. The latter assigns the assumed orientation of the adlayer (see text for more details), while the number addresses the number of iron atoms per unit cell in the iron oxide layer in iron silicate (three or two).

are shown in Fig. 4.21. The corresponding calculated IRAS results are given in Fig. 4.22. The main goal of this calculation is to decide, whether it is more likely to have a three iron atoms per unit cell, as it is the case for a monolayer of FeO or whether the number iron atoms is reduced to two iron atoms per unit cell.

The measured IRAS line is found at $1005\,\mathrm{cm}^{-1}$ [103]. The calculated values for this line using the calculated cases I2, I3, II2 and II3 are $1002\,\mathrm{cm}^{-1}$, $977\,\mathrm{cm}^{-1}$, $979\,\mathrm{cm}^{-1}$, $990\,\mathrm{cm}^{-1}$, respectively (see Fig. 4.22). As it turns out all results lie in the error of the DFT calculation and are therefore not significantly different. Thus, it cannot be decided, whether the iron oxide layer underneath is closed-packed with three iron atoms per silica unit cell or whether it contains only two iron atoms per silica unit cell.

Furthermore, the energetic stability of the models I2 vs. I3 are calculated by R. Włodarczyk and J. Sauer. For these calculations a unit cell is chosen, which has twice the size of the primitive unit cell (see Fig. 4.20, green unit cell). Thus, in this unit cell the FeO layer has six iron atoms and in the reduced case four iron atoms. First the energy difference for iron silicate containing four iron atoms per unit cell on Ru(0001) ($Fe_4\ Si_4\ O_{16}$·2O/Ru(0001)) are addressed. If two additional iron atoms ($2Fe_{bulk}$) are added iron silicate is formed, whereby these two iron atoms are incorporated into the iron oxide unit cell (i.e. having now six iron atoms per unit cell).

$$Fe_4Si_4O_{16} \cdot 2O/Ru(0001) + 2Fe_{bulk} \rightarrow Fe_6Si_4O_{18}/Ru(0001) \qquad \text{(E 1)}$$

The energy difference ΔE is found to be -1.5 eV, i.e. energy is needed, but an excess of iron might be accepted. As a second calculation two iron atoms are taken out of an iron silicate film with six iron atoms per unit cell on Ru(0001) (6 $Fe_4Si_4O_{16}$·2O/Ru(0001)) in

order to form an iron silicate film with only four iron atoms per unit cell on Ru(0001) (4 $Fe_6Si_4O_{18}$/Ru(0001)).

$$6Fe_4Si_4O_{16} \cdot 2O/Ru(0001) \rightarrow$$
$$4Fe_6Si_4O_{18}/Ru(0001) + (SiO_2)_8 \cdot 8O/Ru(0001) + 8O/Ru(0001) + 2O_2 \qquad \text{(E 2)}$$

Here, additionally pristine silica ($(SiO_2)_8$·8O/Ru(0001)) and a pure metal substrate (8O/Ru(0001)) needed to be considered to keep the mass balance. In fact, this reaction influences the system to gain energy of 6.6 eV. Following this calculation a reduction of iron atoms would be preferable. However, the utilized models do not fit exactly to our complete structure and thus, a precise decision cannot be made by these results. At this point the question regarding the structure remains open and will be point of discussion in chapter 4.4.

From the measurements shown in section 4.1.1 an atomic structure for iron silicate can be proposed. On Ru(0001) an iron oxide layer is present with a Moiré structure of "8 on 9" regarding the Ru(0001) substrate. Since the Moiré structure resembles a FeO monolayer (with adapted Fe-Fe distances), a FeO structure is assumed for the iron atoms. Up to now both, a closed FeO layer (i.e. three iron atoms per silica unit cell) is as possible as a reduced number of two iron atoms per silica unit cell. Therefore, two models are considered for each case. The iron oxide layer is bound through a Si-O-Fe bond to a silica monolayer on top of the iron oxide layer. The silica layer has a structure of $(\sqrt{3}\times\sqrt{3})R30°$ regarding a complete iron oxide layer underneath (see Fig. 4.23a-c). In fact, in case the number of iron atoms per silica unit cell is two, the by 30° rotated structure results already from the holes in the iron oxide layer (i.e. positions of missing iron atoms compared to a closed layer). The silica layer on top is in this case unrotated regarding the iron oxide layer. Moreover DFT results indicate a shift between the silica layer on top and the iron oxide layer underneath (see Fig. 4.23d-f. In order to refer to the by 30° rotated spots and the actual structure in a uniform way, in the following these spot are refered to as $(\sqrt{3}\times\sqrt{3})R30°$ regarding a complete iron oxide layer. In contrast to FeO in iron silicate not only Fe^{2+}, but also Fe^{3+} components are found in the XPS Fe 3p spectrum. This indicates an additional oxygen layer between iron and ruthenium. The proposed models using the measured results are shown in Fig. 4.23.

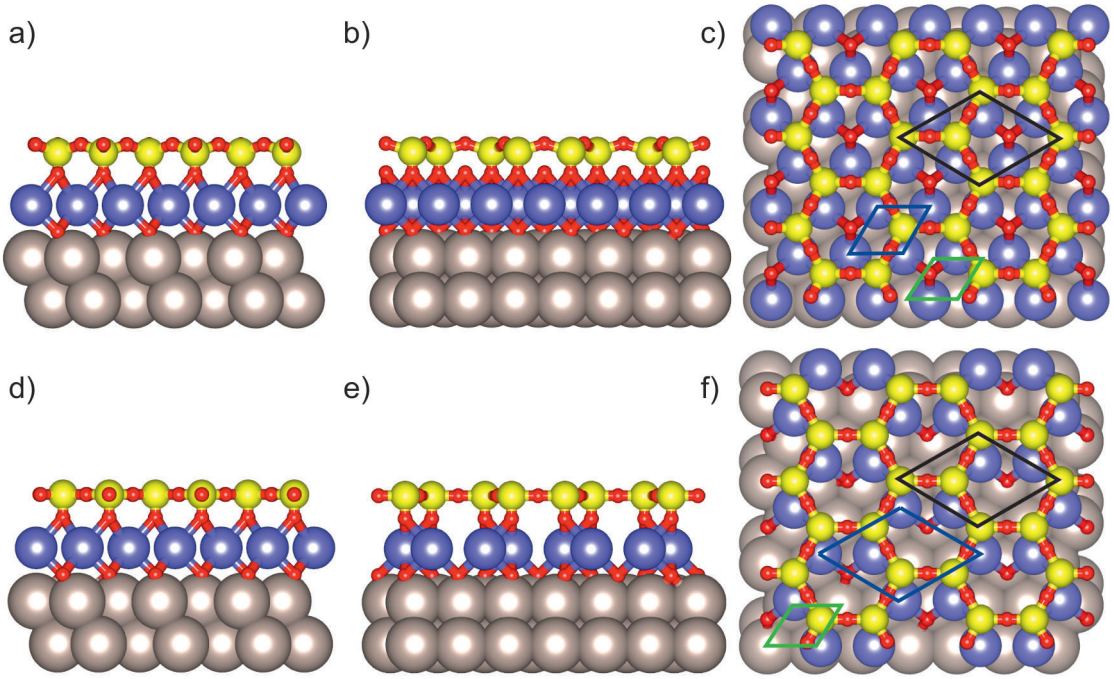

Figure 4.23 Proposed models for iron silicate based on the results of the "combined preparation" method (Si+Fe/3O-Ru(0001)). a-c) assuming three iron atoms per unit cell in the iron oxide layer. d-f) assuming two iron atoms per unit cell in the iron oxide layer. a, d) x-direction. b, e) y-direction and c, f) z-direction. The individual unit cell of silica, iron oxide and ruthenium are indicated in black, blue and green, respectively. Red: Oxygen. Violet: Iron. Yellow: Silicon. Gray: Ruthenium.

4.2 "Stepwise" approach

The iron silicate structure shows a Moiré pattern in LEED that resembles strongly the one of FeO on Ru(0001). Thus, iron silicate is assumed to be a two-layer film with a monolayer of silica on top of a FeO-like layer (see section 4.1.3). Depth profile XPS results in this work (section 4.1.3), as well as IRAS measurements and simulations in [103] confirm the separation of silica and iron oxide. The rotated (2x2) spots can be interpreted as a $(\sqrt{3} \times \sqrt{3})R30°$ regarding a complete FeO-like layer underneath. In case the iron oxide layer contains less iron atoms than the by 30° rotated spots arise by the position of the "missing" iron atoms relative to a complete iron oxide layer.

In chapter 4.1 silicon and iron were deposited at the same preparation step in the so called combined preparation. However, if the presented model is valid, it should also be possible to prepare a silica ML on top of a well prepared FeO layer. The necessary energy to form iron silicate is assumed to be strongly reduced in this preparation, since FeO is already present and silicon must mainly arrange on top of this layer. This preparation method will be called "stepwise preparation" in the following and the results are shown in section 4.2.1.

In section 4.2.2 the opposite approach was used: The deposition of iron on top of a well-prepared ML of silica. This preparation method will be called "stepwise reversed preparation" in the following. The silica ML is known to be chemically bond to the Ru(0001) substrate [34, 107], forming oxygen bonds between silicon and ruthenium atoms. In section 4.1.1 was already discussed that the Si-O bond is relatively strong, even if the silica layer is disordered. Since Ru has also a high oxygen affinity, the Si-O-Ru bond is also very strong. As a result, the formation of iron silicate is assumed to afford much higher (thermal) energy to break the Si-O-Ru bond in favour of iron diffusion underneath the silica layer.

4.2.1 Stepwise preparation (ML FeO + ML SiO_2)

In this chapter iron silicate is prepared in a two-step preparation. First a ML of FeO is prepared on Ru(0001) by direct deposition of iron at 800 K in $2.0 \cdot 10^{-8}$ mbar. A detailed description of the FeO preparation is given in chapter 3.1. For the following iron silicate preparation monolayer phase ML2 is used. This FeO phase shows the typical Moiré pattern with a "6 on 7" reconstruction (see Fig. 4.25a), meaning that six iron atoms are commensurable positioned on seven ruthenium atoms. The characteristic LEEM-IV fingerprint of this phase can be found in Fig. 3.6 of chapter 3.1. The MEM-LEEM border is found at 2.72 eV. The XPS Fe 3p and O 1s line are given in Fig. 4.24. The Fe 3p line shows that the iron atoms are in the Fe^{2+} configuration. Moreover only one O 1s line is present at 528.8 eV. This line the Fe-O-Fe and Fe-O-Ru component overlap.

In principle also the monolayer phase ML1 (rotational domains) can be used (compare chapter 3.1). The final iron silicate film shows the same characteristics for using the iron oxide monolayer phases ML1 and ML2.

The FeO layer is cooled down to RT (without further oxygen dose to maintain the as deposited state) and subsequently oxidized in $2.0 \cdot 10^{-7}$ mbar. The intensity of the film is decreasing as can be followed in LEEM until the FeO layer is saturated. The oxidation step is necessary to differentiate between the influence of the increase of surrounding oxygen

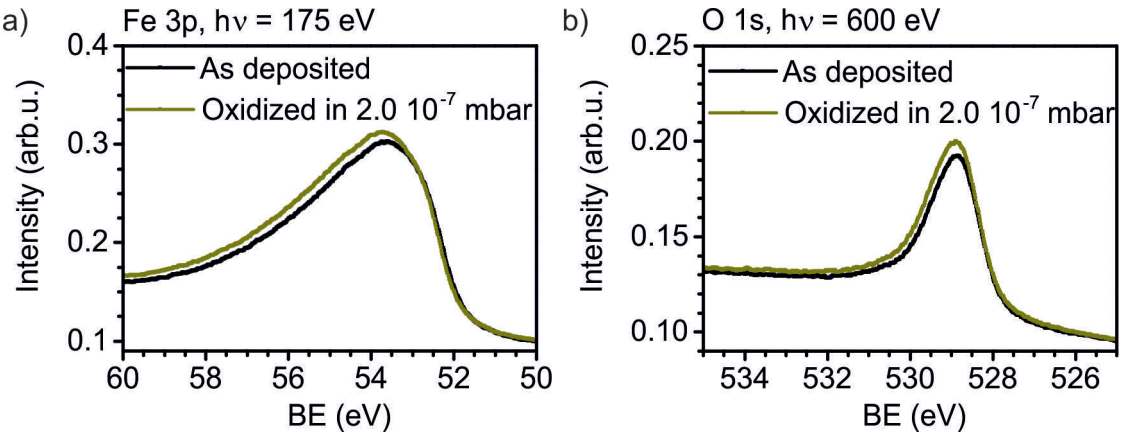

Figure 4.24 XPS characteristics of FeO as prepared and oxidized in $2.0 \cdot 10^{-7}$ mbar for the a) Fe 3p line (h$\nu = 175$ eV) and b) O 1s line (h$\nu = 600$ eV).

and the addition of silicon atoms. The XPS spectra show only subtle changes in the Fe 3p and O 1s line during this step. Hereby, the peak position is not altered, but the intensity of the peaks is slightly increased. In Fig. 4.24 the corresponding XPS Fe 3p and O 1s lines are given for the FeO monolayer phase ML2 as prepared and oxidized in $2.0 \cdot 10^{-7}$ mbar. The oxidation at RT of the FeO layer shows only a minor influence in the LEEM-IV curve and only a minimal reduction in the MEM-LEEM border to 2.64 eV. The O 1s and Fe 3p line show nearly no change regarding the as prepared FeO layer. The Moiré pattern is unchanged.

Silicon is deposited in the same oxygen pressure ($2.0 \cdot 10^{-7}$ mbar) as was used for the FeO oxidation. The silicon amount used equals the amount necessary to form a monolayer of silica. Finally the film was oxidized in $1.0 \cdot 10^{-6}$ mbar, first at RT and then stepwise up to 660 K, 800 K, 900 K and 1000 K. The sample was oxidized for 30 min at 660 K and at higher temperatures for 15 min at the individual temperatures. After each temperature step the film was cooled down to RT without introducing additional oxygen and analyzed with LEED (Fig. 4.25), LEEM-IV (Fig. 4.27) and XPS (Fig. 4.29).

Si deposition extinguishes the Moiré pattern. In LEED mainly the (00) spot, surrounded by a corona is present and, very weakly, a blurry star like feature from the (00) spot towards the position of the $(\sqrt{3} \times \sqrt{3})R30°$ spots (see Fig. 4.25b). The MEM-LEEM border is decreased by 0.14 eV to 2.63 eV (Fig. 4.4b), thus the dipole (present for FeO) is reduced. The LEEM-IV curve resembles strongly the LEEM-IV curve for the "combined preparation" method (section 4.1.1) after silicon and iron are deposited. It shows one main peak at 6 eV. Thus, silicon is disordered on top of the FeO layer. The Fe 3p line shows a partial reduction of iron, i.e. half of the iron atoms are in the metallic state (Fe^0 state), while the other half remains in the Fe^{2+} state. The strong overall reduction of the peak is due to damping of the iron signal by the silicon overlayer. On the contrary silicon is completely oxidized in the Si^{4+} state. Thus, silicon breaks Fe-O bonds in order to oxidize silicon atoms. Metallic iron remains. Also for silicon deposition on top of a 3O-(2x2)-Ru(0001) substrate it was shown, that the available oxygen amount on the surface in consumed [44]. However, the available oxygen on the substrate was not sufficient to completely oxidize a monolayer of silicon (silica). It was shown, that the surrounding oxygen ($p_{O_2} = 2.0 \cdot 10^{-7}$ mbar) is necessary for a complete oxidation. The same is most likely true for the present case, since

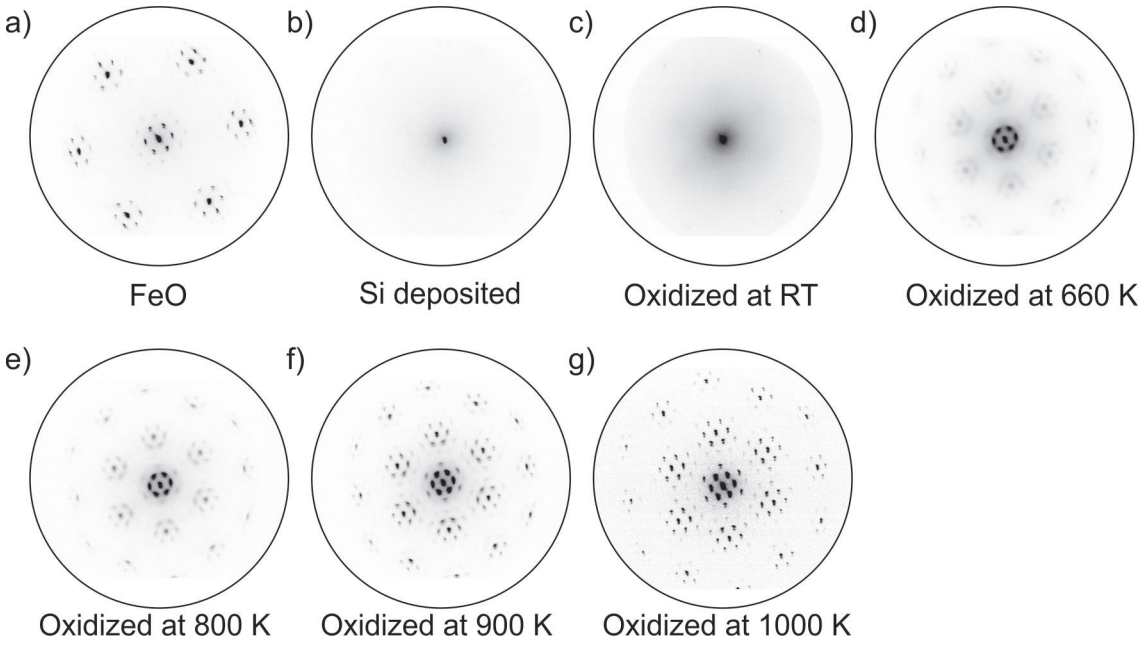

Figure 4.25 LEED evolution for the individual preparation steps for iron silicate prepared with the "stepwise preparation" method (Si/FeO/Ru(0001)). a) iron oxide monolayer before Si evaporation (see chapter 3.1). b) Directly after Si deposition. c-h) oxidation in $1.0 \cdot 10^{-6}$ mbar at c) RT, d) 660 K, e) 800 K, f) 900 K, g) 1000 K. The kinetic energy is 42 eV. Measurements are taken at RT.

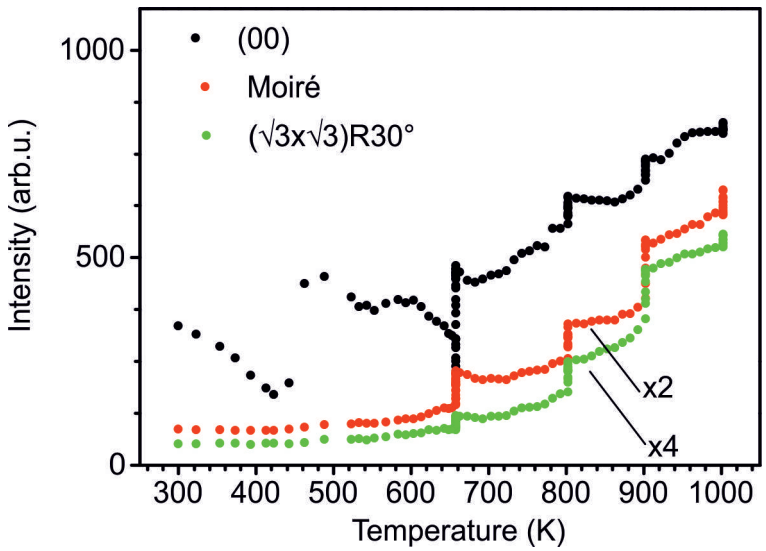

Figure 4.26 Spot intensity of the (00), Moiré and $(\sqrt{3} \times \sqrt{3})R30°$ spot during oxidation in $1.0 \cdot 10^{-6}$ mbar of iron silicate using the "stepwise preparation" method (Si/FeO/Ru(0001)). The $(\sqrt{3} \times \sqrt{3})R30°$ structure refers to a silica structure that is rotated by 30° regarding a complete iron oxide layer.

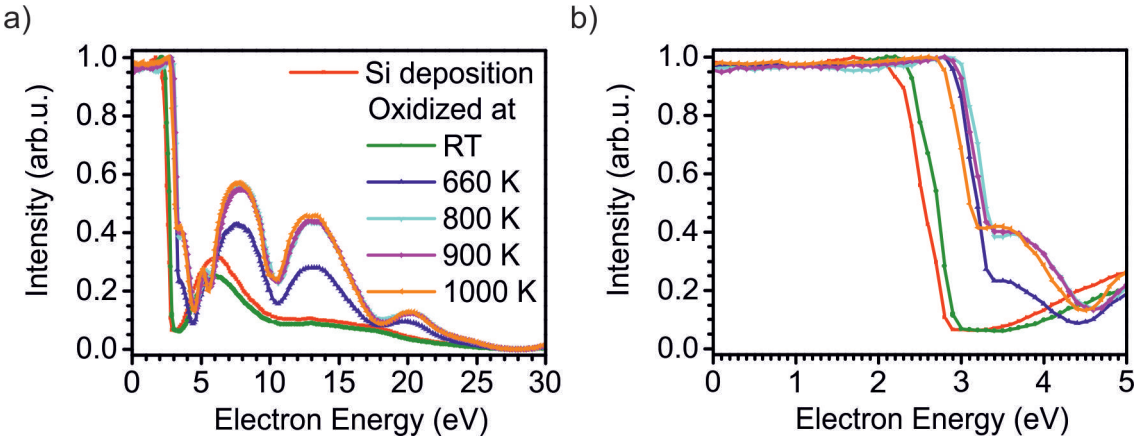

Figure 4.27 LEEM-IV evolution for the individual preparation steps of iron silicate using the "stepwise preparation" method (Si/FeO/Ru(0001)). a) LEEM-IV, b) MEM-LEEM transition. Si is deposited on the FeO layer in $1.0 \cdot 10^{-7}$ mbar. The oxidation was done in $1.0 \cdot 10^{-6}$ mbar. Measurements are taken at RT.

the oxygen density for FeO on Ru(0001) is lower than for 3O on Ru(0001). The O 1s line confirms the reduction of Fe-O bonds in favor of Si-O bonds. The Fe-O-Fe/ Fe-O-Ru line is nearly not present anymore, but the Si-O-Si line is very prominent. Additionally the Fe-O-Si line is strongly present. Using a surface sensitive photon energy of 600 eV the Si-O-Si line has nearly double the intensity of the Fe-O-Si peak. Increasing the probing depth to a photon energy of 780 eV, the intensity ratio I(Si-O-Si):I(Fe-O-Si) shrinks strongly, so that they nearly have the same intensities. This indicates that at RT (as it is expected) the two-layer separation remains as deposited.

The oxidation in $1.0 \cdot 10^{-6}$ mbar for 30 min has mainly influence on the oxidation of iron. The Fe 3p line (Fig. 4.29a) the Fe^{2+} component is slightly increased and the Fe^0 component decreased. The O 1s line (Fig. 4.29b) shows an increase in the Fe-O-Fe line, which is especially visible with a higher electron probing depth using a photon energy of 780 eV.

Preparation step	Energetic position of the MEM-LEEM border (eV)	Workfunction (eV) (referenced to clean Ru(0001) with 5.44 eV [12])
FeO	2.72	5.58
Si deposition	2.63	5.49
Oxidation at RT	2.77	5.63
Oxidation at 660 K	3.24	6.10
Oxidation at 800 K	3.30	6.16
Oxidation at 900 K	3.24	6.10
Oxidation at 1000 K	3.08	5.94

Table 4.4 Overview on the MEM-LEEM border evolution for the individual preparation steps of the "stepwise preparation" method (Si/ FeO/ Ru(0001)). The MEM-LEEM values are measured with an accuracy of $\pm$ 0.02 eV.

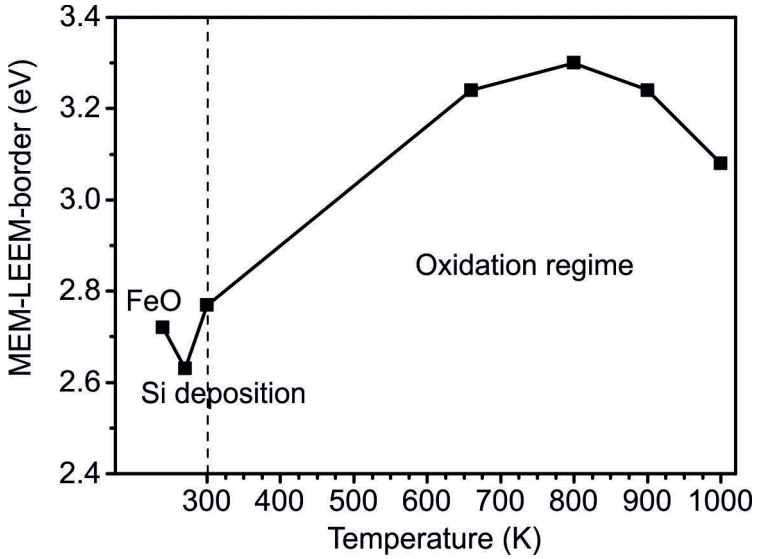

Figure 4.28 MEM-LEEM border for the individual preparation steps of the "stepwise preparation" method (Si/FeO/Ru(0001)). The FeO monolayer is produced by iron deposition at 800 K in $2.0 \cdot 10^{-8}$ mbar (see chapter 3.1). Si is deposited in $2.0 \cdot 10^{-7}$ mbar at RT and the film is oxidized in $1.0 \cdot 10^{-6}$ mbar.

Structurally the LEEM-IV curve remains nearly unchanged. Only the MEM-LEEM border is increased to 2.77 eV, i.e. nearly the same value as for FeO before Si was deposited. In the LEED pattern the intensity of the rotated (2x2) spots increases, but the spot shape is still very blurry and thus, the silicon dioxide layer very disordered.

In the next step the film is oxidized at elevated temperatures. The intensities of the individual LEED spots during oxidation are shown in Fig. 4.26. At around 575 K the $(\sqrt{3} \times \sqrt{3})R30°$ spots increase in intensity and the connection to the (00) spots dissolves (before it had a star-like shape). 40 K higher at 645 K the corona surrounding the (00) spot intensifies until the individual Moiré spots are distinguishable. Finally at 660 K the sample temperature is kept constant and after 6 min an additional corona surrounding the $(\sqrt{3} \times \sqrt{3})R30°$ spots appears und develops to distinct Moiré spots during additional 8 min. However these spots remain lower intense as the $(\sqrt{3} \times \sqrt{3})R30°$ spots. The sample is held for 30 min at 660 K and subsequently cooled down fast without further oxygen dose. The characteristic LEED pattern for iron silicate is already present, but the spots are still slightly blurred. The Moiré spots surrounding the (00) spot are much more intense as all other spots (excluding the (00) spot). The LEEM-IV curve shows the prominent dip at 4.5 eV and peaks at 7.5 eV, 13 eV and 20.4 eV. The MEM-LEEM-border is raised to 3.24 eV. Altogether, this resembles the fingerprint at 800 K, when iron silicate is prepared with the "combined preparation" method (section 4.1.1). Chemically the strongest change is visible in the Fe 3p line, which shows that iron is mainly in the Fe^{3+} state and, with lower intensity, Fe^{2+} state. In order to achieve a Fe^{3+} state, the number of oxygen atoms bound to iron is higher than the number of iron atoms. If it is assumed, that two iron atoms share 2 oxygen atoms, each iron atoms binds to $\frac{1}{2} + \frac{1}{2} = 1$, which is true for FeO. From XPS results before the film was annealed a Si-O-Fe component was measurement. Therefore Fe-O-Fe bonds are replaced by Fe-O-Si bonds. The number of oxygen bonds remains and thus the Fe^{2+} configuration. In order to achieve a Fe^{3+} configuration oxygen must therefore intercalate between the iron oxide and Ru(0001) layer. The O 1s line shows

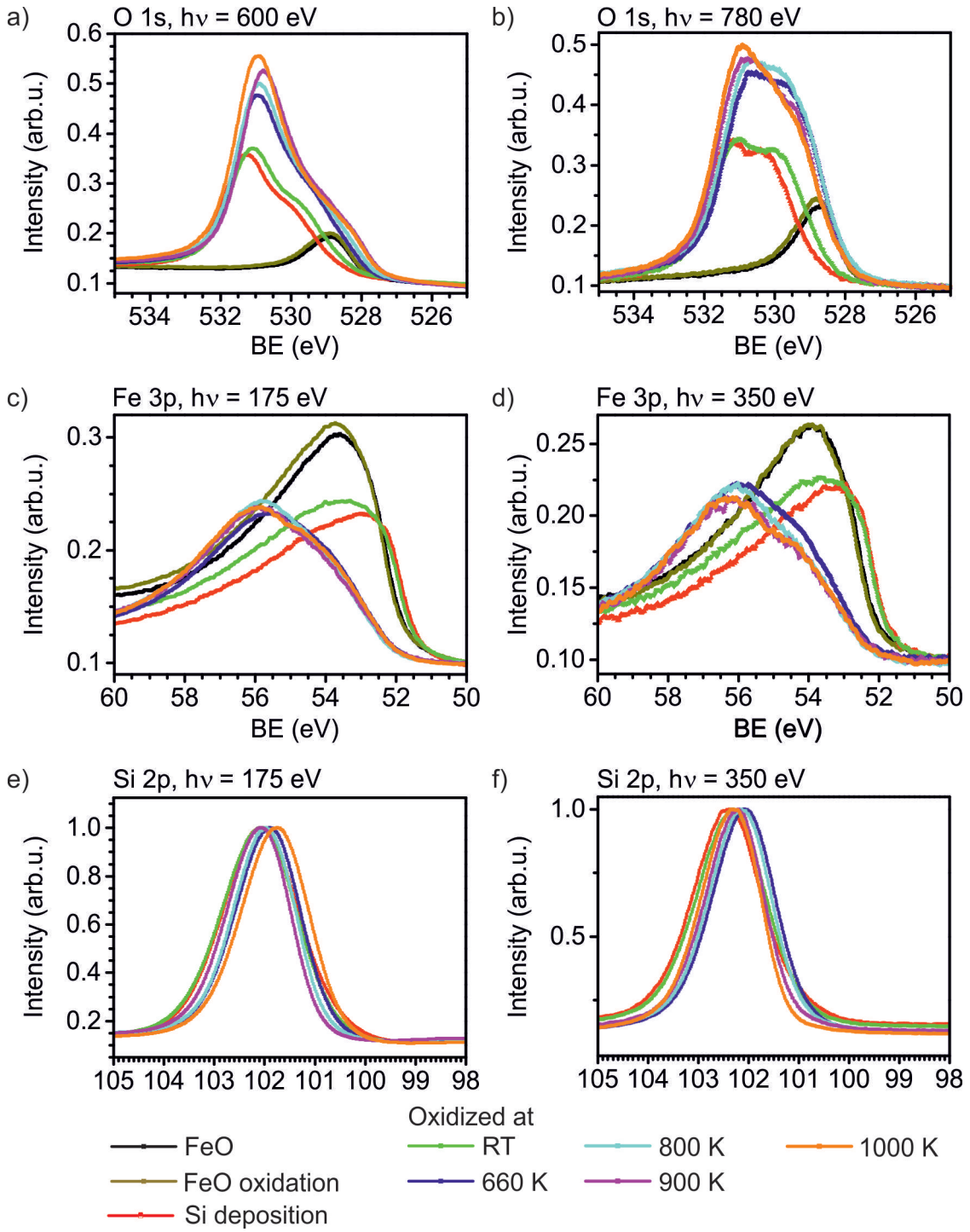

Figure 4.29 Temperature dependent XPS analysis of iron silicate prepared with the "stepwise preparation" method (Si/FeO/Ru(0001)). O 1s line for a photon energy of a) 600 eV and b) 780 eV. Fe 3p line for a photon energy of c) 175 eV and d) 350 eV. Si 2p line for a photon energy of e) 175 eV and f) 350 eV. The measurements are taken at RT.

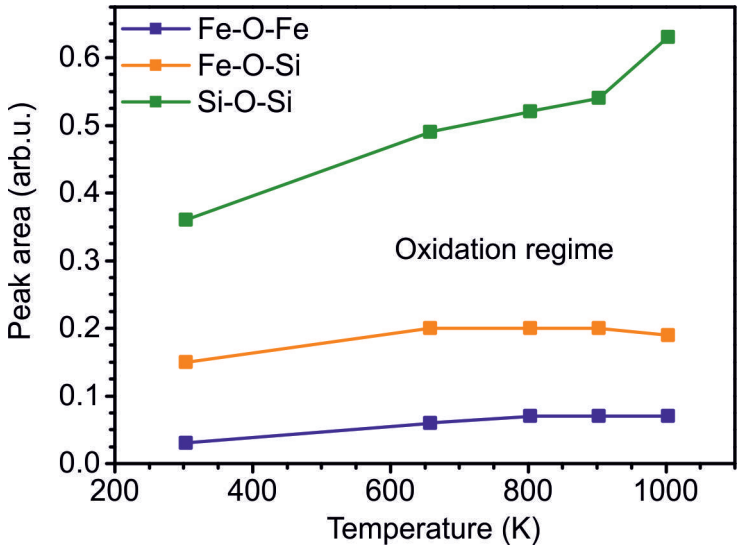

Figure 4.30 Evolution of the Fe-O-Fe, Fe-O-Si and Si-O-Si components of the O 1s line at 600 eV (Fig. 4.29a) of an iron silicate film using the "stepwise preparation" method (Si/FeO/Ru(0001)).

the increase in all three components (Si-O-Si, Fe-O-Si and Fe-O-Fe/Fe-O-Ru), whereby the strongest increase is found in the Si-O-Si line, when using the photon energy of 600 eV. Depth profile (photon energy of 780 eV) on the other hand, shows that the Si-O-Si and Fe-O-Fe component nearly at the same intensity. This again confirms the two-layer nature of the system with iron oxide closer to the Ru(0001) substrate.

As a next step the film was annealed in steps to 800 K, 900 K and finally 1000 K. The iron silicate LEED pattern, already present at 660 K becomes more intense and the individual spots become sharper (Fig. 4.25g). This indicates a better ordering of the film. Chemically, there is a slight increase for the Fe^{3+} signal up to 800 K (for a photon energy of $h\nu$ = 175 eV). This indicates a ongoing oxidation at the Fe/Ru(0001) interface. In comparison with a higher photon energy of $h\nu$ = 350 eV, a clear reduction of the Fe^{2+} component is evident, showing that iron atoms at the interface transform from a Fe^{2+} to the Fe^{3+} state. For higher temperatures than 800 K, the intensity of the Fe 3p line is minimal reduced for photon energies of 175 eV and 350 eV. Also the Fe-O-Fe/Fe-O-Ru component of the XPS O 1s line decreases, when using less surface sensitive photon energies ($h\nu$ = 780 eV). Since iron diffusion into the Ru crystal was never observed (or its reappearance) the material is most likely evaporated. Using surface sensitive energies the Fe-O-Si and Fe-O-Fe/Fe-O-Ru lines appear rather unchanged. However, the Si-O-Si line increases strongly with increasing temperature. Between 900 K and 1000 K the increase is strongest.

In Fig. 4.31 the LEEM-IV curves for 660 K, 800 K and 900 K are given in the range of 2-30 eV. As can be seen neither the shape nor the peak positions are changing between 6.5 and 30 eV. Also the MEM-LEEM border does not change anymore up to 900 K. At 1000 K the MEM-LEEM border is again decreased to 3.08 eV. However, with increasing temperature and improved intensity of the iron silicate LEED pattern an additional dip develops at 5.5 eV. The presence of this dip is can therefore be seen as a measure for the quality of the film.

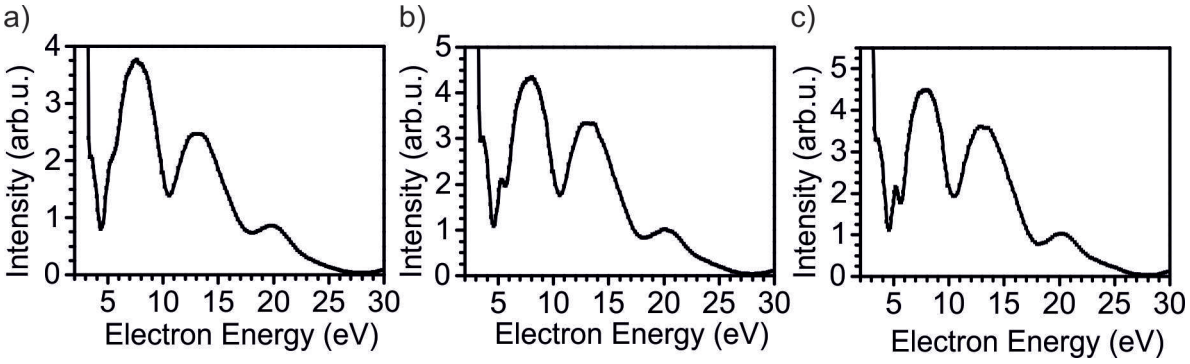

Figure 4.31 LEEM-IV fingerprints of iron silicate prepared with the "stepwise preparation" method (Si/FeO/Ru(0001)) at a) 660 K, b) 800 K and c) 900 K. The ratio of the dips at 4.5 eV and 5.5 eV indicates the state of film evolution. A well developed dip at 5.5 eV is typical for an optimal iron silicate layer of a nominal monolayer of iron and a nominal monolayer of silica. This process is also found in other preparation methods discussed in sections 4.1 and 4.2.2.

As discussed a slight decrease in the Fe-O-Fe/Fe-O-Ru line is present for temperatures higher than 800 K. Moreover, the strong increase of the Si-O-Si lines correlates nicely with the sharpness of the $(\sqrt{3} \times \sqrt{3})R30°$ LEED spots and results out of an increased ordering of the Silica layer. Therefore it can be assumed that the iron reduction is necessary for an optimal iron silicate layer. As a result the reduction of iron might correlate with the occurrence and development of the additional dip at 5.5 eV in the LEEM-IV curve.

Summary of the formation process for the "stepwise preparation" method

The formation process of iron silicate using the "stepwise preparation" method is given in Fig. 4.32. First a monolayer of FeO is prepared (Fig. 4.32a) giving rise to a "6 on 7" Moiré pattern. The FeO layer is oxygen terminated as visible by the MEM-LEEM transition. Silicon is deposited on top (Fig. 4.32b) at RT in an oxygen background of $2.0 \cdot 10^{-7}$ mbar. Silicon binds to the oxygen atoms of the FeO layer, which leads to a partial reduction of iron. Moreover the FeO Moiré pattern disappears. Due to the oxygen atoms on the surface and the surrounding oxygen in the chamber silicon is completely oxidized in the Si^{4+} state. The film is oxidized in $1.0 \cdot 10^{-6}$ mbar. Already at 460 K the $(\sqrt{3} \times \sqrt{3})R30°$ spots appear, i.e. the silica layer starts to order (Fig. 4.32c). In contrast to other preparation methods, shown in chapter 4.1 this temperature is very low. Hence, the pre-ordering of the iron atoms in form of FeO reduces the activation energy. The Moiré spots surrounding the (00) spot, resulting from ordered iron oxide, reappear at 645 K (Fig. 4.32d). The Moiré reconstruction is "8 on 9".

Finally, at 660 K also the Moiré spots surrounding the $(\sqrt{3} \times \sqrt{3})R30°$ spots are visible and with this the characteristic LEED pattern and the typical fingerprint of iron silicate as observed in chapter 4.1 is present. The XPS Fe 3p line indicates a Fe^{3+} component, which can be correlated to an additional oxygen layer between iron and the Ru(0001) substrate (Fig. 4.32d). For higher temperatures the iron amount decreases slightly and the LEED pattern improves in sharpness and intensity of the LEED spots. In the LEEM-IV curve a additional dip at 5.5 eV develops, which can be used as indication for the quality of the film, which might correlate with the minimal iron loss. At 900 K (Fig. 4.32e) the same

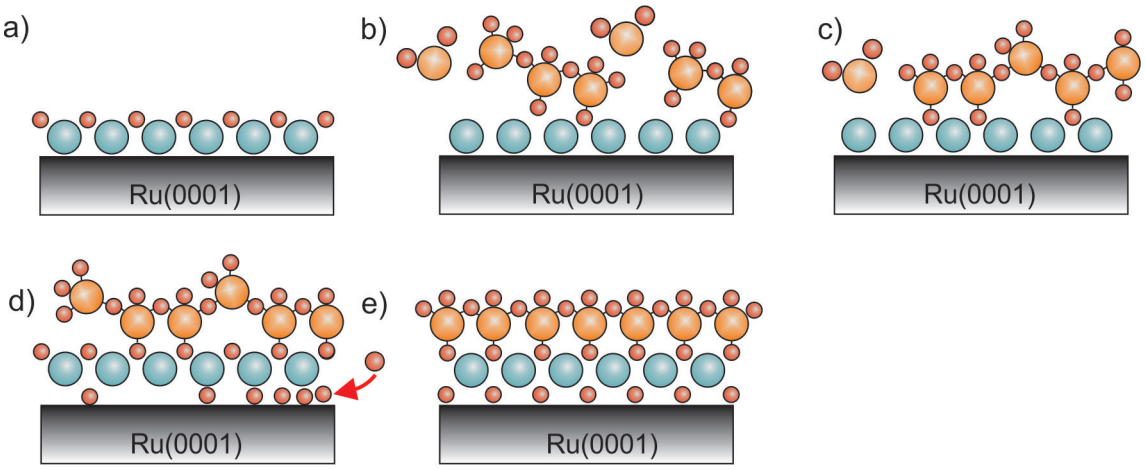

Figure 4.32 Individual steps during oxidation of iron silicate prepared with the "stepwise preparation" method (Si/FeO/Ru(0001)). a) FeO monolayer with "6 on 7" reconstruction, b) Si deposition influences the reduction of the iron oxide layer. Si is completely oxidized but disordered. c) Arrangement of the silica layer starting at 460 K. d) Intercalation of oxygen to the iron layer starting at 645 K and arrangement in a "8 on 9" reconstruction. e) Final iron silicate film present at 900 K. Red: Oxygen. Violet: Iron. Yellow: Silicon.

fingerprint as for the iron silicate preparation using the "combined preparation" method at 1000 K (section 4.1.1) and the "combined UHV preparation" method at 900 K (section 4.1.2) is achieved.

4.2.2 Stepwise reversed preparation (ML SiO_2 + ML Fe)

In the last section 4.2.1 it was shown that iron silicate can be prepared stepwise, when starting with a well-ordered monolayer of FeO. In this chapter the contrary approach is used: First a well-ordered monolayer of Silica is prepared and as a second step iron is deposited. The "combined preparation" method showed that a pre-oxidation of silicon (even if it is disordered) before iron is deposited has a major influence on the necessary (thermal) energy to form iron silicate, since Si-O-Ru bonds need to be broken in order to rearrange silicon and iron diffusion under the silicon layer. The difference to the (nearly) not oxidized silicon is shown in the "combined UHV preparation". The temperature difference has proven to be 100 K.

In this chapter silicon dioxide is not only oxidized, but also well ordered. In chapter "combined preparation" silicon was deposited at RT on an oxygen pre-covered Ru(0001) substrate (3O-(2x2)-Ru(0001), i.e. three oxygen atoms per Ru unit cell) in an oxygen background pressure of $2.0 \cdot 10^{-7}$ mbar. For the preparation of well-ordered silica this silicon-oxide layer needs to be further oxidized in $1.0 \cdot 10^{-6}$ mbar up to 1050 K for 10 min. Subsequently the film is cooled down to RT in the same oxygen background pressure. The LEED pattern of (ordered) silica is a (2x2) reconstruction on top of Ru(0001) (see Fig. 4.33a). At the same time a characteristic LEEM-IV curve evolves, much different to the disordered silica layer. The MEM-LEEM border is increased from 3.05 eV (disordered) to 3.43 eV (ordered), showing the enhanced oxidation (see Tab. 4.5 and Fig. 4.36).

The monolayer of Silica is known to be chemically bond to the Ru(0001) substrate through Si-O-Ru bonds [34, 107]. Thus, a higher effort (higher thermal energy) is expected to be necessary in order to form iron silicate in comparison to disordered silicon-dioxde. The O 1s line of SiO_2 disordered (as deposited) and ordered are shown in Fig. 4.37a. The O 1s line consists of two lines: One line at 529.1 eV and the other at 530.7 eV. The first line

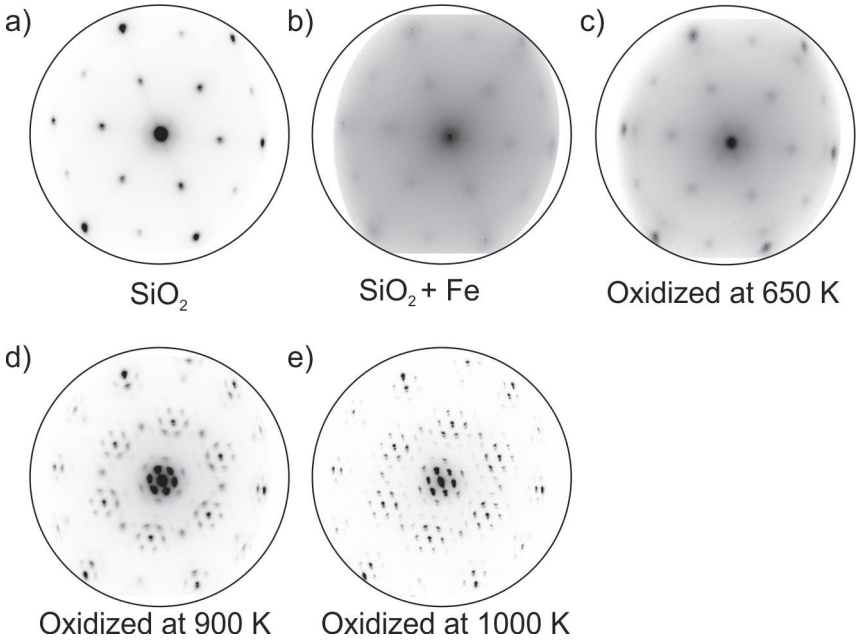

Figure 4.33 LEED pattern of the individual preparation steps of iron silicate prepared with the "stepwise reversed preparation" method ($Fe/SiO_2/Ru(0001)$). All LEED images are taken at 42 eV. a), b), d) and e) are measured at RT. c) is measured at 650 K. Iron is deposited at RT in $2.0 \cdot 10^{-7}$ mbar. The oxidation is done in $1.0 \cdot 10^{-6}$ mbar.

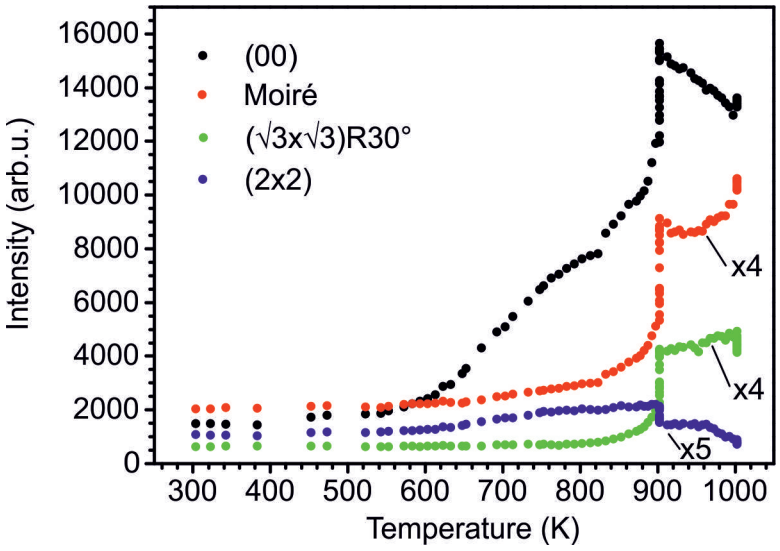

Figure 4.34 Spot intensities of the (00), Moiré, $(\sqrt{3} \times \sqrt{3})R30°$ and (2x2) spots during the oxidation in $1.0 \cdot 10^{-6}$ mbar of iron silicate prepared with the "stepwise reversed preparation" method ($Fe/SiO_2/Ru(0001)$). The $(\sqrt{3} \times \sqrt{3})R30°$ structure refers to a silica structure that is rotated by 30° regarding a complete iron oxide layer.

can be assigned oxygen bound to Ru (Si-O-Ru or O-Ru) and the later to Si-O-Si bonds. Comparing the spectra of disordered and ordered Silica the difference in the intensity ratio I(Si-O-Ru): I(Si-O-Si) is evident, being much higher for ordered silica as for disordered silica. This indicates that most Si-O-Ru bonds are developed during the final oxidation step to 1050 K. As already shown in chapter "combined preparation" method silicon is already completely oxidized after deposition, as a combination of binding to oxygen present on the Ru(0001) substrate and the surrounding oxygen pressure of $2.0 \cdot 10^{-7}$ mbar [44]. Correlated to this the Si 2p line shows only one peak at 102.5 eV (Si^{4+} state) for both, the disordered and ordered silica layer.

At RT iron is deposited on the silica monolayer in $2.0 \cdot 10^{-7}$ mbar. The (2x2) LEED spots of the Silica layer become weaker, but are still present after iron deposition (Fig. 4.33b). However, the LEEM-IV curve is strongly damped compared to the one of the silica monolayer and resembles strongly the one of disordered (as deposited) silicon. The MEM-LEEM border is strongly decreased to 2.48 eV, matching the one for a clean Ru(0001) substrate. Thus, an earlier dipole on the surface is not present anymore. Chemically, iron has only a minor influence on the peak distribution of the O 1s line. Still there are two peaks visi-

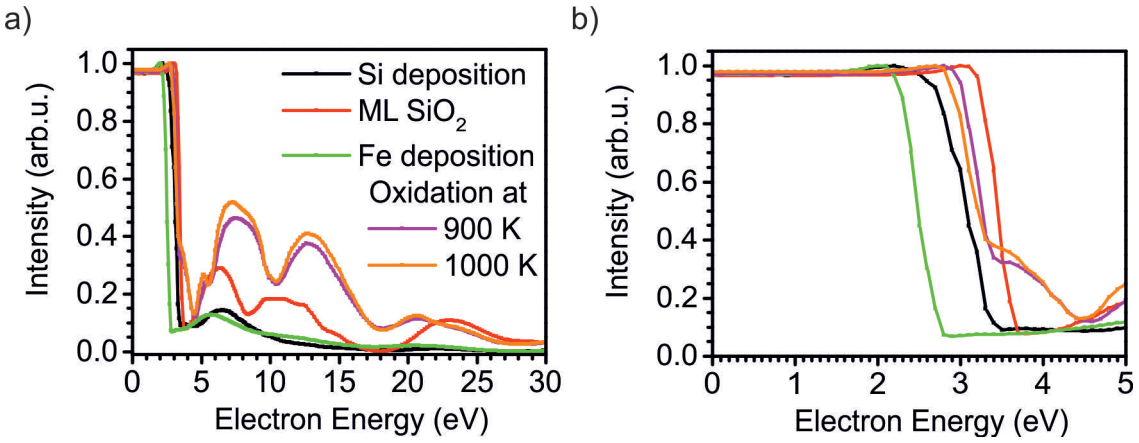

Figure 4.35 LEEM-IV curve for the individual preparation steps of iron silicate prepared with the "stepwise reversed preparation" method ($Fe/SiO_2/Ru(0001)$). a) LEEM-IV curve, b) MEM-LEEM border. The oxidation is done in $1.0 \cdot 10^{-6}$ mbar.

Preparation step	Energetic position of the MEM-LEEM border (eV)	Workfunction (eV) (referenced to clean Ru(0001) with 5.44 eV [12])
Si deposition	3.05	5.91
SiO_2	3.43	6.29
Fe deposition	2.48	5.34
Oxidation at 900 K	3.18	6.04
Oxidation at 1000 K	3.09	5.95

Table 4.5 Overview on the MEM-LEEM border evolution for the individual preparation steps of the "stepwise reversed preparation" method ($Fe/ SiO_2/ Ru(0001)$). The MEM-LEEM values are measured with an accuracy of $\pm$ 0.02 eV.

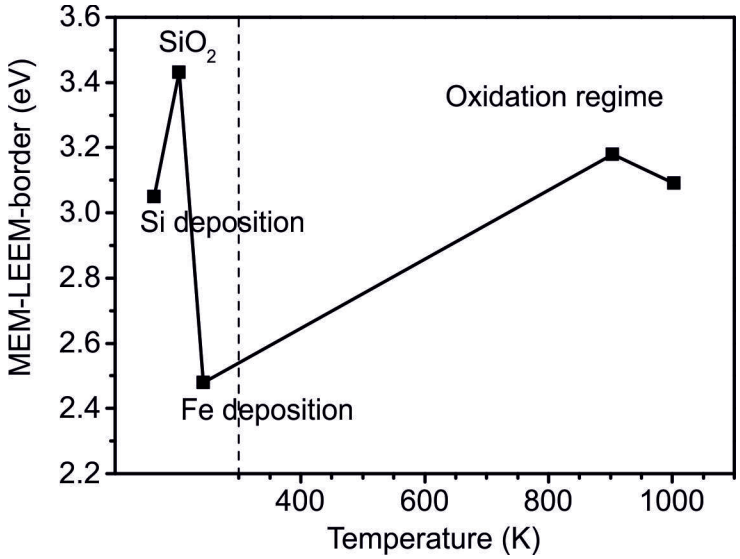

Figure 4.36 MEM-LEEM border for the individual preparation steps of iron silicate using the "stepwise reversed preparation" method ($Fe/SiO_2/Ru(0001)$). The oxidation takes is done in $1.0 \cdot 10^{-6}$ mbar. The MEM-LEEM values are determined by a fit of the MEM-LEEM border presented in Fig. 4.35b. The error of this fit is 0.02 eV.

ble one at 529 eV and one at 531 eV. The peak intensity of the line at 529 eV is increased through iron deposition, since the Fe-O-Fe line is matching the position of the O-Ru line. The silica layer appears to be rather unchanged, as the still visible (2x2) structure, O 1s non-altered Si-O-Si line and the remaining Si^{4+} state in the Si 2p line indicate. Iron atoms are found to be in the Fe^{2+} configuration, which results most likely from the surrounding oxygen in the chamber. For the FeO monolayer on Ru(0001) (section 3.1) it was shown that even a pressure of $2.0 \cdot 10^{-8}$ mbar was sufficient for iron to be in the Fe^{2+} state. In the present preparation the pressure is even one order of magnitude higher ($2.0 \cdot 10^{-7}$ mbar). Moreover, the silicon atoms remain completely oxidized during iron deposition.

The film is oxidized in $1.0 \cdot 10^{-6}$ mbar first at RT, stepwise to 900 K and finally up to 1000 K. The temperature of 900 K was held constant for 30 min and the final temperature of 1000 K was held for 10 min. The oxidation was followed in LEED. The intensity evolution of the individual LEED spots is shown in Fig. 4.34. The corresponding LEED images after cooling down to RT after oxidation to 900 K and 1000 K are given in Fig. 4.33d and e, respectively. After iron deposition the (2x2) spots of the silica monolayer are still present. During the oxidation the (2x2) spots start to increase in intensity at 570 K and continue to gain intensity up to 900 K. While the temperature of 900 K was kept constant the (2x2) spots drastically decrease its intensity. When the sample was annealed further up to 1000 K, they diminish even further, until they nearly disappear. Especially during the constant oxidation at 1000 K this is the case. When the sample was cooled down, the (2x2) spots reappeared at temperatures ≤ 500 K. Moiré spots surrounding the (00) spots appear at 525 K. The Moiré pattern indicates an ordering of iron. With rising temperature the Moiré pattern increases in intensity and sharpness of the spots.

At 825 K $(\sqrt{3} \times \sqrt{3})R30°$ develop, directly surrounded by Moiré spots. This temperature is much higher than was observed for the other preparation methods. Up to 900 K the intensity strongly enhanced, whereby the $(\sqrt{3} \times \sqrt{3})R30°$ spots become much more intense

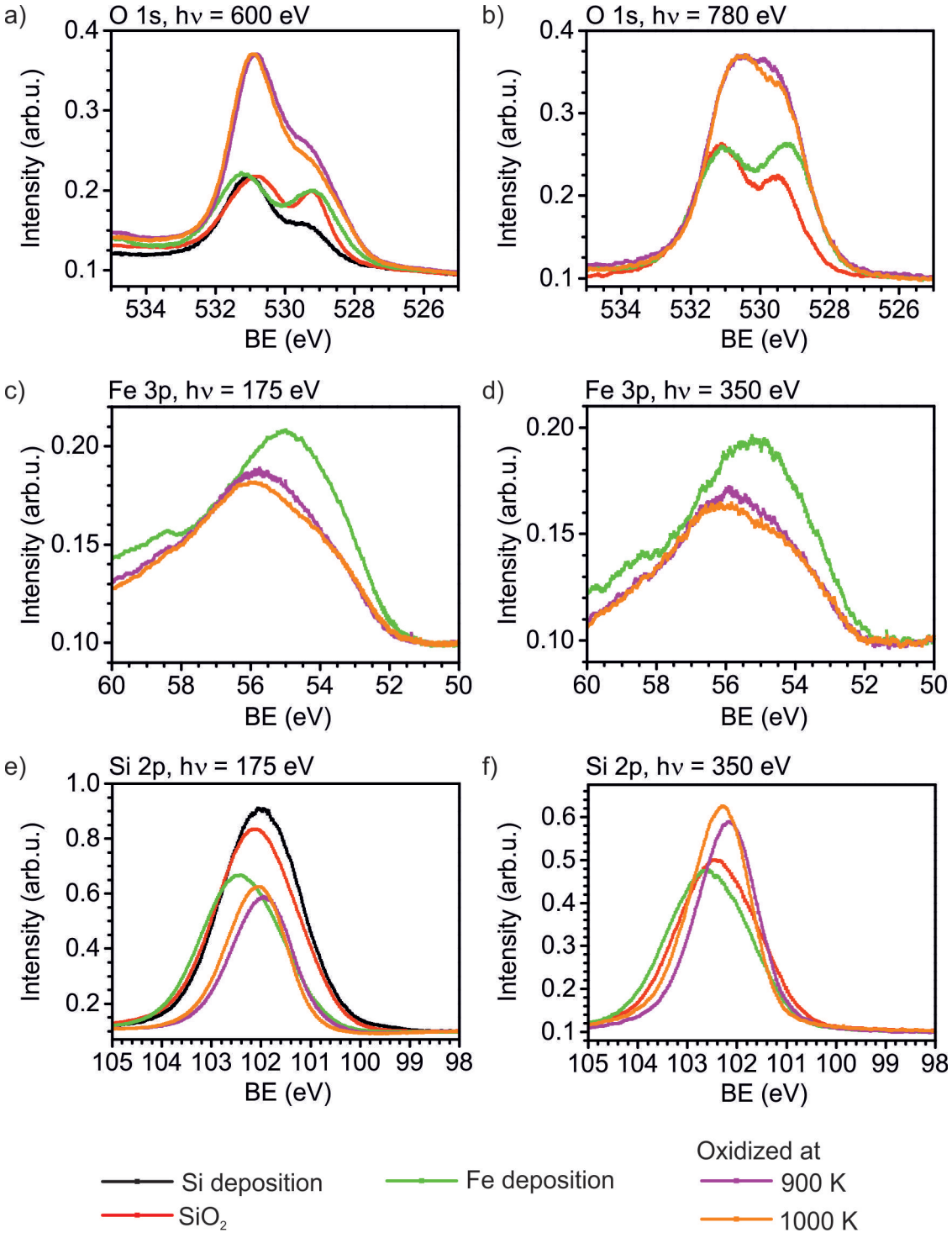

Figure 4.37 XPS analysis of iron silicate prepared with the "stepwise reversed preparation" method ($Fe/SiO_2/Ru(0001)$). O 1s line for a photon energy of a) 600 eV and b) 780 eV. Fe 3p line for a photon energy of c) 175 eV and d) 350 eV. Si 2p line for a photon energy of e) 175 eV and f) 350 eV. The measurements are performed at RT.

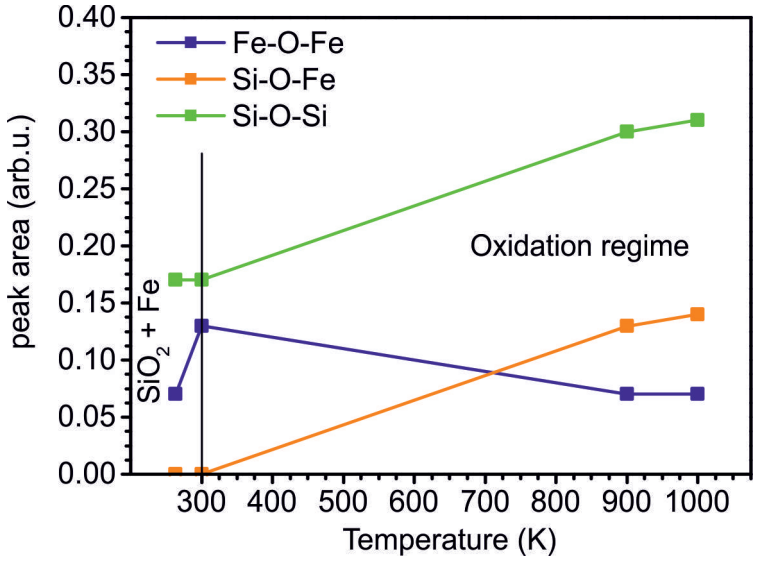

Figure 4.38 Evolution of the Fe-O-Fe, Fe-O-Si and Si-O-Si components of the O 1s line at 600 eV (Fig. 4.37a) of iron silicate using the "stepwise reversed preparation" method ($Fe/SiO_2/Ru(0001)$).

than the Moiré spots surrounding them. Especially during the constant temperature of 900 K they gain strongly intensity, which is continued for further annealing up to 1000 K. Only during the constant oxidation at 1000 K the intensity of the $(\sqrt{3} \times \sqrt{3})R30°$ spots is again decreased. The intensity increase of the $(\sqrt{3} \times \sqrt{3})R30°$ spots correlates nicely with the intensity decrease of the (2x2) spots. In LEEM the presence of domains are visible after oxidation to 900 K. By dark field imaging (Fig. 4.39) the individual domains can be assigned either to a $(\sqrt{3} \times \sqrt{3})R30°$ structure or a (2x2) structure. The domains giving rise to a (2x2) structure appear to be very small. From this information together with the evolution of the individual LEED spots it can be concluded that the monolayer of silica (with iron atoms on top) are transformed to domains of iron silicate simultaneously everywhere on the surface. The transformation starts slowly at 825 K and is faster the higher the temperature is. During the constant temperature of 900 K this transformation seems to be very effective. The Moiré structure is present everywhere on the surface (Fig. 4.39c and d) showing the effect of the different terraces of Ru(0001) (by bright-dark contrast change, when choosing neighbouring spots). The LEEM-IV characteristics are shown in Fig. 4.35 (as a sum of all domains) for 900 K and 1000 K. The LEEM-IV curves are showing nicely the characteristics of the final of iron silicate structure, as seen already in the earlier presented preparation methods in chapters 4.1 and 4.2.1. Since, the domains with (2x2) structure are very small and in much lower concentration as the iron silicate domains, the presented LEEM-IV curves (Fig. 4.35) account to iron silicate only. All characteristic peaks at 7.5 eV, 13 eV and 20.4 eV are present and moreover both dips at 4.5 eV and 5.5 eV. For 900 K and 1000 K a MEM-LEEM border of 3.18 eV and 3.09 eV, respectively are measured. This fits nicely to similar temperatures for the "stepwise preparation" method in section 4.1.1. The chemical XPS data for 900 K and 1000 K are very similar. The Si 2p line shows that silicon remains in the Si^{4+} state. The Si-O-Si bond is the strongest component in the O 1s for surface sensitive photon energies (600 eV). The Fe-O-Fe/Fe-O-Ru line has a much lower intensity of the Si-O-Si bond. However, at a photon energy of 780 eV both lines have nearly same intensity. This again is a sign of the two-layer system with silicon-dioxide on

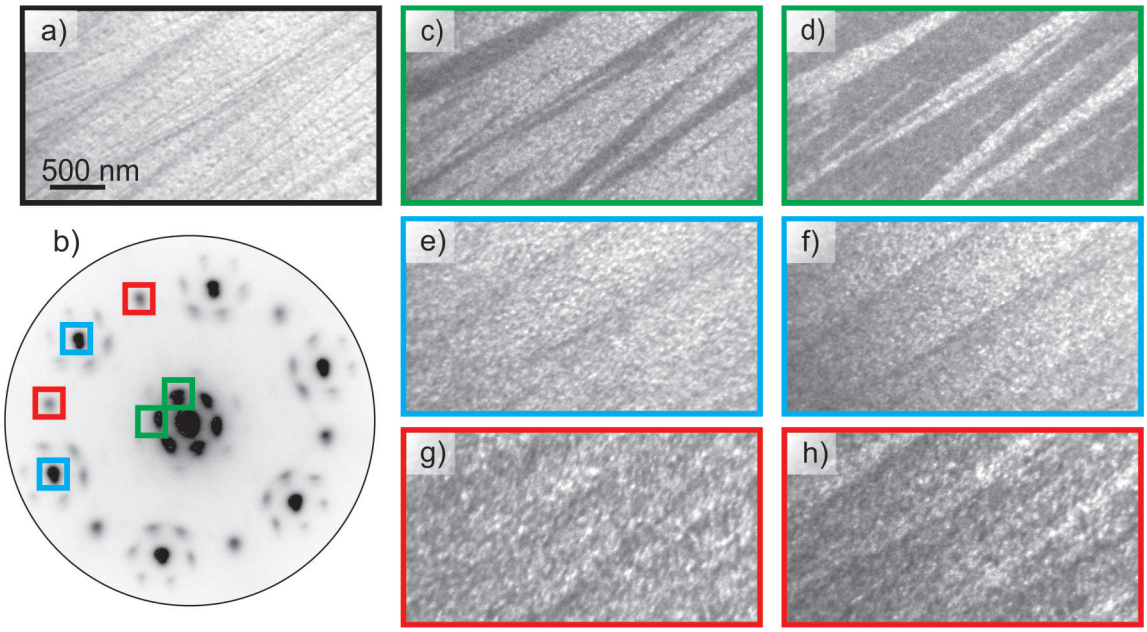

Figure 4.39 Dark field analysis of iron silicate oxidized at 900 K prepared with the "stepwise reversed preparation" method ($Fe/SiO_2/Ru(0001)$). LEEM image at 20 eV (a), LEED image at 20 eV (b) and dark field analysis at 21 eV (c-h) using the in b) indicated spots anticlock-wise.

top of iron oxide. The Fe-O-Si bond between the two layers is present. The Fe 3p line shows as main component Fe^{3+} and moreover Fe^{2+} components. The Fe^{2+} component is decreased at 1000 K in contrast to the XPS spectra at 900 K. At 1000 K the $(\sqrt{3}\times\sqrt{3})R30°$ LEED spots decrease in intensity. The XPS O 1s, as well as Fe 3p line show a small decrease of the iron component. This indicates iron dissociation from the surface.

Summary of the formation process for the "stepwise reversed preparation" method

The formation process of iron silicate with the "stepwise reversed preparation" method is depicted in Fig. 4.40. The basis is a monolayer of silica on the Ru(0001) substrate (Fig. 4.40a). Iron is deposited at RT in $2.0 \cdot 10^{-7}$ mbar (Fig. 4.40b). After the depoistion iron is already oxidized in the Fe^{2+} and Fe^{3+}. The silica layer is unchanged with silicon atoms in the Si^{4+} state. Moreover XPS O 1s measurements indicate that no Si-O-Fe bond is established. The film is oxidized in $1.0 \cdot 10^{-6}$ mbar at RT, 900 K and 1000 K. At 525 K the Moiré pattern typical for iron oxide on Ru(0001) is formed, which indicates a diffusion of iron to the interface (Fig. 4.40c). From the silica layer no spots are found. At 825 K (2x2) spots and $(\sqrt{3} \times \sqrt{3})R30°$ appear. Both pattern correspond to silica. The (2x2) pattern corresponds to the inital silica monolayer on Ru(0001) and the $(\sqrt{3} \times \sqrt{3})R30°$ to iron silicate formation (Fig. 4.40d). In the XPS O 1s line also Si-O-Fe bonds are present. Dark field analysis indicates that the domain size is in the range of 100 nm, respectively. With an oxidation temperature of 1000 K the transformation of the strongly bound silica monolayer (+Fe) towards iron silicate is enhanced until nearly all domains transformed to iron silicate layer.

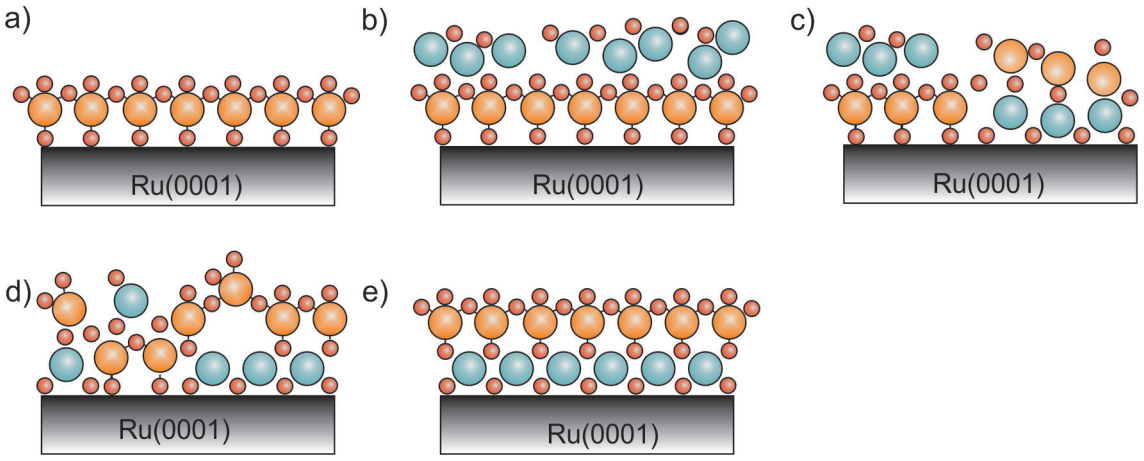

Figure 4.40 Iron silicate formation process using the "stepwise reversed preparation" method ($Fe/SiO_2/Ru(0001)$). a) Silica monolayer. b) Iron deposition at RT in $2.0 \cdot 10^{-7}$ mbar. Silicon remains in the Si^{4+} state, iron is in the Fe^{2+} and Fe^{3+} state. No Si-O-Fe bond present. c-e) Oxidation in $1.0 \cdot 10^{-6}$ mbar. c) Oxidation at 525 K. Iron diffuses underneath the silica layer and orders in a "8 on 9" Moiré pattern. Silica on top is disordered. Domains with silica bound to Ru remain. d) Oxidation at 825 K. Transformation of more silica domains (with Fe) to iron silicate. Silica on top of iron oxide orders in form of a $(\sqrt{3} \times \sqrt{3})R30°$ pattern. e) Oxidation at 1000 K. Homogeneous layer of iron silicate nearly reached. Red: Oxygen. Violet: Iron. Yellow: Silicon.

4.2.3 Summary of the "stepwise" approach

In this chapter it is shown that iron silicate can be prepared with a "stepwise" approach, i.e. the transformation of either a ML of FeO (section 4.2.1) or a ML of SiO_2 (section 4.2.2) to iron silicate by addition of silicon or iron, respectively. The resulting fingerprints match the ones found for the "combined" approach in chapter 4.1. This shows that ultrathin iron silicate is the energetically most stable phase. In table 4.6 an overview of the necessary temperatures for the formation of Moiré and the $(\sqrt{3} \times \sqrt{3})R30°$ spots, as well as the necessary temperature to fit the iron silicate fingerprint are given.

In section 4.2.1 a ML of FeO is used as a basis in the so-called "stepwise preparation" method. The FeO monolayer is oxygen terminated and arranged in a "6 on 7" configuration on Ru(0001) (more details are discussed in chapter 3.1). The iron silicate layer can be described as a two-layered system with a silica monolayer on top of an iron oxide layer, which is FeO-like. Thus, this preparation method enables to investigate how the iron oxide layer must be modified in order to match the iron oxide layer as part of iron silicate. With silicon deposition the Fe-O bonds are broken in favor of Si-O-Si and Si-O-Fe bonds and the Moiré pattern disappears. The reason is the large bond dissociation energy of the Si-O bond of 798 kJ/mol. The bond dissociation energy of Fe-O and Ru-O is 409 kJ/mol and 481 kJ/mol, respectively [2]. Thus, the system gains energy by forming Si-O bonds instead of Fe-O bonds. Already at 460 K the Moiré pattern recovers, however the Fe-O-Fe bonds are minimized to a "8 on 9" reconstruction, fitting to the optimal Si-O-Si bond length [67]. This shows that the silica layer on top has a major influence on the FeO-like layer underneath. In a pure FeO ML iron is in the Fe^{2+} oxidation state. In contrast in iron silicate

	Stepwise	**Stepwise reversed**
preparation	Monolayer FeO +Si at RT in $2.0 \cdot 10^{-7}$ mbar	Monolayer SiO_2 + Fe at RT in $2.0 \cdot 10^{-7}$ mbar
	Si/FeO/Ru(0001)	Fe/SiO_2/Ru(0001)
Necessary T	900 K	1000 K
Appearance of Moiré spots	645 K	525 K
Appearance of $(\sqrt{3} \times \sqrt{3})R30°$ spots	460 K	825 K
Strongest intensity rise of Moiré spots	660 K	900 K
Strongest intensity rise of $(\sqrt{3} \times \sqrt{3})R30°$ spots	660 K	900 K

Table 4.6 Temperature dependencies of preparation methods using the "stepwise" approach. The $(\sqrt{3} \times \sqrt{3})R30°$ structure refers to a silica structure that is rotated by 30° regarding a complete iron oxide layer.

most iron atoms are found in the Fe^{3+} oxidation state. The Fe^{3+}:Fe^{2+} ratio increases with oxidation time and temperature. The reason is assumed to be oxygen intercalation to the iron/ruthenium interface. The necessary energy for iron silicate formation is strongly reduced regarding the "combined preparation" method (section 4.1.1).

The fingerprint for the "stepwise preparation" method at 660 K is the same as for the "combined preparation" method at 800 K. The reason is assumed to be the pre-ordering of the iron-oxide layer and the fact that no Si-O-Si bonds need to be broken before iron silicate arranges. At temperatures higher than 660 K a small reduction of iron is found with increased oxidation temperature. This indicates that the final iron silicate layer has lower iron content as the pure FeO layer. In chapter 4.1 it was discussed, whether three (as in FeO) or only two iron atoms per silica unit cell are present in iron silicate. The measured reduction of iron is an indication that only two iron atoms per silica unit cell are likely. However, the iron reduction is too low to be certain. In the same temperature range in the LEEM-IV curve a dip at 5.5 eV develops. The rest of the LEEM-IV spectra (between 6.5 and 30 eV) is unchanged, apart from an intensity increase of the individual peaks. If the iron content is reduced in order to form iron silicate, also the LEEM-IV fingerprint should be varied. Since the dip at 5.5 eV is the only visible change, it seems to be a good measure for the condition of the iron silicate film.

The "stepwise reversed preparation" method in section 4.2.2 has shown that iron silicate is energetically favoured, even if a well-prepared monolayer of silica is present before iron deposition. As already assumed, the (thermal) energy to form iron silicate is much higher than in other preparation methods and in particular 30 K higher than for the disordered silicon layer in the "combined preparation" method (see section 4.1.2). Thus, a broken Si-O bond needs much higher energies (or temperatures) as a broken Fe-O bond, as it would be the case for the "stepwise preparation" (section 4.2.1) and the "combined UHV

preparation" method (section 4.1.2). The transformation process from silica (with iron) to iron silicate is starting everywhere on the surface in small domains. This confirms that Si-O-Si bonds or Si-O-Ru bonds need be broken, before iron silicate can be formed. The necessary oxidation temperature for the characteristic iron silicate fingerprint is 1000 K, similar as for the "combined preparation" method.

4.3 Multiple layers

In the previous chapters 4.1-4.2 iron silicate layers proved to be stable with different preparation methods. Irrespective whether silicon and iron were deposited together or whether FeO or SiO_2 was pre-prepared, the resulting final film was identical. Iron silicate is a two-layer film with an FeO-like monolayer on top of Ru(0001) giving rise to a Moiré pattern, and a silica monolayer on top. In LEED by 30° rotated spots are present. As discussed in section 4.1.3 these might either arise from silica arranged in a $(\sqrt{3} \times \sqrt{3})R30°$ structure relative to a complete iron oxide layer (three iron atoms per silica unit cell) or in case of two iron atoms per silica unit cell, from the position of the "missing" iron atoms in respect to a complete layer. The individual preparation methods influenced the order of ideal layer formation (first FeO vs. first SiO_2) and the necessary temperatures (activation energy) to form the final film differed strongly. The "stepwise preparation" method proved optimal for the iron silicate formation, since the preordered FeO layer decreases the necessary activation energy (temperature) strongly. Apart from the pre-given structure of the iron oxide layer, no energy is necessary for diffusion of iron and more importantly, no silicon dioxide bonds need to be broken in order to form Fe-O-Si bonds (see sections 4.1.1 and 4.2.2). In the “stepwise preparation” method, first FeO is prepared by iron deposition at elevated temperatures (800 K). The preparation of the FeO layer is described in detail in chapter 3. At RT silicon is deposited, and subsequently the film is oxidized up to 900-1000 K.

In the following chapters the iron or silicon amount is increased. Since only one of the two elements is varied the results can be well compared to the pure iron silicate layer from section 4.2.1.

In section 4.3.1 a bilayer of FeO is used as basis for iron silicate formation. With this the influence of the Ru(0001) substrate is smaller. In section 4.2.1 it was found that the silica monolayer stabilizes the underlaying FeO layer to much higher temperatures than without silicon (compare section 3.1). The reason is most likely the strong Fe-O-Si bond. The Moiré pattern of iron silicate indicates a smaller Fe-Fe distance in the iron oxide layer as part of iron silicate (3.044 Å) versus the freshly prepared FeO layer (3.157 Å). Thus, the silicon layer has a strong influence on the underlying iron atoms. In section 4.3.1 two layers of FeO are present. Thus, it will be investigated how strong the influence of the silica layer is on the second FeO layer. One possibility might be a weak influence. As a result the second FeO layer might dissolve and the iron atoms could evaporate. Moreover the Moiré pattern is defined by the superposition of iron atoms on top of Ru(0001) atoms. In case the second layer is disordered or remains in the original "6 on 7" arrangement this should be visible in the LEED pattern. Furthermore, the arrangement of silicon is of interest.

In section 4.3.2 the silicon amount necessary to form a bilayer of SiO_2 is deposited on a monolayer of FeO. Here the question arises how strong the Fe-O-Si bond is. A pure silica monolayer on Ru(0001) is strongly chemically bound to the substrate, whereas a bilayer is

only Van der Waals-bound and lifts up from the substrate [107]. For metal single crystals it was found that the metal-oxygen bond decides whether a strongly bound monolayer or a physisorbed silica bilayer is formed [89, 109]. Molybdenum has a high heat of dissociative adsorption of O_2 (554 kJ/mol). On Mo(112) only a silica monolayer is formed. In contrast Pt has a low heat of dissociative adsorption of O_2 (133 kJ/mol). On Pt(111) only a silica bilayer is formed independent of the deposited material. On Ru(0001) both, monolayer and bilayer exist and the heat of O_2 dissociative adsorption is intermediate (220 kJ/mol). In this work an ultrathin layer of FeO can be seen as the "substrate" for silicon deposition. Its heat value of O_2 dissociative adsorption is 534 kJ/mol and thus very similar to Mo. Hence, only monolayer formation is expected. The given values for heat of O_2 dissociative adsorption are taken from [75]. In the presented study it will be of interest how strong the Si-O-Fe bond is and how the influence on the additional material is. It might be that iron silicate is formed with a monolayer of silica only and the second layer separates from this layer. The iron oxide layer should thus fit in its Fe-Fe dimensions to the iron silicate films presented in chapters 4.1-4.2. It will also be interesting how the silicon layer orders in this scenario. It might either follow the underlying silica layer or form a different structure. Alternatively the additional silicon material might also bind to the iron oxide layer in form of two or three strongly bound silica layer on iron oxide. Moreover a variation in the necessary energy (temperature) might be possible, since a pure silica bilayer needs clearly higher temperatures (1100 K), when formed on Ru(0001). Since iron is catalytically reducing the silicon oxidation temperature, the iron silicate formation needs much lower temperatures. It will be interesting whether this is also true for a higher silicon amount.

4.3.1 Stepwise (bilayer FeO) preparation

This chapter concentrates on the iron silicate formation on the basis of a bilayer of FeO using the "stepwise preparation" method. For this a bilayer of FeO is prepared by iron deposition at 800 K in $1.0 \cdot 10^{-7}$ mbar. At these conditions FeO is formed in a layer-like growth, so that the closed layer can be easily estimated. Moreover XPS results showed not only an Fe^{2+} component but also an Fe^{3+} component. As a result the grown bilayer of FeO (as is visible by the structure in LEED) has an additional oxygen layer (assumed as oxygen-iron-oxygen-iron-oxygen-layer). Further information is given in section 3.2. At RT a monolayer of silicon is deposited in $2.0 \cdot 10^{-7}$ mbar. Afterwards the film is oxidized in $1.0 \cdot 10^{-6}$ mbar. For better clarification the preparation in this chapter is addressed to as "iron(bilayer) silicate", while the preparation from section 4.2.1 with a monolayer of FeO is addressed to as "iron(monolayer) silicate". In both cases the "stepwise preparation" method is used, which includes the preparation of well-ordered FeO first, before silicon is deposited at RT.

The data shown here are taken from an intermixed FeO template with bilayer and monolayer FeO domains. The whole surface is closed with FeO. The bilayer FeO phase is considerably larger than the monolayer areas. Thus, the measured characteristics correspond mainly to the bilayer-thick FeO domains. The LEEM-IV curves are taken solely from the bilayer-thick iron silicate areas (Fig. 4.43), while the LEED images and XPS curves are a superposition of both domains. The monolayer-thick iron silicate areas show the expected behavior from section 4.2.1 and are not further discussed. The analysis in this section will correspond to the iron(bilayer) silicate areas.

In Fig. 4.41 the LEED images for the individual preparation steps are shown. The temperature dependent intensity behavior of the (00), a Moiré and a $(\sqrt{3} \times \sqrt{3})R30°$ spot are depicted in Fig. 4.42. The individual LEEM-IV curves are shown together with their enlarged energy range for MEM-LEEM transition in Fig. 4.43a and b, respectively. The energy values of the MEM-LEEM transition and their graphical curve are given in Fig. 4.44. XPS curves of the O 1s at 600 eV and 780 eV are shown in Fig. 4.45a and b, the Fe 3p line at 175 eV and 350 eV in Fig. 4.45c and d and the Si 2p line at 175 eV and 350 eV in Fig. 4.45e and f, respectively. The individual XPS lines are given for a surface sensitive kinetic energy of 70 eV (for Fe 3p: 120 eV) and a less surface sensitive kinetic energy of 250 eV (for Fe 3p: 295 eV). The O 1s line can be de-convoluted into three components: Fe-O-Fe at 529 eV, Fe-O-Si at 530 eV and Si-O-Si at 531 eV. The individual contributions are shown for different temperatures in Fig. 4.46.

The LEED pattern of the bilayer-thick FeO template is given in Fig. 4.41a. The typical Moiré pattern for FeO with higher order spots is visible. The Moiré pattern shows a "6 on 7" reconstruction, meaning that six iron atoms fit commensurably on seven ruthenium atoms. The Moiré spots arise due to the fact that the lattice constants of iron oxide and ruthenium are quite similar. In fact in the "6 on 7" reconstruction the lattice constants differ by 16 percent.

A silicon amount equal to a monolayer of silica is deposited at RT in $2.0 \cdot 10^{-7}$ mbar of oxygen. In LEED the Moiré spots surrounding the (00) spot of the underlying iron-oxide layer remain (see Fig. 4.41b) and their distances to the (00) spot do not change. The LEEM-IV curve in Fig. 4.43 exhibits the characteristics for a disordered silicon layer with peaks at 6.6 eV and 12.5 eV. Their intensity referred to the intensity of MEM (energies

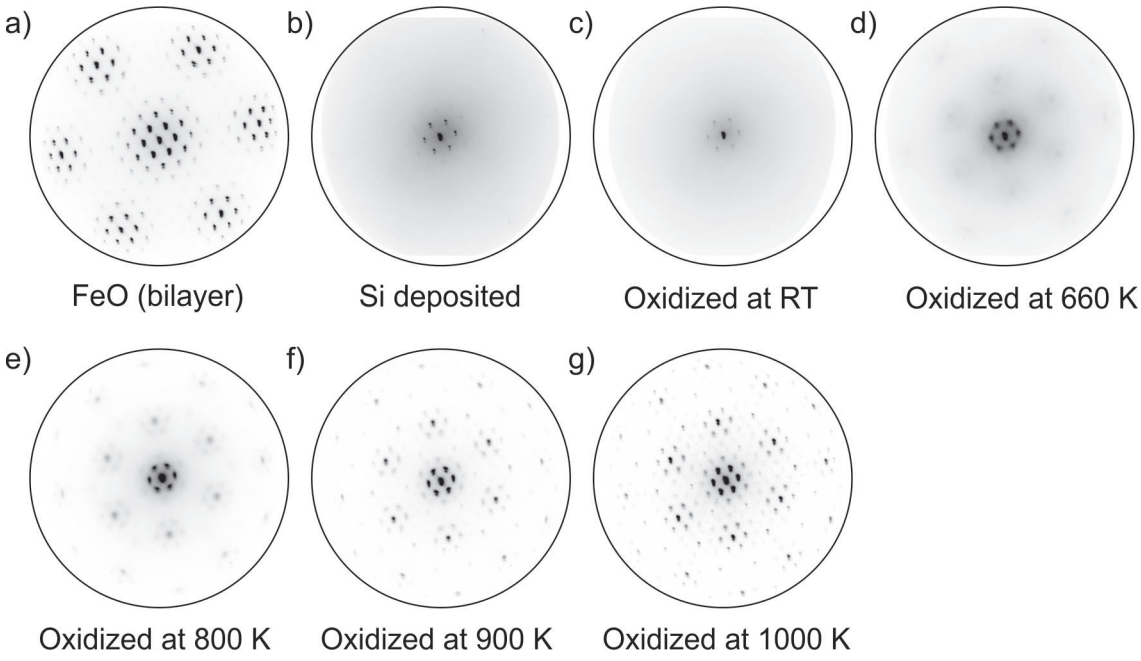

Figure 4.41 LEED study of individual preparation steps of an iron(bilayer) silicate film (ML SiO_2/BL FeO/Ru(0001)). The FeO layer is prepared by iron deposition at 800 K in $1.0 \cdot 10^{-7}$ mbar. Si is deposited in $2.0 \cdot 10^{-7}$ mbar and the oxidation steps in $1.0 \cdot 10^{-6}$ mbar. The LEED images are taken at RT and 42 eV.

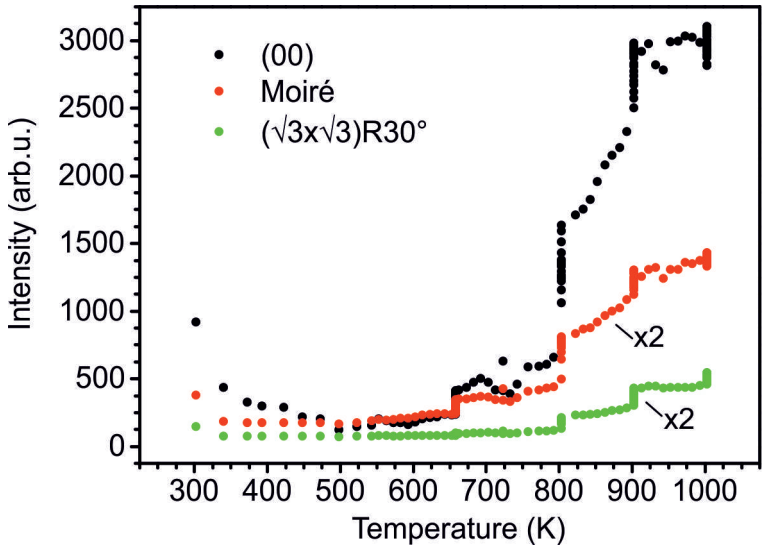

Figure 4.42 Spot intensities of the (00), Moiré and $(\sqrt{3} \times \sqrt{3})R30°$ spots during the oxidation in $1.0 \cdot 10^{-6}$ mbar of an iron(bilayer) silicate film (ML SiO_2/BL FeO/Ru(0001)). The $(\sqrt{3} \times \sqrt{3})R30°$ structure refers to a silica structure that is rotated by 30° regarding a complete iron oxide layer. Several steps at a specific temperature indicate how the intensity behaves while keeping the temperature constant.

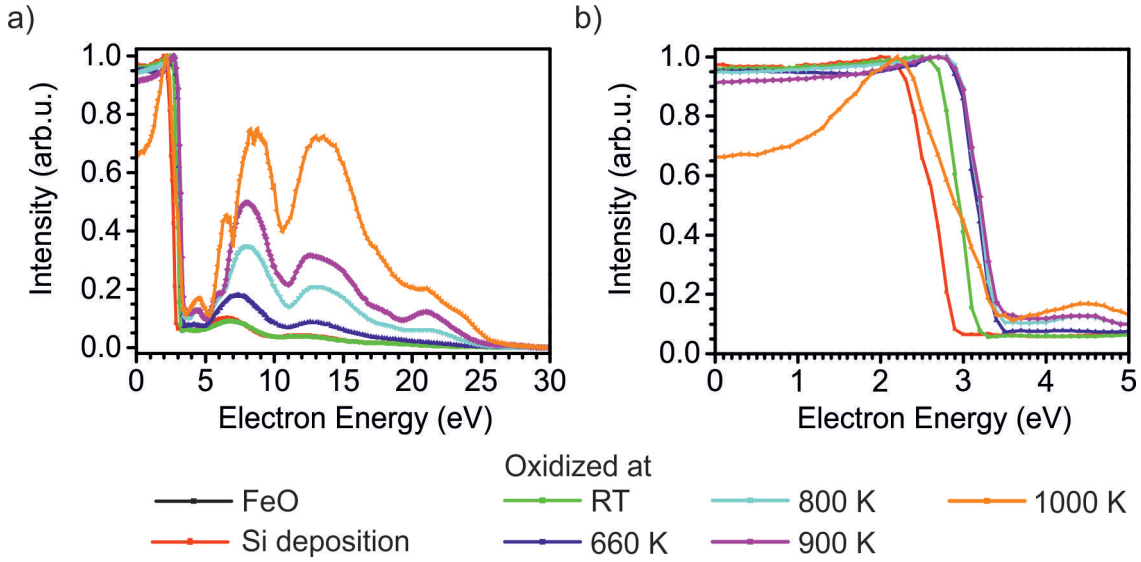

Figure 4.43 LEEM-IV curve for the individual preparation steps of a iron(bilayer) silicate film (ML SiO_2/BL FeO/Ru(0001)). The individual curves are measured at RT.

≤2.6 eV) is much weaker than for iron(monolayer) silicate films at the same preparation step. The MEM-LEEM transition energy increased by 0.2 eV to 2.61 eV, most likely due to the additional oxygen (clean Ru(0001): 2.58 eV). The XPS analysis is given in Fig. 4.45. The surface sensitive O 1s spectrum ($h\nu = 600$ eV) consists of three components: Fe-O-Fe at 529 eV, Fe-O-Si at 530 eV and Si-O-Si at 531 eV. The strongest component is the Fe-O-Si line. Thus, the silicon atoms form directly bonds to the underlying iron-oxide layer. During this process the iron atoms are not reduced, as it was the case for iron(monolayer)-silicate. The Fe-O-Fe line is clearly observable. This indicates that interlayer oxygen atoms must

Preparation step	Energetic position of the MEM-LEEM border (eV)	Workfunction (eV) (referenced to clean Ru(0001) with 5.44 eV [12])
FeO bilayer	2.41	5.27
Si deposition	2.61	5.47
Oxidation at RT	2.94	5.80
Oxidation at 660 K	3.15	6.01
Oxidation at 800 K	3.17	6.02
Oxidation at 900 K	3.18	6.03
Oxidation at 1000 K	2.79	5.65

Table 4.7 Overview on the MEM-LEEM border evolution for the individual preparation steps of iron(bilayer) silicate (ML SiO_2/ BL FeO/ Ru(0001)). The MEM-LEEM values are measured with an accuracy of ± 0.02 eV.

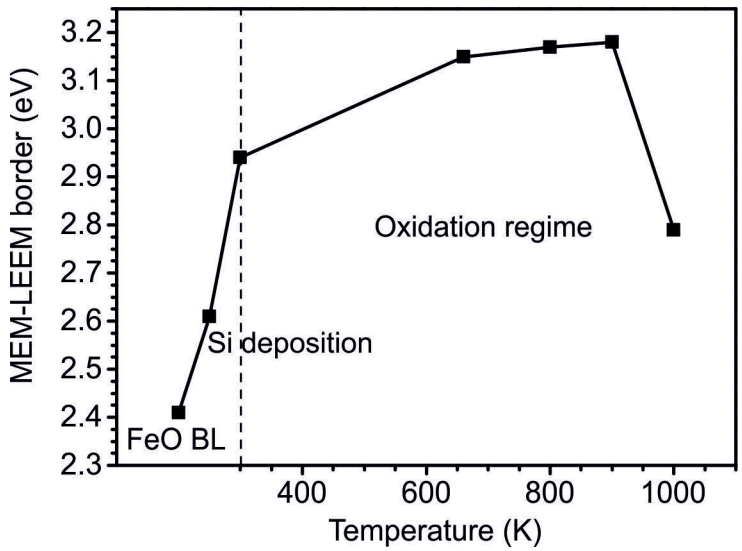

Figure 4.44 MEM-LEEM border for the individual preparation steps of an iron(bilayer) silicate film (ML SiO_2/BL FeO/Ru(0001)). The Si deposition is performed in $2.0 \cdot 10^{-7}$ mbar, the oxidation steps at $1.0 \cdot 10^{-6}$ mbar. The MEM-LEEM values are determined by a fit of the MEM-LEEM border presented in Fig. 4.43b. The error of this fit is ± 0.02 eV.

exist and be able to oxidize the first iron oxide layer. As the still visible Moiré spots indicate, the second layer is most likely unchanged. Using a less surface sensitive photon energy of 780 eV the high iron oxide amount is visible. The Si-O-Si line is clearly less intense than the Fe-O-Si and Fe-O-Fe components. In the Fe 3p line Fe^{2+} and Fe^{3+} components are present, but slightly damped due to the additional silicon layer. Finally, the Si 2p line shows that silicon is completely oxidized to the Si^{4+} state. The FWHM is relatively broad with 2.05 eV, which might correspond to the disordering of the silicon atoms. Taken all these results into account, it is found that silicon atoms bind directly to the iron atoms underneath in a Fe-O-Si bond. Due to the oxygen atoms on top of the iron oxide layer, and the available oxygen in the surrounding silicon is completely oxidized, but disordered. The second FeO layer is unchanged as shown by the still visible Moiré spots. In contrast to the

iron(monolayer) silicate preparation, iron is not reduced during this step. This indicates that a sufficient amount of oxygen atoms must be present in the iron-iron interlayer.

After silicon is deposited the film is oxidized in hν mbar at RT for 15 min. The influence of oxygen can be disentangled from the temperature influence at this step. The Moiré pattern in Fig. 4.41c becomes less intense and the distance to the (00) spot becomes smaller. In fact, a rearrangement of iron atoms must take place during the oxidation, as now a "7 on 8" Moiré pattern is seen. The distances between the iron atoms decrease from 3.157 Å ("6 on 7") to 3.093 Å ("7 on 8"). The MEM-LEEM border increases strongly by 0.3 eV to 2.94 eV. Apart from this shift the LEEM-IV curve is unchanged. The O 1s line shows an increase in the Fe-O-Si line. Most likely the silicon atoms, binding more and more to iron, support the decrease in the Fe-Fe distances. The Fe 3p line shows an increase in the Fe^{3+} component, accompanied with a slight decrease of the Fe^{2+} component. Thus, iron atoms become more strongly oxidized by the surrounding oxygen. Using the less surface sensitive energy of hν = 350 eV it becomes evident that mainly the Fe^{2+} line is decreased in comparison to the last preparation step. Thus, also in the second iron-oxide layer a higher oxidation state is reached. The FWHM is slightly decreased to 1.98 eV (-0.07 eV).

The increase of available oxygen during this preparation step enhances the number of Si-O-Fe bonds. This and the freshly available oxygen atoms lead to an adaption of the iron-oxide layer underneath by minimizing their Fe-Fe distances. An intercalation of the oxygen atoms to the second iron oxide layer is possible and leads to an increase in the Fe^{3+} line intensity (with a corresponding decrease in Fe^{2+} state). Since only one kind of Moiré spots is present, it can be assumed that the second iron oxide layer does equally decrease their Fe-Fe distances. The oxidation leads furthermore to a strong increase in the MEM-LEEM border, which indicates a stronger surface dipole and increased presence of oxygen atoms at the surface. In the iron(monolayer) silicate the MEM-LEEM border was only increased by half this value (0.14 eV) during the oxidation at RT. This again indicates the oxidation in both iron oxide layers, so that also the second iron oxide layer has an impact on the overall surface dipole.

The film is oxidized at 660 K in $1.0 \cdot 10^{-6}$ mbar of oxygen for 30 min. At 660 K (Fig. 4.41d) a $(\sqrt{3} \times \sqrt{3})R30°$ pattern develops. First the spots are very blurry, and after 10 min additional Moiré spots surrounding these $(\sqrt{3} \times \sqrt{3})R30°$ form. The $(\sqrt{3} \times \sqrt{3})R30°$ corresponds to the formation of an ordered silica structure. The Moiré pattern surrounding the (00) spot was present during the complete oxidation process. The distances of the Moiré spots to the (00) spot are further decreased and indicate a "8 on 9" reconstruction, i.e. the Fe-Fe distance of 3.044 Å. As a result, the distances and LEED spots mirror the one of iron(monolayer)-silicate. The MEM-LEEM border increases further to 3.15 eV (+ 0.2 eV). In LEEM-IV two pronounced peaks at 7.3 eV and 13 eV exist, which are at similar positions as for iron(monolayer) silicate. However the characteristic peak at 4 eV is missing. In XPS, the intensity of O 1s line (see Fig. 4.46), corresponding to the Si-O-Si bonding increases strongly during this oxidation step. This fits to the formation of the $(\sqrt{3} \times \sqrt{3})R30°$ structure as observed in LEED. There is a slight increase in the O1s line corresponding to the Fe-O-Si bonding, but no change in the Fe-O-Fe line. This shows that the iron-oxide layer is not only ordered but also optimally oxidized (saturated). At 780 eV (Fig. 4.45b) the intensity of the Si-O-Si line is still lower than the Fe-O-Si and Fe-O-Fe component. Thus, the two layers of iron oxide are still present. The Fe 3p line (Fig. 4.45c) shows an increase in the Fe^{3+} component, while the Fe^{2+} line is decreased. Even though silicon begins to re-arrange (as seen in LEED), the FWHM of the Si 2p line remains nearly unchanged at

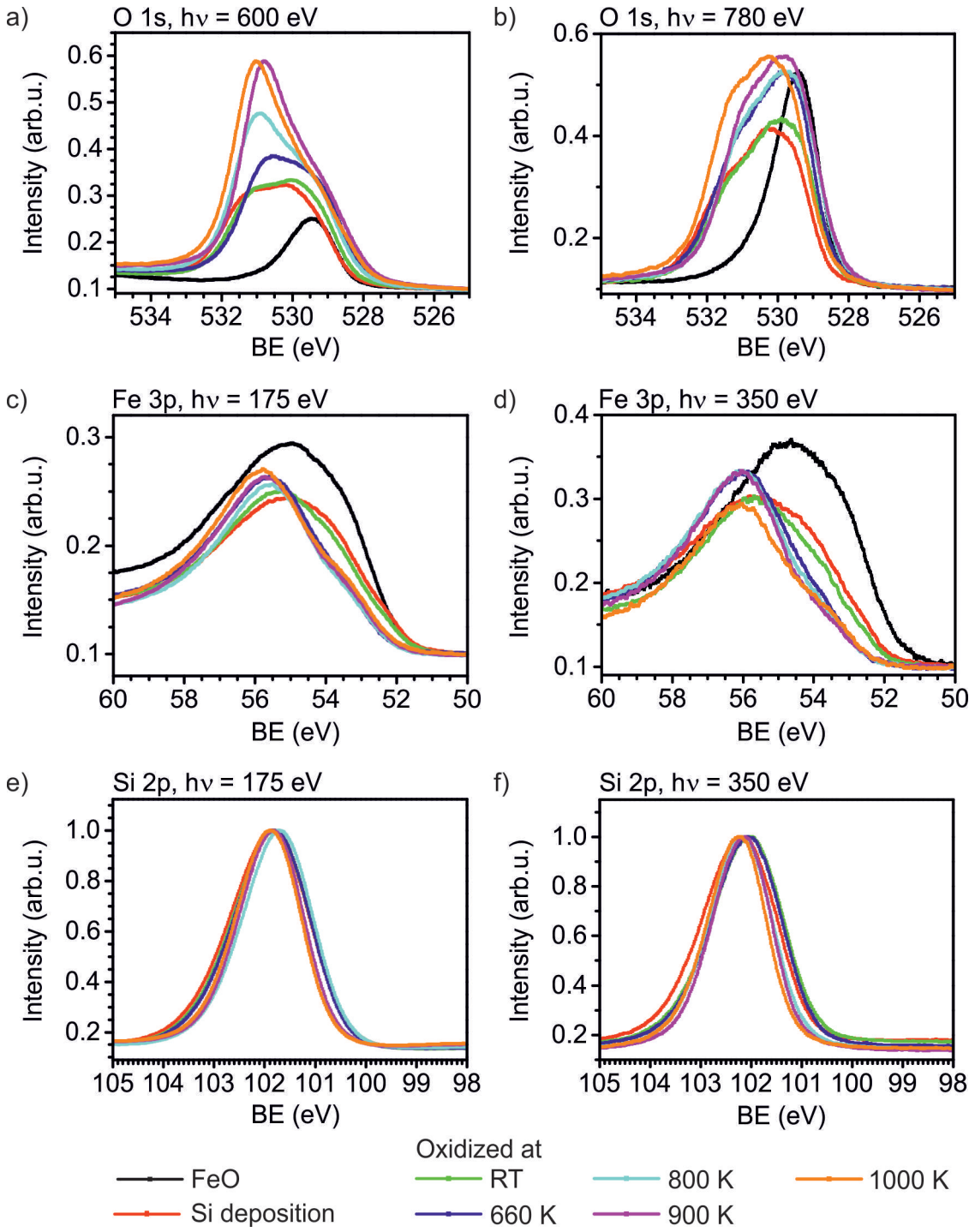

Figure 4.45 Temperature dependent XPS analysis of an iron(bilayer) silicate film (ML SiO_2/ BL FeO/Ru(0001)). O 1s line for a photon energy of a) 600 eV and b) 780 eV. Fe 3p line for a photon energy of c) 175 eV and d) 350 eV. Si 2p line for a photon energy of e) 175 eV and f) 350 eV. The measurements are taken at RT.

1.95 eV. As a conclusion, during the oxidation at 660 K mainly the silica layer starts to form. This is visible by the increase in the Si-O-Si line and the formation of LEED spots at the $(\sqrt{3} \times \sqrt{3})R30°$ position. At the same time, the Fe-Fe distance of the iron oxide

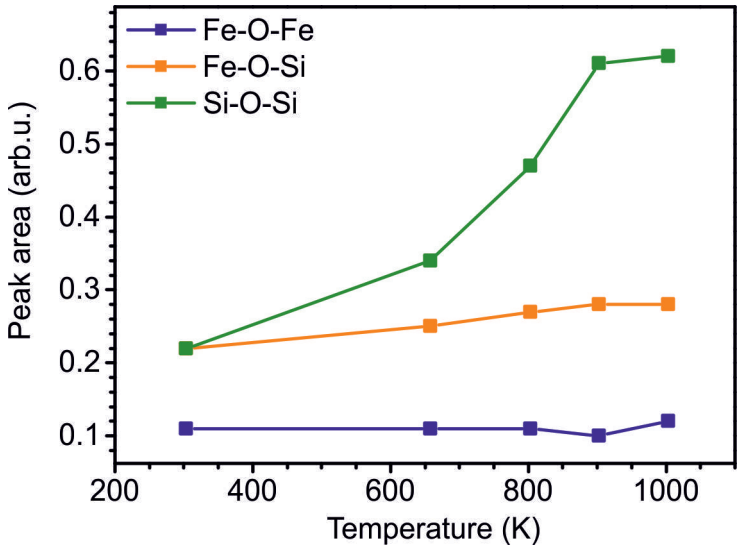

Figure 4.46 Evolution of the Fe-O-Fe, Fe-O-Si and Si-O-Si components of the O 1s line at 600 eV (Fig. 4.45 a) of an iron(bilayer) silicate film (ML SiO_2/BL FeO/Ru(0001)).

layer is decreased to 3.044 Å ("8 on 9" reconstruction). Most iron atoms are now in the Fe^{3+} state. At this step the structure resembles strongly that of iron(monolayer) silicate.

Subsequently, the film is oxidized at 800 K in $1.0 \cdot 10^{-6}$ mbar for 15 min. During the annealing process the $(\sqrt{3} \times \sqrt{3})R30°$ spots become more intense (at around 770 K) (see Fig. 4.41e). At 800 K the intensity rises for all LEED spots. For the (00) spot and the Moiré spots surrounding the (00) spot this is the strongest intensity increase (see Fig. 4.42). The Moiré spots correspond to the ordering of the iron oxide layer underneath. Thus, at this temperature the arrangement of the atoms in the iron silicate layer is optimized. The MEM-LEEM border remains unchanged, but the peaks at 8 eV and 13 eV are much more pronounced. Thus, the structure becomes better ordered. Additionally, a peak at 21.1 eV is visible. Moreover, a new peak arises at low energies (4.3 eV), which is accompanied by dips at 3.8 eV and 5.0 eV. Additionally a shoulder at 5.9 eV develops. In the O 1s XPS components (Fig. 4.46) the trend visible at 660 K continues: The Si-O-Si line increases strongly, while the Fe-O-Fe line is unchanged. Both layers of iron-oxide are still present as is visible in the lower Si-O-Si line (in contrast to the Fe-O-Si and Fe-O-Fe line), when using the less surface sensitive photon energy of 780 eV (Fig. 4.45b). In the Fe 3p line no change is observed. Moreover the FWHM of the Si 2p line is decreased by 0.1 eV to 1.85 eV, which indicates a better homogeneity of the silica layer. In this oxidation step mainly the silicon atoms arrange, as is visible by the increased Si-O-Si line and improved LEED spots. The iron oxide layer seems to be rather unchanged in its oxidation level. However, the strong increase in the Moiré pattern (surrounding the (00) spot) indicates an improved iron ordering (Fig. 4.41e). The second iron oxide layer still exists.

Subsequently the sample is oxidized at 900 K in $1.0 \cdot 10^{-6}$ mbar for 15 min. The LEED pattern is given in Fig. 4.41f). During this process all LEED spots become sharp and intense A Moiré pattern is visible, together with $(\sqrt{3} \times \sqrt{3})R30°$ spots (assigned to the iron oxide layer). All these spots were present for the iron(monolayer) silicate films, too. Additionally, a new pattern is visible: a (3x3) structure relative to the iron oxide spot (not the Ru substrate). A further discussion of this superstructure is given later in this

chapter. The MEM-LEEM border as well as the peak positions of the LEEM-IV curve are unchanged (Fig. 4.43). Only the peak intensity is enhanced, indicating again a better homogeneity. The O 1s curve (Fig. 4.46) shows a strong Si-O-Si enhancement, which indicates an improved arrangement of the silicon layer. This correlates with the decreased FWHM of the Si 2p (Fig. 4.45e) line by 0.16 eV (now: 1.69 eV). The Fe 3p line (Fig. 4.45c) is rather unchanged. As a conclusion, at this temperature on one hand the iron oxide layer is unchanged. On the other hand the silica layer optimizes further.

The oxidation at 1000 K enhances the intensity and sharpness of all spots (see Fig. 4.41g). The MEM-LEEM border (Fig. 4.44) decreases to 2.79 eV. The LEEM-IV peaks (Fig. 4.43a) mentioned before are further enhanced and the prior shoulder at 5.9 eV separates as a peak. In XPS, the O 1s line (Fig. 4.45 a) is unchanged in intensity and shape, but slightly shifted. This might be a result of the observed work function shift. The Si 2p line (Fig. 4.45 e) is also unchanged. In the Fe 3p line (Fig. 4.45c) at $h\nu = 175$ eV the Fe^{3+} component is slightly increased. Using a less surface sensitive photon energy of 350 eV the Fe^{3+} signal is smaller (Fig. 4.45d). This shows that the Fe^{3+} component is present mainly close to the surface (first iron oxide layer).

Summary and conclusion of the formation process of iron(bilayer) silicate

In summary, stable iron(bilayer) silicate exists. The LEED pattern is a combination of the a "8 on 9" Moiré reconstruction, a $(\sqrt{3} \times \sqrt{3})R30°$ and additionally a (3x3) structure. The LEEM-IV fingerprint and the intensity of the O 1s XPS components in comparison to an iron(monolayer) silicate film indicate that still both iron oxide layers are present. Since only one Moiré pattern is present, it can be assumed that both layers arrange in a similar way. Thus, the silica layer on top decreases the distances of both iron oxide layers from 3.157 Å to 3.044 Å ("6 on 7" reconstruction in the pure FeO bilayer and "8 on 9" reconstruction in the later iron(bilayer) silicate film). Since, these spots are not present in the typical iron(monolayer) silicate pattern (i.e. $(\sqrt{3} \times \sqrt{3})R30°$ pattern and Moiré spots) the (3x3) structure must be a result of the second iron oxide layer. A possible explanation might be that iron atoms diffuse from the two iron layer up to the top. In fact the (3x3) structure fits commensurably to one iron atom in every silica six-fold ring. Either these iron atoms are positioned on top of the silica layer or maybe just underneath as a "third

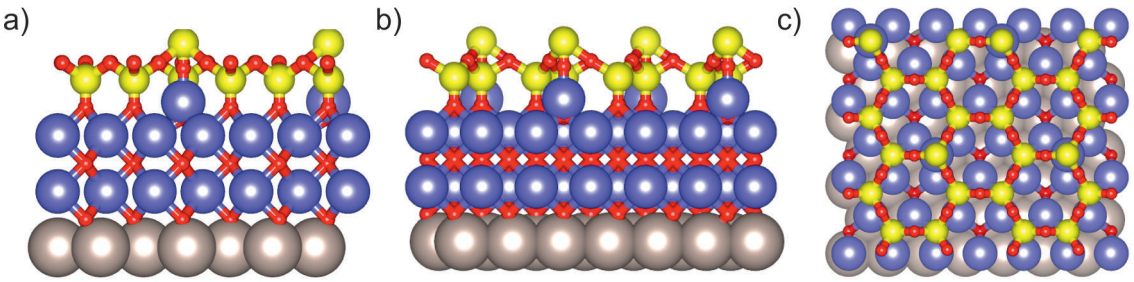

Figure 4.47 Structural model of an iron(bilayer) silicate (ML SiO_2/ ML FeO/ Ru(0001)) film in a) x-direction, b) y-direction and c) z-direction. In this model the iron oxide layer is depicted with three iron atoms per silica unit cell. However, the number of iron atoms per silica unit cell may also be reduced to two. Red: Oxygen. Yellow: Silicon. Violet: Iron. Gray: Ruthenium.

incomplete" iron layer. Since the silica layer can be assumed as a diffusion barrier, the latter seems more likely. A model for this arrangement is given in Fig. 4.47. Here, iron atoms arrange between the last iron oxide layer and the silica layer in a (3x3) structure, i.e. one iron atom per silica six-fold ring. LEED only gives information about the structure of specific layer, but not their translation regarding the other layer. Thus, it cannot be decided whether the iron atom might be positioned in the center of a six-fold silica ring or underneath a silica atom. In the given model in Fig. 4.47 the additional iron atoms are positioned underneath a silica atom. The silica layer follows the iron corrugation underneath, and is thus buckled in form of a (3x3) structure.

In Fig. 4.48 the oxidation and structural arrangement of the individual preparation steps are depicted. Both iron oxide layers remain intact up to 1000 K. At this step it is not clear whether this depends on the border condition (closed layer) or whether incomplete films are also stable. In order to investigate this question further, in section 4.4.3 incomplete layers will be analyzed. Interestingly, the Fe-Fe distances in both iron oxide layers is decreased from 3.157 Å to 3.044 Å, which is the same value as for the iron-oxide layer in iron(monolayer) silicate (see section 4.2.1). This shows that the influence of silica is very strong. Most likely the reason is a combination of the very strong in-layer Si-O-Si bond defining the optimum distances of the silicon atoms, together with a strong Fe-O-Si bond which transfers the in-layer silica bond distance to that of the iron oxide layer underneath. It is found that oxygen supports the change in Fe-Fe distance. Already at RT a rearrangement of the iron atoms is visible. For iron(monolayer) silicate it was found that the deposited silicon layer reduces the iron atoms. As a result silicon is completely oxidized after its deposition. In iron(bilayer) silicate silicon is completely oxidized after deposition as well, but iron is not reduced. This indicates that oxygen might be strongly present between the two iron oxide layer. As a result, oxygen atoms on top can be bound to silicon without a reduction of iron atoms. At 660 K $(\sqrt{3} \times \sqrt{3})R30°$ spoots regarding a complete iron oxide layer apper, which indicates that silica atoms order. Also the iron atoms are already completely oxidized at this temperature and arranged in the "8 on 9" Moiré pattern. For temperatures higher than 850 K an additional superstructure appears with a (3x3) reconstruction regarding the iron atoms.

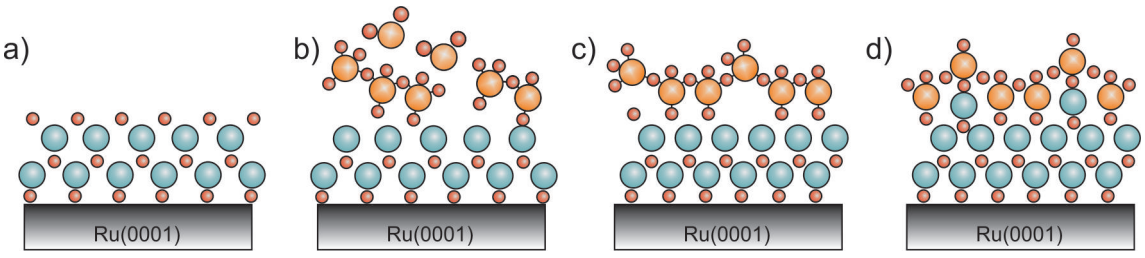

Figure 4.48 Model for the individual steps of iron(bilayer) silicate (ML SiO_2/ BL FeO/ Ru(0001)) using the stepwise preparation method. a) FeO bilayer with "6 on 7" reconstruction. b) after Si deposition. The position of the iron atoms is unchanged. Silicon is disordered and forms Fe-O-Si bonds. c) Oxidation at 660 K. Iron oxide layer with "8 on 9" reconstruction. Si begins to order. Iron is completely oxidized. d) Oxidation at 900 K. Silicon and iron are optimally arranged. The second iron-oxide layer is still present. Additionally a (3x3) reconstruction is present due to iron migration between the first iron oxide layer and the silica film.

4.3.2 Stepwise (bilayer SiO_2) preparation

When silica is prepared directly on a 3O-covered Ru(0001) substrate, the silica monolayer differs strongly from a silica bilayer in their bonding properties. The silica monolayer is very strongly bound to the Ru(0001) substrate, while the silica bilayer is only Van der Waals-bound [107]. As a consequence the silica bilayer lifts off from the substrate and is relatively inert. Lately it was even shown that the silica bilayer can be fully separated from the surface and placed onto another substrate [11]. The strength of the metal-oxygen bond decides whether a monolayer or a bilayer of silica can form on a specific substrate. Metals with high oxygen adsorption energy favor a monolayer network, while on noble metals only bilayers are formed [89,109]. As an example only a monolayer is formed on Mo(112), while on Pt(111) only the bilayer is found. Ru(0001) has an intermediate oxygen adsorption energy. As a result both, a monolayer and a bilayer exist. The heats of dissociative adsorption for Mo, Ru and Pt are 554 kJ/mol, 220 kJ/mol and 133 kJ/mol, respectively [75].

In the presented studies, the substrate is a FeO monolayer on Ru(0001). The heat of O_2 dissociative adsorption of Fe is 534 kJ/mol [75], which is similar to that of Mo. Thus, following this model only the monolayer formation is expected, but not the bilayer. In this chapter two layers of silicon are deposited in order to prove whether this finding also applies to ultrathin films on metal substrates.

In the previous chapter 4.1-4.2 a very strong Fe-O-Si bond was found to influence the film formation. Iron silicate is a two-phase material with an iron oxide layer on Ru(0001) and a monolayer of silica on top. The iron oxide layer gives rise to a Moiré pattern that has a "8 on 9" reconstruction, i.e. eight iron atoms are commensurate to nine ruthenium atoms. The pure FeO pattern shows a "6 on 7" reconstruction. As a result, the Si-O-Fe bond causes a shrinking of the Fe-Fe bond from 3.157 Å to 3.044 Å. This happens even when the FeO layer is pre-prepared, before silicon is deposited (see section 4.2.1). This preparation can be used for comparison reasons of the film formation of iron silicate with two layers of silica. In the following the individual preparations of iron silicate with silicon deposition equal to one and two layers of silica will be addressed as iron silicate(monolayer) and iron silicate(bilayer), respectively. It is of interest, how the second layer of silicon binds to the iron oxide film. It can be imagined that only one layer binds to the iron oxide layer, while the second layer is only physisorbed and finally evaporates. Alternatively both layers might be strongly bound. Iron silicate is prepared using the "stepwise preparation" method, thus preparing a monolayer of FeO on Ru(0001). Silicon is deposited at RT in $2.0 \cdot 10^{-7}$ mbar of oxygen. The amount of Si necessary to form a bilayer of SiO_2 is used. Finally, the film is oxidized in $1.0 \cdot 10^{-6}$ mbar of oxygen in temperature steps up to 1000 K. The individual preparation steps will be discussed. The corresponding LEED, LEEM-IV, XPS results are given in Fig. 4.49, 4.51 and 4.53. The intensity evolution of the (00), a Moiré spot and a $(\sqrt{3} \times \sqrt{3})R30°$ spot are shown in Fig. 4.50.

The LEED pattern of the FeO structure is given in Fig. 4.49a. The typical "6 on 7" reconstruction is visible in form of a Moiré pattern. This Moiré pattern vanishes through silicon deposition. Only the (00) spot remains visible. One reason is the disordered silicon layer. However, in section 4.3.1 it was shown that a Moiré pattern can remain even if the silicon layer on top is disordered. In the iron silicate(monolayer) it was found that silicon binds to the oxygen atoms of the FeO layer underneath. As a consequence the Fe^{2+} atoms become reduced to metallic iron, and the Moiré pattern disappears. When two layers of FeO are present (see section 4.3.1) not all Fe-O-Fe bonds are broken. Only the top-most

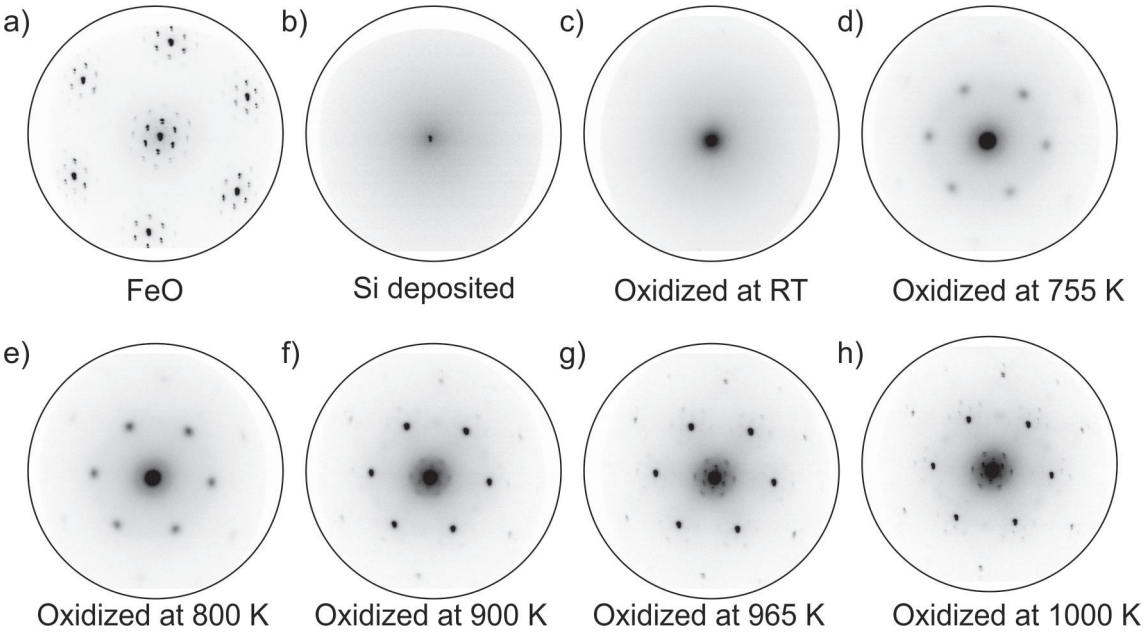

Figure 4.49 LEED evolution at 42 eV for the individual preparation steps for iron silicate(bilayer) (BL SiO_2/ML FeO/Ru(0001)) using the "stepwise preparation" method. LEED images are taken at a-b) RT and c-h) at the indicated temperatures.

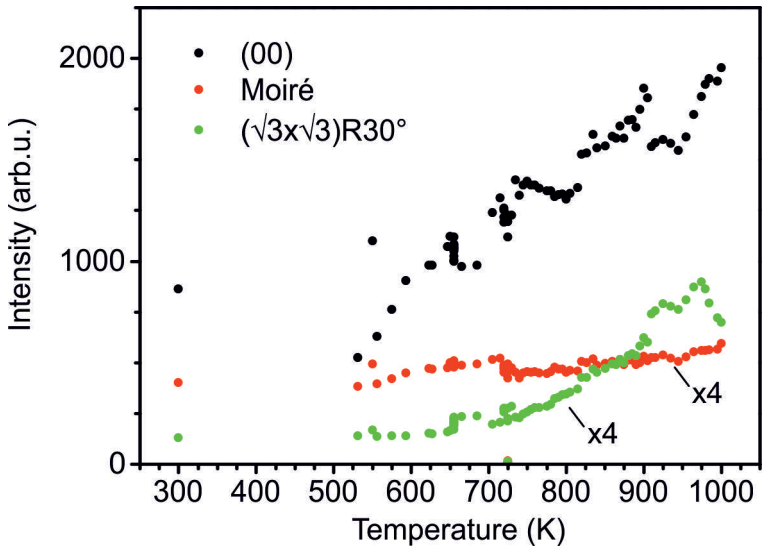

Figure 4.50 Spot intensity of the (00), a Moiré and a $(\sqrt{3} \times \sqrt{3})R30°$ spot during annealing of an iron silicate(bilayer) (BL SiO_2/ML FeO/Ru(0001)). The $(\sqrt{3} \times \sqrt{3})R30°$ structure refers to a silica structure that is rotated by 30° regarding a complete iron oxide layer. The oxidation takes place in an oxygen pressure of $1.0 \cdot 10^{-6}$ mbar.

oxygen atoms bind to silicon, while the interlayer Fe-O-Fe bonds are still present. As a result the Moiré pattern surrounding the (00) spot remains. The MEM-LEEM border of the iron silicate(bilayer) film increases strongly through silicon deposition by 0.5 eV (now: 3.24 eV). For iron silicate(monolayer) this was not observed, but instead a decrease of the MEM-LEEM border of 0.1 eV. The reason might be the double deposition time for two layers in contrast to one layer of silicon. Since the iron oxide layer has a very low oxygen

amount the incorporated oxygen atoms are mainly in the silicon layer. As a result a surface dipole increases the MEM-LEEM border. The LEEM-IV curve (Fig. 4.51) shows only one very broad peak at 6 eV, due to the disordered silicon layer. The O 1s line is given in Fig. 4.53a). Two lines are found at 531.8 eV and 530.6 eV, respectively. In comparison to the typical lines for iron silicate(monolayer) these two lines are clearly shifted relative to the typical energies of the Si-O-Si line (typically at 531.0 eV) and the Si-O-Fe line (at 530.0 eV), respectively. The reason must be the high silicon amount, which gives rise to more complex Si-O-Si bond angles and the strong workfunction shift. A line at 529 eV (Fe-O-Fe) is not found. This confirms the assumption that iron is reduced during the silicon deposition. Similar to the iron silicate(monolayer) preparation the Fe-O-Si bond is present. The Si 2p line in Fig. 4.53b) shows that silicon is not completely oxidized, but shows reduced components. The deposition of the same amount of silicon on 3O covered Ru(0001) shows also reduced components [44]. A monolayer of silicon is oxidized both by the present oxygen on the Ru(0001) substrate and the surrounding gaseous oxygen. Both oxygen resources are necessary for a completely oxidized silicon monolayer film. However, for the silicon atoms of the second layer the oxygen reservoir on the substrate is missing. As a consequence a high number of silicon atoms remain non-oxidized or only partially oxidized. In case of iron silicate(bilayer) one can argue similarly. The FWHM of the Si 2p line is with 1.7 eV relatively broad, due to the disordered film and thus varying bonding surroundings of the silicon atoms.

An oxidation in $1.0 \cdot 10^{-6}$ mbar at RT is sufficient to oxidize the silicon (bilayer) completely. However, the O 1s line is unchanged. This shows that the oxygen atoms cannot intercalate to the iron layer underneath silicon (no Fe-O-Fe line). The structure remains unchanged as can be seen in LEED.

In the following the temperature is increased in an oxygen pressure of $1.0 \cdot 10^{-6}$ mbar. Very weak intensity at the $(\sqrt{3} \times \sqrt{3})R30°$ distance develops starting at 555 K. In comparison to iron silicate(monolayer) this can be correlated to a beginning ordering of the silica layer. At 645 K the individual spots are recognizable. Subsequently, the sample was held at a temperature of 660 K for 15 min. At this temperature the spots become more pronounced and more intense. An increased temperature of 755 K enhances the silica arrangement even more. At this temperature the substrate spots become visible (see Fig. 4.49d). The iron layer is still disordered, which is indicated by the missing Moiré spots. The ordering and oxidation of the silicon atoms decrease the MEM-LEEM border by 0.2 eV to 3.05 eV (Fig. 4.52). In LEEM-IV (Fig. 4.43a) two peaks are visible at 6.2 eV and 12.5 eV. In comparison the LEEM-IV curve of iron silicate(monolayer) shows two peaks at 7.3 eV and 13 eV for similar preparation conditions. In the O 1s curve an additional component at 528.9 eV is present. As a conclusion, oxygen must be able to intercalate to the iron layer, which starts to be oxidized. Even though an ordering of the silica layer is found, the Si 2p line is unchanged (same FWHM) (Fig. 4.53b).

At a temperature of 800 K intensity surrounding the (00) spots is found, which can be interpreted as a beginning Moiré formation and thus iron re-arrangement. With increasing oxygen intercalation to the iron oxide layer the MEM-LEEM border (Fig. 4.52) decreases to 2.77 eV (-0.3 eV). The surface dipole is reduced due to the more homogeneous oxygen distribution within the film. The LEEM-IV curve (Fig. 4.43a) has not only more intense peaks, but also additional peaks for energies larger than 8 eV. The second silicon layer must still be present, since the LEEM-IV curve is very different compared to the one of iron silicate(monolayer). The O 1s line (Fig. 4.53a) confirms that the intercalation of oxygen

corresponds to the ordering of the iron oxide layer. The peak at 530.5 eV (Fe-O-Si) and 528.9 eV (Fe-O-Fe) are enhanced. The Si-O-Si line is unchanged, as well as the Si 2p line (Fig. 4.53b).

With increasing temperature up to 965 K a Moiré structure is formed, surrounding the (00) spot and the $(\sqrt{3} \times \sqrt{3})R30°$ spots (Fig. 4.49h). A strong intensity increase in the Moiré area starts already at 890 K. Interestingly, the Moiré pattern indicates a "8 on 9" structure, and thus an Fe-Fe distance of 3.044 Å, i.e. the iron atoms are similarly positioned as in the iron silicate(monolayer). The MEM-LEEM border (Fig. 4.52) is at 2.88 eV (+0.1 eV), which seems to results from the iron arrangement. The LEEM-IV characteristics (Fig. 4.51a) show a high number of peaks, completely different from the iron silicate(monolayer). In chapters 4.1-4.2 it was shown that very different preparation methods for iron silicate(monolayer) lead to the same LEEM-IV curve and structure. Since in

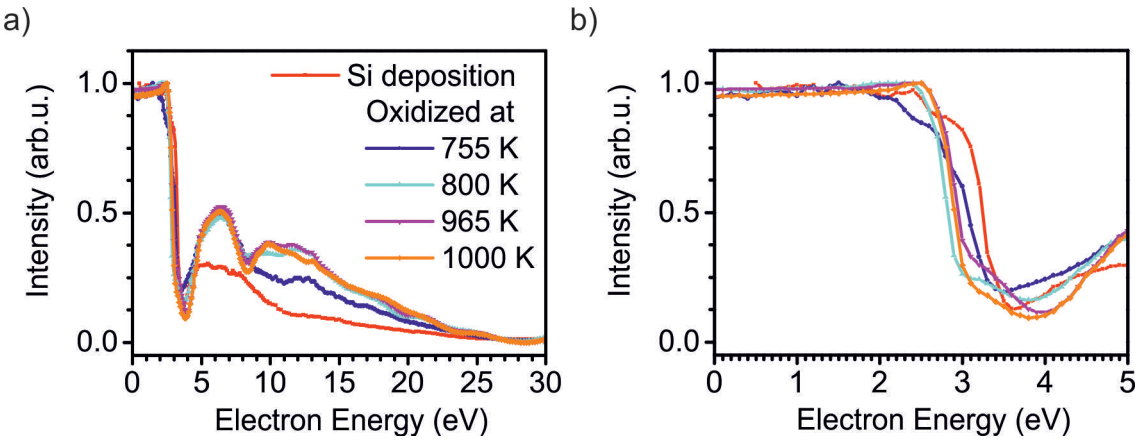

Figure 4.51 Reflectivity characteristics of an iron silicate(bilayer) (BL SiO_2/ ML FeO/ Ru(0001)) The Si deposition is performed in $2.0 \cdot 10^{-7}$ mbar, the oxidation steps at $1.0 \cdot 10^{-6}$ mbar. The measurements are taken at RT. a) LEEM-IV curve. b) MEM-LEEM border.

Preparation step	Energetic position of the MEM-LEEM border (eV)	Workfunction (eV) (referenced to clean Ru(0001) with 5.44 eV [12])
FeO monolayer	2.72	5.58
Si deposition	3.24	6.10
Oxidation at 775 K	3.05	5.91
Oxidation at 800 K	2.77	5.63
Oxidation at 965 K	2.88	5.74
Oxidation at 1000 K	2.88	5.74

Table 4.8 Tabular of the MEM-LEEM border in the individual preparation step for iron silicate(bilayer) (BL SiO_2/ ML FeO/ Ru(0001)). The MEM-LEEM values are measured with an accuracy of ± 0.02 eV.

the iron silicate(bilayer) preparation the structure differs from the iron silicate(monolayer), it can be assumed that the deposited two layers of silica are still present. The XPS O 1s line is unchanged (Fig. 4.53a). Thus, while the iron oxide layer orders, no difference in the oxidation level results. In contrast the Si 2p line has a 0.2 eV lower FWHM (1.5 eV). This indicates that the silica layer becomes more homogeneous.

A further oxidation at 1000 K leads to a intensity decrease in the O 1s and Si 2p line

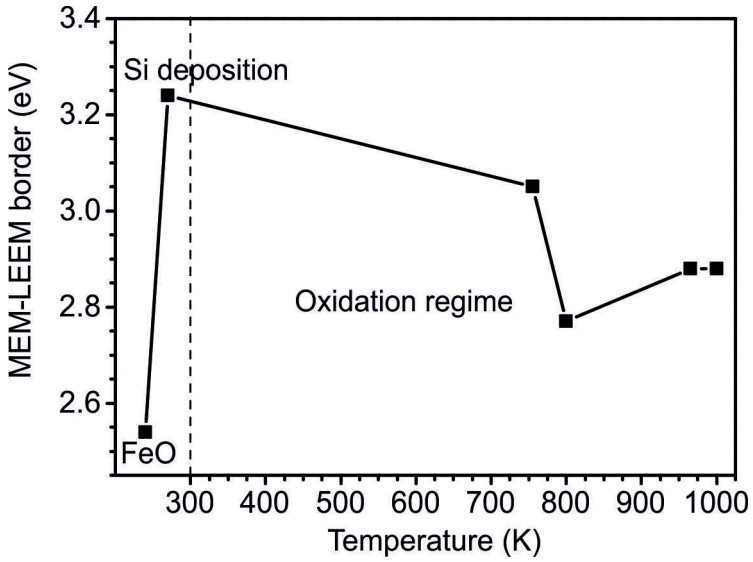

Figure 4.52 MEM-LEEM border for the individual preparation step of an iron silicate(bilayer) (BL SiO_2/ML FeO/Ru(0001)). The Si deposition is performed in $2.0{\cdot}10^{-7}$ mbar, the oxidation steps at $1.0 \cdot 10^{-6}$ mbar. The MEM-LEEM values are determined by a fit of the MEM-LEEM border presented in Fig. 4.51b. The error of this fit is ± 0.02 eV.

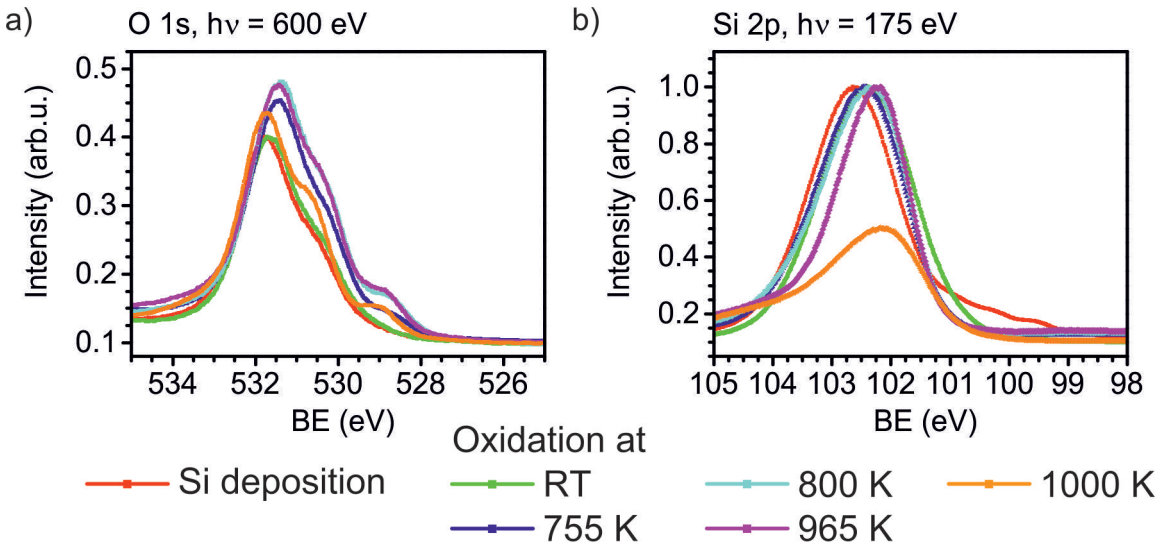

Figure 4.53 XPS study of the individual preparation steps of an iron silicate(bilayer) (BL SiO_2/ML FeO/Ru(0001)). The Si deposition is performed in $2.0 \cdot 10^{-7}$ mbar, the oxidation steps at $1.0 \cdot 10^{-6}$ mbar. The measurements are taken at RT. a) O 1s, hν = 600 eV. b) Si 2p, hν = 175 eV.

(Fig. 4.53a, b and e, f). This indicates that silicon evaporates. As a result slight changes in the LEEM-IV curve are present (Fig. 4.51a). The MEM-LEEM border (Fig. 4.51b) is unchanged. The LEED-structure is unchanged as well. A further oxidation up to 1170 K does not reveal a ring structure in LEED indicating a transformation to a vitreous silica bilayer.

Summary and conclusion of the formation process of iron silicate(bilayer)

As summary, an ordered iron silicate(bilayer) exists. A silica bilayer is arranged on a monolayer of FeO on Ru(0001). The iron oxide layer gives rise to a Moiré pattern with "8 on 9" reconstruction regarding the Ru(0001) substrate. The silica bilayer is still present as indicated by the difference of the LEEM-IV fingerprints of iron silicate(monolayer) and iron silicate(bilayer) films. Moreover the by 30° rotated spots are present, either coming from silica rotated by 30° on a complete iron oxide layer (three iron atoms per silica unit cell) or by the positions of the "missing" iron atoms in the iron oxide layer for two iron atoms per silica unit cell (see also section 4.1.3). Thus, the LEED pattern of the iron silicate(bilayer) matches the LEED pattern of the iron silicate(monolayer).

As indicated in the beginning the heat of dissociative O_2 adsorption on Fe is similar to that on Mo and thus, (for an iron crystal) only the formation of a silica monolayer formation is expected. Here, only one layer of iron oxide is used. This must be the reason why a silica bilayer is found in contrast to the expectation. The pure silica bilayer on Ru(0001) is inert and only Van der Waals-bound to the Ru(0001) substrate. This is not the case for the present iron silicate(bilayer) film, where a Fe-O-Si bond is indicated in the O 1s line. Another indication is the "8 on 9" reconstruction of the iron oxide layer, which differs from a pure FeO layer on Ru(0001) ("6 on 7"reconstruction) and demonstrates the influence of the silica layer on the iron oxide layer. Moreover, no vitreous phase of the silica bilayer can be achieved, even by oxidation to high temperatures (1220 K) as is the case for a silica bilayer on Ru(0001) and Pt(111). The model shown in Fig. 4.54 combines

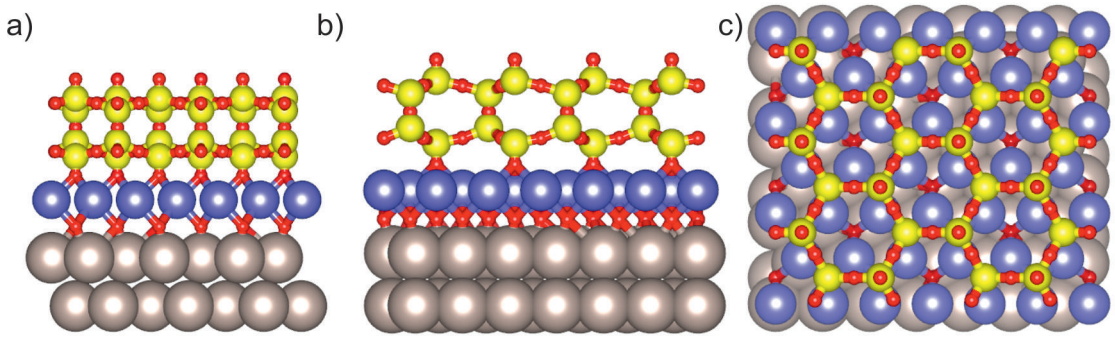

Figure 4.54 Structural model of the proposed structure of the final iron silicate(bilayer) film. In this model the iron oxide layer is depicted with three iron atoms per silica unit cell. However, the number of iron atoms per silica unit cell may also be reduced to two. Every second silicon atom binds either up or down, i.e. either to the other silica layer or the metal substrate. The presented cuts are in a) x-direction, b) y-direction and c) z-direction. Red: Oxygen. Violet: Iron. Yellow: Silicon. Gray: Ruthenium.

the formation of a silica bilayer with the strong Fe-O-Si. The silicon atoms bind vertically, alternately to the metal substrate and the other silica layer. In fact, a similar structure is found for three-dimensional crystalline silicate structures (as an example see Fig. 4.7.b in [55]). Nevertheless, in the proposed structure dangling bonds are present on top of the iron silicate(bilayer). If this is the case then it is likely that these structures are saturated by OH groups, always present in a UHV chamber.

The process of oxidation and structural arrangement during the preparation is depicted in Fig. 4.55. Similar to the deposition on top of Ru(0001) silicon is partially reduced and disordered after the silicon is deposited (Fig. 4.55b). The iron atoms are reduced during the silicon deposition. An oxidation at RT oxidized silicon completely, but the oxygen atoms cannot intercalate to the iron layer, which remains non-oxidized (Fig. 4.55 c). Silicon binds directly to iron via a Si-O-Fe bond. At 555 K the silicon atoms start to arrange in a $(\sqrt{3}\times\sqrt{3})R30°$ structure (Fig. 4.55d). At 755 K low amounts of oxygen are able to intercalate to the iron oxide layer underneath, which can be seen by the Fe-O-Fe component in the O 1s line (Fig. 4.55e). However, the iron oxide layer is still disordered (Fig. 4.55e). Finally at 800 K, iron becomes better oxidized and begins to order slowly. At 955 K finally a Moiré pattern with "8 on 9" reconstruction is formed (Fig. 4.55f). At 1000 K silicon starts to desorb partially. In agreement with earlier results, the oxygen atoms are very

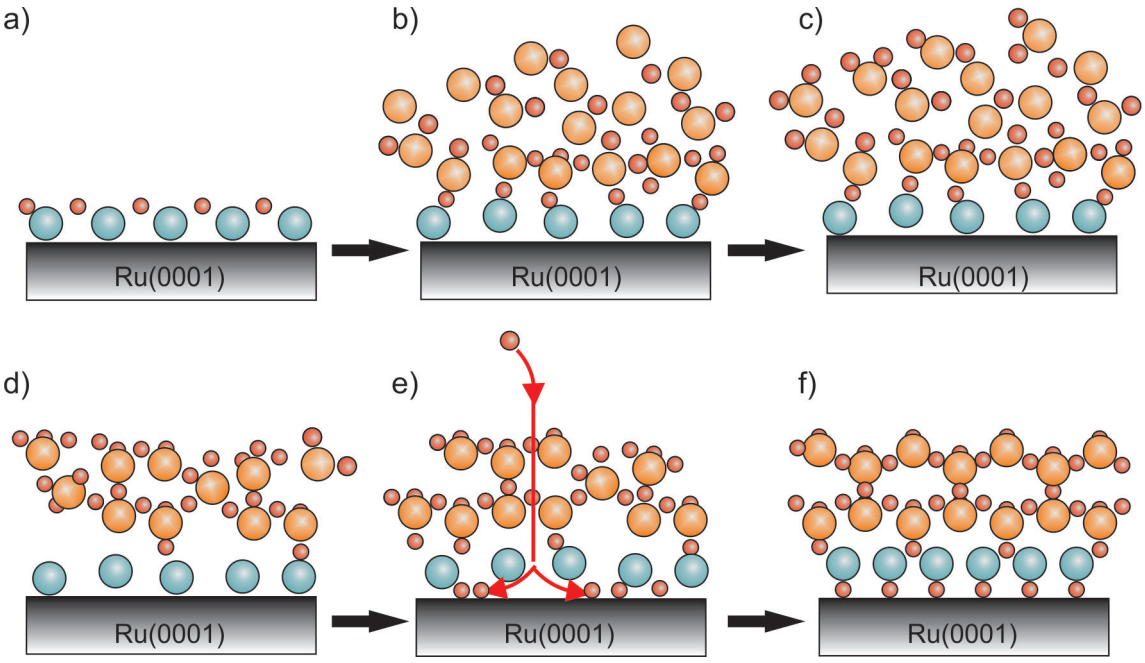

Figure 4.55 Schematic model of the structural arrangement and oxidation of the individual layer of a iron silicate(bilayer) (BL SiO_2/ML FeO/Ru(0001)) in the specific preparation steps. a) FeO layer with "6 on 7" reconstruction. b) Si deposition. Iron becomes reduced and the upper silicon layer is partially reduced. Fe-O-Si bonds are established. c) Oxidation at RT oxidizes silicon, but not iron. d) Oxidation at 660 K. Silicon begins to order in a $(\sqrt{3}\times\sqrt{3})R30°$ pattern. Iron is still not oxidized and disordered. e) Oxidation at 755 K. Oxygen intercalates to the iron layer. Iron begins to be oxidized, but remains disordered. f) Oxidation at 955 K. Iron-oxide ordered in a "8 on 9" reconstruction. SiO_2 bilayer ordered. Red: Oxygen. Violet: Iron. Yellow: Silicon. Gray: Ruthenium.

important for the iron oxide formation. Without intercalating oxygen, the film does not order. Up to 965 K this seems to be also stable. At 1000 K a loss of silicon material begins. This can either be the second layer or additional silicon atoms.

4.3.3 Summary and conclusion of multiple layers

This chapter discusses iron silicate preparation with multiple layer of either FeO or silica. The focus lies on the structural formation and stability of the additional layer, since iron silicate with only a ML of FeO and a ML of silica proved to be stable for all preparations discussed in chapters 4.1-4.2. Since the "stepwise preparation" method (compare section 4.2.1) proved to be ideal to build iron silicate, this method is adapted in this chapter. An overview on characteristic temperatures of the individual preparations are given in Tab. 4.9.

In section 4.3.1 the amount needed for a silica monolayer is deposited on a FeO bilayer. The characteristics of the bilayer are well known from chapter 3.2. In the following the film is addressed to as iron(bilayer) silicate. The normal iron silicate layer, as prepared in chapters 4.1-4.2, is addressed in this context as iron(monolayer) silicate.

Iron(bilayer) silicate forms a stable structure up to 1000 K. The second iron oxide layer is preserved as visible by the LEEM-IV curve different to iron(monolayer) silicate. In principle the silica layer orders on top of the iron oxide layer in the same way as for iron(monolayer) silicate. Thus, the by 30° rotated spots may either arise from the silica layer rotated regarding a complete iron oxide layer (three iron atoms per silica unit cell) or by the position of the "missing" iron atoms in respect to a complete iron oxide layer (two iron atoms per

	Iron(bilayer) silicate	**Iron silicate(bilayer)**
Preparation	stepwise preparation	stepwise preparation
	ML Si/BL FeO/Ru(0001)	BL Si/ML FeO/Ru(0001)
Stability T	1000 K	965 K
Appearance of Moiré spots	"6 on 7": Deposition "7 on 8": RT "8 on 9": 660 K	"8 on 9": 900 K
Appearance of $(\sqrt{3}\times\sqrt{3})R30°$ spots	660 K	645 K
Strongest intensity rise of Moiré spots	800 K	800 K
Strongest intensity rise of $(\sqrt{3}\times\sqrt{3})R30°$ spots	800 K	755 K
Additional LEED structure	(3x3)	-

Table 4.9 Temperature dependencies of preparation methods with multiple layers. The $(\sqrt{3}\times\sqrt{3})R30°$ structure refers to a silica structure that is rotated by 30° regarding a complete iron oxide layer.

silica unit cell). Moreover both iron oxide layer adapt to the optimal Si-O-Si distance, as discussed in in chapter 4.1.3 and thus reduce their Fe-Fe distance from of 3.157 Å (pure FeO BL) to 3.044 Å, i.e. the Moiré pattern changes from a "6 on 7" reconstruction to a "8 on 9" reconstruction. This indicates that the Si-O-Si bonds and Si-O-Fe bonds have even a strong influence on the second iron oxide layer. Additional to the typical iron(monolayer) silicate LEED pattern, a (3x3) structure develops. In chapter 4.2.1 a small reduction of iron was found when oxidized at elevated temperatures. Therefore it can be assumed that some iron atoms are free to move. Hence, the (3x3) spots might result out of iron, which is either migrating to the top of the layer or single iron atoms from the top most iron oxide layer rearrange. In the previous chapters the silica layer was found to stabilize the iron oxide layers underneath. Therefore it can be assumed that iron does not intercalate through the silica layer and remains underneath. If this is the case the iron atoms giving rise to a (3x3) structure on top would then lead to a buckling of the overlaying silica layer. In section 4.3.2 a bilayer of silica is prepared on top of a monolayer of FeO. These films are addressed to as iron silicate(bilayer). For comparison reason the normal iron silicate layer with one ML of FeO and one ML of silica is called iron silicate(monolayer), when directly compared. The iron silicate(bilayer) shows the same LEED structure as the iron silicate(monolayer). However, the LEED spots related to the silica layer on top, a $(\sqrt{3} \times \sqrt{3})R30°$ pattern, are much more intense than the Moiré spots. Moreover the LEEM-IV curve is different to the characteristic iron silicate(monolayer) fingerprint and the XPS curve shows a much higher Si-O-Si component than for iron silicate(monolayer). All these components indicate that the second silica layer remains. In fact, the film is stable up to 965 K, before silicon evaporates. Silicon binds to the oxygen atoms of the FeO layer. Before the iron oxide layer can be completely reoxidized temperatures of 755 K are necessary, most likely due to oxygen intercalation through the silica bilayer. The results indicate that the silica bilayer on top is both, stable and thus, the upper and lower silica layer must be bound through a Si-O-Si bond, and moreover strongly bound to the iron oxide layer underneath (Fe-O-Si bonds). These determining factors indicate a structure found also for three-dimensional crystalline silicate structures (for an example see Fig. 4.7.b in [55]). In the lower silica structure every second bond is either a Fe-O-Si bond to the iron oxide layer or a Si-O-Si bond to the second silica layer. In the upper silica layer this structure is followed, however the Si-O bonds showing upwards are unsaturated. However OH groups that are always present in the chamber might bind to these dangling bonds.

4.4 Incomplete layers

In the previous chapters complete layers of iron silicate were investigated. In chapters 4.1 and 4.2 different preparation methods showed that the silicon and iron amounts necessary for one monolayer of SiO_2 and FeO, respectively, lead to a complete and homogenous monolayer of iron silicate. In chapter 4.3 the utilized amount of material was increased either for iron or for silicon. As a result complete layers were formed. In contrast to the previous chapters, in this chapter the iron amount is lower than necessary for a complete monolayer of FeO. As a result incomplete layers of iron silicate films are formed. The utilized silicon amount equals in most cases a monolayer SiO_2. The formation process of incomplete iron silicate layers is followed in situ and in real-time and thus, gives access to the dynamic processes of the individual films.

In the following the influence of different preparation methods on the film formation is analyzed. One interest is the structural distribution of iron. Either the formation of iron-rich and iron-poor domains or alternatively, a homogenous distribution of iron within the SiO_2 layer is possible. The latter has been observed for incomplete aluminosilicate films [14]. In case iron is concentrated in separate domains, the influence on the iron-free areas is of interest. It should be investigated, whether for silicon it is energetically favorable to bind to iron or alternatively to the Ru(0001) substrate. And if silicon covers the iron-rich areas, it is of interest whether iron has an influence on the growth mode in neighboring iron-free areas. For instance, it should be checked whether silicon oxidizes in iron-free and iron-rich areas at the same temperatures or whether iron acts as a catalyst. Moreover, the influence of temperature on the stability of separate iron silicate areas is to be determined. In section 3.1 it was reported that a FeO monolayer is not stable under oxidation at 800 K in $1.0 \cdot 10^{-6}$ mbar. Nevertheless, complete layers of iron silicate films have proved to be stable to temperatures above 1100 K. Thus, silicon is stabilizing the iron oxide layer underneath. In complete layers of iron silicate, the iron atoms are in an encapsulated area. In contrast, in incomplete films they have more degrees of freedom. Thus, an ideal structure can be formed. Up to now it is unclear, whether the number of iron atoms in iron silicate equals the number of iron atoms in a pure FeO layer, or whether the iron amount is reduced. In section 4.1.1 calculations of R. Włodarczyk and J. Sauer were shown. The intention of these calculations was to find out which phase is energetically favored and fits to the experimental IRAS results in [103]. As it turns out the calculated IRAS lines do not show significant changes for three iron atoms per silica unit cell (i.e. unchanged number of iron atoms as in a FeO layer) and two iron atoms per silica unit cell (reduced situation). In the calculation, both structures are stable. Only the generated energy gained by transformation of iron silicate with three iron atoms per silica unit cell to two iron atoms per silica unit cell is higher than for the opposite case. Up to now the utilized preparation methods in [96, 103] have not been able to solve this question which of the two structures is formed. Thus, in situ measurements with real-time observation are necessary in order to give the possibility to observe individual islands upon oxidation at elevated temperatures. A migration of iron from a specific iron silicate domain would mean a reduction of the iron-content in this specific island. Moreover, the fingerprint of individual iron silicate islands enables a direct comparison with complete layers of iron silicate from the chapters 4.1-4.2. As a result the information on isolated iron silicate islands can be transferred easily to complete layers.

In order to clarify these questions three different preparation methods are used for iron silicate formation: the "combined preparation"method (section 4.4.1), and the "stepwise preparation" method for monolayer FeO islands (section 4.4.2) and bilayer FeO islands (section 4.4.3).

4.4.1 Incomplete layers with "combined preparation" method

In chapter 4.1.1 it was shown that a complete layer of iron silicate can be prepared with 1 ML of Si and 1 ML of Fe. To prepare this, first silicon and subsequently iron are deposited onto a 3O-covered Ru(0001) substrate in $2.0 \cdot 10^{-7}$ mbar and finally oxidized in $1.0 \cdot 10^{-6}$ mbar. In this chapter the same preparation recipe is used, however the individual amount of iron and silicon is reduced. Two different cases are discussed in this chapter. In case A only the iron amount is reduced, while the silicon amount still covers the whole surface (Data shown for 1 ML of Si and 0.7 ML of Fe). In cases B both, the silicon and

the iron amount is not sufficient to cover the surface (Data shown for 0.7 ML of Si and 0.5 ML of Fe). Overview LEEM images for case A and case B are shown in Fig. 4.56a and b, respectively. In Fig. 4.56c a zoom of case A is shown. As marked in the image, three different domains co-exist on the surface: type α, type β and type γ. Domains of type α are isolated island-like domains (bright in Fig. 4.56c). In contrast, domains of type β are typically large domains well connected over the whole surface (dark in Fig. 4.56c). Domains of type γ exist always close to domains of type α and in contact to domains with type β (gray in Fig. 4.56c). The three domains can be assigned to the following structures: Domains of type α are pure silica monolayer films with a (2x2) orientation. The layer is not completely oxidized at the used temperature. Domains of type β are iron silicate, similar to the complete films described in chapters 4.1-4.2. Domains of type γ are pure silica bilayer films, with a (2x2)R30° orientation, i.e. the same orientation as the silica layer of the iron silicate phase. A model of the individual domains is given in Fig. 4.61. In the following the experimental data are shown for identifying the individual domains.

In Fig. 4.57b the overall LEED pattern is given for case A. In LEED the characteristic pattern for iron silicate ($(\sqrt{3}\times\sqrt{3})R30°$ spots and a Moiré pattern) are visible. Additionally, a (2x2) structure is present. A (2x2) structure is characteristic for 3O-(2x2)-Ru(0001) [31], i.e. holes in the film, but also for a mono- or bilayer of pure SiO_2 [107]. Dark field measurements in Fig. 4.57 show nicely that these (2x2) spots corresponds to domains with type α. Comparing neighboring LEED spots of the same kind (Fig. 4.57c and d) show a contrast inversion, depending on the individual terrace. This effect is well known for the 3O covered Ru(0001) substrate [23] but also for the mono- and bilayer of SiO_2 [44]. This effect arises from the ABAB stacking of the hexagonally close-packed Ru substrate. As neighboring terraces contain different surface terminations (either A or B type) a different contrast in the dark field imaging is achieved. In fact the presence of this effect identifies areas which form depending on the underlying Ru(0001) substrate. The same intensity inversion is present for adjacent LEED spots of the Moiré pattern surrounding the (00) spot. A Moiré pattern results from a superposition of two lattices with very similar unit cells. Thus, the influence of the Ru(0001) substrate is to be expected. As visible in Fig. 4.57e and f, domains of type β and type γ give rise to the Moiré structure. However, only domain β shows the discussed contrast inversion between neighboring spots. Domains of type γ have the same intensity for all energies in the investigated energy range of 10-30 eV. In fact,

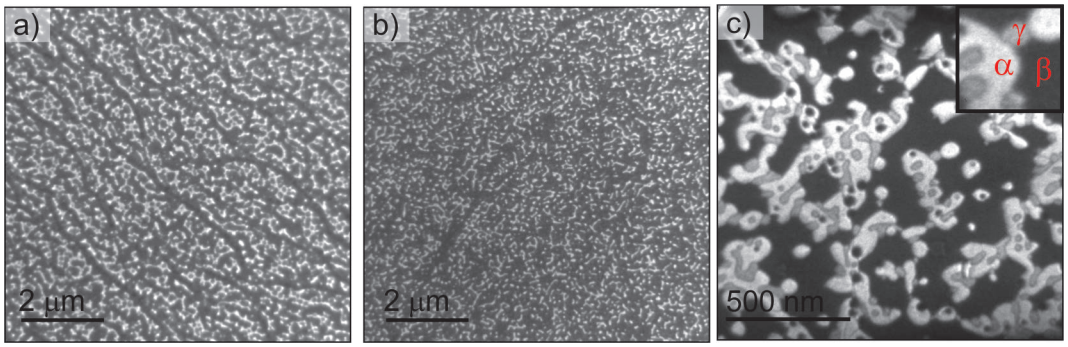

Figure 4.56 LEEM images of incomplete layers using the "combined preparation" method. a) case A (1 ML Si and 0.7 ML Fe) at 4 eV and b) case B (0.7 ML Si and 0.5 ML Fe) at 15 eV. c) Zoom of case A at 14.5 eV reveals the presence of domains of three types: α, β, γ as marked in the inset). The contrast of the visible domains is the same for all chosen energies in a-c).

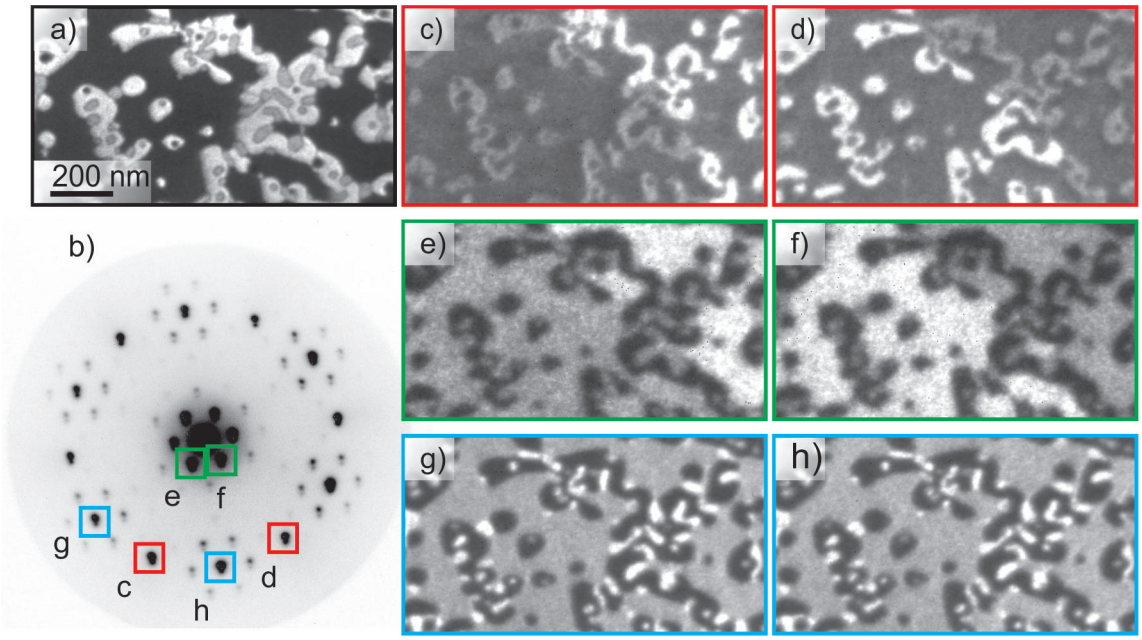

Figure 4.57 Structure of the individual domains of incomplete iron silicate films using the "combined preparation" method (Si+Fe/3O-Ru(0001)): a) LEEM image at 14.5 eV. b) LEED at 20 eV. c-h) Dark field images of the spots labeled in LEED (b). c-d) (2x2) structure (marked in red), e-f) Moiré structure (marked in green) and g-h) by 30° rotated spots (marked in blue).

the intensity of domains of type γ (independent of the individual terrace) resembles the intensity of domains of type β for the terrace with the lower reflectivity. Both, type β and γ give rise to the $(\sqrt{3} \times \sqrt{3})R30°$ spots. As a conclusion, both, types β and type γ share the same long-range Moiré structure, as well as the same orientation and distances as the $(\sqrt{3} \times \sqrt{3})R30°$ structure. We note that the definition of the $(\sqrt{3}x\sqrt{3})R30°$ corresponds to a silica layer corresponding to a complete iron oxide layer underneath (iron silicate phase). However, if one of the types is pure silica, the LEED pattern should be addressed to as (2x2)R30° regarding the Ru(0001) substrate.

In Fig. 4.58 LEEM-IV curves corresponding to the domains of the individual types are given. As discussed before, LEEM-IV depends on the backscattering coefficient of a specific element and the specific structural information [7, 46]. Due to these multiple dependencies it is suitable to be used as a fingerprint. The characteristic LEEM-IV curves of the individual domains of type α, β and γ are given in Fig. 4.58a, b and c, respectively. Additionally, reference spectra are added. The comparison to the reference spectra reveals the nature of the individual phase. In Fig. 4.58a the characteristic LEEM-IV curve of type α is given (in red). As was shown before this type gives rise to a (2x2) structure and is sensitive to the individual Ru terrace, when using neighboring spots. However, these characteristics are similar for both a 3O-(2x2) Ru(0001), as well as for silica (mono- and bilayer). The LEEM-IV curves of these three possibilities are added for comparison. The LEEM-IV curve of the (2x2) monolayer SiO_2 is very similar to the fingerprint of the 3O-(2x2)-Ru(0001) substrate. They differ mainly in their peak intensities. The fingerprint of type α, resembles both of them. The fingerprint of the (2x2)-bilayer SiO_2 is very different and can be excluded. The MEM-LEEM borders of domain α, (2x2)-ML SiO_2 and 3O-(2x2)-Ru(0001) are 3.10 eV, 3.43 eV and 3.75 eV, respectively. So type α being the

monolayer silica layer is more likely. Nevertheless, a final conclusion is not possible at this point.

Fig. 4.58b shows the fingerprint of domain β. As it turns out, it is the fingerprint of iron silicate consisting of 1 ML of SiO_2 and 1 ML of FeO. In chapters 4.1 and 4.2 this fingerprint was found for all four preparation methods of complete layers of iron silicate. As an example, Fig. 4.58b displays the fingerprint of a complete layer of iron silicate, prepared with the same method as these incomplete films ("combined preparation" method). Finally, the fingerprint of type γ is shown in Fig. 4.58c). Dark field imaging exhibits that the LEED structure by 30° rotated (2x2) structure of this phase is the same as for type β (the iron silicate phase). However, the LEEM-IV curve is very different. Since the coverage of silicon exceeds the iron content it can be assumed that type γ is pure silica.

Silica prepared on Ru(0001) by oxidation in $1.0 \cdot 10^{-6}$ mbar typically gives rise to a (2x2) structure for both, the mono- and the bilayer of silica. The monolayer of SiO_2 is strongly bound to the Ru-surface, while the bilayer is only van-der-Waals bound [107]. In the formation of the (2x2) structure of the silica monolayer the interfacial oxygen O(2x2) between the SiO_2 and the Ru(0001) surface has a severe impact in the arrangement of the film [106]. An annealing in UHV conditions removes this oxygen layer, which leads to a rotation of the silica monolayer film by 30°. This is possibly due to the large flexibility of the Si-O bonds and thus, an additional degree of freedom [106]. The corresponding LEED structure in such a film shows a (2x2)R30° pattern, together with a Moiré structure [44]. The unit cell of silica in this configuration is twice the unit cell of the Ru(0001) substrate (5.42 Å for silica vs. 2.71 Å for ruthenium) [44]. Due to this similar unit cell and the rotation of the lattices the Moiré pattern exists. Also in bilayer silica films a (2x2)R30° structure is found [45]. Here, this structure often appears in a state, when transforming a crystalline (2x2) silica bilayer into a vitreous layer (ring in LEED pattern). During this process it may happen that single domains, homogenously distributed in a silica bilayer film, rotate first by 30° [45], before the rest of the film transforms into a variation of silica rings in the size of four up to eight-membered silica rings [54]. Additionally the LEEM-IV curve of a vitreous bilayer silica film is given. Since the signature of the vitreous bilayer is much stronger than that of a crystalline bilayer, the LEEM-IV curve of the partially rotated bilayer is very similar to a completely vitreous film. The corresponding fingerprints of a mono- and a bilayer film with a (2x2)R30° configuration and the vitreous silica bilayer film are added together with the fingerprint of type γ in Fig. 4.58c. The direct comparison shows that type γ is a silica bilayer film.

Domains of type γ are nearly always found in contact to phase β This and the fact that the pure silica layer has the same distances and orientation as the silica layer of iron silicate indicates that the pure silica layer determines the film structure of the silica monolayer as part of iron silicate. Thus, it can be concluded that silicon covers areas with iron oxide first, and then continues to form a silica layer right next to the iron silicate island. As a consequence it must be energetically preferred for silicon to bind to iron rather than to Ru(0001). An additional reason might be a lack of oxygen in close surrounding to the iron silicate layer, which might influence the rotation of the silica bilayer.

The XPEEM results of case A and case B are given in Fig. 4.59 and 4.60, respectively. In Fig. 4.59a and 4.60a the individual LEEM images are given. At the chosen energies for both preparations the contrast of the domains is inverted. Therefore the individual domains are marked with boxes. In both cases domain α is indicated in violet, while do-

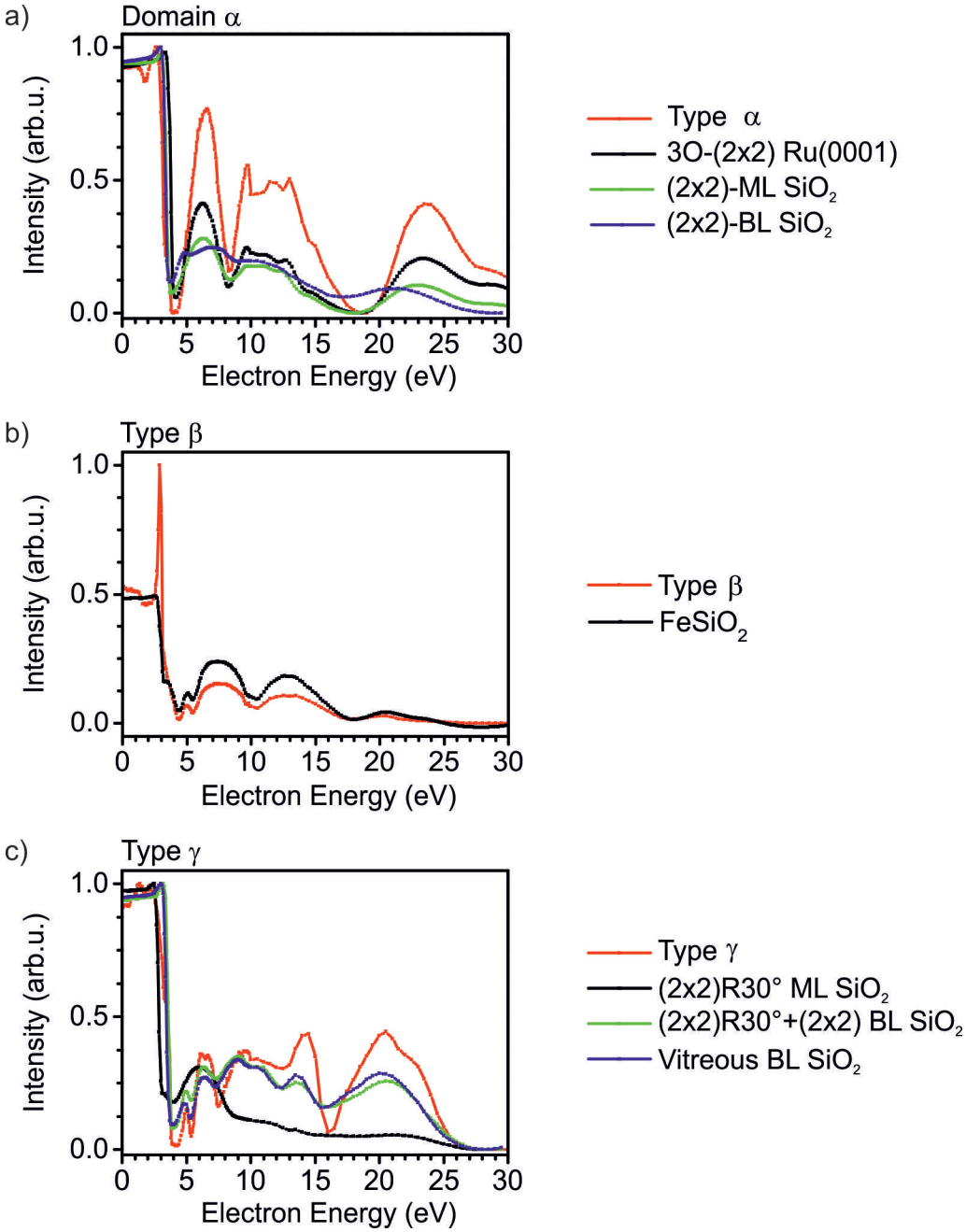

Figure 4.58 a-c) LEEM-IV curves for the domain types α, β and γ, respectively, observed in LEEM. Additional reference data is given for the identification of the individual domains.

main β is indicated in red. The corresponding XPEEM images are found in Fig. 4.59b-e for case A and in Fig. 4.60b-c in case B. Additionally corresponding XPEEM scans taken at the indicated squares are shown for case A in Fig. 4.59f-h for the Si 2p, Fe 3p and Ru $3d_{5/2}$ line. For case B the Si 2p line is given in Fig. 4.60d. Due to the limited lateral resolution in these images, domain type γ cannot be resolved.

The Fe 3p signal can only be found in domain β, which fits nicely to the fingerprint in Fig. 4.58b, in domain α only the background signal is present. Although the Ru signal is

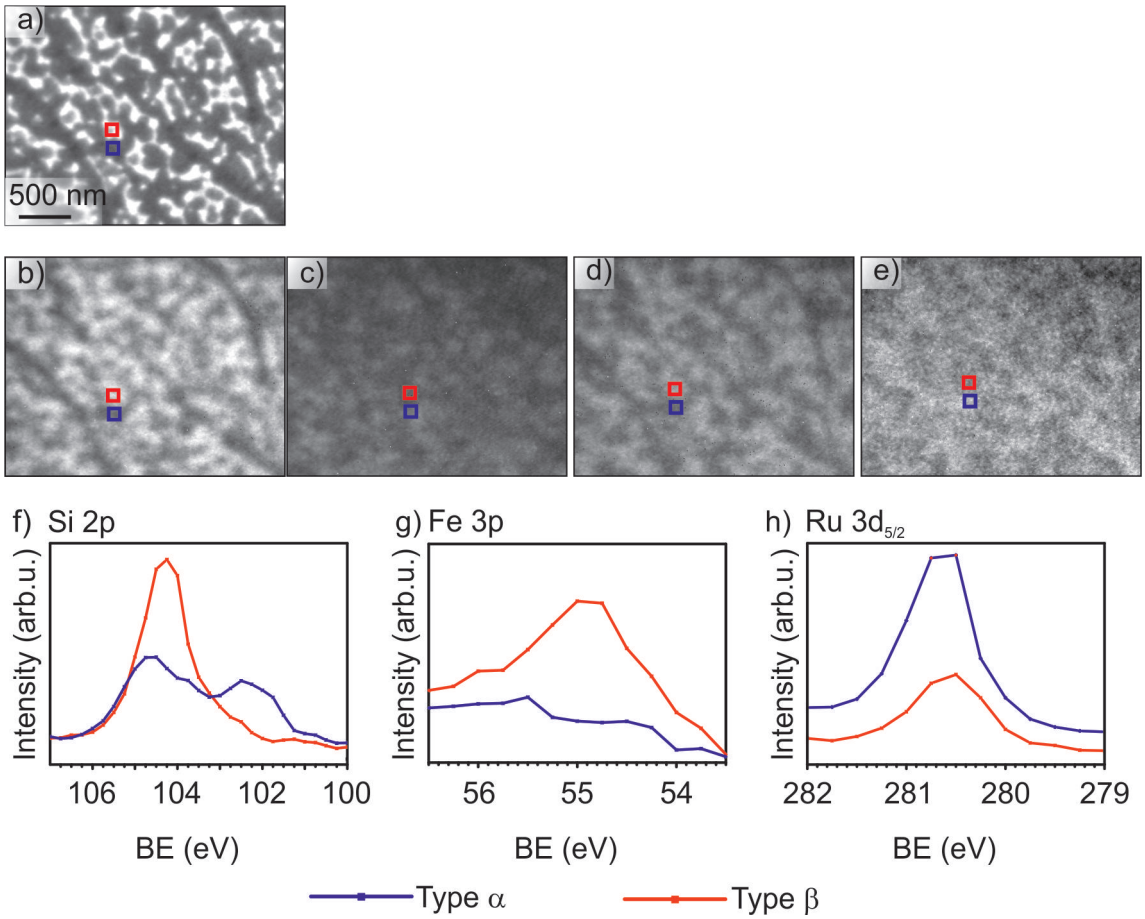

Figure 4.59 XPEEM study of a iron silicate preparation with 1 ML Si and 0.7 ML Fe. a) LEEM image at 4 eV. b-e) XPEEM images. b-c) Si 2p at BE = 104.5 eV (b) and BE = 102.5 eV (c) (hν = 175 eV), d) Fe 3p line at BE = 54.75 eV (hν = 125 eV) and e) Ru $3d_{5/2}$ line at BE = 280.5 eV (hν = 353 eV). f-h) XPEEM scans of the domains indicated in (b-e). f) Si 2p line (hν = 175 eV), g) Fe 3p line (hν = 125 eV) and h) Ru $3d_{5/2}$ line (hν = 353 eV).

detected in both domains, the signal is much stronger in the domains of type α. The reason can be explained by higher damping properties of the iron silicate. In case A, enough Si material was deposited in order to cover the whole surface. Indeed the overall intensity in the Si 2p line is the same for both domains. Thus, domain α can be identified as a (2x2)-SiO_2 monolayer. The local degree of oxidation differs in the two types, though. In type β only a single Si 2p line is visible at 104.25 eV (red line). Thus, all silicon atoms are completely oxidized in the iron silicate phase. The pure silicon monolayer has two contributions at 104.65 eV and 102.5 eV binding energy, which correspond to fully oxidized silicon atoms (Si^{4+} state) and to partially reduced species, respectively. The small difference of the of 0.4 eV in the Si^{4+} state between type α and β, corresponds to the different bonding surroundings for silicon atoms in type α (Ru-substrate) and type β (FeO-like layer). For interfacial oxygen it is observed that an increase of the interface dipole causes a decrease in binding energy [104]. This seems to be the case for the silicon atoms on top of the iron oxide layer as well. For case B (Si amount smaller than 1 ML), the same peak positions are found as for case A for the Si 2p line. However, the silicon amount in domains with type β exceeds clearly the silicon amount of domains with type α. As a result, silicon

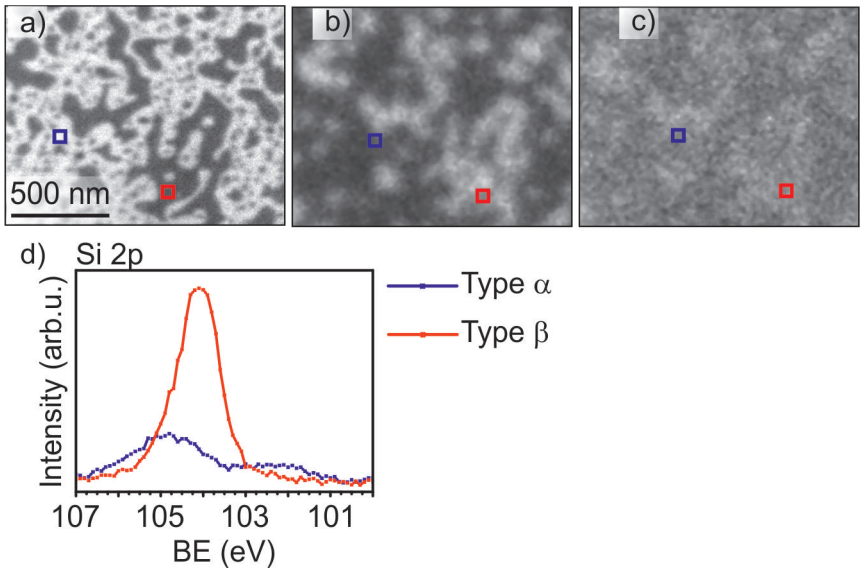

Figure 4.60 XPEEM study of a iron silicate preparation with 0.7 ML Si and 0.5 ML Fe. a) LEEM image at 145 eV. b-c) XPEEM images of the same region. b) Si 2p line at 104 eV ($h\nu = 200$ eV), c) Fe 3p line at 55 eV ($h\nu = 200$ eV). d) XPEEM scan of the areas marked in a-c). Si 2p line at $h\nu = 200$ eV.

prefers to bind to iron than covering the Ru(0001) substrate. The finding that silicon is fully oxidized in the iron oxide containing domains, but not in the iron-free domains, is remarkable. This indicates that iron decreases the oxidation temperature of SiO_2. In fact, also for complete layers of iron silicate the temperature reduction was already found. While silicon needs to be annealed at 1050 K [44], the final temperature of the films could be significantly reduced to 900-1000 K, depending on the preparation method (see chapters 4.1-4.2). In preparation methods "combined preparation", "combined UHV preparation" and "stepwise preparation" silicon was already completely oxidized at RT (but not well ordered).

Summary of incomplete iron silicate layers using the "combined preparation" method

In summary, three different domains α, β and γ are found for incomplete layers of iron silicate prepared with the "combined preparation" method. In Fig. 4.61 the individual domains are indicated. i) type α is a monolayer silica film, giving rise to a (2x2) structure. ii) type β is iron silicate, having the same fingerprint as complete layers, as discussed in chapters 4.1-4.2. iii) type γ is crystalline silica bilayer, which is rotated by 30° and thus, has the same structure as the silica layer in iron silicate. As can be seen in LEED the silica monolayer in iron silicate is arranged at lower temperatures than necessary for a silica monolayer on Ru(0001). Moreover iron decreases the oxidation temperature for complete oxidation of silica, as is visible in XPEEM. These findings lead to the conclusion that iron silicate formation is energetically preferred in contrast to direct silica formation on the Ru(0001) substrate. In fact, if the silica amount is lower than necessary for a complete layer of silica, the silicon amount in iron silicate exceeds the one on pure Ru(0001). Silica bilayer domains are nearly always found in contact to iron silicate domains. Therefore it

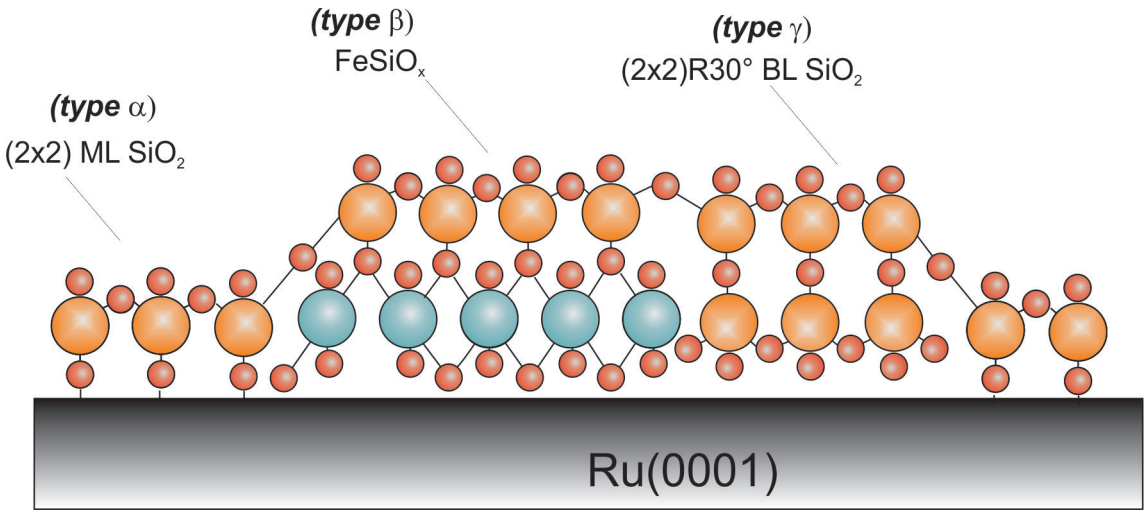

Figure 4.61 Schematic model for the individual domains on the surface for an incomplete layer of iron silicate using the "combined preparation" method. Red: Oxygen. Blue: Iron. Yellow: Silicon.

can be concluded that silica is formed on iron first and then continues to grow in contact to iron with the same structure as a rotated silica bilayer. The silica monolayer (type α) is a result of silicon agglomerates on nucleation centers.

4.4.2 Incomplete layers with "stepwise preparation" method: Monolayer FeO

The previous section 4.4.1 focused on the self-arrangement of iron silicate islands. This was achieved by applying the "combined preparation" method, where silicon and iron are deposited in oxygen environment, forming disordered layers. The arrangement of the individual materials and the later formation of domains are solely determined by energetic optimization during the final oxidation process.

In this section monolayer-thick FeO islands have already been prepared, before silicon is deposited. With this "stepwise preparation" method the shape of the FeO islands, as well as the structural arrangement of iron and oxygen atoms, are already pre-defined. Changes in the layer can nicely be compared with a well-known initial state of FeO. In order to prepare monolayer-thick FeO islands, iron is deposited in an O_2 pressure of $2.0 \cdot 10^{-8}$ mbar at 800 K. At these conditions FeO grows in layer-like mode. By variation of the deposition time, the average size of the FeO islands can be controlled. In LEED a Moiré pattern is visible, due to the commensurable superposition of 6 iron atoms on 7 Ru atoms (the so-called "ML2" phase). Further information about the growth characteristics of monolayer-thick FeO is given in section 3.1. On top of the pre-prepared FeO islands, silicon is deposited in an oxygen pressure of $2.0 \cdot 10^{-7}$ mbar at RT. Finally, the layer is oxidized in a pressure of $1.0 \cdot 10^{-6}$ mbar. For the films discussed in this chapter a final oxidation temperature of 900-920 K was used. Information about a complete layer of iron silicate using the same preparation method, has been given in section 4.2.1.

It will be shown that the percentage of the FeO covered area has a major impact on the

final film. In this chapter two different cases are discussed. In case A less than 60 % of the surface are covered with FeO, while in case B the FeO coverage is higher than 80 %. In both cases a migration of iron towards the initially iron-free areas is observed. In case A small isolated islands with the size about 50 nm form, having similar structural properties as the originally iron-rich areas. In case B a growing front is visible, migrating towards the center of the originally iron-free holes. In both cases the migrating iron forms only small domains, which are intermixed with small domains of a silica monolayer with (2x2) ordering. The migration of iron out of the iron silicate islands based on monolayer thick FeO shows that the optimal iron silicate film contains less iron atoms than a FeO layer. Following calculations the iron amount per silica unit cell is reduced from three to two iron atoms.

In Fig. 4.62a series of different preparation steps are shown for case A (Fig. 4.62a-f, 54 % of the surface covered with FeO and 2/3 ML of SiO_2) and case B (Fig. 4.62g-h, 87 % of the surface covered with FeO and 1 ML of SiO_2) in LEEM and LEED.

In Fig. 4.62a-b) the incomplete FeO layer is shown before Si is deposited. The LEEM image at 17.2 eV reveals iron-rich areas (from now on called domains α) and iron-free areas (domain β) in bright and dark, respectively. At this step domain α is pure monolayer-thick FeO, giving rise to the Moiré spots in LEED and domains β the oxygen covered Ru(0001) substrate with a (2x2) structure. In Fig. 4.62c-d) the same layer is shown after the deposition of silicon (2/3 ML). Due to the covering silicon layer the Moiré spots disappear. In LEEM the contrast between domains α and domains β is inverted and depleted.

In Fig. 4.62e-f) the film after the final oxidation step for case A is shown. The inset shows a zoom-in of a domain of type β, surrounded by a domain of type α. During the oxidation

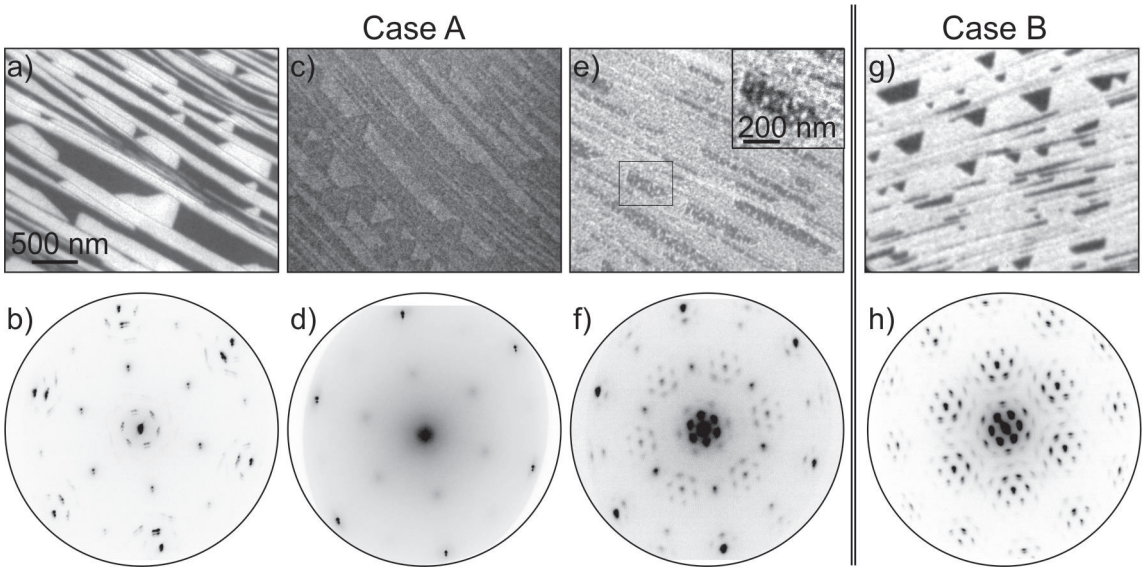

Figure 4.62 Preparation steps for an incomplete layer of iron silicate using the "stepwise preparation" method. a-f) Case A (iron oxide coverage of 58 %). a-b) FeO islands (domain α bright) as-prepared, c-d) after Si deposition of 2/3 ML (domain α dark) and e-f) oxidized at 920 K (domain α bright). g-h) Case B (iron oxide coverage of 87 %, silicon coverage of 1 ML) after oxidation to 900 K. LEEM images at 17.2 eV and LEED images at 42 eV. Images are taken at different surface spots.

process the contrast in domain β changes with time and temperature. A mixture of different image intensities is visible in domain β: bright gray, gray and dark. The main intensity is still low, as the intensity of the entire domain β was before the final oxidation step took place. The bright gray and gray intensities are new, and resemble the reflectivity of the surrounding domain α. The LEED pattern reveals the superposition of Moiré, $(\sqrt{3}\times\sqrt{3})R30°$ and (2x2) spots. In order to assign the individual LEED structures to the in LEEM visible areas a dark field analysis of the same film is given in Fig. 4.63. In Fig. 4.63c-d) Moiré spots, in 4.63e-f) $(\sqrt{3}\times\sqrt{3})R30°$spots and in 4.63g-h) (2x2) spots are probed. Domain α gives rise to Moiré spots and the $(\sqrt{3}\times\sqrt{3})R30°$structure. The dark-field imaging using Moiré pattern spots shows a contrast inversion between neighboring substrate terraces, when probing neighboring LEED spots. As already discussed in previous chapters this indicates a dependency on the A or B terraces of the ABAB structured Ru(0001) substrate. In contrast to the Moiré spots the reflectivity of all terraces is similar when neighboring $(\sqrt{3}\times\sqrt{3})R30°$spots are chosen. This fits nicely to the findings of complete layers of iron silicate. Thus, in domain α iron silicate is formed. Further evidence will be given later in this chapter by analysis of the LEEM-IV curve. The small isolated islands in domain β appearing bright gray in LEEM at 17.2 eV, share the same structure as domain α, namely Moiré spots overlapped with $(\sqrt{3}\times\sqrt{3})R30°$spots. In contrast, the gray and dark areas in domain β give rise to the (2x2) structure. Hereby, some areas have a higher reflectivity than others, which indicates less defects.

The oxidation step for case B is shown in Fig. 4.64. At the shown example 87 % of the surface is covered with FeO islands. As a result domains of type β (iron-free areas) are relatively small, while the available iron amount is large. In the center of the images of sequence a)-e) in Fig. 4.64 a domain of type β (dark) is shown, surrounded by type α

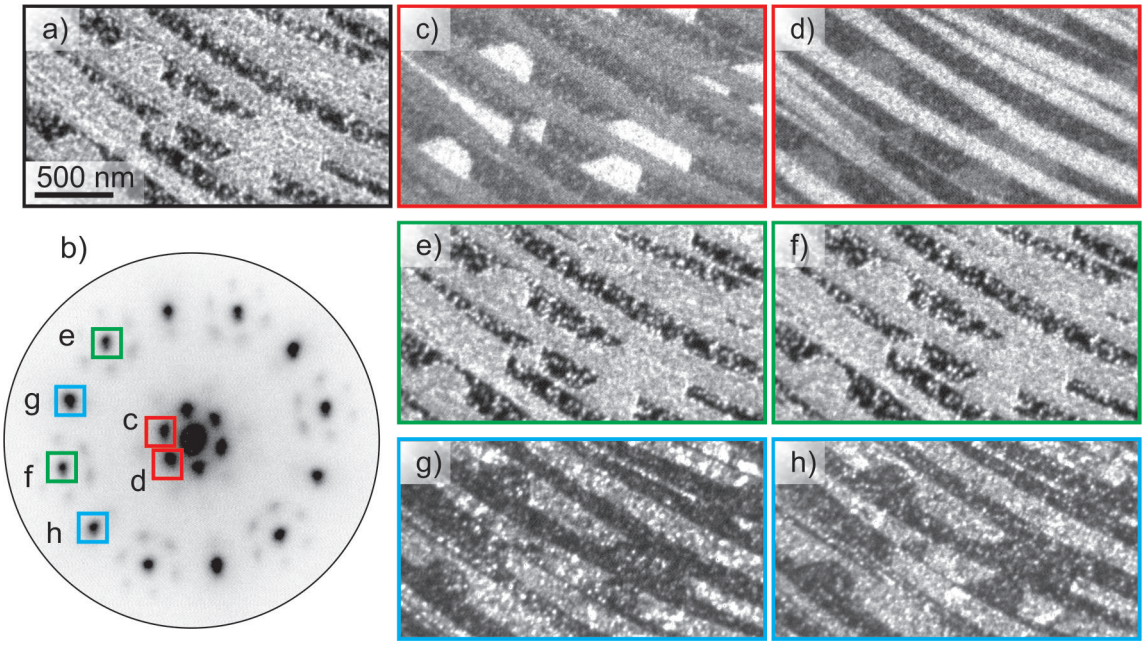

Figure 4.63 Dark field analysis of an incomplete iron silicate film prepared with the "stepwise preparation" method for an iron coverage of 58% (Case A). The film was oxidized at 920 K. a) LEEM image at 17.2 eV, b) LEED image at 20 eV, c-h) dark field images of the LEED spots marked in b. c-d) Moiré spots, e-f) $(\sqrt{3}\times\sqrt{3})R30°$spots and g-h) (2x2) spots.

(gray). During the temperature rise in an oxygen atmosphere of $1.0 \cdot 10^{-6}$ mbar a front appears, starting at the border of domain α and moves towards the center of domain β. In Fig. 4.64 the ongoing front is visible. In Fig. 4.64a) the front has crossed half of the area of domain β, thus three different contrasts area visible. The individual areas are marked with green and red squares in domain β and a black square in domain α. The red area is the area of domain β which the front has already passed. The green area is still unchanged. The intensity evolution at the positions marked by colored squares in Fig. 4.64h are plotted in Fig. 4.64g. The corresponding LEEM images at selected temperatures are given in Fig. 4.64a-f. The heating rate was 0.15 K/s in average. During the oxidation process from 665 K up to 680 K the front continues towards the center of domain β until domain β is completely covered. The intensity in the green-marked area rises drastically when the front passes through. Afterwards the intensity increases linearly with a lower slope. Similarly the already changed red-marked area undergoes a linear behavior with a similar slope. The intensity of domain α remains nearly constant during this process. With further temperature increase the contrast between the black-marked (domain α) and the red- and green-marked (domain β) areas diminishes.

The LEEM-IV curves for domain α and domain β are given in Fig. 4.65a) and b), respectively. Here, cases A and B are plotted, respectively. Domain α shows for both cases the characteristic LEEM-IV curve of iron silicate (Fig. 4.65a). This fits nicely to the structural findings of a Moiré pattern and $(\sqrt{3} \times \sqrt{3})R30°$ structure in these areas. This is another indication that iron silicate is the most stable configuration and will be formed independently of the domain size.

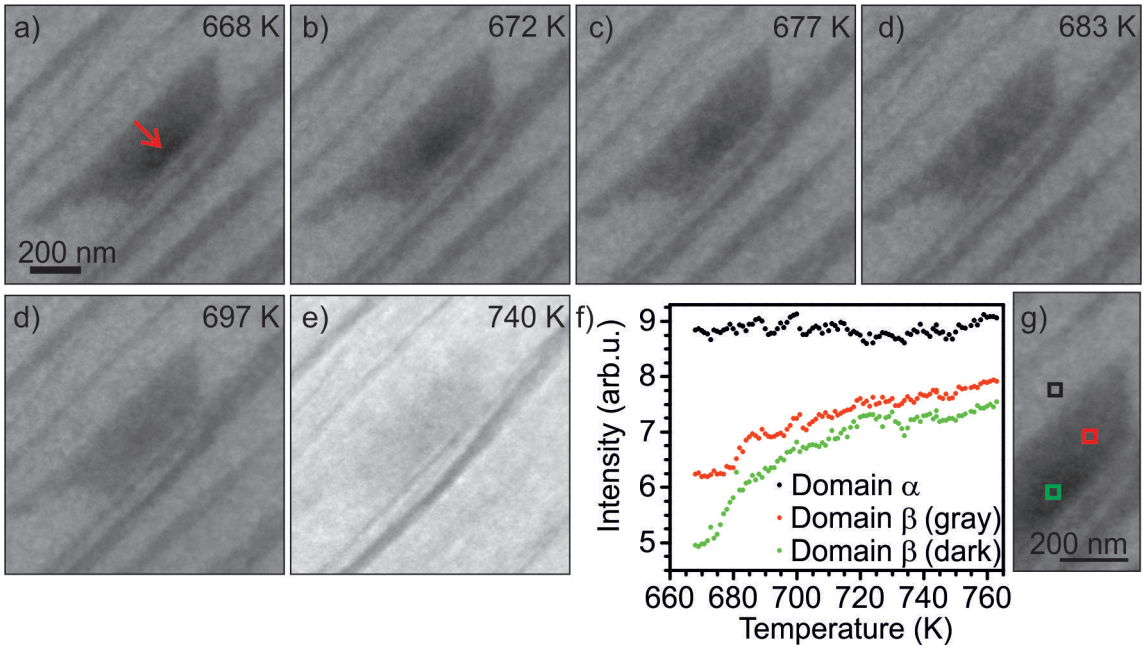

Figure 4.64 LEEM series during oxidation of an incomplete iron silicate layer prepared with the "stepwise preparation" method. The iron coverage of this film is 87 % (Case B). Light gray: domain α. Dark area: domain β. LEEM images are taken at 15 eV. The heating rate was 0.15 K/s in average. Oxidation at a) 668 K, b) 672 K, c) 677 K, d) 683 K, e) 697 K and f) 740 K. The direction of the front is indicated by the red arrow in a). f) Intensity evolution during the oxidation process in the in g) marked areas. g) zoom in of a).

The LEEM-IV curves in domain β differ for cases A and B (Fig. 4.65b), but have the same peak positions. In fact, the measured LEEM-IV curves can be constructed by a superposition of the fingerprint of iron silicate with the typical fingerprint of a monolayer of SiO_2 with (2x2) pattern. In Fig. 4.65 c) the constructed LEEM-IV curves for varying $FeSiO_x$:SiO_2 ratios are plotted. The individual measured curves of domain β correspond to different ratios: the bright isolated islands visible in Fig. 4.62e (case A) can be constructed with a ratio of 3:7, while the surrounding dark gray and dark areas fit better to a ratio of 2:8. Domain β in case B fits to a ratio of 5:5 (which equals 1:1), i.e. in this case domain β combines iron silicate and pure silica areas in similar amounts. For cases A and B the LEEM-IV curves of domain β can be decomposed as an overlap of domains of iron silicate and silica next to each other. The domain size is smaller than the used resolution in the shown measurement. However, in LEEM a high number of different intensities are visible,

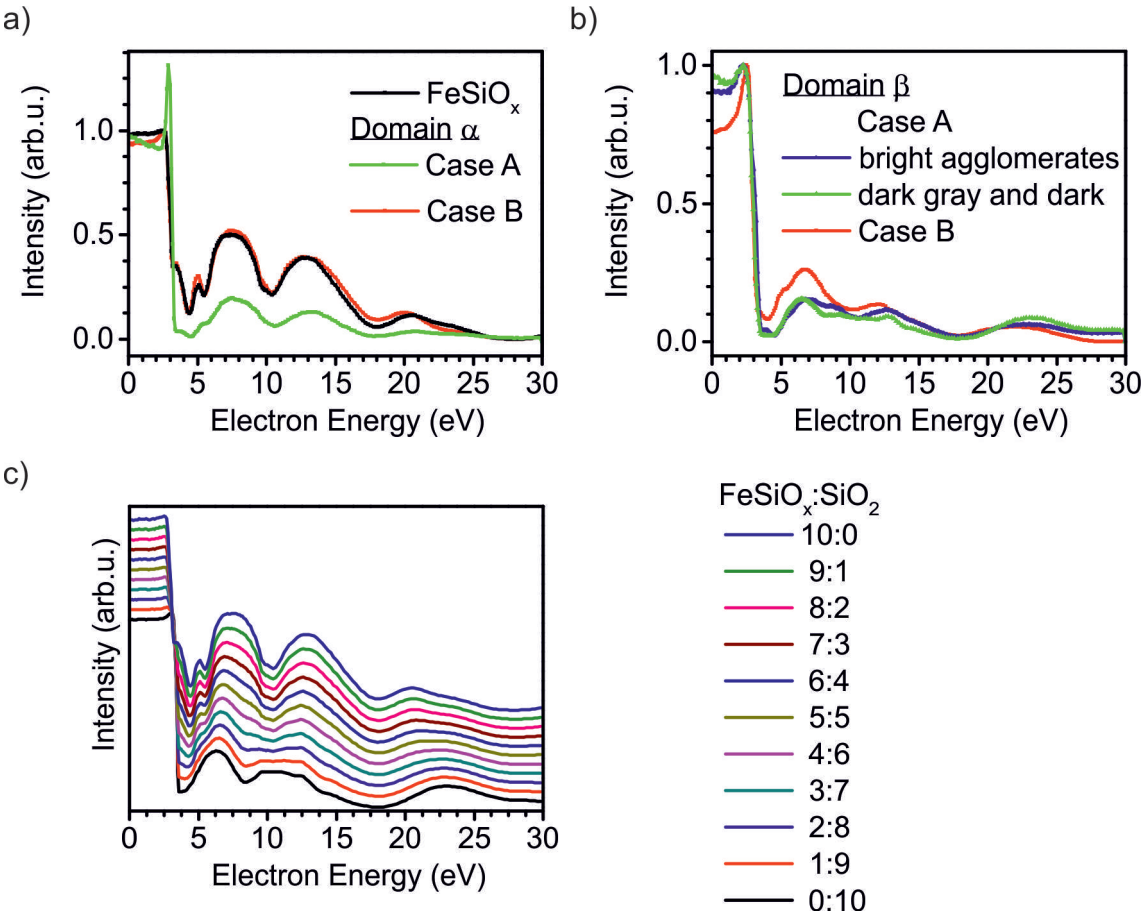

Figure 4.65 LEEM-IV characteristics of a) domains α and b) domains β for incomplete iron silicate films prepared with the "stepwise preparation" method. The curves for case A and case B are taken from preparations with 58 % and 87 % of iron oxide coverage, respectively, after the final annealing step. a) as a comparison the $FeSiO_x$ fingerprint is added, taken from complete layers of $FeSiO_x$ (sections 4.1-4.2). The curves from case A are taken from the preparation shown in Fig. 4.62e). The bright isolated islands correspond to the dot-like areas visible in the inlet. The dark and gray areas correspond to the additional contrast in domain β. The curves for case B are taken from the preparation shown in Fig. 4.62g). c) curves constructed by variable superpositions of the fingerprints of $FeSiO_x$ and a monolayer of SiO_2 (giving rise to a (2x2) curve).

giving rise to an inhomogeneous appearance of domain β (see Fig. 4.63a or Fig. 4.64e).

Finally, XPEEM measurements were performed in order to prove that the front can be indeed explained by migrating iron and is not just a structural transformation. In Fig. 4.66 the Fe 3p and Si 2p lines for case B are given. In both areas, domains α and β the Fe 3p line shows, the presence of iron. The iron amount in domain α is considerably higher than in domain β. The peak positions overlap. The Si 2p line shows the presence of Si in both domains. In domain α the intensity is higher and the FWHM is smaller than in domain β. This corresponds to the better uniformity of the homogeneous iron silicate phase. The peak positions of the Si 2p line of domain α and β are shifted by 0.1 eV, only. This is a big contrast to the XPEEM results in the previous section 4.4.1, where a self-arrangement during oxidation was possible. There, domains with and without iron were found. As a result the Si 2p line of these areas was shifted by 0.4 eV. The smaller difference between domains α and β in the present case underlines that no large areas of unaffected silica are found in the observed size regime.

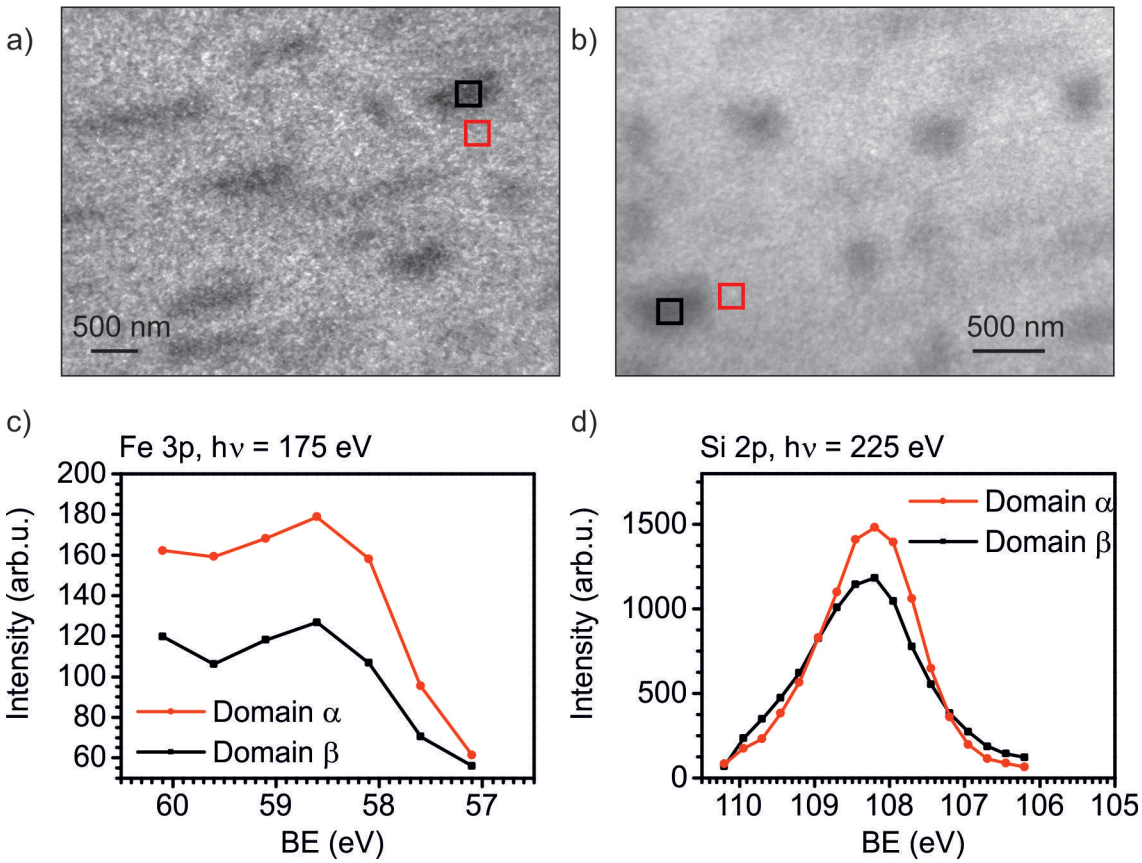

Figure 4.66 XPEEM analysis for an iron silicate preparation using the "stepwise preparation" method for case B (iron oxide amount larger than 80%). Fe 3p (a,c) and Si 2p line (b,d). XPEEM images a) Fe 3p image at E_{kin} = 120 eV and b) Si 2p image at E_{kin} = 120.5 eV. XPEEM scans at the in a) and b) marked areas, respectively. The surface region in a) does not equal the surface position in b). c) Fe 3p scan (hν = 175 eV), d) Si 2p scan (hν = 225 eV).

Summary of incomplete iron silicate layers using the "stepwise preparation" method

As a conclusion, incomplete layers of iron silicate can be prepared by using the "stepwise preparation" method. The fingerprint of the iron silicate islands matches the ones of complete layers of iron silicate. Thus, iron silicate is the most stable form, independent of the domain sizes. However, it turns out that iron migrates from the FeO islands (+Si) into the iron-free areas. Thus, the optimal iron silicate film contains a decreased number of iron atoms.

The migration of iron can be observed in domain β starting at domain α. In case A the percentage of iron is smaller than the one of silicon in domain β. Thus, isolated islands of about 50 nm size are formed, next to a monolayer of SiO_2. While the isolated islands are small domains of $FeSiO_x$, for case A domain β is mainly silica-rich (70-80 % SiO_2 as estimated by the LEEM-IV curves) and thus, a (2x2) structure is visible in LEED. If the iron content is large and with it the average FeO island size (case B), a large number of iron atoms leave domain α and form a front. This front starts at iron-rich terraces and migrates to the center of the iron-free areas. Thus, the complete domain β is filled with these small isolated iron silicate islands and in LEED the (2x2) spots are missing. However, the LEEM-IV curve indicates the presence of SiO_2 islands for 50 % of the area. Furthermore the typical iron silicate LEED pattern is much stronger in case B than case A, which indicates a better long-range order. Since there are no (2x2) spots anymore, the long-range order seems to be missing for the SiO_2 islands. A model for the final structures is given in Fig. 4.67, which compares the state right after silicon deposition (Fig. 4.67a) with the final situation (Fig. 4.67b).

Up to now, it was not possible to solve the question whether the iron oxide layer in iron silicate contains the same number of iron atoms as in FeO (three iron atoms per silica unit cell). R. Włodarczyk and J. Sauer calculated a similar IRAS line position for two iron and three iron atoms per silica unit cell (see chapter 4.1.3). Models for iron silicate for three and two iron atoms per silica unit cell are given in Fig. 4.68 or 4.23. Thus, from these calculations alone a decision was not possible. The experiments reported in this chapter show that iron silicate prepared on the basis of FeO islands decrease the number of iron atoms during the final oxidation step. Since iron is not diffusing into the Ru(0001) substrate, the unnecessary iron atoms diffuse into the neighboring (iron-free) domains. The final fingerprint of the domain α after oxidation and annealing matches the ideal iron silicate fingerprint. Thus, the number of iron atoms per silica unit cell is most likely two rather than three. These findings are of general importance and can be transferred to complete layers of iron silicate, independent of the preparation method (section 4.1-4.2).

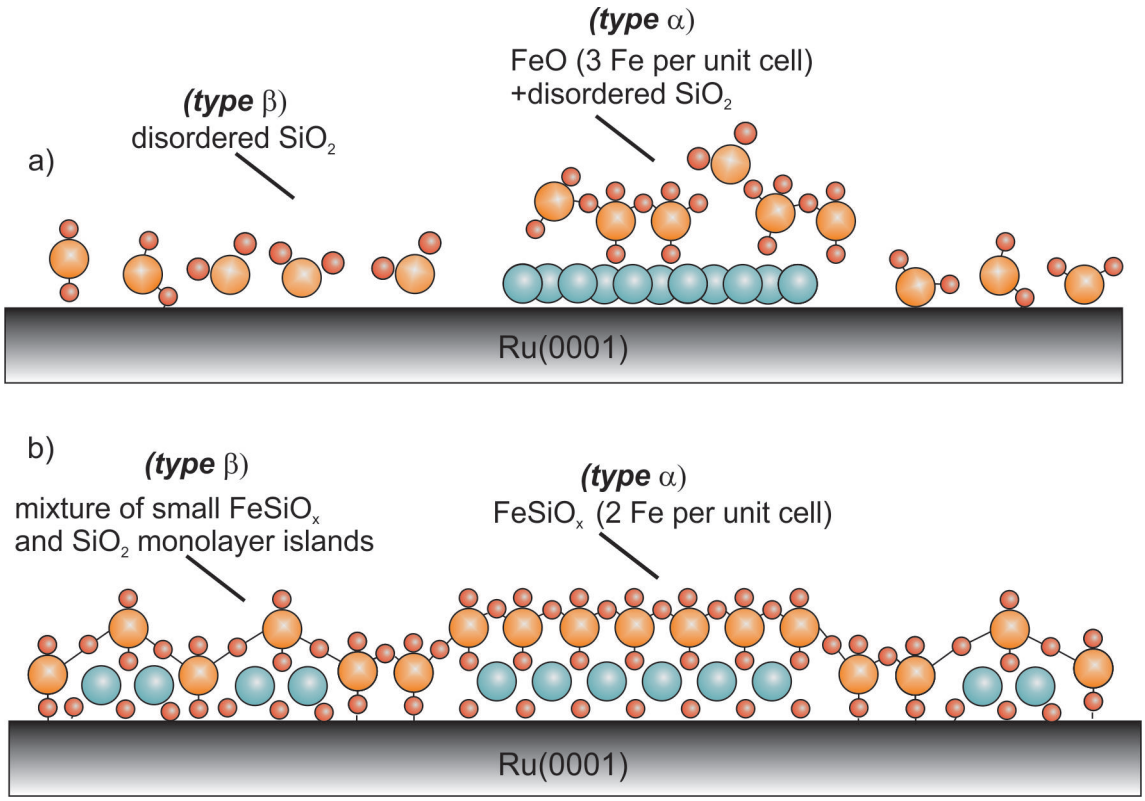

Figure 4.67 Model of the incomplete iron silicate films with the "stepwise preparation" method. a) after Si deposition, b) after final oxidation. Red: Oxygen. Violet: Iron. Yellow: Silicon.

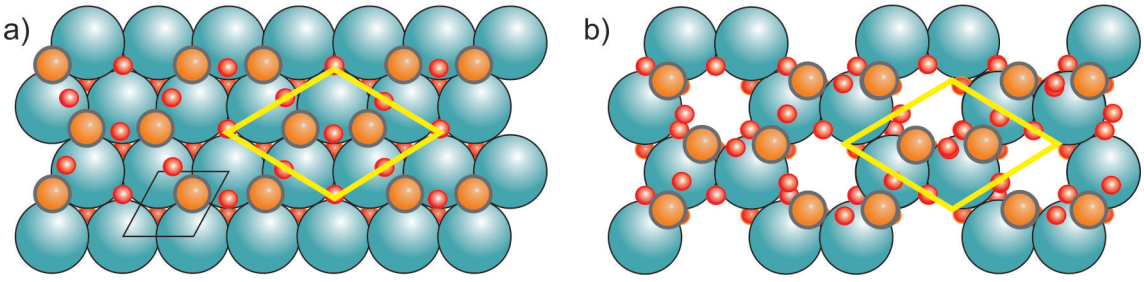

Figure 4.68 Model of $FeSiO_x$ with a) Three iron atoms per silica unit cell and b) Two iron atoms per silica unit cell on basis of calculation from R. Włodarczyk and J. Sauer, HU Berlin (see chapter 4.1.3). In yellow the silica unit cell is indicated. Red: Oxygen. Violet: Iron. Yellow: Silicon.

4.4.3 Incomplete layers with "stepwise preparation" method: Bilayer FeO

In the previous sections 4.4.1 and 4.4.2 incomplete layers of iron silicate were prepared either by self-arrangement with the "combined preparation" method or on basis on pre-prepared FeO islands with the "stepwise preparation" method. In all cases the arranging iron silicate domains give rise to the same fingerprint as for complete layers in sections 4.1-4.2. Thus, iron silicate is energetically favorable even if the degrees of freedom are increased by minimizing the boundary conditions (in this case free lateral movability). As it turned out, the optimal iron silicate structure contains less iron atoms per silica unit cell than FeO. This leads to a diffusion of superfluous iron atoms towards iron-free areas.

In this chapter again the "stepwise preparation" method is used. Bilayer-thick FeO islands are used as a basis for the later iron silicate formation. For this, FeO is prepared by iron deposition in $1.0 \cdot 10^{-7}$ mbar at 800 K. FeO grows in a layer growth, so that the size of FeO islands can be chosen by varying the deposition time of iron. A detailed study for bilayer-thick FeO growth was given in section 3.2. At RT, silicon is deposited (in most cases a ML of SiO_2) in $2.0 \cdot 10^{-7}$ mbar oxygen. Subsequently, the film is oxidized at 1000 K in $1.0 \cdot 10^{-6}$ mbar.

In section 4.3.1 results for a complete layer of iron(bilayer) silicate is shown. As it turned out the two layers of FeO are stabilized by the boundary conditions of the Ru(0001) substrate underneath and the silicon-dioxide layer on top. Iron does not migrate into the Ru(0001) substrate, if an oxygen coverage is present. Furthermore, in section 4.2.1 it was shown that silicon stabilizes the structure of the FeO layer underneath. The LEED pattern resemblance the LEED pattern of iron(monolayer) silicate. However, the LEEM-IV fingerprint is clearly different. Thus, iron(monolayer) silicate and iron(bilayer) silicate can be clearly distinguished. As mentioned before, the usage of only FeO islands minimizes the boundary conditions of the single iron silicate island. Thus, a free arrangement of iron atoms is possible. With this the stability of the second FeO layer and thus, the interlayer bonding strength (Fe-O-Fe) can be tested.

From now on the iron-rich islands will be addressed as domain α, while the iron-free area is called domain β. As will be shown, a Two-step process takes place. The first phase starts at 660 K, while the second phase is observed at around 850 K.

Phase 1: Rim formation

Fig. 4.69 shows a typical oxidation process. In LEEM at 8 eV the iron-rich domains (domain α) are dark, while the iron-free domains (domain β) are gray. The silicon coverage equals the amount necessary for one monolayer of silica. The temperature increases with a rate of 0.5 K/s.

At around 660 K (maintained for 15 min) a rim forms surrounding domain α. The intensity of the rim is very low in the beginning, but it gains intensity very fast until its reflectivity is higher than that of domain α. The rim formation takes place for small and large FeO islands. It should be pointed out that the temperature range in which the rim appears is very similar to that for the ordering of silicon atoms in iron silicate. This is evident through appearance of the typical $(\sqrt{3} \times \sqrt{3})R30°$ LEED spots in the same temperature range. In fact also in the overall LEED pattern of incomplete iron(bilayer) silicate films Moiré spots and the $(\sqrt{3} \times \sqrt{3})R30°$ develop (see Fig. 4.71). After the formation at 660 K

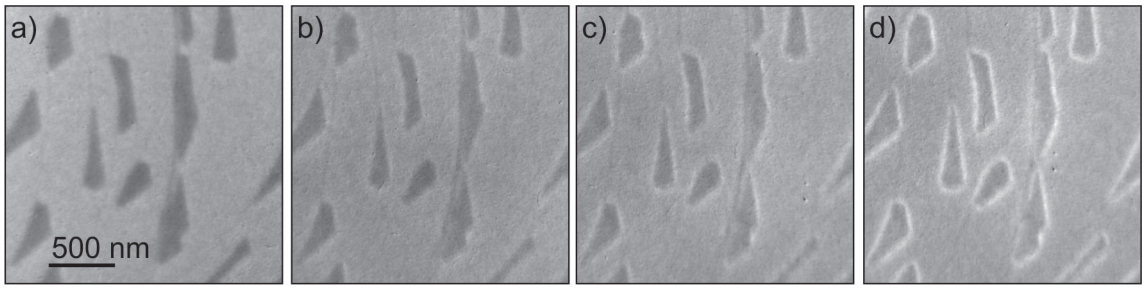

Figure 4.69 Oxidation process of an incomplete layer of iron(bilayer) silicate prepared with the "stepwise preparation" method in LEEM at 8 eV. Images taken at an oxidation temperature of a) 630 K, b) 680 K, c) 695 K and d) 700 K.

the enlargement of the rim can be followed with increasing temperature or time up to a specific length, which seems to be limited. With increasing temperature the rim is appearing faster and also growing faster. The specific length is unchanged by the temperature.

In Fig. 4.70 high resolution images of the rim are shown. In this image domain α is gray, while domain β is dark. Steps and step bunches are nicely visible in domain β. The very bright area is the rim. The edges of domain α are seen to be very sharp and homogeneous. In contrast, the rim, while uniform at the side of domain α, is very inhomogeneous towards domain β. As seen in the images, the rim is an agglomeration of many small domains of the same intensity. The inhomogeneous border of the rim indicates a diffusion process. The size of the rim correlates with the FeO coverage.

As mentioned before, the LEED pattern in Fig. 4.71 shows the superposition of a Moiré pattern, a $(\sqrt{3} \times \sqrt{3})R30°$ structure, both typical for iron silicate, and a weak (2x2) structure. A dark field analysis is performed Fig. 4.71b-c, 4.71e-f for the Moiré spots and $(\sqrt{3} \times \sqrt{3})R30°$, respectively. The FeO coverage for the given measurements is relatively large so that the rim is well distinguishable. The Moiré pattern can be found in domain α as well as in the rim. Individual terraces have a bright/dark contrast, which is switched when probing neighboring LEED spots. The rim itself shows also a bright/dark contrast, which is nearly always opposite to the island in contact. The reason for the different contrast is a large influence of the Ru(0001) ABAB substrate. As a result different contrasts

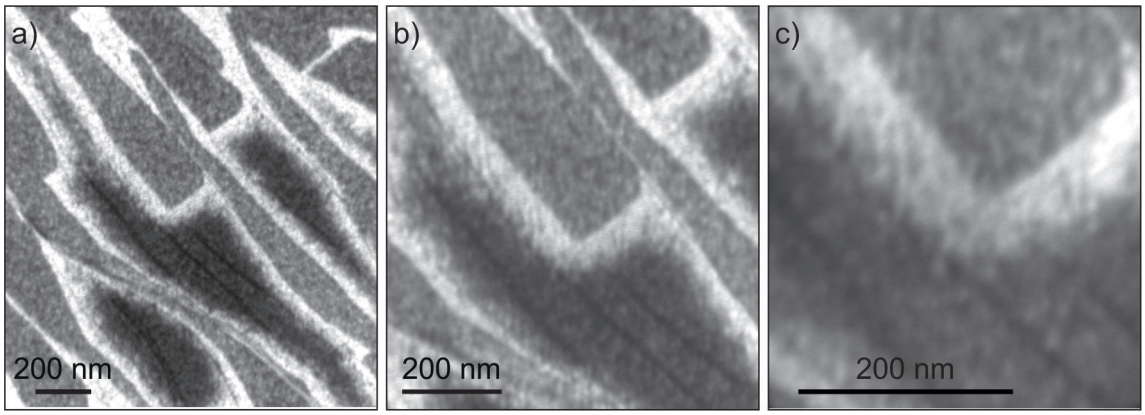

Figure 4.70 High resolution images of an incomplete iron(bilayer) silicate film prepared with the "stepwise preparation" method. LEEM images at 8 eV of an area after annealing at 800 K.

are present for terraces A and B. The results show that the rim forms rather at the next terrace than on the same terrace of domain α. Indications for this finding are also given in the high resolution images (Fig. 4.70), where the individual step bunches in domain β can be followed easily. The dark-field analysis (Fig. 4.71e-f) shows that the rim and domains α give rise to the $(\sqrt{3} \times \sqrt{3})R30°$ spots. However, the rim has a much higher intensity than domain α.

In summary, the dark field analysis shows that the rim has the same LEED structure as domain α a Moiré pattern and a $(\sqrt{3} \times \sqrt{3})R30°$ structure. However, the crystallinity of the rim is already better than domain α, which results in a higher reflectivity in the dark field image. Moreover, the rim preferentially forms on the next terrace. The reason is the influence of the terrace size on the FeO formation. Thus, migrating material has to cross the step edges. The weak (2x2) structure is neither found in the rim nor in domain α. Therefore it must come from the areas in between, which are covered with silicon atoms.

The characteristic LEEM-IV curves for domains α and β and the rim (domain γ) are given in Fig. 4.72. The MEM-LEEM border is similar for all three domains at 3.18 eV (clean Ru(0001): 2.58 eV). The most intense curve by direct comparison corresponds to the rim area. Domain α and domain γ show both nearly the same curve with peaks at 7.4 eV, 13.3 eV. The curves resemble the fingerprint for iron silicate. However, they are in different development states. Domain α resembles the fingerprint for iron(bilayer) silicate at 660 K (see section 4.3.1). In contrast, the rim shows the fingerprint of iron(monolayer) silicate,

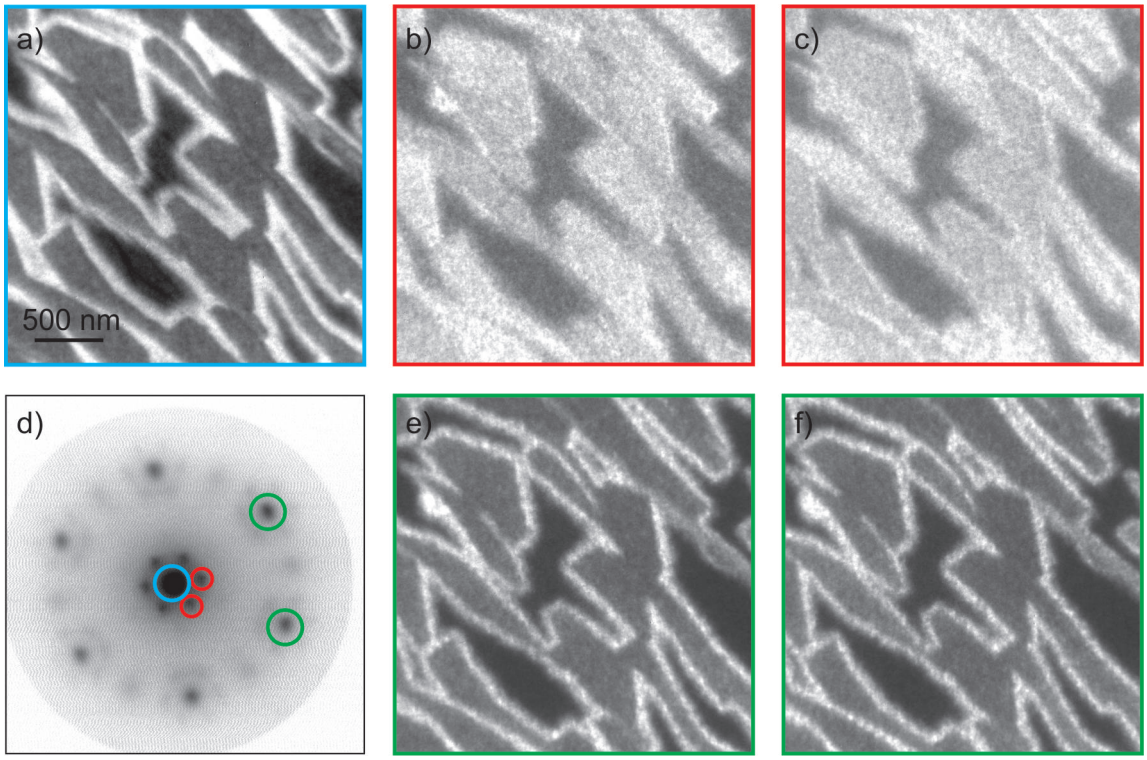

Figure 4.71 Dark field analysis of an incomplete iron(bilayer) silicate film prepared with the "stepwise preparation" method. The images are taken in phase 1 (T = 800 K). a) LEEM at 8 eV. b-c) Moiré spots at 17 eV. d) LEED at 20 eV. e-f) $(\sqrt{3} \times \sqrt{3})R30°$ spots at 17 eV. The chosen spots are indicated in d) and are depicted clockwise.

having a dip at 4.5 eV and a peak at 20.4 eV. Domain β equals a disordered monolayer of silica.The LEEM-IV curve is similar to disordered silica and does not show the peaks, typically present with iron.

XPEEM results for the Fe 3p, Si 2p and O 1s line are given in Fig. 4.73a-b), 4.73c-d) and 4.73e-f), respectively. Only at the Fe 3p line the rim can be properly identified in the XPEEM image. In fact, the rim does contain iron, but in a lower percentage as domain α.

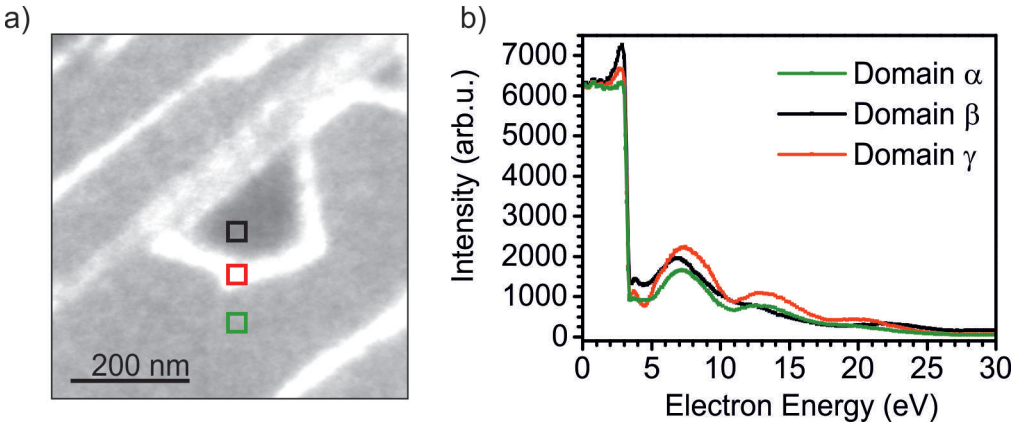

Figure 4.72 Phase 1 (Oxidation temperature T = 800 K) of an incomplete iron(bilayer) silicate film prepared with the "stepwise preparation" method. a) LEEM at 14 eV. b) LEEM-IV curves at the in a) indicated domains.

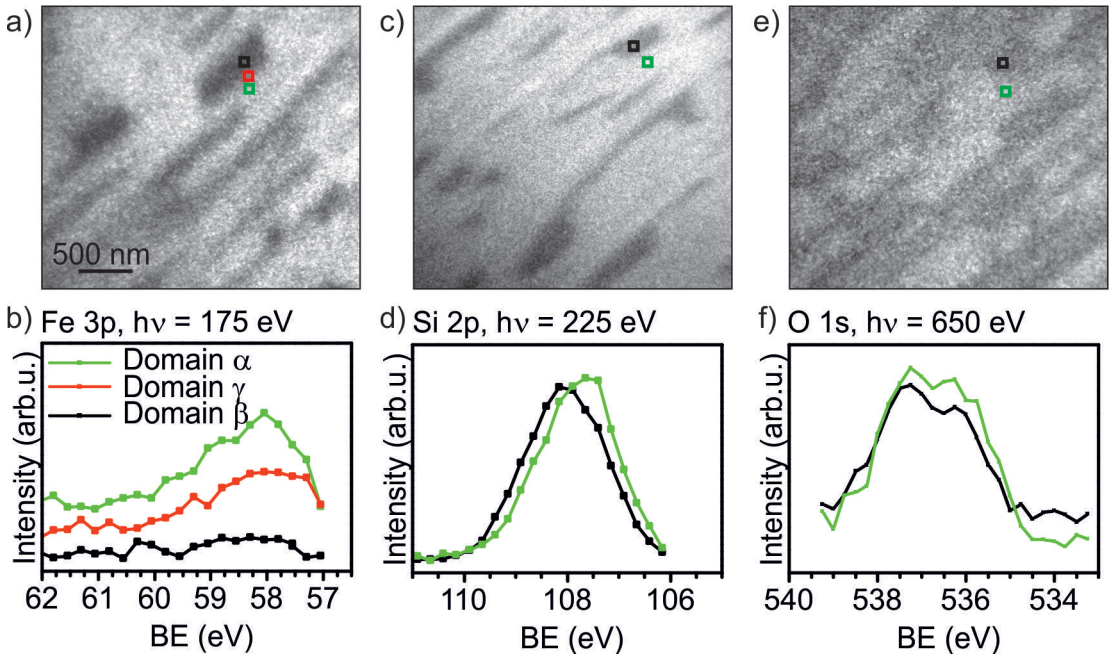

Figure 4.73 XPEEM analysis of an incomplete iron(bilayer) silicate film prepared with the "stepwise preparation" method for phase 1 (oxidation temperature: 695 K). Fe 3p ($h\nu$ = 175 eV) a) XPEEM image at 58.8 eV binding energy. b) local Fe 3p XPS. Si 2p ($h\nu$ = 225 eV) b) XPEEM image at 107.4 eV, c) Si 2p line scan. O 1s line ($h\nu$ = 650 eV). e) XPEEM image at 535 eV. f) XPEEM O 1s scan. The XPEEM images and scan have each been taken at new positions.

This fits well to the LEEM-IV and darkfield results, which already indicated an increased iron concentration in the rim. Thus, the rim consists of the agglomeration of small islands of diffusing iron, leaving domain α. In the Si 2p and the O 1s line only the difference between domain α and domain β can be probed. While the O 1s line gives nearly the same results for both domain, the Si 2p line reveals a clear shift between domain β and domain α. The reason is that in domain α Si binds to iron and in domain β to the Ru(0001) substrate. The O 1s line indicates a slightly higher oxygen concentration in domain α, most likelely due to the two layers of iron oxide.

In summary, the first phase is as follows: Bilayer-thick FeO islands are covered with a monolayer of silicon. At around 660 K the iron atoms are sufficiently mobile to migrate out of the iron-rich islands towards the iron-free areas. The iron atoms leaving the iron-rich domain bind directly to the disordered silica layer and form ordered iron(monolayer) silicate. This happens in form of a rim, surrounding the iron(bilayer) silicate islands. The rim size depends on the size of the island. In contrast to section 4.4.2 the iron amount seems to be much higher per area and thus, the individual isolated domains are stopped by other iron silicate domains. Also the temperature is much lower than for the incomplete iron(monolayer) silicate film in section 4.4.2. In the previous experiments it was found that silicon binds directly to iron through oxygen (Fe-O-Si bond). As XPS results show this takes place already at RT (see section 4.2.1). Taking these results into account it can be assumed that the Si-O-Fe bond is relatively strong and much stronger than the interlayer Fe-O-Fe bond or the Fe-O-Ru bond. This and the relatively low temperature in contrast to the films in 4.4.2 indicate that mainly iron atoms from the second FeO layer (in contact to the Ru(0001)) layer migrate out of the islands.

Phase 2: Further evolution

The second phase depends strongly on the size of the iron-rich islands. Two different cases will be discussed: case A low FeO coverage ($\leq$50 %) and case B large FeO coverage ($\geq$50 %). Both types show the formation of the rim at the border of iron(bilayer) silicate islands. The rim characteristics for both cases are the same.

In Fig. 4.74 the temperature evolution for case A is shown for increasing temperature. In Fig. 4.74a) the rim formation developed in phase 1 is nicely visible. For temperatures higher than 800 K phase 2 takes place. For small islands (case A) the sharpness of the rim diminishes and the border becomes fuzzy. Finally single isolated islands of the size of about 50 nm appear in close surrounding of domain α (Fig. 4.74c), with similar reflectivity as the original rim.

The temperature evolution for large iron(bilayer) silicate islands (case B) is shown in Fig. 4.75. Similar to case A, the rim becomes fuzzy. While in case A isolated islands appear, in case B a front grows, which starts at the rim and moves towards the center of the domain β. The LEEM images indicate that the front itself consists of a high number of small isolated islands. If domain β is very small (and the domain α very large) a complete transformation of domain β is possible, so that domain β assimilates domain α. In Fig. 4.75j) the intensity evolution of domain α, domain β and domain γ (rim) is depicted. The intensity behavior of domains α and γ are comparable for cases A and case B. However, the intensity behavior of case B depends on the size of domain α and the size of the individual domain β. The intensity evolution is taken from a LEEM series at 8 eV. The

first temperature point is at 770 K, where the second phase has not yet started. Under this condition the reflectivity of the rim is nearly 1.5 times higher than that of domain α. The reflectivity of domain β is even lower, which is solely filled with silicon-dioxide. The intensity curves are plotted up to the temperature of 840 K. In the given temperature

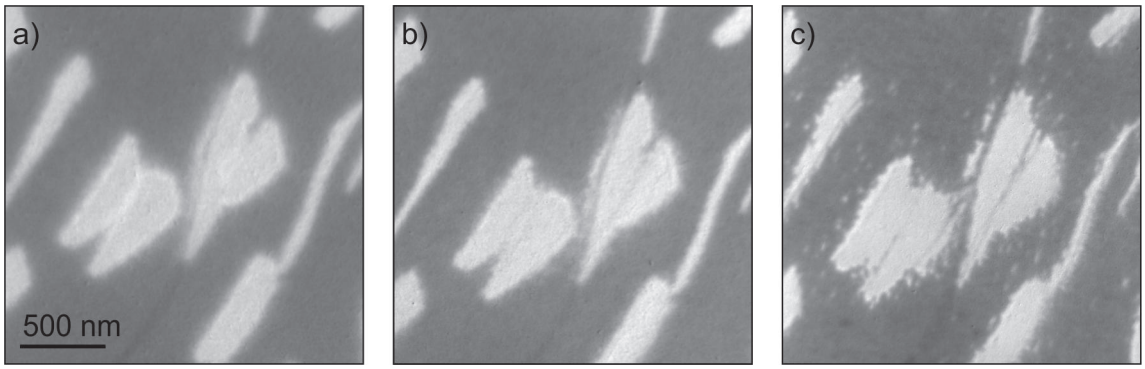

Figure 4.74 Growth mode for small iron amount (case A) of an incomplete iron(bilayer) silicate film prepared with the "stepwise preparation" method. Bright: domain α. Dark: domain β. LEEM images at 8 eV during the oxidation at a) 790 K, b) 850 K and c) 990 K.

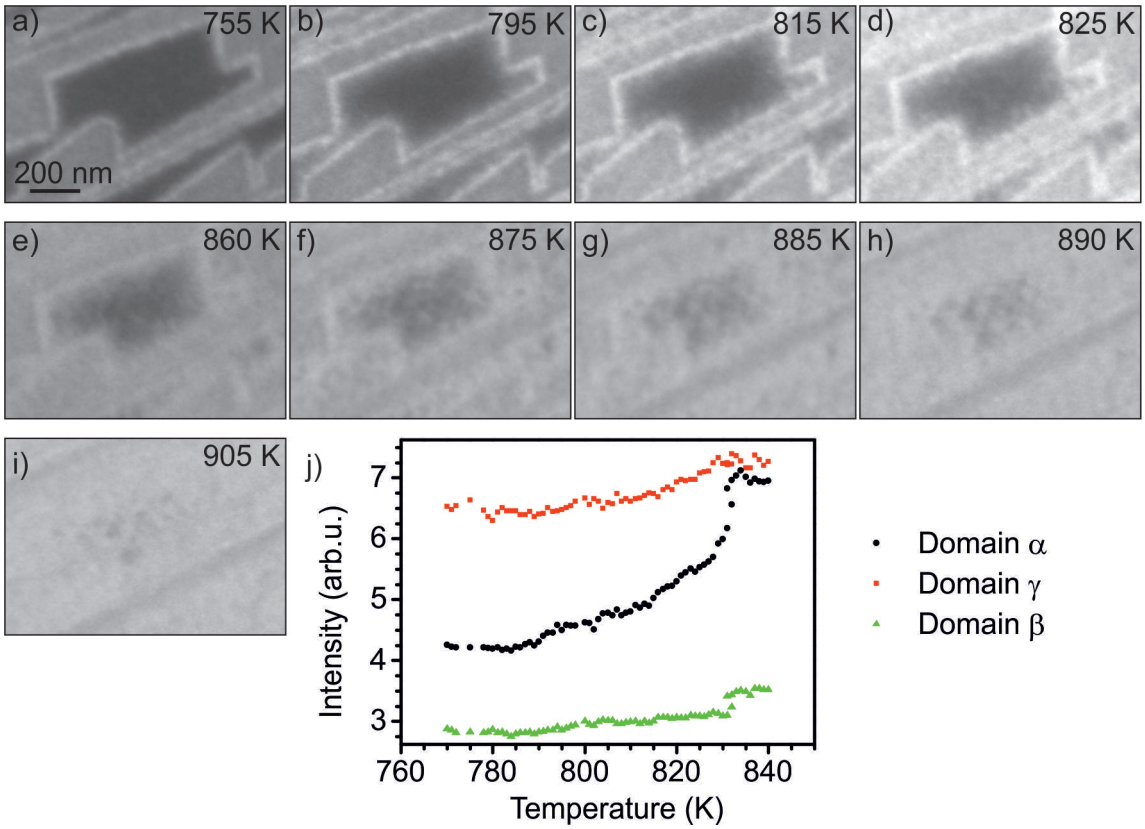

Figure 4.75 Oxidation process of an incomplete iron(bilayer) silicate preparation using the "stepwise preparation" method. LEEM images at 15 eV. The FeO coverage of this sample is 61 % (case B). a)-i) Oxidation series in $1.0 \cdot 10^{-6}$ mbar at the in the image indicated temperatures. j) Intensity behavior during oxidation for a similar preparation with a LEEM series of 8 eV.

range, the reflectivity of the rim increases only by 10 %. This indicates that the rim itself is very stable and in an energetic optimum. In contrast, the intensity of domain α increases drastically in the shown temperature range until the same intensity as the rim is achieved. As a result domains α and γ are not distinguishable anymore. Domain β remains at a low reflectivity until the front passes the measured point and then its reflectivity slightly increases.

A high resolution image after the final oxidation is given for case A in Fig. 4.76. The LEEM images were taken at 8 eV, where domain α (and γ) are bright and domain β is dark. The intensity curves, as well as the LEEM images themselves, show the assimilation of domain α to domain γ. The homogeneity of the iron-rich island is nicely visible. Thus, it can be concluded that the rim and domain α are now structurally and chemically identical. In phase 1 the rim was identified to have the same fingerprint as iron(monolayer) silicate, while domain α still had two layers of FeO (forming iron(bilayer) silicate). The same contrast for both domains indicates that domain α lost its second FeO layer. Also, in the high resolution images, the inhomogeneous border is nicely visible, as well as the small isolated islands in close surrounding. From now on the combined iron-rich island is addressed as domain α.

In Fig. 4.77d) LEED is shown for case A. The signature of iron silicate (Moiré spots and $(\sqrt{3}\times\sqrt{3})R30°$ spots) is well developed. Additionally a blurry (2x2) pattern is present. In Fig. 4.77b-c) and 4.77e-f) Moiré spots and $(\sqrt{3}\times\sqrt{3})R30°$ spots are probed with dark field imaging. Domain α gives rise to both, Moiré spots and $(\sqrt{3}\times\sqrt{3})R30°$. Additionally the Moiré spots show terrace dependent contrast and a contrast change, when probing neighboring terraces. As explained in earlier chapters this is an effect of the Ru(0001) substrate. Very often the border domain α (previously rim) is found at the neighboring terrace. The reasons are growth characteristics of the FeO islands, which prefer to move along a terrace before crossing step edges. As a result the migrating iron must cross step edges. The signal of the $(\sqrt{3}\times\sqrt{3})R30°$ spots is found step-independent in domain α. However the step edges themselves are clearly visible as not covered by iron. The small isolated islands observed in case A in close surrounding of domain α show the same signature as domain α: the Moiré spots and $(\sqrt{3}\times\sqrt{3})R30°$ spots. Nevertheless, the reflectivity in the isolated islands is

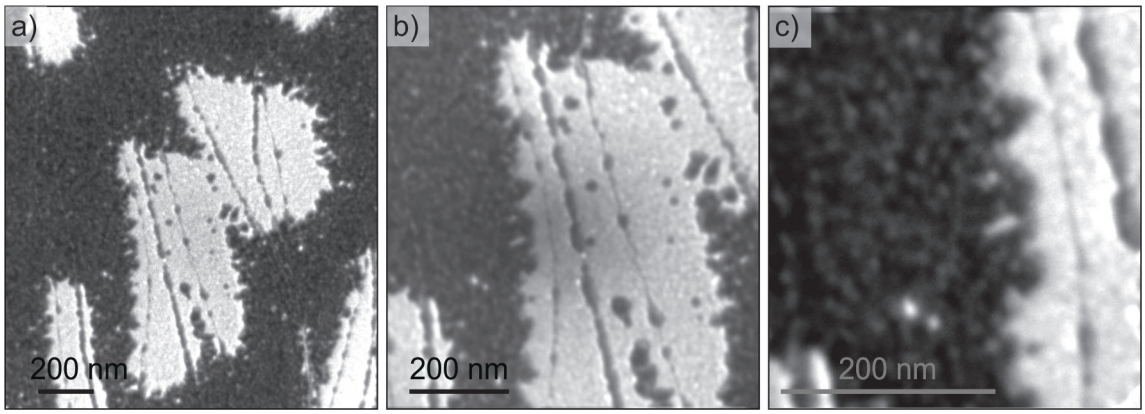

Figure 4.76 High resolution of an incomplete iron(bilayer) silicate film prepared with the "stepwise preparation" method in phase 2 (T = 1000 K) for case A (iron coverage $\leq$50 % after FeO preparation). The individual images are measured images, using different magnifications. LEEM images at 8 eV. Bright: domain α. Dark: domain β.

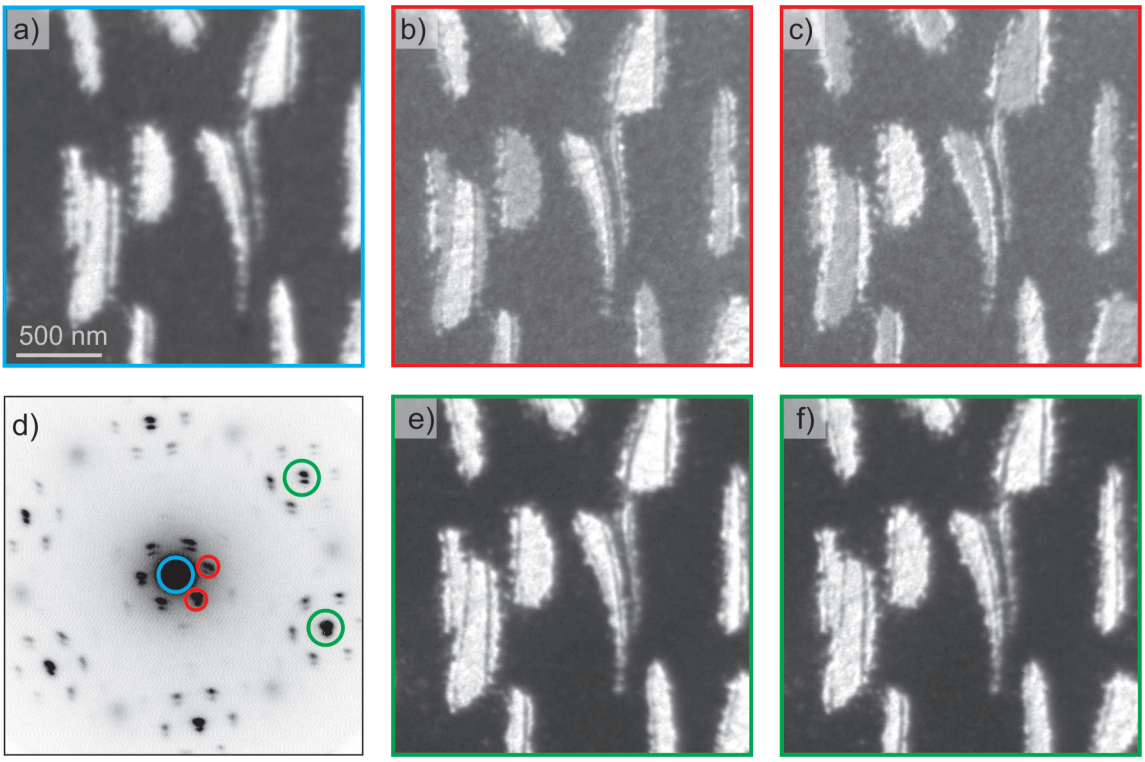

Figure 4.77 Dark field analysis of an incomplete iron(bilayer) silicate film prepared with the "stepwise preparation" method for case A (iron oxide coverage ≤50 %) in phase 2 (T = 900 K). a) LEEM at 8 eV. b-c) Dark field at 17 eV of the Moiré pattern indicated in d) (clockwise). e-f) Dark-field image at 15.2 eV of the rotated spots indicated in d) (clockwise). d) LEED image at 20 eV.

often lower than in domain α. The reason might either be a smaller amount of material or a lower crystallinity. However, the small isolated islands can be identified as iron silicate. Since domain β is neither giving rise to the Moiré spots, nor the $(\sqrt{3} \times \sqrt{3})R30°$ it must give rise to the (2x2) pattern, which is too weak to be imaged with dark field imaging.

In Fig. 4.78 the LEEM-IV curves for case A and case B are given. For both cases domain α shows the typical signature for iron(monolayer) silicate (compare sections 4.1-4.2). This suggests that the originally bilayer-thick FeO layer is reduced to only one iron oxide layer. Since the fingerprint resembles nicely the one shown in the previous section 4.4.2 the iron concentration of this iron oxide layer must be even further reduced to only two iron atoms per silica unit cell (FeO: three iron atoms per silica unit cell per layer). The migration of iron into domain β strongly depends on the individual size of domain α. Thus, their LEEM-IV curves differ strongly for case A and case B. In case A, only a very small amount of iron diffused into domain β. As a result, the LEEM-IV signature fits to a monolayer of silica. For case B, however, the LEEM-IV fingerprint shows the iron silicate signature with only one dip in the low energy range. As was discussed in section 4.2.1 for complete layers of iron silicate the LEEM-IV curve transforms from one dip between MEM-LEEM border and 6 eV to two dips with improved iron silicate film structure. Moreover, a decrease in the iron amount was found to accompany this evolution. Thus, domain β for case B is also iron silicate, but either with more iron than the in domain α which has the double dip), or with a lower film quality.

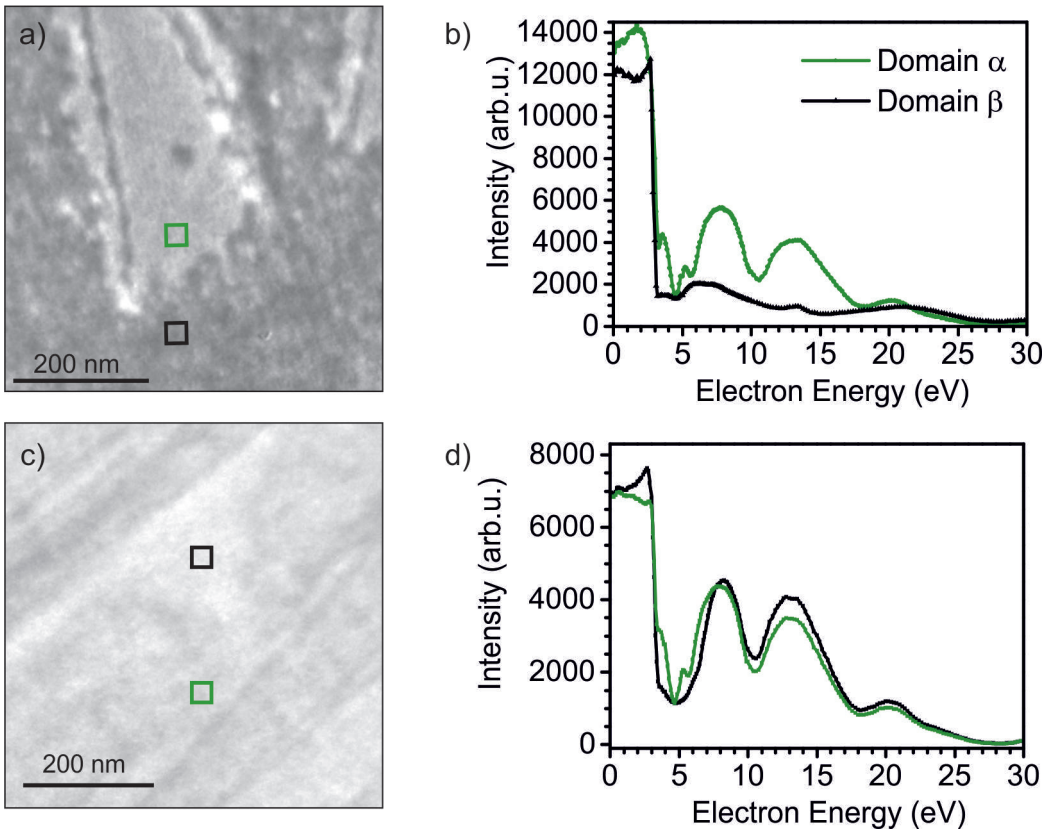

Figure 4.78 LEEM-IV analysis of an iron(bilayer) silicate film prepared with the "stepwise preparation" method for Phase 2 (T = 900 K) for case A (low iron oxide coverage) (a-b) and case B (high oxide coverage) (c-d). LEEM images at 20 eV. LEEM-IV curves in b) correspond to the areas indicated in a). LEEM-IV curves in d) correspond to the areas indicated in c).

Finally, the XPEEM results for the Fe 3p, Si 2p and O 1s line are given for case B in Fig. 4.79a-b), 4.79c-d) and 4.79e-f), respectively. In the Fe 3p as well as the Si 2p line only small differences between domain α and domain β are found. The peak positions in both domains overlap for both elements, only the individual amounts differ. As seen, in domain α, higher iron and silicon concentrations are present. In the O 1s line strong differences are obvious. Especially, the Si-O-Si component (here, at 537.5 eV) is much lower in domain β than in domain α. The Fe-O-Fe line (here at 536.5 eV) is also slightly reduced, which corresponds to the lower iron amount.

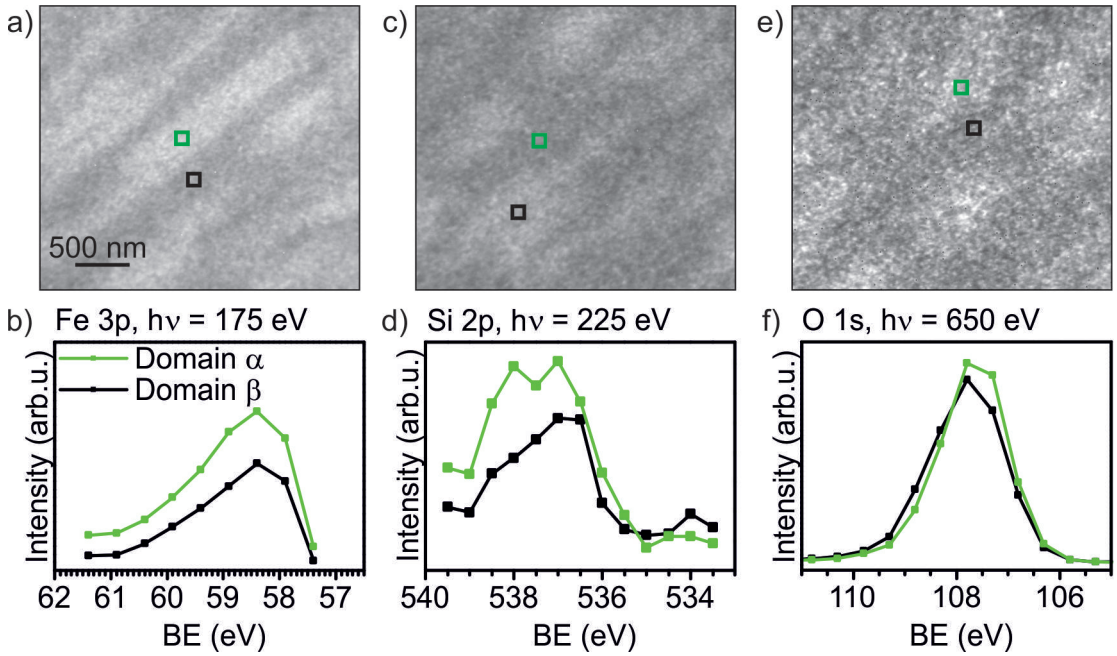

Figure 4.79 XPEEM analysis of an iron(bilayer) silicate film prepared with the "stepwise preparation" method in phase 2 (T = 900 K). XPS Fe 3p line (hν= 175 eV) a) Fe 3p XPEEM image at 57.9 eV binding energy. b) XPEEM Fe 3p line scan. Si 2p (hν = 225 eV) c) Si 2p XPEEM image at 108.8 eV, c) Si 2p line scan. O 1s line (hν = 650 eV). e) XPEEM image at 538 eV. f) XPEEM O 1s scan.

Summary of incomplete iron(bilayer) silicate layers

The complete formation process is depicted in Fig. 4.80. In Fig. 4.80a the situation after the deposition of silicon is shown. Bilayer-thick FeO islands (with three iron atoms per silica unit cell) (domain α) are present next to areas without iron (domain β). The entire surface is covered with a disordered silica layer. In Fig. 4.80b) the first phase is shown. Iron atoms diffuse in all directions out of domain α and bind at the border directly to silicon-dioxide. As a result iron(monolayer) silicate is formed as a well-ordered and homogeneous rim (domain γ). In domain α the iron concentration per silica unit cell is reduced during this process. In the iron-free areas silicon is completely oxidized and begins to order. In Fig. 4.80 c) the second phase is shown. For temperatures higher than 800 K a second wave of iron atoms starts to diffuse out of domain α. For small iron-rich islands the diffusing iron atoms form small isolated islands in close surrounding of the island. For large iron-rich islands the number of iron atoms is very high and thus a high number of small isolated islands are formed, which appear as a front towards the center of domain β. The small isolated islands themselves are again iron(monolayer) silicate islands with the same structure as the original island.

With the leaving iron atoms the reflectivity of domain α increases strongly, while the reflectivity of the rim is nearly unchanged. During this process one of the FeO layer is depleted and only one iron oxide layer remains. Structurally and chemically, domain α matches domain γ (rim) after this process. Both show the fingerprint of two iron atoms per silica unit cell (compare section 4.4.2). Since, the Fe-O-Si bond is found to be really strong and already formed at RT (see section 4.2.1), it is most likely the lower iron oxide layer

(between the Ru-substrate and the next iron oxide layer), which migrates in phase 2. The rim and the later front appear at different temperatures. In fact, when the temperature is held at 690 K for hours, the second phase does not take place. Thus, the activation energy for the individual processes is different.

The results show that that the stability of iron(bilayer) silicate strongly depends on the border conditions (i.e. in a closed layer the reduction of the second is not possible). Iron(monolayer) silicate is the most stable species, energetically preferred and formed with ease.

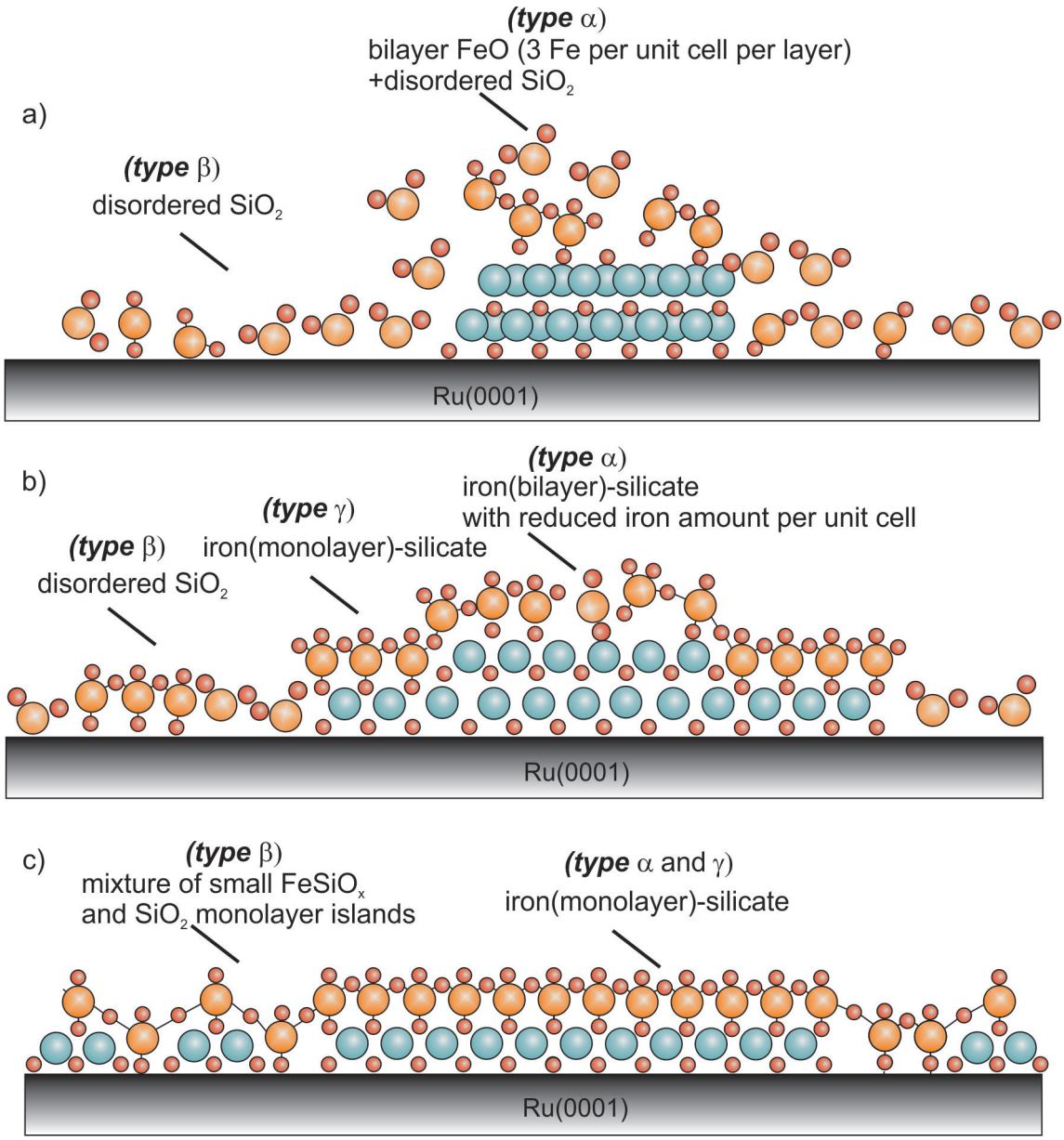

Figure 4.80 Schematic model for the formation process for incomplete iron(bilayer) silicate films using the "stepwise preparation" method. a) after silicon deposition, b) phase 1 ($T \leq 800\,K$) and c) phase 2 ($T \geq 800\,K$). Red: Oxygen. Blue: Iron. Yellow: Silicon.

4.4.4 Summary and conclusion of incomplete layers

In this chapter incomplete layers of iron silicate were discussed. The following preparation methods have been used: the "combined preparation" method (section 4.4.1), and the "stepwise preparation" method for monolayer FeO islands (section 4.4.2) and bilayer FeO islands (section 4.4.3).

The "combined preparation" method gives information about the formations process, when neither silicon nor iron is pre-crystallized. Three individual domains are formed: (i) an iron silicate phase, (ii) a (2x2) monolayer of SiO_2 and (iii) a bilayer of SiO_2 with rotated (2x2) structure. The iron silicate phase equals the phase for complete iron silicate film (i.e. has the same fingerprint). Interestingly monolayer and bilayer SiO_2 phases have different structures. In fact, the bilayer SiO_2 phase shares the same distances and orientations of the silica layer on top of iron oxide. Incomplete layers with less silicon than necessary for a complete monolayer of silica prefer the growth with iron rather than covering the Ru(0001) substrate. This indicates that silicon atoms start to order first on top of iron oxide and might even continue the growth in areas where no iron is present (in bilayer films). Other nucleation centers on the free Ru(0001) substrate in turn lead to the formation of typical (2x2) SiO_2 monolayer films. As it was observed already for complete iron silicate layers, iron lowers the oxidation temperature of Si to SiO_2. As a result, the monolayer of SiO_2 shows reduced components in the Si 2p line, while in the iron silicate areas silicon is already completely oxidized (Si^{4+} state).

The "stepwise preparation" method enables the observation of dynamical processes with pre-defined iron oxide islands. Thus, the processes can be directly compared with silicon-free iron oxide islands from sections 3.1 and 3.2. In section 4.4.2 monolayer-thick FeO islands are used as a basis for iron silicate formation. As a result iron-rich areas and iron-free areas are pre-defined. The sample is covered with a monolayer of SiO_2. Upon oxidation at elevated temperatures, iron is found to migrate from the iron-rich areas towards the initially iron-free areas. In the iron-free areas the diffusing iron forms small isolated islands, which can be identified as small iron silicate domains. Next to the iron silicate domains small SiO_2 domains are present. The fact that a decrease of the iron concentration in the FeO based iron silicate islands gives rise to the iron silicate fingerprint, shows that iron silicate contains a lower amount of iron atoms than a FeO layer. This indicates that the iron silicate layer contains only two iron atoms per silica unit cell.

In section 4.4.3 bilayer-thick islands of FeO are used as a basis for the incomplete layers. Similar to the case with monolayer thick FeO islands iron migrates from the iron-rich areas to the iron-free areas. However, the process is different. After silicon deposition the iron-rich islands consist of 1 ML of silica on top of 2 ML of iron oxide. With rising temperature iron atoms migrate from the center of the island to its border. Since the temperature is much lower than those observed for the monolayer-FeO islands (section 4.4.2) it can be assumed that during this phase the second layer (in contact to the Ru-substrate) is migrating. When the iron atoms reach the outer border of the individual island, they bind to the silicon dioxide present in the iron-free areas and form again an iron silicate film (appearing and addressed as rim). This newly formed iron silicate film has only one iron oxide layer left and grows in nearly perfect crystallinity up to a specific rim size that depends on the deposited iron amount and the relative island sizes. The crystallinity of the original island improves during this step, as could be seen by the increased reflectivity and the approach to the known iron silicate fingerprint from closed layers. When the rim is reformed at an

increased temperature of 800 K a second phase starts, which depends again on the island sizes. For small islands the rim and the original island reach the same crystallinity (seen in the electron reflectivity) and iron concentration. The LEM-IV fingerprint shows that the islands only have two iron atoms per silica unit cell left (instead of six in the as-prepared FeO layer). In the close surrounding very small isolated islands form, which have a similar electron reflectivity as iron silicate and are most likely very small iron silicate domains. If the iron-rich domains are small enough, a (2x2)-ML of SiO_2 forms in the iron-free domains. If most of the surface is covered with iron oxide islands ($\leq$60 %) in the second phase the rim growth continues and the iron-free holes are transformed to iron silicate. The crystallinity of the iron silicate film formed in the second phase of the process is below that of the original iron silicate islands.

As a conclusion the formation of incomplete films gives rise to a high number of information of the dynamical processes and thermal stabilities of iron silicate films. Silicon dioxide stabilizes the iron oxide layer. In comparison to silicon-free iron oxide islands the iron silicate film is stable up to much higher temperatures. However, the energetically optimal situation includes a reduction of iron atoms per silica unit cell, so that only 2/3 of the iron atoms per silica unit cell of a FeO layer remain. The additional iron atoms are free to diffuse, in case the layer is not close, but iron-free areas are present. This effect is strongly visible for the bilayer-thick iron silicate films. In section 4.3.1 it was shown that the second layer of iron oxide neither diffuses into the Ru(0001) substrate nor desorbs from the surface. However, islands of bilayer-thick iron silicate transform into monolayer-thick iron silicate islands (with a reduced number of iron- atoms per silica unit cell). But not only for iron oxide iron silicate is the most stable situation, but also for silicon the formation of iron silicate is energetically favorable compared to the formation of a silica monolayer directly on top of the Ru(0001) substrate. Moreover it was reconfirmed that iron acts a catalyst and lowers the oxidation temperature of silica.

4.5 Summary and conclusion of ultrathin $FeSiO_x$ films

This chapter discusses ultrathin iron silicate film on Ru(0001) and is divided in the investigation of complete (chapter 4.1 - 4.3) and incomplete layers (chapter 4.4). This has the advantage to study homogeneity and structural changes in the layer by means of XPS and LEED. Furthermore it is possible to investigate the complete and incomplete layers regarding their stability and dynamic processes using characteristic fingerprints.

In chapter 4.1 - 4.2 iron silicate, consisting of a ML of Fe and a ML of Si is prepared with different preparation methods. An overview of the different methods is shown in Tab. 4.10. Two different approaches are chosen: the "combined" approach (chapter4.1) and the "stepwise" approach (chapter 4.2). In the "combined" approach iron and silicon are deposited at the same preparation step under the same conditions. In section 4.1.1 this takes place in oxygen surrounding ("combined preparation" method), while in section 4.1.2 UHV conditions are chosen ("combined UHV preparation" method). In contrast, in the "stepwise" approach either FeO (section 4.2.1, "stepwise preparation" method) or silica (section 4.2.2, "stepwise reversed preparation" method) are pre-prepared before silicon or iron are deposited, respectively. In the "combined" approach iron and silicon have more freedom to diffuse and order than in the "stepwise" approach, where a structure is already pre-set. In all cases the final step is an oxidation in $1.0 \cdot 10^{-6}$ mbar at elevated temperatures. In sections 4.4.1 and 4.4.2 investigations and findings on incomplete layers, which were prepared using the "combined preparation" and "stepwise preparation" method, are discussed. All preparation methods lead to the same iron silicate fingerprint, which proves that this is the most stable configuration in the measured temperature ($\leq$ 1000 K) and pressure regime ($1.0 \cdot 10^{-6}$ mbar).

In the following the individual preparations are addressed and their main information is summarized.

The *"combined" approach* (chapter 4.1) starts with disordered films and thus enables free arrangement of the atoms. In the "combined preparation" method silicon is deposited first in oxygen surrounding and on an oxygen pre-covered Ru(0001) substrate. As a result, silicon becomes completely oxidized (Si^{4+} state) and Si-O-Si and Si-O-Ru bonds are formed before iron is deposited. In the "combined UHV preparation" method this is prevented by deposition of iron first. Temperatures at which the iron oxide layer and the silica layer on top of iron begins to order are measured by the appearance of the Moiré pattern and by 30° rotated spots, respectively. The deposition in UHV conditions lowers the temperature for iron oxide arrangement from 660 K to 570 K and the arrangement of the silica layer from

Preparation method	Abbreviation	Section (complete layer)	Section (incomplete layer)
combined	Si+Fe/3O-Ru(0001)	4.1.1	4.4.1
combined UHV	Fe+Si(UHV)/Ru(0001)	4.1.2	-
stepwise	Si/FeO/Ru(0001)	4.2.1	4.4.2
stepwise reversed	Fe/SiO_2/Ru(0001)	4.2.2	-

Table 4.10 Overview on different preparation methods for iron silicate consisting of a monolayer of silicon and a monolayer of iron.

660 K to 650 K. Moreover the characteristic LEEM-IV fingerprint for the final iron silicate is found already at 900 K, and thus 100 K lower as for the deposition in oxygen. At around 660 K ("combined preparation") and 650 K ("combined UHV preparation") the iron silicate LEED pattern and the position of nearly all features in the LEEM-IV fingerprint are already present. For higher temperature only one dip at 5.5 eV is formed additionally in the LEEM-IV curve, which can be used as a indication for iron silicate film composition and quality. Apart from that with increasing temperature the other LEEM-IV peaks further gain intensity, as well as the LEED spots. This can be attributed to a defect reduction inside the film.

Incomplete films, prepared using the "combined preparation" method (section 4.4.1), show that for silicon it is energetically preferred to bind to iron and rather form iron silicate than solely covering the clean Ru(0001) substrate. As a consequence different domains are found depending on the Fe:Si ratio. First domains of iron silicate form. If the silicon amount exceeds the iron amount two different silica phases form: 1) a silica bilayer, which is rotated by 30° and found in most cases in contact to iron silicate. Since the dimensions and structure fit exactly to the silica layer in iron silicate, it can be assumed that silicon indeed starts to form silica first on iron and then continues to grow next to iron in pure bilayer silica films. 2) In the rest of the iron-free area silicon atoms form small monolayer silica domains on nucleation centers. The iron free silica films are found to have reduced components in the Si 2p line, while the silica in iron silicate is completely oxidized. This indicates that iron acts as a catalyst for silicon oxidation.

In the *"stepwise" approach* (chapter 4.2) first either FeO or silica are prepared, before silicon or iron are deposited, respectively. This procures a pre-ordering of one of the elements as an oxide, which makes it suitable to study the transformation from this layer to iron silicate.

The "stepwise preparation" method (section 4.2.1) is closest to the iron silicate structure, which consists of a FeO-like layer with a silica monolayer on top. The characteristics of the iron oxide layer in iron silicate are one of the main questions of this thesis. The structure and characteristics of a pure FeO layer is well-known from chapter 3.1. Therefore, the "stepwise preparation" method gives direct information about the changes a FeO layer (+Si) must undergo in order to form iron silicate. The FeO layer reduces the Fe-Fe distance during the preparation process in order to form a "8 on 9" reconstruction. While these Fe-Fe distance were already measured for the "combined preparation" in the "stepwise preparation" the "6 on 7" reconstruction of FeO is actively altered. This becomes possible since silicon has a higher bond dissociation energy than iron (bond dissociation energies for Si-O: 798 kJ/mol, for Fe-O : 409 kJ/mol, and Ru-O: 481 kJ/mol [2]). As a consequence silicon binds to the oxygen layer in FeO and forms Fe-O-Si bonds, while reducing the iron atoms. In a subsequent oxidation step silicon arranges first (already at 460 K), before oxygen can intercalate to the iron layer underneath and iron oxide is ordering in a Moiré pattern. The temperature is similar to the "combined UHV preparation" method at 645 K. In contrast to a pure FeO layer iron is not only found in the Fe^{2+} state, but mainly in the Fe^{3+} state. This indicates an additional oxygen layer at the iron/ruthenium interface. At higher temperatures the iron content is slightly reduced in complete films, which takes place at the same temperatures as the additional dip at 5.5 eV in the LEEM-IV spectra develops. This indicates a correlation between this dip and the iron reduction. The final film is already present at 900 K.

Incomplete layer using the "stepwise preparation" method confirm the reduction of iron in the iron silicate islands with increasing temperatures. In fact iron migrates from the initial iron silicate islands towards iron-free areas (covered with silicon) and form with the present silicon small isolated islands of iron silicate in close surrounding to the initial iron silicate islands. If the iron coverage is very high these isolated islands can even combine to a front starting at the initial iron silicate islands and migrate to the center of the iron-free holes. For an iron content larger than 0.8 ML (i.e. small holes) in the initially iron-free areas a 1:1 distribution of (iron silicate): (silica ML) is found. The initial iron silicate island itself shows the typical iron silicate signature with a dip at 5.5 eV in the LEEM-IV curve. From the reduction of iron when transforming FeO (+Si) to iron silicate it can be concluded that the number of iron atoms per silica unit cell is reduced from three to two.

The "stepwise reversed preparation" method (section 4.2.2) investigates the transformation from a silica monolayer (+Fe) to iron silicate. The silica monolayer is strongly bond to the Ru(0001) substrate. Thus, a very high temperature of 825 K is needed before Si-O-Si and Si-O-Ru bonds are broken and the ML silica transforms to iron silicate. In fact Fe-O-Si bonds are not formed at RT, as it was the case for the other investigated preparation methods. The transformation takes place everywhere on the surface in small domains. Surprisingly a Moiré pattern is already found at 525 K, which is either iron arranging on top of the silica monolayer or in silica free areas, like the substrate steps. The final iron silicate signature is found at 1000 K. This preparation shows that iron silicate is not only the energetically preferred film if iron and silicon are disordered (like in the "combined preparation" method), but also it is preferred regarding a silica monolayer (+Fe), which is already strongly bound to Ru(0001) and saturated (no dangling bonds).

In chapter 4.3 the stepwise preparation is used in order to prepare iron silicate with *multiple layer* of either FeO (section 4.3.1) or silica (section 4.3.2). The individual films are addressed to as iron(bilayer) silicate and iron silicate(bilayer), respectively. Iron silicate with only one monolayer of iron and silicon will be addressed to as iron(monolayer) silicate or iron silicate(monolayer) in order to highlight the difference in the films. An overview of the different preparations are given in tab. 4.11. Incomplete layers of iron(bilayer) silicate are discussed in section 4.4.3.

In section 4.3.1 a FeO BL is used as a basis for iron(bilayer) silicate formation. The FeO BL is characterized in chapter 3.2. In complete layers the two layer of FeO remain and silica orders in the same way as on a ML FeO. The strength of the Si-O-Si bond and its influence on both of the layers is confirmed, since both FeO layer reduce its Fe-Fe distance to a "8 on 9" Moiré reconstruction. Additional to the characteristic iron silicate pattern, also found in iron silicate out of ML FeO (iron(monolayer) silicate), a low intense (3x3)

Preparation method	Abbreviation	Section (complete layer)	Section (incomplete layer)
iron(bilayer) silicate	ML Si/BL FeO/Ru(0001)	4.3.1	4.4.3
iron silicate(bilayer)	BL Si/ML FeO/Ru(0001)	4.3.2	-

Table 4.11 Overview on iron silicate films with multiple layer of either iron oxide or silica. In both cases the "stepwise preparation" method is used, i.e. first the FeO layer is prepared, and as second step silicon is deposited in $2.0 \cdot 10^{-7}$ mbar, before the film is oxidized in $1.0 \cdot 10^{-6}$ mbar.

pattern is visible. It can be assumed that this results out of iron atoms arranging in a (3x3) pattern. These iron atoms can either be iron atoms in the top most layer or iron atoms which diffuse to the top. Since silicon is found to stabilize the iron oxide layer underneath it can be assumed that this is also the case for these iron atoms. Thus, they remain most likely underneath the silica layer, leading to a buckling of the silica layer.

In incomplete films of iron(bilayer) silicate (section 4.4.3) it is found that the two iron oxide layer are only stable for complete layer, but not in incomplete films. Iron diffuses out of the iron silicate films in two phases. In the first phase the number of iron atoms per silica unit cell and per layer is reduced from three iron atoms to two. This takes place in both iron oxide layers. The migrating iron atoms bind to silica atoms at the border of the initial island and form a rim. This rim shows the signature of iron(monolayer) silicate. In the second phase iron atoms in the lower iron oxide layer in the initial iron(bilayer) silicate island leave the islands as well and migrate further than the rim into the iron-free holes (covered with disordered silica). There iron forms small isolated islands, which again show the iron(monolayer) silicate signature. In case the initial iron(bilayer) silicate coverage was larger than 60 % these isolated islands combine to a front, which closes the holes. As a result these initial iron-free holes transform to iron(monolayer) silicate as well, however, missing the dip at 5.5 eV in the LEEM-IV spectra, which indicates a higher defect state. The initial iron(bilayer) silicate islands transform due to the iron loss to iron(monolayer) silicate (including the dip at 5.5 eV in LEEM-IV). The size of these islands is enlarged by the size of the rim, which cannot be distinguished anymore form the initial iron(bilayer) silicate island.

Finally in section 4.3.2 complete layer of iron silicate(bilayer) are discussed, i.e. a bilayer of silica on top of a monolayer of FeO. Again the "stepwise preparation" method is used. The LEED pattern of iron silicate(bilayer) equals the one of iron silicate(monolayer). The reason is the strong Fe-O-Si bond, which connects the lower silica layer to iron oxide. However, the second silica layer seems to be strongly bond as well, as no transformation from this crystalline bilayer to a vitreous bilayer is observed. In order to combine strong Fe-O-Si bonds with Si-O-Si bonds of the second silica layer a structure is proposed in which every second silicon atom in the lower silica layer binds to iron or the second silica layer on top. The upper silica layer follows this bonding. Nevertheless, this structure would have dangling bonds. As there are always OH groups in the chamber, they might be likely to bind to these dangling bonds.

In summary, iron silicate can be described as a two-layer system consisting of an iron oxide monolayer in contact to the Ru(0001) substrate with a monolayer of silica on top. In Fig. 4.81 the proposed structure is depicted. The iron oxide layer resembles a ML of FeO, however the Fe-Fe distances are decreased to 3.044 Å (FeO: 3.157 Å), which corresponds to a "8 on 9" Moiré pattern on Ru(0001) (FeO: "6 on 7" Moiré pattern). Moreover, the number of iron atoms per silica unit cell is reduced to two (FeO: three iron atoms per silica unit cell). The positions of "missing" iron atoms in respect to a complete iron oxide layer (with three iron atoms per silica unit cell) gives rise to the by 30° rotated structure. Iron atoms are found in the Fe^{2+} and Fe^{3+} state. This indicates a higher number of oxygen atoms than iron atoms, which is most likely resulting out of an oxygen layer on top as well as underneath the iron layer, i.e. at the iron/ruthenium interface. As a result Fe-O-Fe and Fe-O-Ru bonds exist. The oxygen atoms on top of the iron layer are connecting the silica layer with the iron oxide layer (Fe-O-Si bonds). The silica layer is in a tetrahedral coordination, with three Si-O bonds in plane and one bond pointing downwards to the iron

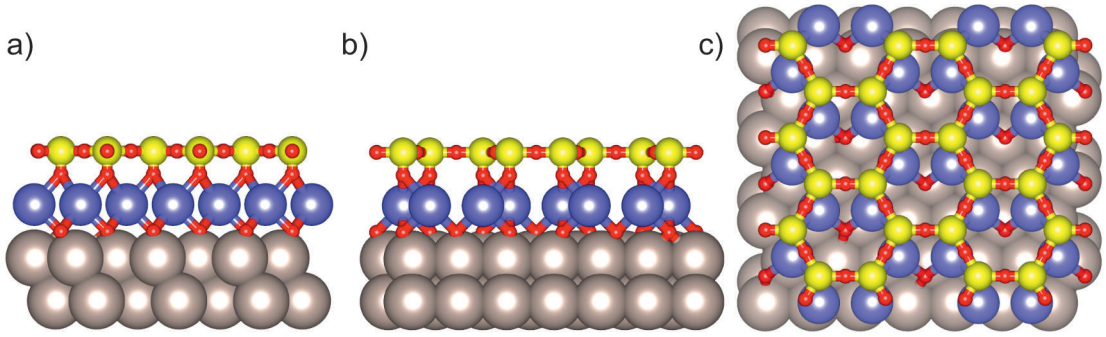

Figure 4.81 Proposed structure for ultrathin iron silicate films with two iron atoms per silica unit cell. Red: Oxygen. Violet: Iron. Yellow: Silicon. Gray: Ruthenium.

oxide layer. Thus, the silicon atoms are completely oxidized in the Si^{4+} state. The silica layer is unrotated regarding the iron oxide layer underneath, but shifted in respect to the positions of the iron atoms. The optimal Si-O-Si bond length defines the Fe-Fe distances in the iron oxide layer, which indicates a strong Fe-O-Si and Si-O-Si bond. The silica layer stabilizes the iron oxide layer underneath.

Chapter 5

Ultrathin layers of $FeGeO_x$ on Ru(0001)

Germanium is in the same main group as silicon, but in one period higher. As a result the number of valence electrons is the same for silicon and germanium. The number of electrons in a germanium atom ($1s^2$ $2s^2$ $2p^6$ $3s^2$ $3p^6$ $3d^{10}$ $4s^2$ $4p^2$) exceeds the one of silicon ($1s^2$ $2s^2$ $2p^6$ $3s^2$ $3p^2$), as is its size. Similar to silica germania exist in vitreous and quartz forms [69]. Moreover they share similar bond lengths. It should be noted, that the average Ge-O-Ge bond (3.17 Å, see Fig. 5.18) exceeds the average Si-O-Si bond (3.06 Å, see Fig. 4.20), due to the larger size of the germanium atoms [92]). Germania investigated in ambient pressures can be used as models for silica structures at higher pressures [29].

On Ru(0001) a monolayer of germania can be prepared [51]. It consists of corner-sharing GeO_4 tetrahedra. As a result germania can be described as a six-fold ring system parallel to the surface, where the germanium atoms are connected through oxygen atoms (Ge-O-Ge bonds). Germania atoms in the corner sit on top and the fcc hollow sites on the Ru(0001) atoms. Moreover there is a strong link between corner sharing GeO_4 blocks and the substrate through oxygen (forming Ge-O-Ru bonds). In contrast to ultrathin silica monolayers the germania monolayer has more variations in the angular arrangement of the tetrahedral building units and a more strongly coupled interaction of the films system with Ru(0001) [51].

The integration of iron into germania opens the possibility to modify the reactivity of these films. In the literature especially melted powders are used to investigate these kinds of glasses, for instance in magnesium iron germanate [65] or sodium iron germanate glasses [61]. Moreover, a phase diagram for the GeO_2-FeO-Fe_2O_3 system is given in [94]. Even though the preparation of these melted powders is very different to the preparation in this work, as not only very high temperatures are used but also the samples are produced in air, some characteristics might be comparable. In these glasses iron was found to be in the Fe^{2+} and Fe^{3+} oxidation state, where the increase of iron increases the Fe^{3+} concentration. However, atoms with the Fe^{3+} oxidation state are most likely in intermediate positions. Germanium has a lower electronegativity than silicon. As a result the O 1s splitting between the Ge-O-Ge line and the Ge-O-Na lines is decreased in contrast to sodium iron silicate glasses [60] (germanium: 1.6 eV, silicon: 2.1 eV). The Ge-O-Fe(II) and Ge-O-Fe(III) peaks are calculated to be at an energetically intermediate position to the Ge-O-Ge and Ge-O-Na line. Nevertheless, the intensity is expected to be very small and in particular much smaller than for Si-O-Fe composites.

In this work ultrathin two-dimensional layers of iron germanate are prepared on Ru(0001). While silicon and germanium can be seen as analogues in their properties and structures, it will be interesting whether this is also the case for ultrathin iron germanate films in contrast to iron silicate (chapter 4). Two different preparation principles are used: the "stepwise reversed preparation" method (Section 5.1) and the "combined UHV preparation" method (Section 5.2). These very different preparation principles enable the evaluation of the influence of pre-prepared structure and oxidation state.

The "stepwise reversed preparation" method starts with a pre-prepared germania film. Iron is only deposited in a second step. Here, the influence of structural pre-order and pre-oxidation of germanium is of interest. In case of silicon (Section 4.2.2) it was found that the pre-ordered silica layer increases the necessary energy to form iron silicate. Mostly the reason for this is the high Si-O dissociation energy in contrast to Fe-O bonds. In contrast, Ge-O bonds have a lower bond dissociation energy than Si-O [2]. Thus, the pre-ordered Germania layer is expected to have a different influence on the film formation as it is the case for iron silicate. In the "combined UHV preparation" neither iron nor germanium are ordered or considerably oxidized during deposition, as seen by LEED and XPS. As a result the structure can arrange more freely than in the "stepwise reversed preparation" method. Moreover, iron is covered by germanium, thus oxygen must intercalate in order to reach the iron layer.

In both cases the germanium amount is less than needed to form a monolayer of Germania. Thus, germanium is free to move and able to form domains or to build a homogeneous layer. In the "stepwise reversed preparation" the germanium-rich and germanium-free areas are controlled by the germania formation, while in the "combined UHV preparation" method the material is free to arrange in an optimal manner. The germanium and iron amounts are kept constant for both preparation methods. The germanium amount equals a germania coverage of 58 %, while the iron amount equals the amount of a monolayer of FeO.

5.1 Stepwise reversed preparation ($Fe/GeO_2/Ru(0001)$)

In this section the "stepwise reversed preparation" method is used. First, a GeO_2 layer is prepared. As a second step, iron is deposited at RT in $2.0 \cdot 10^{-7}$ mbar on the as prepared GeO_2 layer. Finally the film is oxidized in $1.0 \cdot 10^{-6}$ mbar in separate temperature steps at RT, at 620 K, at 720 K and finally at 890 K. While the iron amount equals the amount necessary to form a monolayer of FeO (see section 3.1), the germanium amount equals only a coverage of 58 %. The usage of an incomplete germania layer gives the possibility to evaluate differences between the germania covered areas and the hole areas. With this the stability of the single germania island upon iron deposition can be evaluated. Moreover it can be evaluated, whether iron prefers to bind to germanium or to cover the germanium-free domains. Additionally changes in the domain sizes through iron could be determined.

In the following, first the characteristics of the GeO_2 monolayer film are described, before the individual preparation steps containing iron are analyzed.

GeO_2 monolayer film characteristics

First the preparation of the GeO_2 layer and its characteristics regarding the LEED, LEEM-IV and XPS data are discussed. In the literature up to now only STM, LEED-IV and DFT results were shown for ultrathin layers of germania [51]. In order to prepare GeO_2, first germanium is deposited at elevated temperatures (540 K) in UHV conditions. At this temperature germanium covers the Ru(0001) substrate homogeneously with germanium atoms in low concentration (1/9 of the Ru(0001) unit cell are covered with germanium). Due to the low germanium coverage this layer is invisible in LEEM . However, in LEED a (3x3) structure forms. After a critical germanium amount is deposited, germanium starts to form islands starting at the step edges. These islands again have a (3x3) structure in LEED. However the germanium amount is considerably higher (1/3 of the unit cell is filled with germanium). These domains will be addressed to as "close-packed". For the presented $FeGeO_x$ preparation a coverage of 58 % of these islands is used.

Subsequently to germanium deposition the film is oxidized in $1.0 \cdot 10^{-6}$ mbar of oxygen for 10 min at 670 K and finally cooled down in this oxygen pressure to RT. In Fig. 5.1 the characteristics of this GeO_2 film are shown. In LEED a (2x2) pattern is formed (Fig. 5.1a). In the LEEM image (Fig. 5.1b) the two different domains of germanium "close-packed" and germanium "loosely-packed" are visible. At 19 eV they appear bright and dark, respec-

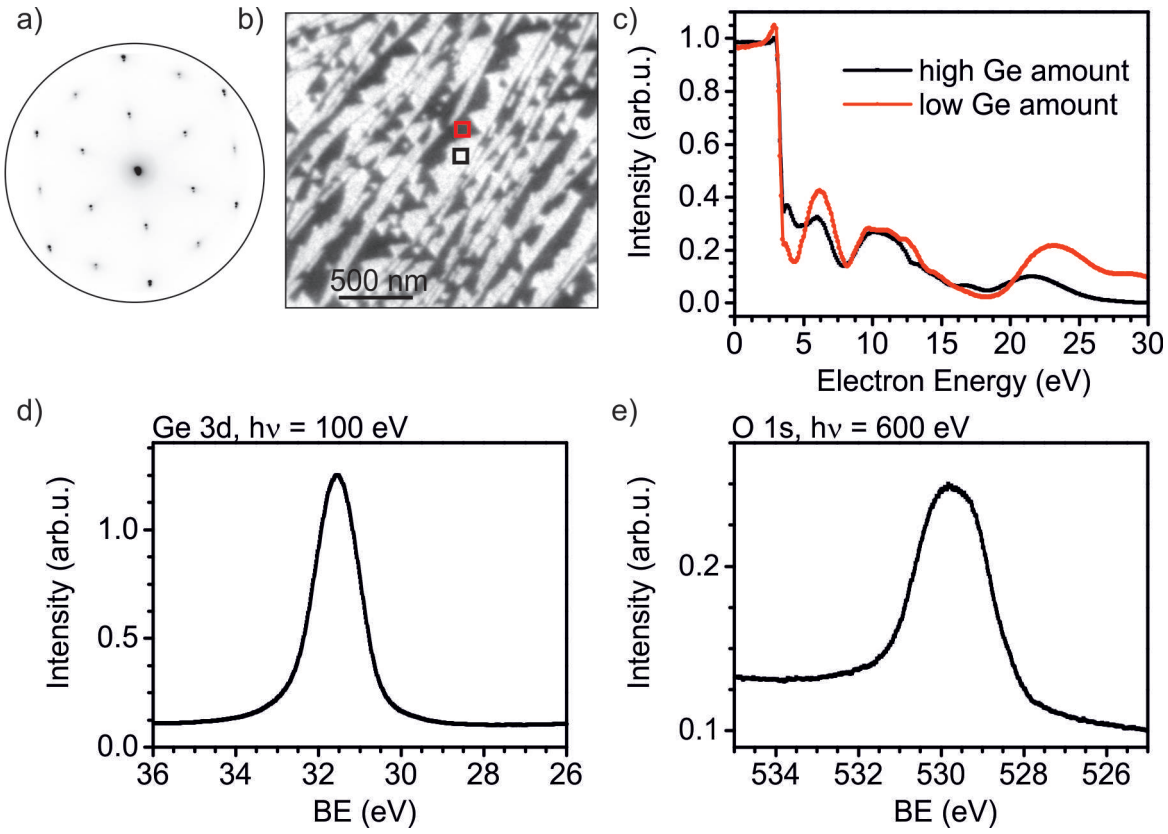

Figure 5.1 Characteristics of the used GeO_2 film. a) LEED image at 42 eV, b) LEEM at 19 eV, c) LEEM-IV curves of the in b) indicated areas, d) Ge 3d line ($h\nu$ = 100 eV) and e) O 1s line ($h\nu$ = 600 eV). The XPS curves are taken from an area with both germanium coverages.

tively. In fact, the corresponding LEEM-IV curves in Fig. 5.1c) indicate that the initially "loosely-packed" areas show the LEEM-IV fingerprint of a 3O-covered Ru(0001) substrate (compare Fig. 4.1). Since, the oxidation temperature is not sufficient to evaporate germanium, it can be assumed that the germanium atoms either diffuse to the "close-packed" areas, or the amount is so low, that it does not influence the fingerprint. As a consequence, in the following the "close-packed" area is addressed as germanium-rich and the "loosely-packed" area as germanium-free. In the germanium-rich areas the germania LEEM-IV (black curve) is given. For future reference this curve can be used as the fingerprint for the germania monolayer on Ru(0001). It contains three main features at 3.8 eV, 6.0 eV, 10.6 eV and 21.6 eV. The MEM-LEEM border is found at 3.29 eV (+0.71 eV compared to pure Ru(0001)). The XPS results of the Ge 3d and O 1s line are given in Fig. 5.1d and e, respectively. The data is taken from an area containing the GeO_2 islands and germania-poor holes. The Ge 3d shows that all germanium atoms are completely oxidized by the Ge^{4+} component (at 31.5 eV), i.e. one germanium atom is bound to two oxygen atoms, respectively. The O 1s line has two components at 529.3 eV and 530.2 eV. They correspond to the Ge-O-Ru and Ge-O-Ge bonds, respectively. Most likely, the component at 529.3 eV is overrepresented, since the energetic position of Ru-O overlaps with this line and is expected in the hole regions.

Iron germanate preparation

On the freshly prepared germania monolayer islands a monolayer of iron is deposited at RT in $2.0 \cdot 10^{-7}$ mbar. In the following the individual preparation steps from iron deposition up to final film preparation of $FeGeO_x$ will be evaluated in detail.

The LEED pattern of the individual preparation steps are given in Fig. 5.2. The LEEM-IV curves of the germanium-rich and germanium-free domains are given in Fig. 5.4a-b and c-d, respectively. The corresponding values of the MEM-LEEM border are shown in Fig. 5.5. XPS is taken from an area with both, germanium-rich and germanium-free domains. The O 1s taken at photon energy of $h\nu = 600$ eV and 780 eV are given in Fig. 5.6a and b, respectively. The Fe 3p and Ge 3d lines, each taken at $h\nu = 175$ eV and 360 eV are given in Fig. 5.6c-d and e-f, respectively.

The deposition of iron diminishes the (2x2) structure of germania. Moiré spots appear, surrounding the (00) spot (Fig. 5.2b). The Moiré structure typically correlates to the arrangement of iron and indeed a "6 on 7" reconstruction is found. However, the formation of the Moiré structure already at RT is surprising. In section 4.1.2 iron was deposited in UHV conditions at RT. In fact, no Moiré pattern was visible, but a star-like pattern (see Fig. 4.9a). Either the high accessible oxygen amount on the surface (due to the oxidation in $1.0 \cdot 10^{-6}$ mbar) or the germania layer influence this iron arrangement. The LEEM-IV curve 5.4a in the germanium-rich area is unobtrusive with one main peak at 5.2 eV. This indicates that iron is disordered, as it is expected for RT deposition. The MEM-LEEM curve 5.5 is strongly shifted down to 2.21 eV (-0.9 eV in contrast to GeO_2). This shows that the layer is not oxygen terminated (Ru(0001): 2.58 eV). The Ge 3d line is given in Fig. 5.6e-f. Through the iron contact on top of germania, some of the germanium atoms are reduced in the Ge^{2+} state (component at 30.5 eV), i.e. these germanium atoms are bound to one oxygen atom only. Thus, iron atoms partially break the bonds between germanium atoms in order to build Fe-O-Fe bonds. Iron is oxidized to the Fe^{2+} and Fe^{3+}

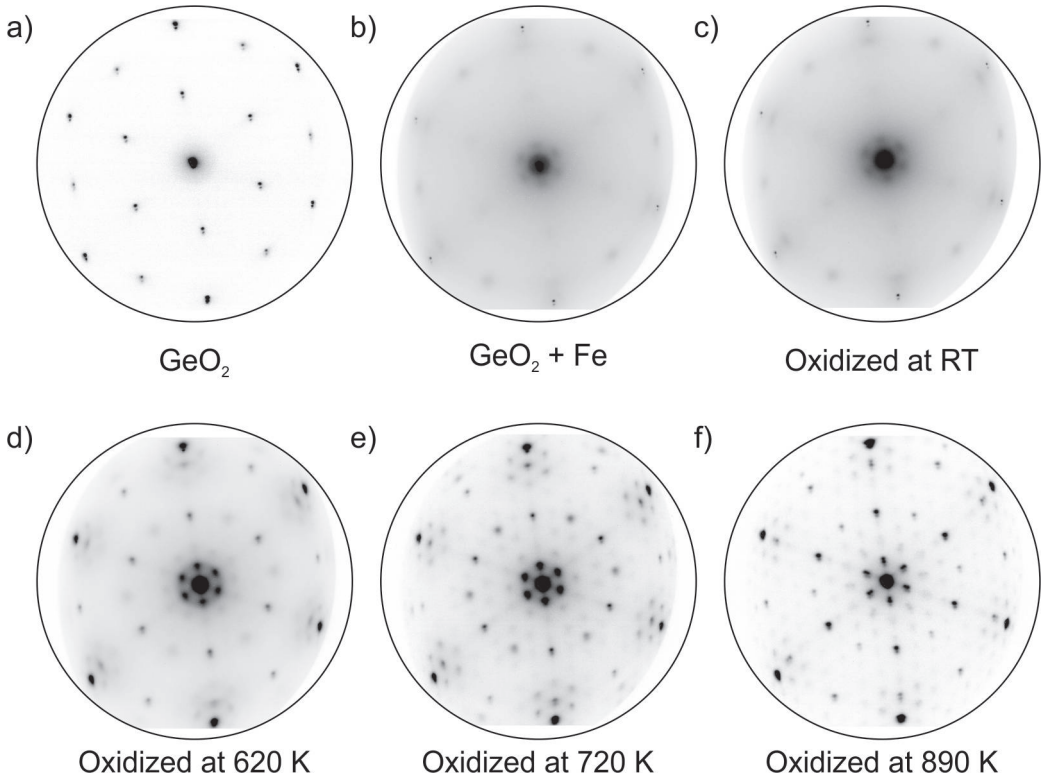

Figure 5.2 LEED pattern of the individual preparation steps of iron germanate using the "stepwise reversed preparation" method ($Fe/GeO_2/Ru(0001)$). LEED images are taken at RT and 42 eV.

state (see Fig. 5.6c-d) due to the additional oxygen atoms of the germania film. Also metallic components are found (Fe^0). The O 1s line (Fig. 5.6a-b) shows a strong increase in the component at 529.3 eV, while the component at 530.2 eV (Ge-O-Ge) is unchanged. In fact, the component at 529.3 eV does not only correspond to Ge-O-Ru bonds, but also to Fe-O-Fe and Fe-O-Ru. Thus, the increase in this component correlates with the formation of Fe-O-Fe or Fe-O-Ru bonds. Here the Fe-O-Fe on top of Germania and Fe-O-Ru in the holes region contribute to this line.

The layer is oxidized at RT in $1.0 \cdot 10^{-6}$ mbar for 30 min. In LEED (Fig. 5.2c) no structural change is visible, which correlates with the low diffusion length at RT. However, the LEEM-IV curve (Fig. 5.4) has changed slightly showing small peaks at 3.4 eV, 5.6 eV and 11.8 eV. Moreover, the MEM-LEEM border (Fig. 5.5) is increased by 0.35 eV to 2.57 eV, which fits to the MEM-LEEM border of Ru(0001) (2.58 eV). While the effect on the structure was relatively small, chemical changes are found in the degree of oxidation. Germanium atoms originally in the Ge^{2+} state partially become better oxidized to Ge^{4+} states (Ge 3d line Fig. 5.6e-f). Moreover, iron atoms in the Fe^{2+} state partially oxidize further into Fe^{3+} states (Fe 3p line: Fig. 5.6e-f). Nearly no Fe^0 components are found anymore. The ratio Fe^{3+}:Fe^{2+} is higher for the less surface sensitive energy of 360 eV compared to 175 eV. Thus, the Fe^{2+} component is rather on top than close to the Ru(0001) substrate. The O 1s line (Fig. 5.6a-b) indicates an increase in the Ge-O-Ru, Fe-O-Fe and Fe-O-Ru component. This correlates with the higher amount of the Fe^{3+} line especially close to the substrate.

Afterwards the layer is oxidized at 620 K in $1.0 \cdot 10^{-6}$ mbar. While increasing the temper-

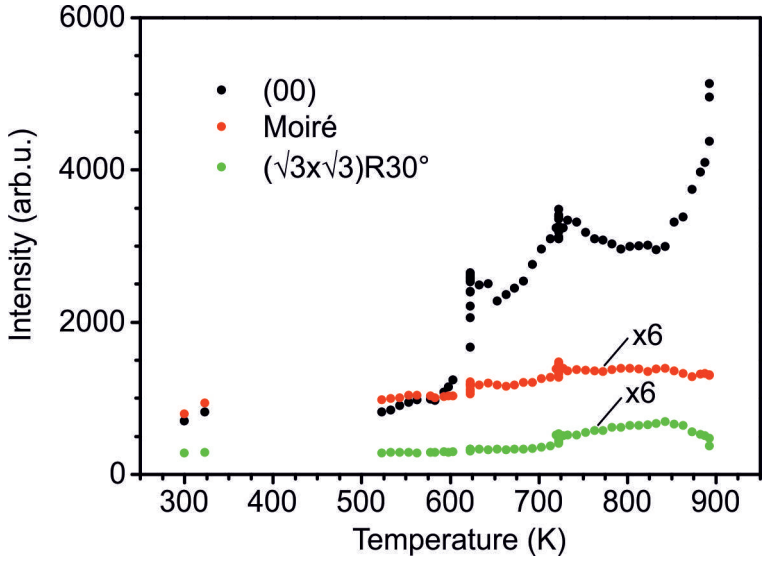

Figure 5.3 Spot intensity of the (00), Moiré and $(\sqrt{(3)} \times \sqrt{(3)})R30°$ spot during oxidation in $1.0 \cdot 10^{-6}$ mbar of iron germanate prepared with the "stepwise reversed preparation" method ($Fe/GeO_2/Ru(0001)$). The $(\sqrt{3} \times \sqrt{3})R30°$ structure refers to a germania structure that is rotated by 30° regarding a complete iron oxide layer. The heating rate was about 0.5-1 K/s, except at 625 K and 730 K, where the temperature was kept constant for 10 min.

ature at 540 K a (2x2) structure is formed, which increases in intensity with temperature. The Moiré structure surrounding the (00) spot becomes more pronounced and sharper. Additionally Moiré spots close to the (10) spots (Ru(0001) substrate) appear, as it is typical for FeO on Ru(0001). The Moiré structure fits to the superposition of six iron atoms on seven ruthenium atoms ("6 on 7" reconstruction, i.e. Fe-Fe distance of 3.157 ,Å). This is the same distance as for a pure FeO layer on Ru(0001). At 620 K (Fig. 5.2d) an additional superstructure, namely a $(\sqrt{3} \times \sqrt{3})R30°$ structure appears. In case of iron silicate this indicated the arrangement of silicon atoms on top of iron oxide. Therefore, it can be assumed

	On basis of germania		Germania-free	
Preparation step	MEM-LEEM border (eV)	Work function (eV)	MEM-LEEM border (eV)	Work function (eV)
GeO_2	3.29	6.15	3.27	6.13
Fe deposition	2.21	5.07	2.25	5.11
Oxidation at RT	2.57	5.43	2.50	5.36
Oxidation at 620 K	2.92	5.78	2.98	5.84
Oxidation at 720 K	3.05	5.91	3.05	5.91
Oxidation at 890 K	2.88	5.74	2.79	5.65

Table 5.1 Overview of the individual values of the MEM-LEEM border of an incomplete layer of iron germanate using the "stepwise reversed preparation" method ($Fe/GeO_2/Ru(0001)$). The MEM-LEEM values are measured with an accuracy of ± 0.02 eV. The work function is referenced to the value of 5.44 eV for clean Ru(0001) [12].

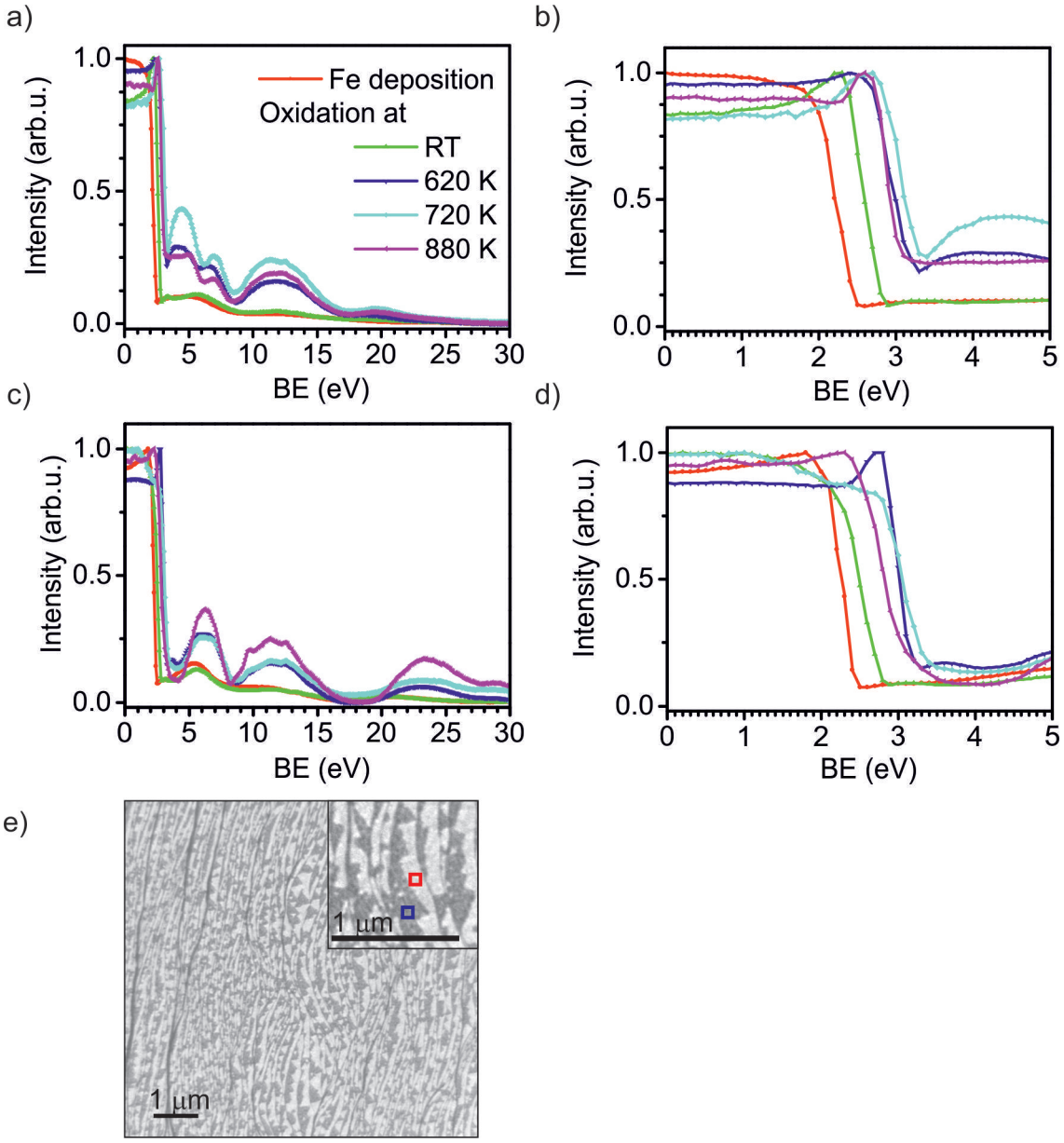

Figure 5.4 LEEM-IV curves for iron germanate with the "stepwise reversed preparation" method ($Fe/GeO_2/Ru(0001)$). a-b) In areas with germania basis. c-d) In germania-free areas. e) LEEM at 20 eV after oxidation at 720 K. The areas on basis of germania and germania-free areas are indicated in red and violet, respectively.

that indeed the germanium atoms begin to arrange. The arrangement of germanium and iron is also visible in the LEEM-IV curve in the germanium-rich domains (Fig. 5.4a) The LEEM-IV curve is on the one hand more intense and on the other hand a new structure has formed. Peaks are present at 4.2 eV, 6.7 eV and a very broad one at 11.8 eV. The MEM-LEEM border is increased during the oxidation by 0.35 eV (2.92 eV) (Fig. 5.5). In the germanium-free domains the LEEM-IV structure resembles the LEEM-IV fingerprint of 3O on Ru(0001) strongly (for comparison see Fig. 4.1). Together with these structural changes, also chemical changes are visible. The Fe 3p line (Fig. 5.6c-d) decreases, while

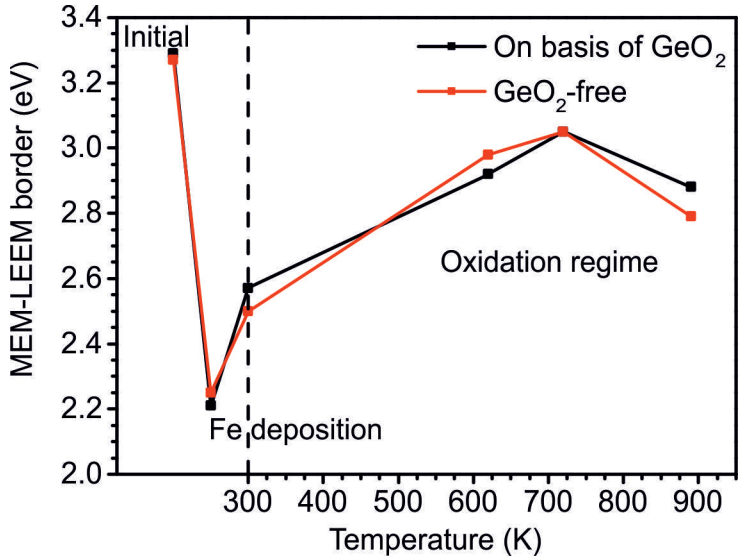

Figure 5.5 MEM-LEEM border for the individual preparation steps of the incomplete iron germanate layer using the "stepwise reversed preparation" method ($Fe/GeO_2/Ru(0001)$). The MEM-LEEM values are determined by a fit of the MEM-LEEM border presented in Fig. 5.4b and d. The error of this fit is $\pm$ 0.02 eV.

the Ge 3d line (Fig. 5.2e-f) increases. This indicates the diffusion of iron underneath the germanium layer. As a result $FeGeO_x$ seems to be similarly arranged as $FeSiO_x$ with an iron oxide layer underneath and a monolayer of germania on top. Similar to the silica layer in $FeSiO_x$, the germania layer in $FeGeO_x$ is rotated by 30° and arranged regarding the iron atoms underneath. Now, the germanium atoms are completely oxidized to the Ge^{4+} state. The Fe^{2+} component is strongly decreased. In fact for both an oxidized iron oxide layer (section 3.1), as well as for iron silicate (chapter 4.2) a transformation of Fe^{2+} towards Fe^{3+} is found. Therefore, this transformation is expected for both the germanium free holes, as well as the germania "close-packed" islands. The O 1s line (Fig. 5.6a-b) indicates a strong increase of the Ge-O-Ge component at 530.2 eV. The comparison between a photon energy of 600 eV and 780 eV shows that the ratio of the intensities I(530.2 eV): I(529.3 eV) is larger for surface sensitive probing. Since the component at 350.2 eV only corresponds to germanium, while the component at 529.3 eV corresponds to both, germanium and iron bound to oxygen, the results show that germanium is indeed on top of iron.

The layer is further oxidized at 720 K. During the annealing process Moiré spots surrounding the $(\sqrt{3}\times\sqrt{3})R30°$ spots appear. Furthermore, Moiré and $(\sqrt{3}\times\sqrt{3})R30°$ become more pronounced, i.e. the film becomes better arranged. In fact, the (2x2) structure already present at 620 K turns out to correlate to holes in the film, since they are only present for temperatures lower than 670 K. In fact, the LEEM-IV curve of the germanium-free areas (Fig. 5.4c) indicates that iron is nearly gone in these areas and mainly a 3O covered Ru(0001) substrate remains. Altogether, the germanium-free areas behave like pure iron oxide on Ru(0001). There also domains have been found, where the iron concentration was reduced, either by migration or evaporation (see section 3.1). This suggests that the germanium concentration in these areas must be either really low or most likely depleted during GeO_2 formation. The LEEM-IV curve in the germanium-rich domains (Fig. 5.4a) is unchanged in the peak position, but strongly increased in the individual peaks. Again, this

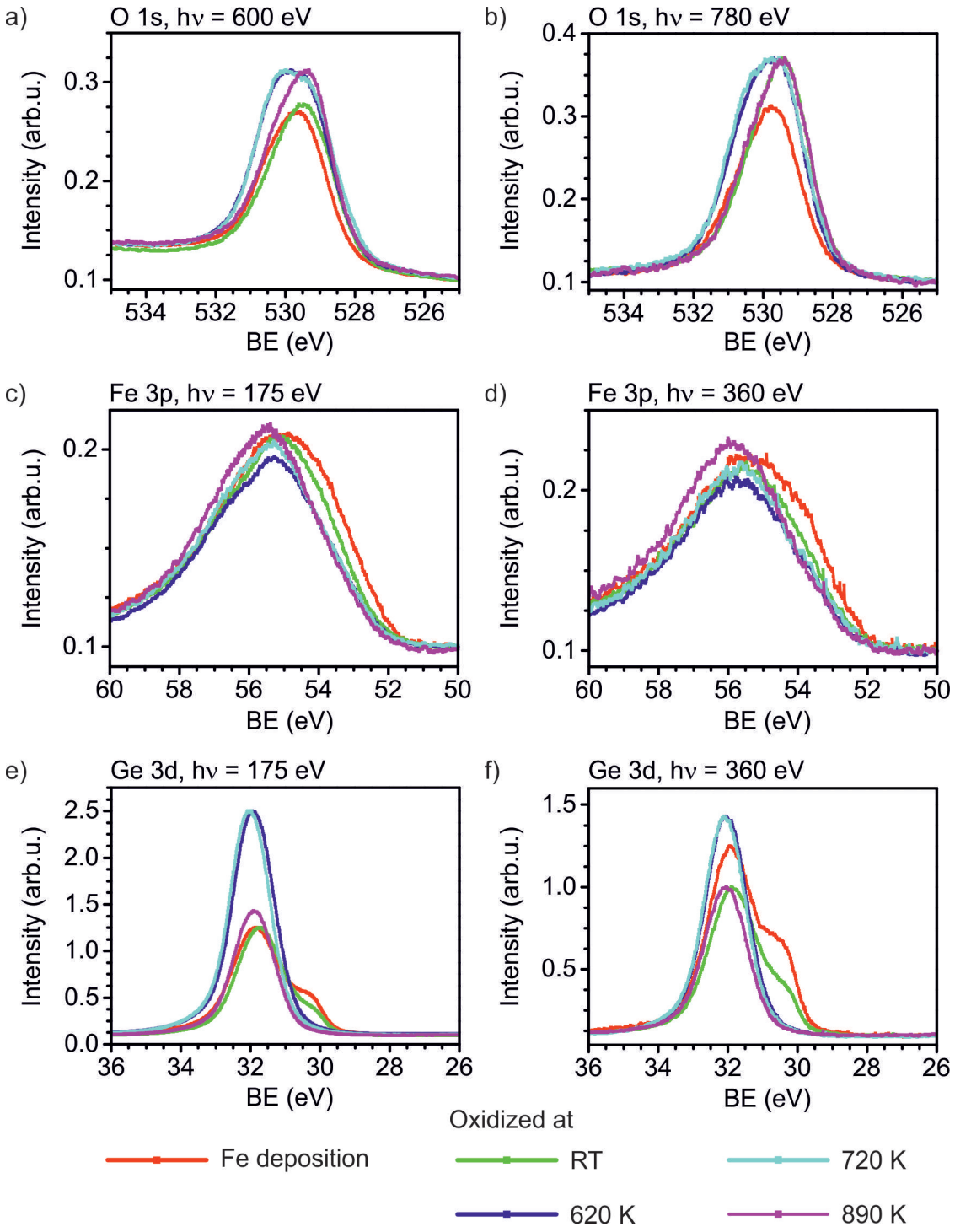

Figure 5.6 XPS analysis of an incomplete iron germanate layer for the "stepwise reversed preparation" method ($Fe/GeO_2/Ru(0001)$). O 1s line for a photon energy of a) 600 eV and b) 780 eV. Fe 3p line for a photon energy of c) 175 eV and d) 360 eV. Ge 3d line for a photon energy of e) 175 eV and f) 360 eV. The measurements summarize both germanium-rich and germanium-free domains and are taken at RT.

implies the improved ordering of the film. The MEM-LEEM border (Fig. 5.5) is increased by 0.1 eV (3.05 eV). No strong chemical changes are found. The Ge 3d (Fig. 5.6e-f) and O 1s line (Fig. 5.6a-b) are rather unchanged. Only the Fe 3p line (Fig. 5.6c-d) indicates a slight increase in the Fe^{3+} component, possibly due to intercalation of oxygen.

Up to 860 K the film is stable and becomes better ordered. Additionally higher order Moiré spots appear. For temperatures higher than 860 K the $(\sqrt{3} \times \sqrt{3})R30°$ spots decrease in intensity and the Moiré spots surrounding them disappear. The peak positions of the LEEM-IV curve (fingerprint) remains, but the intensity is strongly decreased (see Fig. 5.4a). Only the peak at 4.5 eV shifts to 5.0 eV. The XPS curves reveal the evaporation of germanium in the strong decrease of the Ge 3d line (Fig. 5.6e-f), while the Fe 3p line (Fig. 5.6c-d) is increased. This correlates with the decrease in the intensity of the $(\sqrt{3} \times \sqrt{3})R30°$ spots, which correlates with GeO_2 ordering. Also in the O 1s line (Fig. 5.6a-b) the Ge-O-Ge line is decreased, while the component for Fe-O-Fe/ Fe-O-Ru and Ge-O-Ru is unchanged.

Summary and conclusion of the formation process of iron germanate using the "stepwise reversed preparation" method

In summary the $FeGeO_x$ has a similar structure as $FeSiO_x$ (see chapter 4). A monolayer of GeO_2 is arranged on top of a monolayer of iron oxide. The LEED pattern gives rise to a "6 on 7" Moiré pattern, together with by 30° rotated spots. In fact, the iron oxide layer shares the same Fe-Fe distances as the pure FeO layer (Fe-Fe distance: 3.157 Å, as calculated from the measured "6 on 7" Moiré reconstruction, see chapter 3.1). This is a strong difference compared to silicon, where a reduction of the Fe-Fe distance to a value of 3.044 Å takes place (Chapter 4). Moreover in the O 1s line only two components are found. For sodium iron germinate melts the expected energy of a Ge-O-Fe line is calculated by the usage of the ionic field strength Z/r (Z is the nominal charge on the ion and r the mean radius in nm). It was found that Ge-O-Fe(II) and Ge-O-Fe(III) are expected at 530.0 eV and 530.5 eV, with the Ge-O-Ge bond at 531.0 eV [61]. However, the individual peak area of the Ge-O-Fe peak is very low and in particular much lower than for Si-O-Fe bonds [60]. Thus, they are not easy to distinguish in the given spectra.

The formation process of iron germanate islands using the "stepwise reversed preparation" method is depicted in Fig. 5.7. The basis is an incomplete layer of germania (58 % coverage) on the Ru(0001) substrate (Fig. 5.7a). At RT in $2.0 \cdot 10^{-7}$ mbar iron in the amount necessary to form a monolayer of FeO is deposited on top. The formerly well-oxidized germania layer becomes reduced, since iron dissociates Ge-O-Ge bonds, in favor of Fe-O-Fe bonds. Already at RT Moiré spots with a "6 on 7" reconstruction appear. Subsequently the film is oxidized at RT, 620 K, 720 K and 890 K in $1.0 \cdot 10^{-6}$ mbar of oxygen. The oxidation at RT leads to an improved oxidation of germanium and iron. In particular, the Fe^{3+} component is increased, which correlates to Fe-O-Ru bonds. At 540 K (2x2) spots appear, indicating the formation of holes in the germanium-free areas. As depth profile measurements of the O 1s line show, with increased oxidation temperature iron, originally on top of germania, intercalates to the germania/ruthenium interface. At 620 K by 30° rotated spots appear (Fig. 5.7c), indicating germanium arrangement regarding the iron oxide layer underneath. Up to 860 K the structure improves its crystallinity (Fig. 5.7f). For higher temperatures germanium evaporates (Fig. 5.7e).

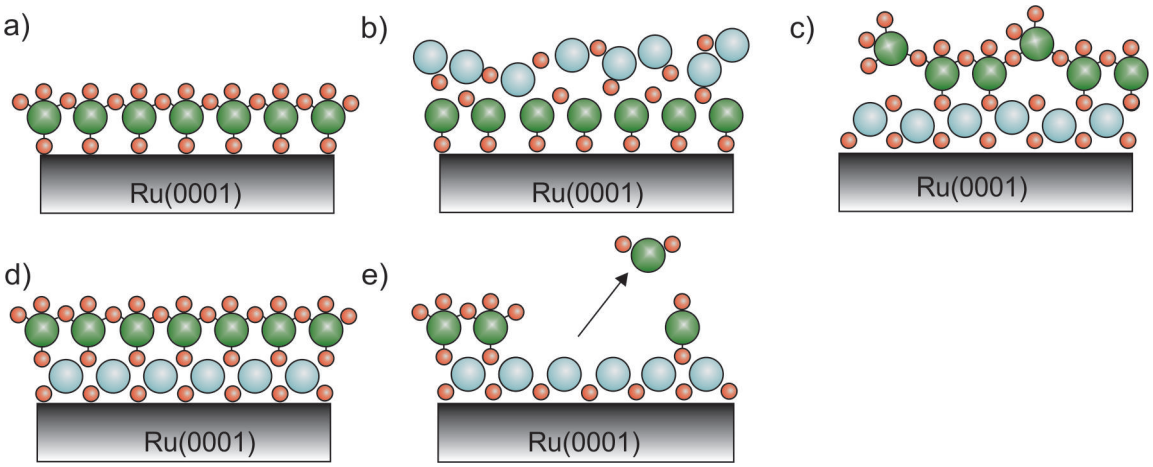

Figure 5.7 Individual steps during oxidation of iron germanate prepared with the "stepwise reversed preparation" method ($Fe/GeO_2/Ru(0001)$). a) Germania monolayer. b) Deposition of iron in $2.0 \cdot 10^{-7}$ mbar of oxygen. Iron reduces the germanium atoms, in order to form Fe-O-Fe bonds. At this stage Moiré spots are already present in LEED. c-e) Oxidation in $1.0 \cdot 10^{-6}$ mbar. c) Iron intercalates to Ge/Ru interface and germanium is completely oxidized in the Ge^{4+} state. Iron is mainly in the Fe^{3+} state. At 620 K beginning formation of by 30° rotated spots due to germania arrangement on top of the iron oxide layer. d) Up to 860 K the structure improves its crystallinity. e) Above 860 K germanium evaporates. Red: Oxygen. Blue: Iron. Green: Germanium.

The domains where germanium was only "loosely-packed" after germanium deposition prove to be germanium free after GeO_2 formation. The deposited iron is found in both domains. The oxidation reduces the iron amount in the germanium-free domains strongly at elevated temperatures, which indicates either the evaporation of iron or the migration of iron to the germanium-rich domains. In the oxidized monolayer FeO film (section 3.1) the diffusion of iron in single domains was found, so that holes started to appear. In comparison to this effect, similarly iron might diffuse to the $FeGeO_x$ domains as well. Moreover, germanium stabilizes the iron oxide layer up to 890 K. At this temperature GeO_2 is evaporated. In contrast, $FeSiO_x$ is even stable to temperatures much higher than 1000 K.

5.2 Combined UHV preparation (Fe+Ge(UHV)/Ru(0001))

In this chapter the "combined UHV preparation" method is used. Hereby, iron and germanium are deposited subsequently at RT in UHV. Afterwards the layer is oxidized stepwise at RT, 620 K, 720 K and 880 K in $1.0 \cdot 10^{-6}$ mbar. The deposited material amount equals the one deposited in section 5.1: germanium in the amount of 58 % of a monolayer of germania, and iron in the amount needed for a complete monolayer of FeO. In contrast to section 5.1 both, iron and germanium are found to be disordered after deposition. As a result a free arrangement of the individual atoms is possible. Moreover, neither germanium nor iron is completely oxidized after their deposition. Therefore, the possibility for new bonds and a different order of oxygen bonds are given.

The LEED images (in Fig. 5.8), the LEEM-IV curves (Fig. 5.10) and their MEM-LEEM

border (Fig. 5.11) show the structural changes for the individual preparation step. Moreover the intensity change during annealing in oxygen is given for the (00) spot, a Moiré spot and a $(\sqrt{3} \times \sqrt{3})R30°$ in Fig. 5.9. Chemical results are shown by XPS. Here, the O 1s lines are given for photon energies of hν = 600 eV and 780 eV in Fig. 5.12a and b, respectively. The Fe 3p and Ge 3d lines, each taken at hν = 175 eV and 360 eV are depicted in Fig. 5.12c-d and e-f, respectively.

First, iron is deposited on a freshly cleaned Ru(0001) substrate. However, residual oxygen atoms on the surface, as well as in the surrounding lead to a star-like pattern in LEED (Fig. 5.8a). Earlier experiments have shown that this pattern is only present for a very low oxygen amount (see chapter 4.1.2. As a second step, germanium is deposited. The layer is disordered and in LEED mainly the (00) spot and the substrate spots are visible (Fig. 5.8b). Moreover, elongated spots are present. The LEEM-IV curve (Fig. 5.10a) shows that the film is disordered, since the intensity is very low. The film is not oxygen terminated, as is visible in the low MEM-LEEM border at 2.22 eV (Ru: 2.58 eV) in Fig. 5.11. The reason is the low oxygen amount (background pressure: $7.0 \cdot 10^{-9}$ mbar). The film is partially oxidized due to the long deposition time of germanium of four hours (iron: 10 min). As a consequence the residual oxygen atoms in the gas surrounding lead

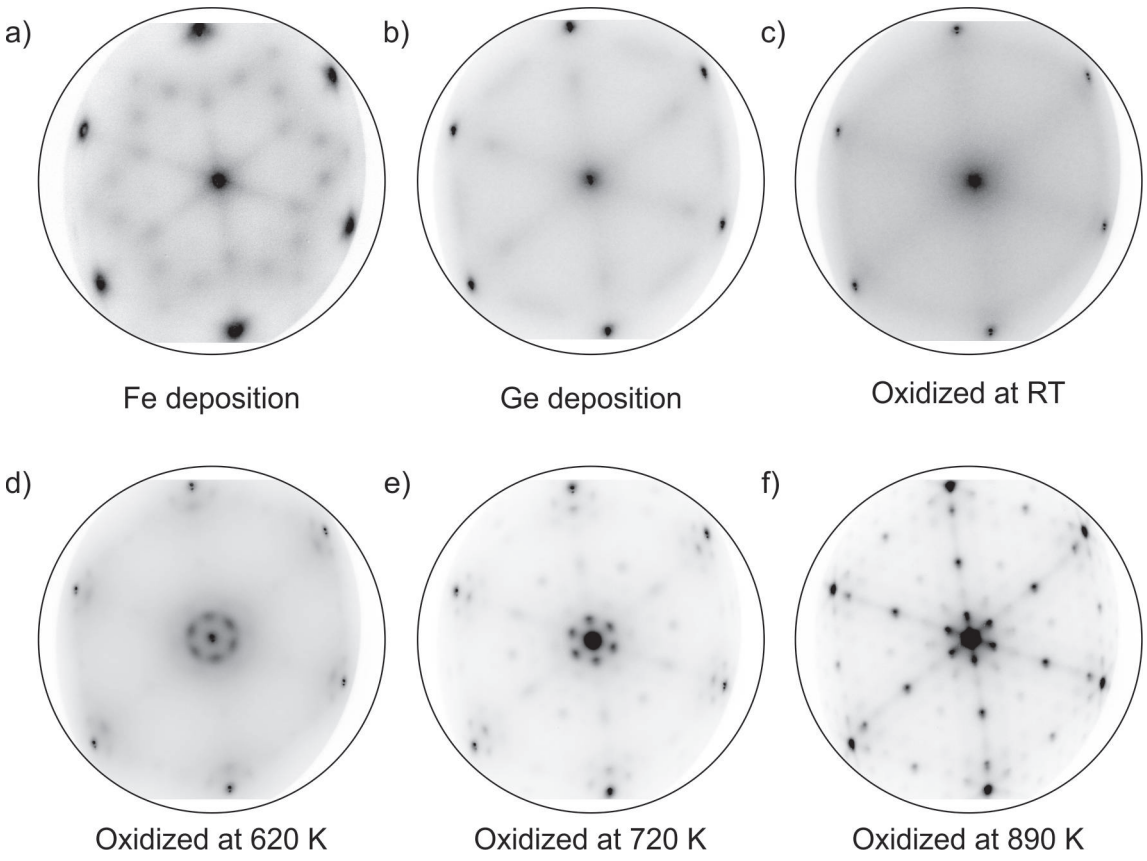

Figure 5.8 LEED images of the individual preparation steps of iron germanate using the "combined UHV preparation" method (Fe+Ge(UHV)/ Ru(0001)). The oxidation takes place in $1.0 \cdot 10^{-6}$ mbar of oxygen. LEED images are taken at 42 eV and RT. The (2x2) structure, formed at oxidation above 640 K, is only present when the LEED is measured at temperatures below 600 K. The LEED image a) is identical with the one used in Fig. 4.9a.

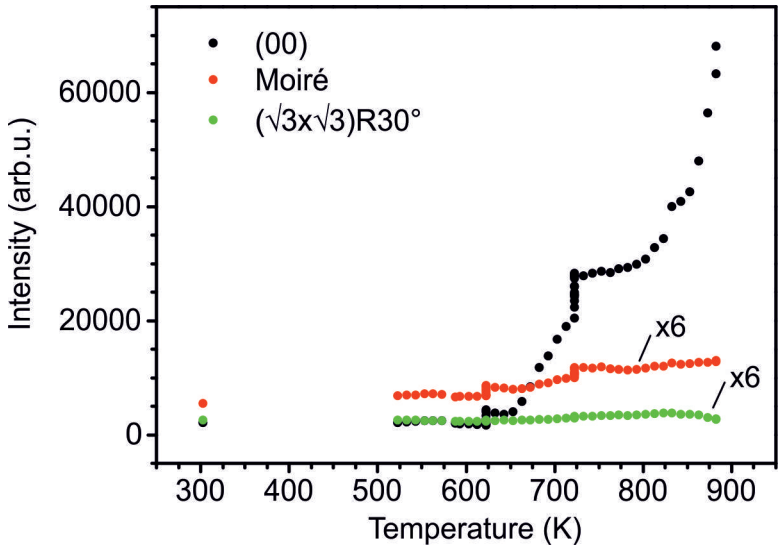

Figure 5.9 LEED spot intensities of the (00), Moiré and $(\sqrt{3} \times \sqrt{3})R30°$ spots during the oxidation in $1.0 \cdot 10^{-6}$ mbar of oxygen, starting with an iron germanate layer prepared with the "combined UHV preparation" method (Fe+Ge(UHV)/ Ru(0001)). The $(\sqrt{3} \times \sqrt{3})R30°$ structure refers to a germania structure that is rotated by 30° regarding a complete iron oxide layer. The heating rate was about 0.5-1 K/s, except at 625 K and 730 K, where the temperature was kept constant for 10 min.

to the partial oxidation of germanium and iron. This is visible by two components in the O 1s line (Fig. 5.12a-b) at 529.3 eV (typically Fe-O-Fe, Fe-O-Ru and Ge-O-Ru bonds) and 530.2 eV (Ge-O-Ge bonds). However, the overall peak intensity is very low. The Fe 3p line in Fig. 5.12c-d) indicates that most of the iron atoms are in the Fe^0 state (at 52.8 eV) with some small parts in the Fe^{2+} state (at 54.1 eV). Equal amounts of germanium atoms are in the Ge^0, Ge^{1+} and Ge^{2+} state and a small portion is even in the Ge^{4+} state (Ge 3d line: Fig. 5.12e-f). An oxidation state of Ge^{2+} indicates that one germanium atom is bound to one oxygen atom, while germanium atoms in the Ge^{4+} state are bound to two oxygen atoms and are thus, completely oxidized. The peak form is homogeneous, which indicates that no oxygen free Fe-Ge bonds are formed.

The film is oxidized for 30 min in $1.0 \cdot 10^{-6}$ mbar. The presence of oxygen increases the amount of oxidized atoms of both, iron and germanium (Fe 3p: Fig. 5.12c-d, Ge 3d: Fig. 5.12e-f). This shows that iron becomes oxidized, even when covered with germanium. A complete oxidation of all iron or germanium atoms is not achieved. Due to the oxidation at RT, the amount of iron atoms which are not oxidized (Fe^0 component) decreases, while the Fe^{2+} component rises. Additionally some iron atoms are already found in the Fe^{3+} state. Also a strong reduction of the Ge^0 and Ge^{1+} state in germanium is found combined with an increase in the Ge^{4+} state. The number of germanium atoms in the Ge^{2+} state is unchanged. Fitting to these results the O 1s line increases considerably (Fig. 5.12a-b). The highest gain correlates to the component at 529.3 eV and thus, to iron oxidation. No structural change is visible. Even the MEM-LEEM border remains at 2.22 eV (Fig. 5.11).

The increase in temperature to 620 K leads to a structural arrangement of the iron atoms. At 520 K a ring forms surrounding the (00) spot and separates at 590 K into individual Moiré spots with a "6 on 7" reconstruction (Fig. 5.8d). No additional superstructure spots corresponding to germanium are present. In LEEM-IV (Fig. 5.10a) the peaks at 5.8 eV

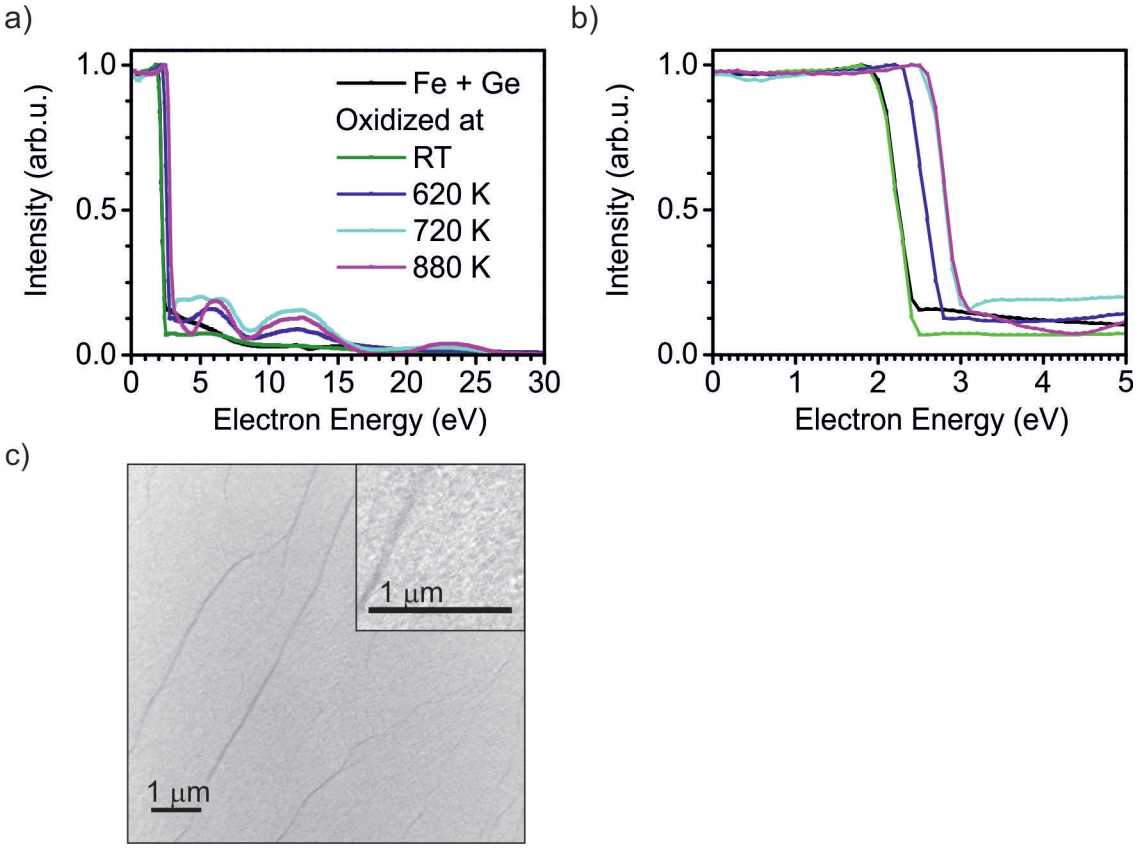

Figure 5.10 a) LEEM-IV and b) MEM-LEEM border for the individual preparation steps of an iron germanate layer using the "combined UHV preparation" method (Fe+Ge(UHV)/Ru(0001)). The measurements are taken at RT. c) LEEM at 20 eV after oxidation at 720 K.

Preparation step	Energetic position of the MEM-LEEM border (eV)	Workfunction (eV) (referenced to clean Ru(0001) with 5.44 eV [12])
Fe + Ge	2.22	5.08
Oxidation at RT	2.22	5.08
Oxidation at 620 K	2.55	5.41
Oxidation at 720 K	2.79	5.65
Oxidation at 880 K	2.81	5.67

Table 5.2 Overview of the individual values of the MEM-LEEM border of an incomplete layer of iron germanate using the "combined UHV preparation" method (Fe+Ge(UHV)/Ru(0001)). The MEM-LEEM values are measured with an accuracy of ± 0.02 eV.

and 12 eV are well pronounced. Also the MEM-LEEM border (Fig. 5.11) is increased to 2.55 eV and thus, comparable to Ru(0001) with 2.58 eV (within the accuracy of the measurements). Even though most iron and germanium atoms become better oxidized, reduced components are still present (Fe 3p: Fig. 5.12c-d, Ge 3d: Fig. 5.12e-f). As for germanium approximately 2/3 of the atoms are in the Ge^{4+} state, the rest in the Ge^{2+}

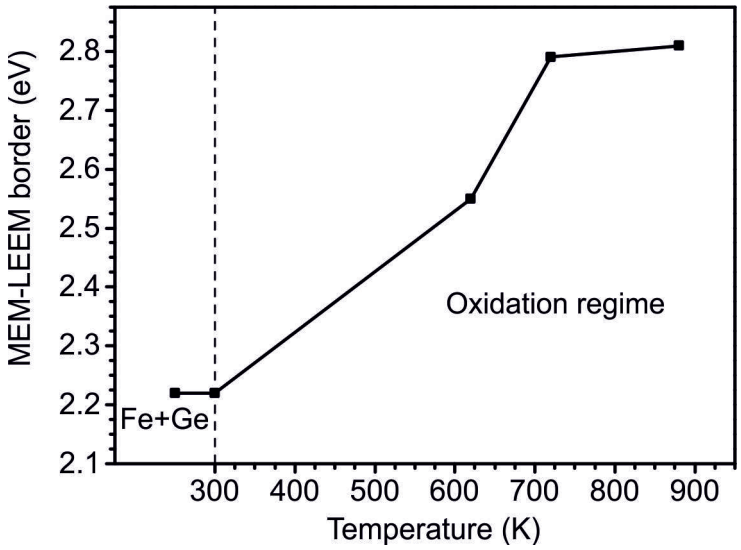

Figure 5.11 MEM-LEEM border for the individual preparation steps of an iron germanate layer prepared with the "combined UHV preparation" method (Fe+Ge (UHV)/Ru(0001)). The MEM-LEEM values are determined by a fit of the MEM-LEEM border presented in Fig. 5.10b. The error of this fit is ± 0.02 eV.

state. The iron atoms are found mainly in the Fe^{2+} and Fe^{3+} states. Some iron atoms are still in the metallic Fe^{0} state. The strong oxidation of the individual components is mirrored in the rise of the O 1s line (Fig. 5.12a-b) in both components at 530.2 eV and 529.3 eV.

At a temperature of 670 K $(\sqrt{3} \times \sqrt{3})R30°$ spots start to appear, and thus, germanium starts to order. Even after oxidation at 720 K for 10 min no Moiré spots surrounding this superstructure are found. Together with the $(\sqrt{3} \times \sqrt{3})R30°$ structure, (2x2) spots become visible; their the intensities decrease with rising temperature. At 720 K the (2x2) spots are not visible anymore, but recover during cooling the sample to RT (Fig. 5.8e). These disappearance of (2x2) spots at high temperatures is typical for a 3O-covered Ru(0001) substrate, and thus, indicates that holes down to 3O covered substrate are present in the film. In LEEM the sample appears to be very homogeneous, however domains smaller than 100 nm can be identified (see the zoom in Fig. 5.10c). The LEEM-IV curve (Fig. 5.10a) shows a broad band from 3.4 eV to 6.8 eV and a broad peak at 11.8 eV. The observed domains in Fig. 5.10c are too small to measure LEEM-IV curves in both areas. Thus, in order to prove the assumption of holes in the film the summed LEEM-IV curve of the complete film can be compared to the superimposed LEEM-IV curve of iron germanate areas and hole areas from the "stepwise reversed preparation" method (section 5.1). In Fig. 5.13a this constructed curve is compared to the one measured in the "combined UHV preparation" method at 720 K. Indeed in both curves the same shape and characteristics (peak positions) of the LEEM-IV curve are found.

This shows that very small holes (less than 30 nm) down to the substrate must be present. The MEM-LEEM border (Fig. 5.11) is increased by 0.24 eV, which fits to the increased ordering and oxidation of the layer. In fact, at 720 K iron and germanium atoms are completely oxidized. This indicates that complete oxidation of germanium (Ge^{4+} state) is necessary, before the ordered structure can be optimized. Indeed the same effect has been

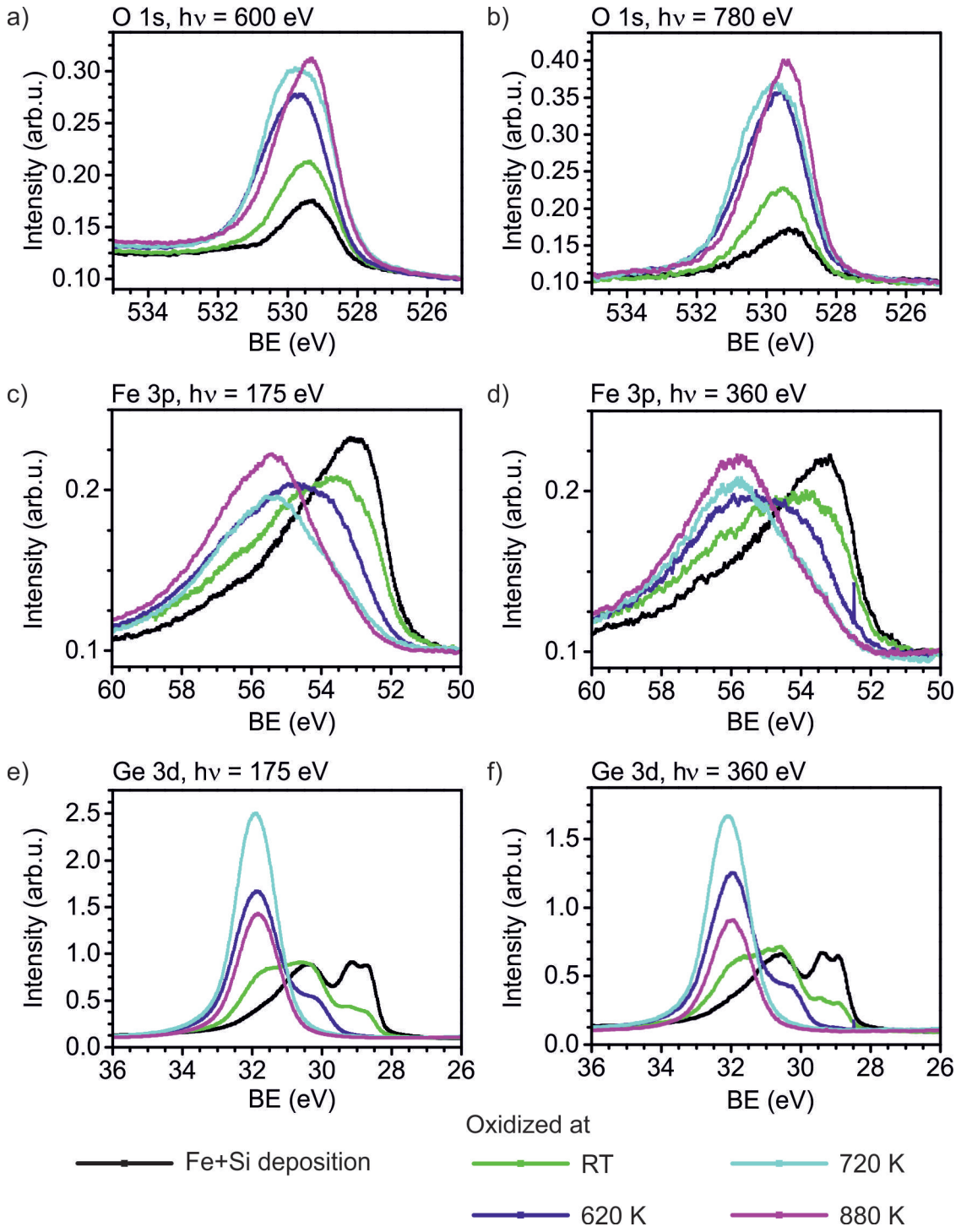

Figure 5.12 XPS analysis of an iron germanate layer prepared with the "combined UHV preparation" method (Fe+Ge(UHV)/Ru(0001)). O 1s line for a photon energy of a) 600 eV and b) 780 eV. Fe 3p line for a photon energy of c) 175 eV and d) 360 eV. Ge 3d line for a photon energy of e) 175 eV and f) 360 eV. The oxidation pressure is $1.0 \cdot 10^{-6}$ mbar. The measurements are taken at RT.

found for multilayer iron silicate films (section 4.3). There it turned out that a complete oxidation of iron was necessary before the typical Moiré structure formed. This seems to be the case for germanium atoms, as well. The Fe^{2+} state is strongly decreased and the dominant state for iron is the Fe^{3+} state. This fits to iron silicate films (chapters 4.1-4.2) or oxidized FeO layer (section 3.1). Both O 1s components are strongly increased (Fig. 5.12a-b).

Further annealing up to 840 K improves the film order considerably. At 830 K Moiré spots surrounding the $(\sqrt{3} \times \sqrt{3})R30°$ spots appear, indicating good crystallinity. For temperatures higher than 840 K the $(\sqrt{3} \times \sqrt{3})R30°$ spot intensity decreases strongly (Fig. 5.8f), due to germanium evaporation, similar to the "stepwise reversed preparation" method. The loss of germanium becomes obvious by the intensity decrease of the Ge 3d line (Fig. 5.12e-f) and increase of the Fe 3p line (Fig. 5.12c-d). Furthermore, the O 1s component (Fig. 5.12a-b) at 530.2 eV, associated with Ge-O-Ge formation, decreases strongly. The LEEM-IV curve has significant peaks at 6.1 eV, 11.8 eV and 22.7 eV. Also at this temperature the comparison of the LEEM-IV curve mirrors the superimposed LEEM-IV curves of the "stepwise reversed preparation" method in germanium-rich and germanium-free domains (Fig. 5.13b).

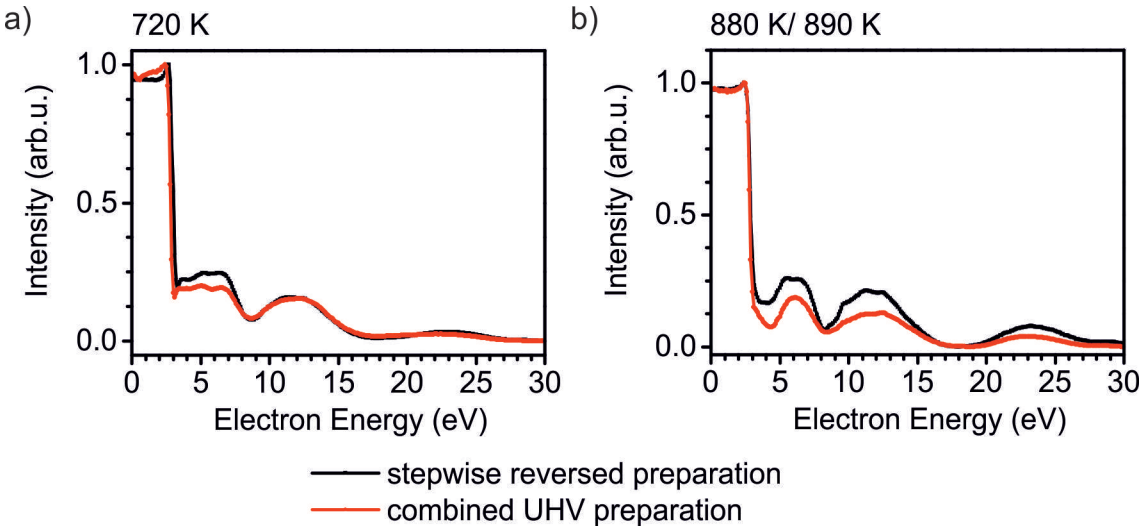

Figure 5.13 LEEM-IV curves of iron germanate preparations using the "stepwise reversed preparation" method (chapter 5.1) ($Fe/GeO_2/Ru(0001)$) and "combined UHV preparation" (this chapter) (Fe+Ge(UHV)/Ru(0001)) at a) 720 K and b) 890 K and 880 K, respectively. The LEEM-IV curve of the "stepwise reversed preparation" method is a sum of the LEEM-IV curves in the iron germanate and 3O-Ru(0001) area assuming 1:1 ratio. The LEEM-IV curve of the "combined UHV preparation" is the as measured curve.

Summary of the "combined UHV preparation" method of iron germanate

The formation process of iron germanate using the "combined UHV preparation" method is depicted in Fig. 5.14. First the amount necessary to form a monolayer of iron and then 0.58 ML necessary for a monolayer of germania are deposited at RT in UHV conditions. After deposition iron and germanium are partially oxidized, most likely during the long deposition time of germanium (four hours) of residual oxygen in the surrounding. The deposited film is disordered (see Fig. 5.14a). Subsequently, the film is oxidized in $1.0 \cdot 10^{-6}$ mbar at RT, 620 K, 720 K and 880 K. Oxidation at RT leads to an improved oxidation of germanium and especially iron (Fig. 5.14b). No structural change is visible. At 520 K, iron begins to arrange, as is visible by the formation of a ring surrounding the (00) spot in LEED. At 590 K (see Fig. 5.14c) this ring separates and reveals Moiré spots with a "6 on 7" reconstruction. Nevertheless reduced components in the Fe 3p and Ge 3d line are preserved. At an oxidation temperature of 670 K (Fig. 5.14d), both, (2x2) spots and $(\sqrt{3} \times \sqrt{3})R30°$ appear. The (2x2) spots show all characteristics of hole formation down to the Ru(0001) substrate, i.e. the film separates in germanium-rich (iron germanate) and germanium-free domains (holes). These domains are in the range of ≤ 100 nm and homogeneously distributed. At 720 K iron and germanium are completely oxidized. The film structure improves up to 840 K (Fig. 5.14e), showing good crystallinity. For higher temperatures than 840 K germanium evaporates, leaving iron behind (Fig. 5.14f).

The "combined UHV preparation" method produces the same structure of iron germanate as the "stepwise reversed preparation" method: A Moiré structure and a $(\sqrt{3} \times \sqrt{3})R30°$. However, the necessary energy for the iron and germanium atoms for the film arrangement and oxidation is much higher. One reason is the lack of oxygen during deposition, the

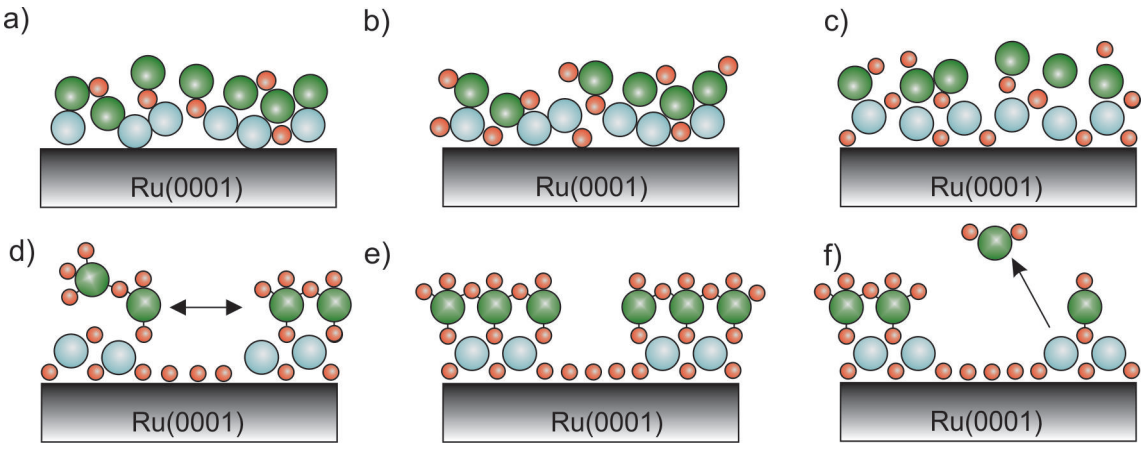

Figure 5.14 Individual steps during oxidation of iron germanate prepared with the "combined UHV preparation" method (Fe+Ge(UHV)/Ru(0001)). a) deposition of iron and germanium at RT. The film is disordered. Iron and germanium are partially oxidized. b-e) Oxidation in $1.0 \cdot 10^{-6}$ mbar. b) Oxidation at RT. Improved oxidation of germanium, and especially iron, but no structural change. c) Oxidation at 590 K. Iron is arranging, giving rise to a "6 on 7" Moiré pattern surrounding the (00) spot. Still reduced germanium components present. d) Oxidation at 670 K. Separation in iron germanate ($(\sqrt{3} \times \sqrt{3})R30°$ spots) and holes down to the Ru(0001) substrate ((2x2) spots). Now also germanium is completely oxidized in the Ge^{4+} state. Iron is mainly found in the Fe^{3+} state. e) Up to 840 K the iron germanate structure improves. f) Temperatures above 840 K lead to germanium evaporation. Red: Oxygen. Blue: Iron. Green: Germanium.

other the disorder of the layer. Since the germanium amount is not sufficient for a closed germania layer, holes down to the 3O-covered Ru(0001) substrate are formed. As was seen for the "stepwise reversed preparation" method, iron atoms not bound to germanium are thermally less stable than those in the iron germanate regions. Thus, germanium stabilizes the iron oxide layer. Moreover, the film is less stable at higher temperatures than the film prepared with the "stepwise reversed preparation" method, most likely due to the large amount of very small holes and with this large rim area of iron germanate.

5.3 Summary and conclusion of ultrathin $FeGeO_x$ films

The results show that ultrathin iron germanate films exist on Ru(0001). Iron germanate can be prepared using different preparation methods, namely the "stepwise reversed preparation" and the "combined UHV preparation" method. The characteristic LEEM-IV fingerprint is given in Fig. 5.15 and the characteristic LEED-IV fingerprints for both preparation methods are shown in Fig. 5.16.

In the "stepwise reversed preparation" method during the germania preparation germanium-rich and germanium-free domains are prepared. The size of these areas is unchanged upon iron deposition. As a result in the germania-rich areas iron germanate forms, while in the germanium-free domains iron oxide is produced. With increased oxidation temperature these iron oxide layers dissolve. Most likely iron diffuses from the germanium-free domains to the iron germanate domains. At 620 K germanium and iron are completely oxidized and the later iron germanate structure is already present. The structure improves up to 860 K, before germanium starts to evaporate.

In the "combined UHV preparation" method also domains of iron-rich and iron-free areas are found. Nevertheless, their dimensions are very small, so that the iron germanate domains are supposedly very small as well. The necessary energy (temperature) to oxidize

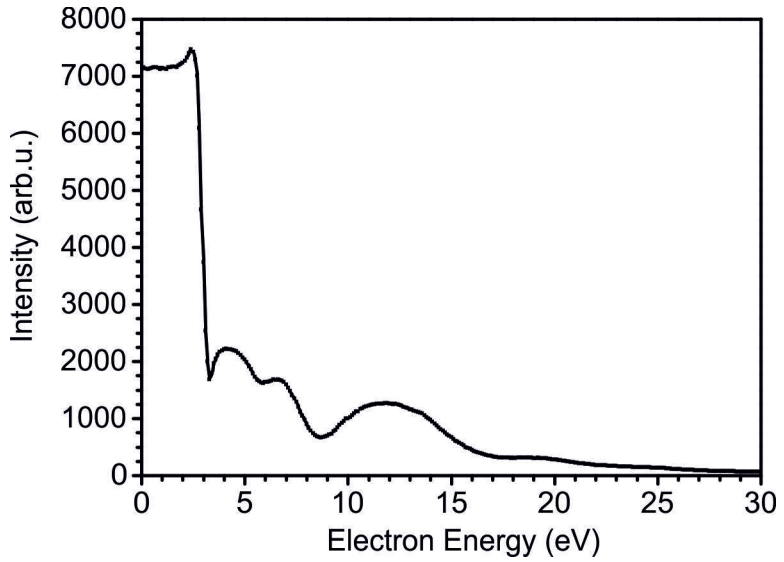

Figure 5.15 Fingerprint for $FeGeO_x$ films. This curve is taken from the germanium-rich areas of the "stepwise reversed preparation" method ($Fe/GeO_2/Ru(0001)$).

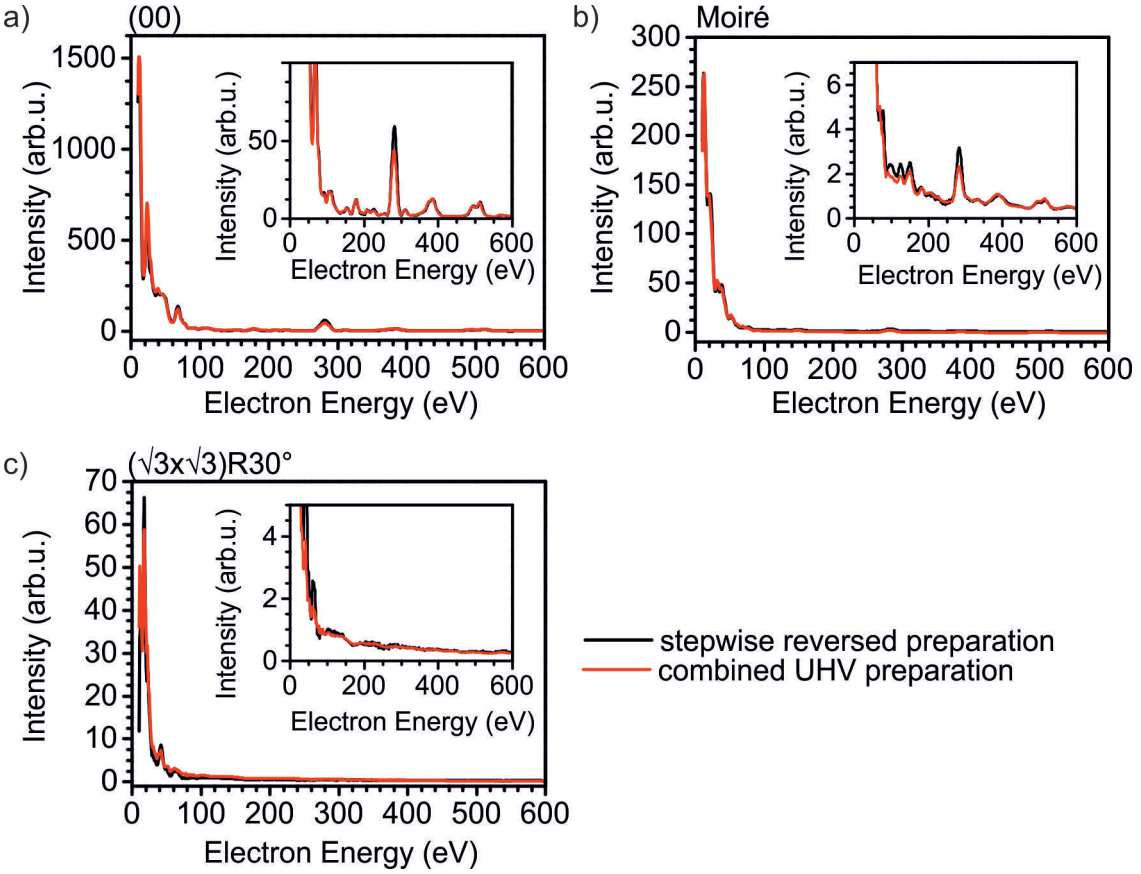

Figure 5.16 LEED-IV curves of $FeGeO_x$ prepared with the "stepwise reversed preparation" method (chapter 5.1) ($Fe/GeO_2/Ru(0001)$) and "combined UHV preparation" (this chapter) ($Fe+Ge(UHV)/Ru(0001)$) at 890 K and 880 K, respectively. a) (00) spot, b) a Moiré spot, surrounding the (00) spot and c) $(\sqrt{3} \times \sqrt{3})R30°$ spot. The $(\sqrt{3} \times \sqrt{3})R30°$ structure refers to a germania structure that is rotated by 30° regarding a complete iron oxide layer.

germanium and iron is considerably higher (720 K) as for the "stepwise reversed preparation" method (620 K). Also the germanium atoms start to arrange and the by 30° rotated structure appears at higher temperatures (670 K). Moreover, the film is less stable, as germanium starts to evaporate already at 840 K. In summary, the pre-prepared germania layer decreases the necessary energy for the arrangement and oxidation of the film. Moreover, the final film is more stable. The reason might be the small size of the domains and thus, large domain borders, which makes desorption of germanium (especially at the border) easier. An overview of the individual temperatures for both preparation methods are given in Tab. 5.3.

Iron germanate prove to have nearly the same structure as iron silicate: a germania monolayer bound through oxygen atoms to a iron oxide layer on top of Ru(0001). A model is given in Fig. 5.17. Since the results of iron silicate indicate only two iron atoms per silica unit cell, the same iron concentration per germania unit cell is assumed for iron germanate.

The structure of the germania layer is nearly the same as the equivalent silica layer, namely unrotated regarding the iron oxide layer underneath, but shifted in respect to the position of the iron atoms. As a difference, the iron oxide layer in iron germanate has the same dimensions as a pure FeO layer (chapter 3), which is a "6 on 7" reconstruction (Fe-Fe distance:

	stepwise reversed	**combined UHV**
Abbreviation	(Fe/GeO_2/Ru(0001))	(Fe+Ge(UHV)/Ru(0001)
T at which Fe and Ge are completely oxidized	620 K	720 K
T of Moiré formation	After Deposition	590 K
T of by 30° rotated spots	620 K	670 K
T of Ge desorption	860 K	840 K

Table 5.3 Temperature dependencies of iron germanate preparations on Ru(0001) using different preparation methods.

3.157 Å). In contrast in iron silicate silicon reduces the Fe-Fe distance to 3.044 Å ("8 on 9" reconstruction). In the following it will be discussed, why the same Fe-Fe distance is found in iron germanate as in pure FeO layers. There can be two possibilities: A) The Fe-O-Ge bond is weak, so that the iron oxide layer is arranged unperturbed. B) The Ge-O-Ge bond defines the distances of the iron atoms (i.e. the Ge-O-Fe bond is strong) and the Fe-Fe distances are accidently overlapping with the ideal Fe-Fe distance in FeO.

Germanium has the same number of valence electrons, since it is the same group of the periodic table. However the period is higher and thus, the overall number of electrons. As a result the diameter of the germanium atom is larger than the diameter of the silicon atoms. This results in a larger Ge-O distance (medium value 1.73 Å [92]) as for Si-O bond (1.61 Å compare section 4.1.3. The angle of the Ge-O-Ge bond is typically smaller (mean value: 133° [99]) than that of Si-O-Si. Using these values the intermediate Ge-Ge distance can be calculated to 3.17 Å. The corresponding geometry is shown in Fig. 5.18. The determined Fe-Fe distance is 3.157 Å, which is a compression of 0.4 % relative to the average Ge-O-Ge distance.

Assuming the same coordination number, i.e. number of nearest neighbors, the electronegativity of germanium χ_{Ge} is found to be slightly higher than the electronegativity of silicon χ_{Si}. For a coordination number of four, which fits to the iron germanate and iron silicate films in this thesis, the electronegativities are determined for silicon and germanium as 1.81 and 1.83, respectively [29]. Since these values are very similar, comparable properties of the Ge-O-Fe and Si-O-Fe bonds are expected. The slightly higher electronegativity of

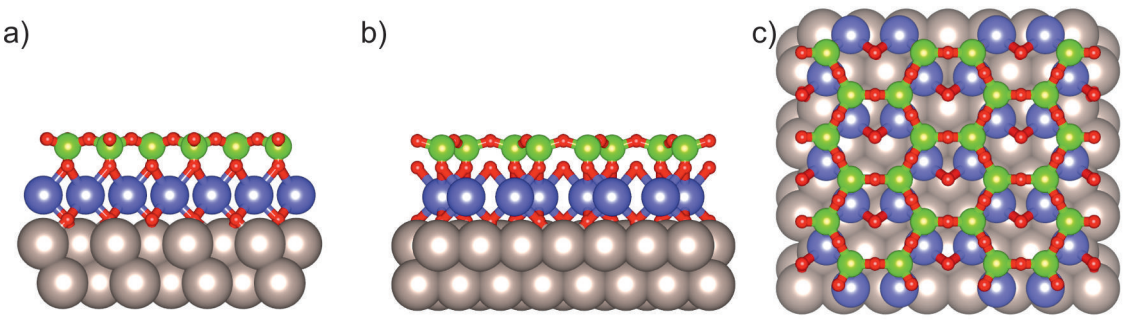

Figure 5.17 Structural model of iron germanate in the a) x-direction, b) y-direction and c) z-direction. Red: Oxygen. Violet: Iron. Green: Germanium. Gray: Ruthenium.

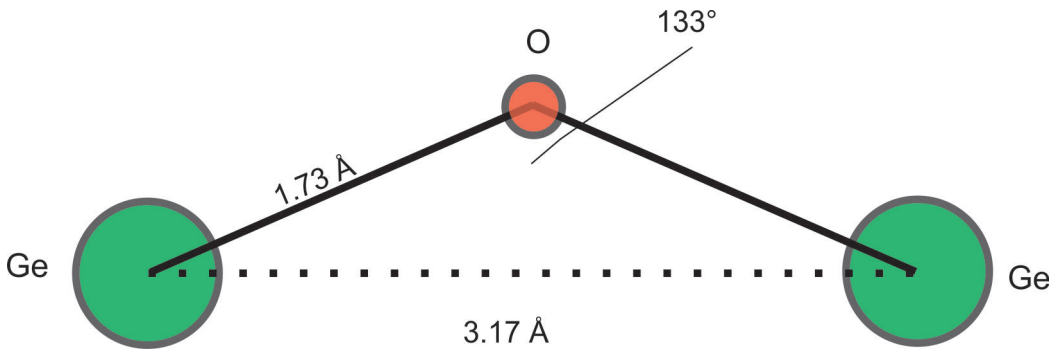

Figure 5.18 Geometry of an unstrained Ge-O-Ge bond with medium values. The medium value of the Ge-O distance in a Ge-O-Ge bond is taken from [92]), the angle from [99].

germanium indicates that iron transfers even more electronic charge to the oxygen atom in the Ge-O-Fe bond than in the Si-O-Fe bond, which shifts the electron density maxima slightly more towards the germanium atom than the silicon atom (compare also section 4.1.3). Moreover the oxygen dissociation energies of Si-O and Ge-O are (with 798 kJ/mol and 662 kJ/mol, respectively) much higher than the oxygen dissociation energies of Fe-O (409 kJ/mol) and Ru-O (481 kJ/mol). The values are valid for the gas phase and taken from [2].

Judging from the electronegativities and oxygen dissociation energies, a similar bond strength for the Si-O-Fe and Ge-O-Fe bond is expected. Therefore, the reason for the achieved Fe-Fe distance might be rather the optimal Ge-O-Ge bond distance than the optimal Fe-Fe distance in FeO. This indicates that the Ge-O-Fe bond is equally strong as the Si-O-Fe bond.

Comparing the "stepwise reversed preparation" with the "combined UHV preparation", the pre-ordering of the GeO_2 layer lowers the necessary oxidation temperature of the arrangement of the iron germanate layer. In contrast the pre-ordered SiO_2 layer increases the temperature of iron silicate formation (compare section 4.2.2). The same is the case for the oxidation of the film. In fact, the deposition of iron on germania leads to a decrease of the Ge 3d oxidation state. For silicon this does not happen. It was even observed that iron oxide becomes reduced after silicon oxidation (see section 4.2.1).

In the O 1s line of iron silicate the Si-O-Fe component is easily distinguishable. For the Ge-O-Fe bond this is not the case. In fact the individual O 1s lines can be fitted also with two lines, only. In literature [61] the intensity and expected position of the Ge-O-Fe line for sodium iron germanate films have been calculated. It was found that the intensity of the Ge-O-Fe line is very low and the position is expected 0.5 eV - 1.0 eV separated from the Ge-O-Ge line. Due to the low intensity a Ge-O-Fe bond cannot be proven using the O 1s line. Nevertheless a Ge-O-Fe bond is expected, since the same structure as for iron silicate is found. The Fe^{3+}:Fe^{2+} ratio is similar for iron silicate and iron germanate.

Germanium and silicon stabilize the iron oxide layer. However, iron germanate is thermally less stable than iron silicate with desorption temperature of 860 K compared to 1000 K. The reason is the different stabilities of germanium and silicon themselves, which is also obvious by their very different melting temperatures of 1210 K and 1688 K for germanium and silicon, respectively [1]. The stability of iron germanate and iron silicate depend in both cases on the preparation method.

	Iron silicate	**Iron germanate**
Fe-Fe distance /Moiré	3.044 Å/ "8 on 9"	3.157 Å/ "6 on 7"
Silica/germania arrangement	unrotated, but shifted regarding iron oxide layer	unrotated, but shifted regarding iron oxide layer
Workfunction	5.83 - 5.95 eV (at 900 K or 1000 K)	5.65 - 5.91 eV (at 720 K)
O 1s lines	Si-O-Si: 531.0 eV Si-O-Fe: 530.0 eV Fe-O-Fe/Fe-O-Ru: 529.3 eV	Ge-O-Ge: 530.2 eV Fe-O-Fe/Fe-O-Ru/Ge-O-Ru: 529.3 eV
Final film temperature	900 K - 1000 K	840 K - 860 K
Desorption temperature	$\leq$1100 K	840 K - 860 K

Table 5.4 Comparison of the characteristics of iron silicate and iron germanate on Ru(0001) as found in this thesis.

In summary iron germanate ultrathin films can be prepared on Ru(0001). In their structure they are very similar to ultrathin iron silicate films, forming a two-layered film with a monolayer of germania on top of an iron oxide layer. Since the results of the iron silicate layer in chapter 4 indicate the number of iron atoms per unit cell to be two, it s assumed, that this is also the case for iron germanate. Thus, in accordance to iron silicate the germania layer is unrotated, but shifted relative to the iron atoms underneath. The Fe-Fe distance in iron germanate equals a "6 on 7" reconstruction. A strong Ge-O-Fe bond can be assumed to present, judging from the similar electronegativity of germanium and silicon and the bond dissociation energies. Nevertheless in the XPS O 1s line the Ge-O-Fe bond is not visible. Calculations of the Ge-O-Fe line for sodium iron germanate indicate that the intensity is expected to be very low and in particular much lower than for the Si-O-Fe line for the same occurrence. Moreover, the position of the Ge-O-Ge line overlaps with the Ge-O-Fe lines. Germanium, similar to silicon stabilizes the iron oxide layer underneath. However the maximum oxidation temperature is considerably lower for germania, which correlates with the lower melting temperature of germanium in contrast to silicon.

Chapter 6

Preliminary results: Influence of the metallic support

In the previous chapters iron oxide based ultrathin film formation was studied on Ru(0001). However, the importance of the substrate was not discussed up to now. For ultrathin silica layer the substrate proved to be decisive for the formation of mono- or bilayer films of silica and possible crystal structures (crystalline or vitreous). In particular, the strength of the metal-oxygen bond defines the possible layer thickness [89] and the lattice mismatch the possible crystallinity [97]. Thus, the variation of the substrate for iron silicate formation should make information accessible about the importance of the oxygen layer at the Fe/Ru-interface and the influence of the Ru(0001) substrate on the iron silicate formation.

In the following, preliminary results at the study of ultrathin layers of iron silicate on a Pt(111) crystal are shown. Pt(111) is known to have a weak metal-oxygen bond [109], which is considerably weaker than for Ru(0001) (dissociative heats of adsorption of O_2 on Pt(111) and Ru(0001) are 133 kJ/mol and 220 kJ/mol [75], respectively).

Iron silicate was prepared with the "combined preparation" method (compare chapter 4.1.1). In this method first silicon and subsequently iron are deposited at RT in $2.0 \cdot 10^{-7}$ mbar oxygen pressure on a freshly cleaned Pt(111) substrate. In contrast to iron silicate on Ru(0001) the Pt(111) substrate is not oxygen-precovered. Subsequently, the film is oxidized stepwise at RT, 770 K, 980 K and 1080 K in $1.0 \cdot 10^{-6}$ mbar .

In Fig. 6.1a and b LEED images after oxidation at 770 K and 980 K are shown. The LEED pattern shows a by 30° rotated structure overlapped with a Moiré pattern with "9 on 10" reconstruction. In fact this structure resembles the one found for iron silicate on Ru(0001). However, no Moiré spots are found surrounding the by 30° rotated structure. From the "9 on 10" reconstruction on Pt(111) (Pt-Pt distance: 2.77 Å) the Fe-Fe distance can be determined to (3.08 ± 0.03) Å (Fe-Fe distance of a "8 on 9" reconstruction on Ru(0001): (3.04 ± 0.03) Å). Thus, the Fe-Fe distance of iron silicate on Pt(111) and the Fe-Fe distance of iron silicate on Ru(0001) are identical in within the error value. The error is defined by the ability to identify the Moiré reconstruction. In Fig. 6.1c the LEEM-IV fingerprint is given for future reference.

XPS spectra of the O 1s and Si 2p line are shown in Figs. 6.2a-b and c-d, respectively, for two different photon energies. The O 1s line contains three components at 530.8 eV, 530 eV and 529.2 eV. In accordance with the iron silicate investigation on Ru(0001) these lines can be assigned to Si-O-Si, Si-O-Fe and Fe-O-Fe bonds. The XPS O 1s line measured at

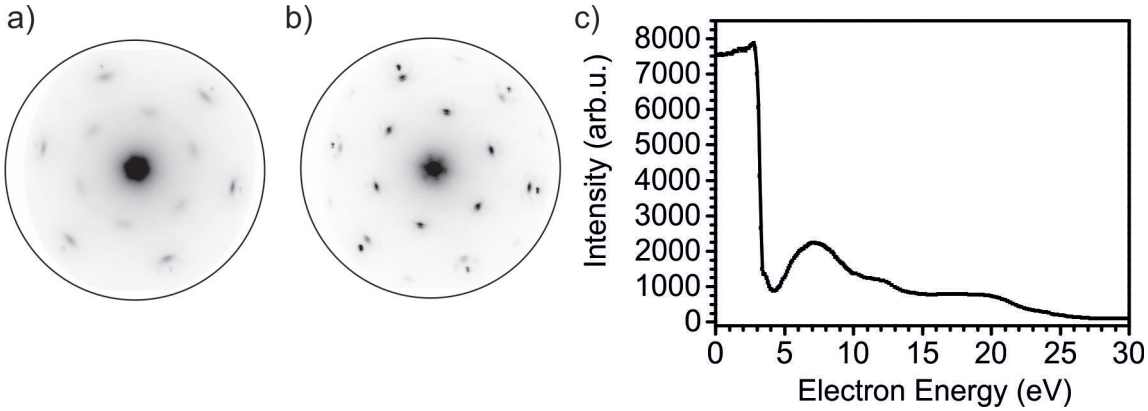

Figure 6.1 Iron silicate preparation on Pt(111), following the "combined preparation" method (Si+Fe/Pt(111)). LEED images at 42 eV, taken after oxidation at a) 770 K and b) 980 K. Similar to iron silicate on Ru(0001) a Moiré pattern as well as a by 30° rotated structure is visible. c) LEEM-IV fingerprint at 770 K.

hν = 600 eV (Fig. 6.2a) shows that the Si-O-Si bond is more prominent than the Fe-O-Fe component. In contrast, using a higher photon energy of hν = 800 eV, i.e. a higher electron mean free path, the Fe-O-Fe component has equal intensity with the Si-O-Si component. This shows that the film consists of two layers with a layer of silica on top of an iron oxide layer.

A temperature rise to 980 K and subsequently 1080 K leads to a depletion of the Fe-O-Fe component in the O 1s line, both at photon energies of 600 eV and 800 eV. In contrast, the silicon amount remains stable, as visible in the Si 2p. Moreover, the comparison of photon energies at 175 eV and 350 eV (Fig. 6.2) suggests that the silicon amount increases with increasing temperatures at the iron silicate/substrate interface (hν = 350 eV), while the silicon amount in the upper monolayer (hν = 175 eV) decreases. These measurements show that iron is reduced with increasing temperature. During this process silicon diffuses from the top of the iron silicate layer towards the iron silicate/Pt(111) interface.

In summary iron silicate can be prepared on Pt(111). The structure of this film fits to the structure determined for iron silicate on Ru(0001), namely the formation of a silica monolayer on top of an iron oxide layer. In LEED spots rotated by 30° are overlapped with a Moiré pattern with "9 on 10" reconstruction. The Fe-Fe distance of iron silicate on Pt(111) is found within the error value of the Fe-Fe distance of iron silicate on Ru(0001). This fits to the assumption that the Fe-Fe distance in the iron oxide layer is determined by the Si-O-Si distance and not by the substrate. The iron silicate layer on Pt(111) is less stable than on Ru(0001), which is apparent by iron depletion for temperatures higher than 770 K. Most likely iron diffuses into the Pt(111) crystal as is known for iron oxide films on Pt(111) [28, 82]. Silicon from the top-most layer diffuses to the iron silicate/Pt(111) interface with iron depletion. A possible explanation for the reduced stability on Pt(111) is a missing oxygen layer between iron silicate and the Pt(111) substrate.

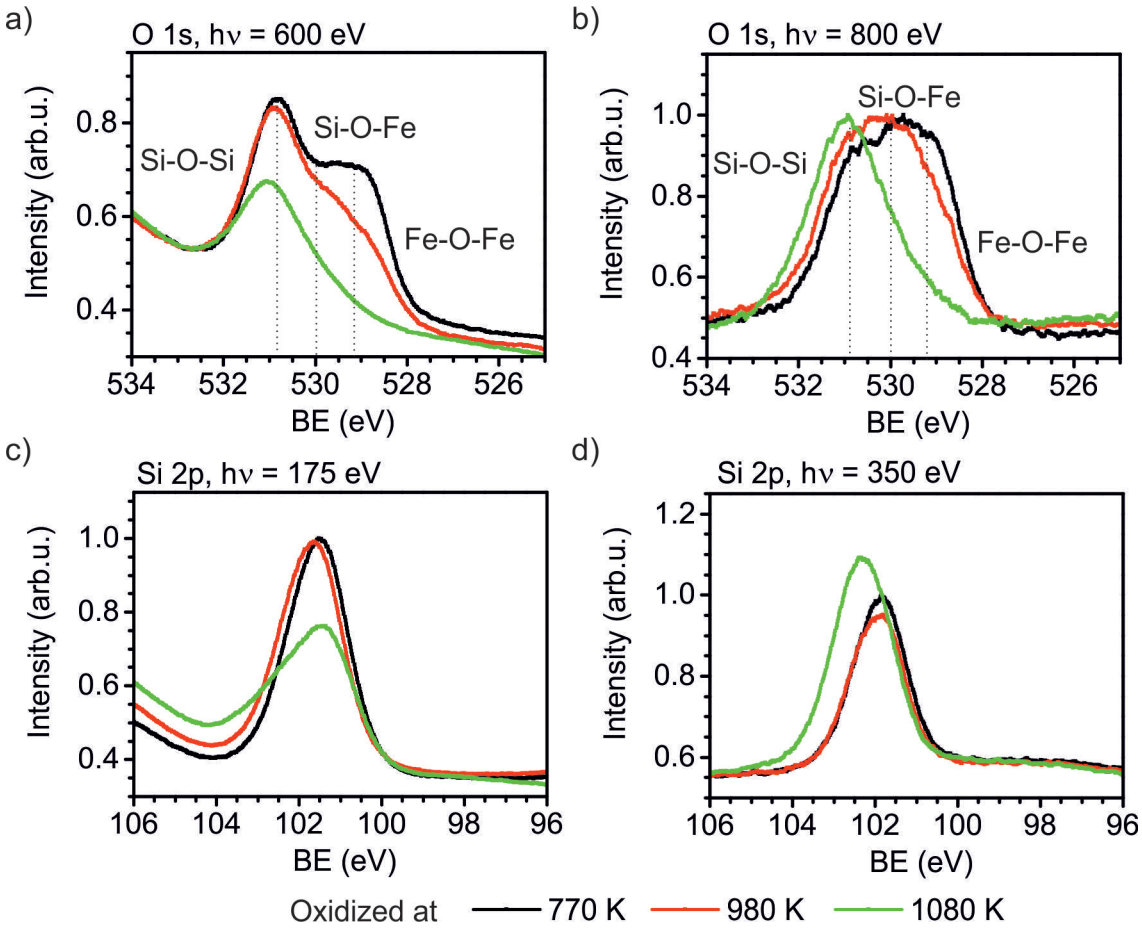

Figure 6.2 Temperature dependent XPS investigation of iron silicate prepared on Pt(111), following the "combined preparation" method (Si+Fe/Pt(111)). O 1s line at a) $h\nu = 600\,eV$ and b) $h\nu = 800\,eV$. Si 2p line at c) $h\nu = 175\,eV$ and d) $h\nu = 350\,eV$. The films are prepared by subsequent oxidation in $1.0 \cdot 10^{-6}$ mbar.

Chapter 7

Conclusion and outlook

This work has explored important aspects in means of film formation, physical and chemical properties, as well as stability of two-dimensional layers on Ru(0001). The focus lies on the understanding of model systems for zeolitic structures containing iron. All films have been prepared in situ and their film formation monitored in real-time. The methods of LEEM, μLEED, μXPS and XPEEM were employed for chemical and physical characterization of the individual preparation steps of these films.

The thesis is divided into three parts, namely the investigations of FeO (chapter 3), iron silicate (chapter 4) and iron germanate (chapter 5). All three chapters are interconnected by the presence of an iron oxide layer. In fact, iron silicate and iron germanate can be understood as a silica or germania layer on top of a FeO-like film. One of the main aims of this study is the characterization of the iron oxide layer in iron silicate and iron germanate. Thus, the study of pure FeO films in the same setup and under similar conditions is crucial.

In chapter 3 FeO_{x+1} mono and bilayers are prepared by direct deposition of iron at elevated temperatures in oxygen background. Stranski-Krastanov layer growth was found, whereby the layer thickness depends solely on the oxygen background pressure. Pure monolayer-thick films grow in the pressure regime of $1.0 - 2.0 \cdot 10^{-8}$ mbar, while pure bilayer-thick FeO films grow in $1.0 \cdot 10^{-7}$ mbar. Intermediate pressures lead to parallel growth of both thicknesses. We show that different sub-phases exist for the mono- and bilayer-thick films, whereby some of these can be transformed into slightly more stable sub-phases. The structures and properties of the individual sub-phases are discussed in detail. We performed a chemical analysis, which revealed that the as-grown FeO bilayer contains more oxygen than expected for FeO, i.e. it also contains iron atoms in the Fe^{3+} state and not only in the Fe^{2+} state. This indicates the presence of an additional oxygen layer. In contrast, the as-grown monolayer has only iron atoms in the Fe^{2+} state, and thus proves to be indeed a FeO monolayer. The as-grown FeO mono- and bilayer-thick films proved to be metastable, and their oxygen related transformation is discussed.

Chapter 4 discusses ultrathin layers of iron silicate in detail. In order to explore bonding and oxidation dependencies within iron silicate, four different preparation methods are developed. In particular, the starting conditions are varied using either a "combined" approach, or a "stepwise" approach. In the "combined" approach, silicon and iron are deposited in the same preparation step and under the same conditions. In the "stepwise" approach either a FeO monolayer or a silica layer is prepared before either silicon or iron is then deposited. Temperature dependent film evolution was followed for all preparation methods in every preparation stage. We found that all examined preparation methods

lead to the same final film in terms of LEEM-IV and LEED-IV fingerprints. However, the formation process differs strongly for the individual preparation methods. In particular, the pre-oxidation and pre-ordering of silica before iron deposition has a strong influence on the necessary temperatures for the oxidation and formation of the iron oxide layer and formation of the silica layer in iron silicate. The reason is the larger dissociation energy of Si-O bonds compared to Fe-O bonds. As a result silicon is always oxidized before iron can be completely oxidized in the near surrounding. The individual temperatures for the formation of the iron oxide and silica layer (on top of iron oxide) can differ by up to 135 K and 365 K, respectively. The final iron silicate signature is achieved by oxidation at 900 K if iron and 1000 K if silicon is deposited first.

Incomplete films of iron silicate using both the "combined" and the "stepwise" approach unveil important information about dynamic processes and stabilities of the films. For silicon the iron silicate formation is more preferred than the formation of pure silica on Ru(0001). Thus, with disordered starting conditions ("combined" approach) silicon binds to iron first, forming iron silicate, before iron-free areas are covered by silica. This takes place in form of a silica bilayer formation in contact to iron silicate. The silica bilayer then follows the orientation of the silica substructure in iron silicate. Moreover, silicon atoms bind at nucleation centers in the iron-free areas, forming agglomerates of silica monolayer.

In contrast, using the "stepwise" approach in combination with incomplete film coverage enables direct observation of iron depletion from iron silicate islands, when these islands are based on silica deposition onto monolayer-thick FeO islands. The fingerprint of these iron silicate domains equals complete layers of iron silicate and thus, proves that the iron oxide layer in iron silicate has a lower iron amount than a FeO monolayer. The migrating iron forms agglomerates of iron silicate in initially iron-free areas. The dynamic processes are followed and discussed in detail.

Our investigations reveal the structure of iron silicate thin films to be as follows: Iron silicate is a two-layered system consisting of a monolayer of iron oxide in contact to Ru(0001) with a monolayer of silica on top. The two layers are bound through Fe-O-Si bonds. Iron is found in the Fe^{2+} and Fe^{3+} oxidation states, which indicates not only a shared oxygen layer at the iron/silicon interface, but also an additional oxygen layer at the iron/ruthenium interface. Thus, additionally to the aforementioned Fe-O-Si, Fe-O-Fe as well as Fe-O-Ru bonds are present. The number of iron atoms per silica unit cell is found to be two, in contrast to the three iron atoms per silica unit cell in a complete FeO layer. The positions of "missing" iron atoms in respect to a complete iron oxide layer (i.e. three iron atoms per silica unit cell) give rise to a by 30° rotated structure in LEED. The silica monolayer consists of corner-sharing tetrahedrons, with oxygen atoms at the corners of these tetrahedrons. The silica layer is unrotated regarding the iron oxide layer underneath, but DFT simulations performed in collaboration with R. Włodarczyk et al. (see section 4.1.3) indicate a shift between the silica atoms and iron atoms. Iron oxide arranges in a "8 on 9" Moiré reconstruction regarding the Ru(0001) substrate. From this, the average Fe-Fe distance is determined to be 3.044 Å (in case of a complete iron oxide layer with three iron atoms per silica unit cell), which is shorter than the Fe-Fe distance in pure FeO layers (3.157 Å). In fact, the Fe-Fe distance in iron silicate fits very well to an unstrained Si-O-Si bond, as found in silicates. This indicates that the Si-O-Si bond distance defines the Fe-Fe distance, which suggests strong Fe-O-Si and Si-O-Si bonds to be present in iron silicate layers.

We show that iron silicate can be prepared on the basis of a FeO bilayer. However, the comparison of complete and incomplete films reveals the influence of the environmental conditions on the stability of these films. In complete films, the second iron oxide layer remains and the Fe-Fe distances are reduced in both iron oxide layers. In contrast, in incomplete films excess iron migrates out of the islands, leaving monolayer-thick iron silicate. We show that this happens in a two-step process, whereby at first, the number of iron atoms per layer is reduced and in a second step, the lower iron oxide layer dissolves.

Moreover, we show that it is also possible to prepare a film of iron silicate containing two layers of silica. The final LEED structure equals that of pristine iron silicate, which indicates a strong bond of between the two silica layers, but also towards the iron oxide layer. This structure is stable up to 955 K, which is considerably lower than iron silicate with only one silica layer. We propose a structure where the perpendicular Si-O bond alternates between a Si-O-Si bond to the upper silica layer and a Si-O-Fe bond to the iron oxide layer. However, this might lead to dangling bonds, which are likely to be saturated by OH groups and might be present on top of the film. This might be the reason for the reduced stability in contrast to other iron silicate preparations.

In chapter 5 the effect of silicon substitution by germanium is examined. We show that ultrathin iron germanate films can be prepared. Different preparation methods lead to the same iron germanate LEEM-IV and LEED-IV fingerprints, suggesting that this is energetically the most stable phase. The structure of a thin film of iron germanate turns out to be very similar to that of iron silicate. It consists of a two-layered system with a iron oxide layer on top of Ru(0001) and a germania layer on top. Since the iron silicate results indicate a reduced number of two iron atoms per silica unit cell, it is assumed that the iron oxide layer in iron germanate contains two iron atoms per unit cell, as well. However, the larger size of the germanium atoms in contrast to silicon atoms leads to a larger Ge-O-Ge bond, which in turn leads to a "6 on 7" Moiré reconstruction of the iron oxide layer (Fe-Fe distance: 3.157 Å). Temperature dependent film formation and in particular differences to iron silicate are discussed in detail.

As the measurements in this work show, iron silicate and iron germanate are found to be the most stable systems in the studied pressure and temperature regime. The two-dimensionality of these films provides the accessibility with surface science techniques and thus, enables the study of structure-reactivity-relations. This is especially interesting in order to study the suitability of iron silicate and iron germanate as model systems for zeolite structures. Zeolites are known for their catalytic activity and their ability to act as molecular sieves and selective catalysts. Thus, as a next step the chemical properties of the iron silicate and iron germanate films should be explored by means of intercalation experiments and chemical reactions.

Similar experiments have been performed before on the silica bilayer and aluminosilicate films on Ru(0001). While for the silica bilayer on Ru(0001) O_2 intercalation is found, aluminosilicate inhibits O_2 intercalation [21, 110]. Moreover, D_2 and CO intercalation are found to be only present in vitreous silica layers with larger Si-O-Si ring sizes [22, 85]. Water dissociation at low temperatures was measured on silica bilayers, resulting in Si-OH groups and OH, where the second oxygen atom is part of the silicate [20]. Moreover, the adsorption of NH_3 on the silica bilayer leads to H-D exchange, i.e. OH groups can be replaced by OD and vice versa [20]. The addition of metal atoms is known to enhance catalytic activity of silicates, hence, chemical reactions should be investigated for the iron

silicate and iron germanate films of this work. This might lead to new insights in the structure related reactivity and as a result to improvements of three-dimensional zeolites.

Apart from the study of chemical reactions the influence of the metal substrate on the iron silicate and iron germanate formation are still unknown. Recent experiments (see chapter 6) indicate that iron silicate formation is possible also on Pt(111). However, the stability of the iron oxide layer is strongly reduced. Thus, the results indicate that the Ru(0001) substrate has a strong influence on the stability of the iron silicate films. Metal substrates with strong metal-oxygen bonds, would lead to further interesting information regarding the role of the substrate on the film formation and stability.

Finally, iron might be exchanged by other metals in order to prepare accessible model systems for other three-dimensional compounds. First results have already been reported for Ti-silicates [25], who found a similar film structure as for iron silicate.

Symbols and Abbreviations

BL	Bilayer
DF	Darkfield
FeGeO$_x$	Ultrathin iron germanate layer consisting of a monolayer of GeO_2 bound on top of a monolayer of iron oxide
FeSiO$_x$	Ultrathin iron silicate layer consisting of a monolayer of SiO_2 bound on top of a monolayer of iron oxide
IRAS	Infrared Reflection Absorption Spectroscopy
LEED	Low Energy Electron Diffraction
LEEM	Low Energy Electron Microscopy
LEEM-IV	Intensity vs. Voltage LEEM
MEM	Mirror Electron Microscopy
ML	Monolayer
SMART	Spectro-Microscope with Aberration correction for many Relevant Techniques
UHV	Ultra-high vacuum
XPEEM	X-ray Photoemission Electron Microscopy
XPS	X-ray Photoelectron Spectroscopy

List of Figures

List of Tables

Bibliography

[1] https://www.virginiasemi.com/pdf/generalpropertiesSi62002.pdf, 03.04.2018.

[2] labs.chem.ucsb.edu/zakarian/armen/11—bonddissociationenergy.pdf, 29.01.2018.

[3] T.L. Alford, L.C. Feldman, and J.W. Mayer. Fundamentals of Nanoscale Film Analysis. 2007.

[4] N.W. Ashcroft and D.N. Mermin. Festkörperphysik. Oldenbourg Wissenschaftsverlag GmbH, München, 5 edition.

[5] R.M. Barrer, J.W. Banham, F.W. Bultitude, and W.M. Meier. J.Chem. Soc., page 195, 1959.

[6] R.M. Barrer and W. M. Meier. Trans. Faraday Soc., 54:1074, 1958.

[7] E. Bauer. Surf. Rev. Lett., 5:1275–1286, 1998.

[8] E. Bauer. Surface Microscopy with Low Energy Electrons. Springer, New York, 2014.

[9] C. Büchner. Adding a Novel Material to the 2D Toolbox: Properties and Transfer of a Silica Bilayer. PhD thesis, HU Berlin, 2017.

[10] C. Büchner and M. Heyde. Prog. Surf. Sci., 92:341–374, 2017.

[11] C. Büchner, M. Heyde, and H.-J. Freund. Reference Module in Chemistry, Molecular Science and Chemical Engineering.

[12] W. Berthold, U. Höfner, P. Feulner, and D. Menzel. Chem. Phys., 251:123, 2000.

[13] A. Boscoboinik, X. Yu, B. Yang, S. Shaikhutdinov, and H.-J. Freund. Micoporous and Mesoporous Materials, 165:158–162, 2013.

[14] J.A. Boscoboinik, X. Yu, B. Yang, F.D. Fischer, R. Wł odarczyk, M. Sierka, S. Shaikhutdinov, J. Sauer, and H.-J. Freund. Angew. Chem. Int. Ed., 51:6005–6008, 2012.

[15] K.M. Burson, C. Buechner, M. Heyde, and H.-J. Freund. J.Phys.:Condens. Matter, 29:035002, 2017.

[16] W.K. Choi, W.K. Chim, C.L. Heng, L.W. Teo, V. Ho, V. Ng, D.A. Antoniadis, and E.A. Fritzgerald. Appl. Phys. Lett., 80:2014, 2002.

[17] T.L. Cottrell. The Strength of Chemical Bonds. Butterworth, London, 2 edition, 1958.

[18] J.D. Cressler. Silicon-germanium heterojunction bipolar transistors. Artech House, Inc. Norwood, USA, 2003.

[19] L.G. Dainyak, B.B. Zviagina, V.S. Rusakov, and V.A. Drits. Eur. J. Mineral, 18:753–764, 2006.

[20] E. Emmez. Adsorption on Metal-Supported Silicate Film: Surface and Sub-Surface Chemistry. PhD thesis, HU Berlin, 2015.

[21] E. Emmez, J.A. Boscoboinik, S. Tenney, P. Sutter, S. Shaikhutdinov, and H.-J. Freund. Surf. Sci., 646:19–25, 2016.

[22] E. Emmez, B. Yang, S. Shaikhutdinov, and H.-J. Freund. J. Phys. Chem. C, 118:29034, 2014.

[23] J. de la Figuera, J.M. Puerta, J.I. Cerda, F. El Gabaly, and K.F. McCarty. Surf. Sci., 600:L105–L109, 2006.

[24] R. Fink, M.R. Weiss, E. Umbach, D. Preikszas, H. Rose, R. Spehr, P. Hartel, W. Engel, R. Degenhardt, R. Wichtendahl, H. Kuhlenbeck, W. Erlebach, K. Ihmann, R. Schlögl, H.-J. Freund, A.M. Bradshaw, G. Lilienkamp, Th. Schmidt, E. Bauer, and G. Brenner. J. Electron Spectroscopy and Related Phenomena, 84:231–250, 1997.

[25] F.D. Fischer, J. Sauer, X. Yu, J.A. Boscoboinik, S. Shaikhutdinov, and H.-J. Freund. J. Phys. Chem. C, 119:15443–15448, 2015.

[26] J.I. Flege and E.E. Krasovskii. Phys. Status Solidi-Rapid Res. Lett., 8:463–477, 2014.

[27] C. Freysoldt, P. Rinke, and M. Scheffler. Phys. Rev. Lett., 99:086101, 2007.

[28] F. Genuzio. Spectro-microscopic investigation of Fe-oxide bbase model catalyst and instrumental development. PhD thesis, Humboldt-Universität Berlin, 2016.

[29] G.V. Gibbs, M.B. Boisen, F.C. Hill, O. Tamada, and R.T. Downs. Phys. Chem. Minerals, 25:574–584, 1998.

[30] S. Günther, B. Kaulich, L. Gregoratti, and M. Kiskinova. Prog. Surf. Sci., 70:187–260, 2002.

[31] M. Gsell, M. Stichler, P. Jakob, and D. Menzel. Israel J. of Chem., 38:339–348, 1998.

[32] E.J.M. Hensen, Q. Zhu, and R.A. van Santen. J. Catal., 220:260, 2003.

[33] E. Hess. Zeitschrift für Physik, 92:274–282, 1934.

[34] H. Heyde, S. Shaikhutdinov, and H.-J. Freund. Chem. Phys. Lett., 550:1–7, 2012.

[35] F.M. Hoffmann and M.D Weisel. Suf. Sci., 253:59–71, 1991.

[36] R.K. Iler. The colloid chemistry of silica and silicates. Cornell Universtiy Press, Ithaka, New York, 1955.

[37] E. Ingerson, G.W. Morey, and O.F. Tuttle. Amer. J. Sci., 54:31, 1946.

[38] B. Jha and D.N. Singh. Fly Ash Zeolites, Advanced Structured Materials 78. Springer, Singapore, 2016.

[39] W.E. Kaden, S. Pomp, M. Sterrer, and H.-J. Freund. Top. Catal., 60:471–480, 2017.

[40] C.R. Kagan and P. Andry. Thin-Film Transistors. Marcel Dekker, Inc. New York, Basel, 2009.

[41] G. Ketteler and W. Ranke. J. Phys. Chem. B, 107:4320–4333, 2003.

[42] G. Ketteler, W. Weiss, W. Ranke, and R. Schlögel. Phys. Chem. Chem. Phys., 3:1114–1122, 2001.

[43] C. Kittel. Einführung in die Festkörperphysik. Oldenbourg Wissenschaftsverlag GmbH, München, 15 edition, 2013.

[44] H.W. Klemm. Formation and properties of ultrathin silicon dioxide films on Ru(0001): an in-situ spectro-microscopy study. PhD thesis, TU Berlin, 2018.

[45] H.W. Klemm, G. Peschel, E. Madej, A. Fuhrich, M. Timm, D. Menzel, Th. Schmidt, and H.-J. Freund. Surf. Sci., 643:45–51, 2016.

[46] E.E. Krasovskii, J. Hocker, J. Falta, and J.I. Flege. J Phys Condens Matter, 27:035501, 2015.

[47] G. Kresse and J. Furthmüller. Comp. Mater. Sci., 6:15–50, 1996.

[48] G. Kresse and J. Furthmüller. Phys. Rev. B, 54:11169–11186, 1996.

[49] D. Kuhness, H.J. Yang, H. Klemm, M. Prieto, G. Peschel, A. Fuhrich, D. Menzel, Th.. Schmidt, X. Yu, S. Shaikhutdinov, A. Lewandowski, M. Heyde, A. Kelemen, R. Wł odarczyk, D. Usvyat, M. Schütz, J. Sauer, and H.-J. Freund. J. Am. Chem. Soc., 140(19), 2018.

[50] N.D. Lang and W. Kohn. Phys. Rev. B, 7(8):3541–3550, 1973.

[51] A. Lewandowski, P. Schlexer, C. Büchner, E. Davis, H. Burrall, K.M. Burson, W.-D. Schneider, M. Heyde, G. Pacchioni, and H.-J. Freund. Angew. Chem. Int. Ed., 57:1261–1265, 2018.

[52] L. Li, Q. Shen, J. Li, Z. Hao, Z.P. Xu, and G.Q. M. Lu. Appl. Catalysis. A: General, 344:131–141, 2008.

[53] L. Li, H. Tissot, S. Shaikhutdinov, and H.-J. Freund. Chem. Mater, 29:931–934, 2017.

[54] L. Lichtenstein, C. Büchner, B. Yang, S. Shaikhutdinov, M. Heyde, M. Sierka, R. Wł odarczyk, J. Sauer, and H.-J. Freund. Angew. Chem. Int. Ed., 51:404–407, 2012.

[55] F. Liebau. Structural Chemistry of Silicates. Structure, Bonding and Classification. Springer, Berlin, Heidelberg, München, 1985.

[56] W. Loewenstein. Am. Mineral., 39:92, 1954.

[57] O. Majerus, L. Cormier, D.R. Neuville, L. Galoisy, and G. Calas. J.Non-Cryst. Solids, 354:2004–2009, 2008.

[58] W.L. Mao, Y. Meng, G. Shen, V. B. Prakapenka, A.J. Campbell, D. L. Heinz, J. Shu, R.E. Caracas, R.and Cohen, Y. Fei, R. J. Hemley, and H. Mao. PNAS, 102:9751–9753, 2005.

[59] U. Martinez, L. Giordano, and G. Pacchioni. J. Phys. Chem. B, 110:17015–17023, 2006.

[60] A. Mekki, D. Holland, C.F. McConville, and M. Salim. J. Non-Cryst. Solids, 208:267–276, 1996.

[61] A. Mekki, D. Holland, Kh. A. Ziq, and C.F. McConville. J. Non-Cryst. Solids, 272:179–190, 2000.

[62] H. Müller, D. Preikszas, and H. Rose. J. of Electron Microscopy, 48:191–204, 1999.

[63] M. Monti. Ultrathin Iron Oxide Films on Ru(0001). PhD thesis, Universidad Autonoma de Madrid, 2014.

[64] D. Mori, H. Oka, T. Hosoi, K. Kawai, M. Morita, E.J. Crumlin, Z. Liu, H. Watanabe, and K. Arima. J.Appl. Phys., 120:095306, 2016.

[65] A. Navrotsky and L. Hughes Jr. J. Solid State Chem., 16:185, 1976.

[66] F. Neuberger. Vorlesungsscript: Script zum Versuch Beugung niederenergetischer Elektronen(LEED), https://www.chemie.tu-darmstadt.de/schaefer/ak_schaefer/lehre_2/fpraktikum/index.de.jsp, 04.05.2018.

[67] M. O'Keeffe and B.G. Hyde. Acta Cryst.B, 34:27–32, 1978.

[68] I. Palacio, M. Monti, J.F. Marco, K.F. McCarty, and J. de la Figuera. J. Phys.: Condens. Matter, 25:484001, 2013.

[69] S.T. Pantelides and W.A. Harrison. Phys. Rev. B, 13:2667–2691, 1967.

[70] H. Pfnür, Held G., M. Lindroos, and D. Menzel. Surf. Sci., 220:43–58, 1989.

[71] D. Pinkert and C. Limberg. Chem. Eur. J., 20:9166–9175, 2014.

[72] D. Preikszas and H. Rose. J. Electron Microscopy, 46:1–9, 1997.

[73] Q.S. Qi and R.T. Yang. Appl. Catal. B, 60:13, 2005.

[74] T.S. Rahman, A.B. Anton, N.R. Avery, and W.H. Weinberg. Phys. Rev. Lett., 51(21):1979–1982, 1983.

[75] C. N. R. Rao, P. Vishnu Kamath, and S. Yashonath. Chem. Phys. Lett., 88:13–16, 1982.

[76] M. Ratuszek, M.J. Ratuszek, and J. Hejna. Bulletin of the polish academy of science, technical science, 61, 2013.

[77] D. Ricci and G. Pacchioni. Phys. Rev. B, 69:161307, 2004.

[78] A.E. Ringwood. Amer. J. Sci., 254:707, 1956.

[79] H. Rong, R. Jones, A. Liu, O. Cohen, D. Hak, A. Fang, and M. Paniccia. Nature, 433:725, 2005.

[80] H. Rose. Science and Technology of Advanced Materials, 9:014107, 2008.

[81] H. Rose and D. Krahl. Electron Optics of Imaging Energy Filters. Springer, Berlin, 1995.

[82] A. Sala. Characterization of iron oxide thin films as a support for catalytically active nanoparticles. PhD thesis, Freie Universität Berlin, 2013.

[83] B. Santos, E. Loginova, A. Mascaraque, A.K. Schmid, K.F. McCarty, and J. de la Figuera. J.Phys: Condens. Matter, 21:314011, 2009.

[84] S. Sasaki, Y. Takéuchi, K. Fujino, and S.-I. Akimoto. Z Kristallogr., 158:279–297, 1982.

[85] P. Schlexer, G. Pacchioni, R. Wł odarczyk, and J. Sauer. Surf. Sci., 648:2–9, 2016.

[86] Th. Schmidt, H. Marchetto, P.L. Lévesque, U. Groh, F. Maier, D. Preikszas, P. Hartel, R. Spehr, G. Lilienkamp, W. Engel, R. Fink, E. Bauer, H. Rose, E. Umbach, and H.-J. Freund. Ultramicroscopy, 110:1358–1361, 2010.

[87] T. Schroeder, A. Hammoudeh, M. Pykavy, N. Magg, M. Adelt, M. Bäumer, and H.-J. Freund. Solid State Electron, 45:1471–1478, 2001.

[88] M.P. Seah and W.A. Dench. Surface and Interface Analysis, 1:2, 1979.

[89] S. Shaikhutdinov and H.-J. Freund. Adv. Mater, 25:49–67, 2013.

[90] S. Shaikhutdinov and H.-J. Freund. J. Phys: Condens. Matter, 27:443001, 2015.

[91] D. Shannon. Acta Crystallogr. Sect. A, 32:751–767, 1976.

[92] J.E. Shelby. Introduction to Glass Science and Technology. Royal Science of Chemistry, New York, USA, 2 edition, 2007.

[93] D. Straub and F.J. Himpsel. Phys. Rev. Lett., 52(21):1922–1924, 1984.

[94] E. Takayama, N. Kimizuka, K. Kato, H. Yamamura, and H. Haneda. J. Solid State Chem., 38:82–86, 1981.

[95] S. Tanuma, T. Shiratori, T. Kimura, K. Goto, S. Ichimura, and C.J. Powell. Surf. Interface Anal., 37:833–845, 2005.

[96] H. Tissot, L. Li, S. Shaikhutdinov, and H.-J. Freund. Phys. Chem. Chem. Phys., 18:25027–25035, 2016.

[97] H. Tissot, X. Weng, P. Schlexer, G. Pacchioni, S. Shaikhutdinov, and H.-J. Freund. Surf. Sci., 2018. in press.

[98] O.B. Tsiok, W. Brazhkin, A.G. Lyapin, and L.G. Khvostantsev. Phys. Rev. Lett., 80:999–1002, 1988.

[99] T. Watanabe, T. Onda, and J. Okdomari. ECS Transections, 33:901–912, 2010.

[100] W. Weiss and W. Ranke. Prog. Surf. Sci., 70:1–151, 2002.

[101] J. Weissenrieder, S. Kaya, J.-L. Lu, H.-J. Gao, S. Shaikhutdinov, H.-J. Freund, M. Sierka, T.K. Todorova, and J. Sauer. Phys. Rev. Lett., 95:076103, 2005.

[102] R. Wichtendahl, R. Fink, R.H. Kuhlenbeck, D. Preikszas, H. Rose, R. Spehr, P. Hartel, W. Engel, R. Schlögl, H.-J. Freund, A. M. Bradshaw, G. Lilienkamp, Th. Schmidt, E. Bauer, G. Benner, and E. Umbach. Surf. Rev. Lett., 5:1249–1256, 1998.

[103] R. Wł odarczyk, J. Sauer, X. Yu, J.A. Boscoboinik, B. Yang, S. Shaikhutdinov, and H.-J. Freund. J.Am. Chem.Soc., 135:19222–19228, 2013.

[104] R. W, M. Sierka, J. Sauer, D. Löffler, J.J. Uhlrich, X. Yu, B. Yang, I.M.N. Groot, S. Shaikhutdinov, and H.J. Freund. Phys. Rev. B, 85:085403, 2012.

[105] T. Yamashita and P. Hayes. Appl. Surf. Sci., 254:2441–2449, 2008.

[106] B. Yang, J.A. Boscoboinik, X. Yu, S. Shaikhutdinov, and H.-J. Freund. Nano Lett., 13:4422–4427, 2013.

[107] B. Yang, W.E. Kaden, X. Yu, J.A. Boscoboinik, Y. Martynova, L. Lichtenstein, M. Heyde, M. Sterrer, R. Wł odarczyk, M. Sierka, J. Sauer, S. Shaikhutdinov, and H.-J. Freund. Phys. Chem. Chem. Phys., 14:11344–11351, 2012.

[108] T. Ytterdal, Y. Cheng, and T.A. Fjeldly. Device Modeling for Analog and RF CMOS Circuit Design. John Wiley & Sons, Ltd, England, 2003.

[109] X. Yu, B. Yang, S. Boscoboinik, J.A.and Shaikhutdinov, and H.-J. Freund. Appl. Phys. Lett., 100:151608–151604, 2012.

[110] J.-Q. Zhong, J. Kestell, I. Wlaluyo, S. Wilkins, C. Mazzoli, A. Barbour, M. Kaznatcheev, K. andShete, M. Tsapatsis, and J.A. Boscoboinik. J. Phys. Chem. C, 120:8240–8245, 2016.

[111] X. Zhong, H. Huan, X. Liu, and Y. Yu. Nano Research, pages 1–8, 2017.

Danksagung

Eine Doktorarbeit hat viele Höhen und Tiefen, die einen fordern und fördern. Hiermit möchte ich den Personen danken, die mich durch diese Zeit begleitet, mich unterstützt und zu dieser Arbeit beigetragen haben.

Zuerst möchte ich meinem Doktorvater Prof. Hans-Joachim Freund für die Ermöglichung dieser Arbeit und das in mich gesetzte Vertrauen danken. Im Fritz-Haber-Institut fand ich großartige Möglichkeiten zum Lernen und zum Wachsen vor. Besonders die Internationalität des Instituts und die zahlreichen Seminare führten zu einer exzellenten Forschungsatmosphäre.

Meiner Zweitgutachterin Prof. Katharina Franke möchte ich für die Betreuung und Begutachtung meiner Arbeit danken, sowie für die hilfreichen Hinweise und Ratschläge.

Prof. Dietrich Menzel möchte ich für die wertvollen fachlichen Diskussionen, sowie ausdrücklich für das unermüdliche Korrekturlesen danken.

Einen besonderen Dank möchte ich meinem Arbeitsgruppenleiter Dr. Thomas Schmidt aussprechen, der mir sets mit Rat und Tat zur Seite stand. Durch ihn habe ich mich nicht nur in physikalischen und technischen Fragen weitergebildet, sondern ich habe auch die regen Diskussionen über historische Themen genossen.

Besonders wertvoll waren auch die Mitglieder der Spektro-Mikroskopie Arbeitsgruppe: Daniel Gottlob, Mauricio Prieto, Liviu Tanase, Hagen Klemm, Francesca Genuzio, Alessandro Sala, Eva Madej und Helder Marchetto, sowie die tatkräftige Unterstützung von Marcel Springer und Stephan Pohl. Insbesondere Alexander Fuhrich möchte ich für die langen gemeinsamen Messzeiten und zahlreichen Diskussionen danken.

Auch Radosław Włodarczyk, Xin Yu und Jorge Boscoboiniak möchte ich für die Zusammenarbeit danken, sowie vielen weiteren Mitgliedern des Departments die auf die ein oder andere Weise zum Gelingen dieser Arbeit beitrugen.

Nicht zuletzt möchte ich meiner Familie und meinen Freunden danken, die mich immer unterstützt und ermutigt haben. Und dir Martin, der all den Stress und Druck abgefedert hat.

List of publications

D. Kuhness, H.J. Yang, H. Klemm, M. J. Prieto, G. Peschel, A. Fuhrich, D. Menzel, Th. Schmidt, X. Yu, S. Shaikhutdinov, A. Lewandowski, M. Heyde, A. Kelemen, R. Wlodarczyk, D. Usvyat, M. Schütz, J. Sauer, H.-J. Freund, J. Am. Chem. Soc, A Two-dimensional 'Zigzag'Polymorph on a Metal Support, 140(19) (2018), 6164-6168, DOI: https://doi.org/10.1021/jacs.8b02905

H. Klemm, G. Peschel, E. Madej, A. Fuhrich, M. Timm, D. Menzel, Th. Schmidt, H.-J. Freund, Preparation of Silica Films on Ru(0001): A LEEM/ PEEM Study, Surf. Sci. 643(2016), 45-51, DOI: https://doi.org/10.1016/j.susc.2015.05.017

Selbstständigkeitserklärung

Hiermit versichere ich, dass ich die vorliegende Arbeit selbstständig verfasst, und alle verwendeten Hilfsmittel und Hilfen angegeben habe. Die vorliegende Arbeit wurde nicht in einem früheren Promotionsverfahren eingereicht.

Berlin, den 16.07.2018